Magnetoelectric coupling at the $La_{1-x}Sr_xMnO_3$/ionic liquid interface

Magnetoelektrische Kopplung an Grenzflächen von $La_{1-x}Sr_xMnO_3$ und ionische Flüssigkeiten
Zur Erlangung des akademischen Grades eines Doktors der Naturwissenschaften (Dr. rer. nat.)
genehmigte Dissertation von M.Sc. Phys. Alan Molinari aus Bologna (Italy)
Tag der Einreichung: 29.11.2017, Tag der Prüfung: 26.01.2018
Darmstadt 2018 — D 17

1. Gutachten: Prof. Dr.-Ing. Horst Hahn
2. Gutachten: Prof. Dr. Ralph Krupke

TECHNISCHE
UNIVERSITÄT
DARMSTADT

Fachbereich
Material- und Geowissenschaften
Technische Universität Darmstadt

Institut für Nanotechnologie (INT)
Karlsruher Institut für Technologie (KIT)

Magnetoelectric coupling at the $La_{1-x}Sr_xMnO_3$/ionic liquid interface
Magnetoelektrische Kopplung an Grenzflächen von $La_{1-x}Sr_xMnO_3$ und ionische Flüssigkeiten

Genehmigte Dissertation von M.Sc. Phys. Alan Molinari aus Bologna (Italy)

1. Gutachten: Prof. Dr.-Ing. Horst Hahn
2. Gutachten: Prof. Dr. Ralph Krupke

Tag der Einreichung: 29.11.2017
Tag der Prüfung: 26.01.2018

Darmstadt 2018 — D 17

Bitte zitieren Sie dieses Dokument als:
URN: urn:nbn:de:tuda-tuprints-72712
URL: http://tuprints.ulb.tu-darmstadt.de/7271

Erklärung zur Dissertation

Hiermit versichere ich, die vorliegende Dissertation ohne Hilfe Dritter nur mit den angegebenen Quellen und Hilfsmitteln angefertigt zu haben. Alle Stellen, die aus Quellen entnommen wurden, sind als solche kenntlich gemacht. Diese Arbeit hat in gleicher oder ähnlicher Form noch keiner Prüfungsbehörde vorgelegen.

Darmstadt, den 29.11.2017

(Alan Molinari)

Abstract

One of the major quests in today's microelectronic era is the development of novel low-power magnetic devices for a variety of applications spanning from memory storage and processing to transduction and sensing. Control of magnetism by means of an electric field, based on the phenomenon of magnetoelectric (ME) effect, may be the key alternative to conventional electronics relying on dissipative electrical currents.

In the last years various strategies to interconnect electric and magnetic degrees of freedom have been put to test. A promising approach to straightforwardly and precisely master ME coupling is via charge carrier doping of a magnetic material using an external voltage. This can be realized, akin to the working principle of the field effect transistor, by gating a magnetic electrode with an electrically-polarizable solid (e.g. a dielectric or a ferroelectric) or a liquid electrolyte.

This dissertation reports on the investigation of ME coupling at solid/liquid interfaces in a prototypical system consisting of a $La_{1-x}Sr_xMnO_3$ (LSMO) magnetic electrode electrically charged with an ionic liquid (IL) electrolyte. LSMO - a magnetic perovskite manganite - belongs to the celebrated class of strongly-correlated oxides featuring multiple magnetic states, which directly depend on the oxidation state of the magnetically-coupled manganese ions ($Mn^{3+/4+}$). Upon voltage-driven charge doping the Mn oxidation state is altered, which, in turn, allows to control the balance between double-exchange and superexchange magnetic interactions in LSMO. Furthermore, LSMO possesses a para/ferromagnetic transition slightly above room temperature, which makes it a promising candidate in the perspective of potential applications.

Epitaxial thin ($\approx$ 13 nm) and ultrathin ($\approx$ 3 nm) LSMO films were grown onto single-crystalline $SrTiO_3$ substrates via Large-Distance Magnetron Sputtering (LDMS). This deposition technique demonstrated to be an ideal tool for fabrication of LSMO films with highest quality in terms of crystallinity, surface smoothness and magnetic properties.

The interfacial ME coupling was investigated by combining *in situ* Superconducting Quantum Interference Device (SQUID) magnetometry and Cyclic Voltammetry (CV). This experimental configuration allowed to concurrently extract quantitative information about surface charge density and magnetization as a function of different applied voltages and temperatures.

The analysis of the interfacial charging/discharging processes revealed that the accumulation/depletion of charge carriers is not only driven by electrostatic (electric double layer capacitance) but also electrochemical (redox pseudocapacitance) doping. The presence of both charging mechanisms indicated that the LSMO/IL system behaves as an archetypal hybrid supercapacitor. Large values of surface charge density up to $\approx 300\,\mu\mathrm{C\,cm^{-2}}$ enabled to robustly and flexibly control the magnetic response of LSMO.

In case of LSMO thin films with a thickness of $\approx$ 13 nm a relative magnetic change $\Delta M/M$ of up to 33% was reached, whereas for thinner LSMO films of $\approx$ 3 nm, featuring an enhanced surface-to-volume ratio, ferromagnetism (FM) could be completely suppressed and restored at will. Together with the significant magnitude of the magnetic tuning effect, IL gating provided an outstanding level of reversibility upon cycling, low energy consumption and remarkable switching speed. Additionally, the magnetic signal could be manipulated in-phase and/or anti-phase with respect to the surface charge modulation by appropriately adjusting the applied voltage.

The observed interfacial ME coupling can be qualitatively explained with the major features of the bulk magnetoelectronic phase diagram of LSMO. However, in this study a more precise and consistent microscopic model is proposed on the basis of the quantitative values of the ME coupling coefficient $|\alpha| = |\Delta M/\Delta Q| \approx 3\,\mu_\mathrm{B}/h^+$ and the phenomenon of magnetic phase separation. In such scenario competing FM and non-FM domains expand or shrink at the expense of each other upon voltage-induced charge doping.

On the whole, this work intends to elucidate the physico-chemical mechanisms behind the ME effect at solid/liquid interfaces with the aim of fostering further studies in the yet unexplored area of ME supercapacitors.

Contents

1 Introduction

1.1 Motivation

The magnetoelectric (ME) effect, defined as the induction of magnetization by an electric field or, vice versa, of an electric polarization by a magnetic field, has triggered intense fundamental and application-oriented research in the last years [1]. The ability to control the correlation between magnetic and electric properties of matter at the nanoscale brings the promise of realizing novel microelectronic devices with enhanced miniaturization, fast switching response and low-power consumption, which would revolutionize the areas of memory storage and signaling transduction.

An elegant way to tackle the challenge of mutual manipulation of electric and magnetic degrees of freedom is by using ME multiferroics (MFs) [2]. These are single-phase materials where at least two ferroic properties such as ferromagnetism and ferroelectricity are inherently coupled to each other. Although ME MFs offer an ideal playground for studying ME coupling, the scarcity in nature of such materials and their generally weak and low-temperature ME effect limit their use to fundamental studies.

An attractive alternative is provided by composite MEs, where ME coupling is realized at the interface between two materials that are magnetically and electrically polarizable. For example, mimicking the gating approach used in the field effect transistor [3], the control of the magnetism can be achieved via electrostatic charge doping of a magnetic material by using dielectrics [4], ferroelectrics [5] or electrolytes [6]. Differently, electrochemical [7] or strain [2] effects can also act as mediator between electric and magnetic properties.

The accessible combinations of materials, geometries and approaches, virtually-infinite thanks to the modern means of nanotechnology, provide invaluable opportunities for investigation of the ME effect. Currently, most of the ongoing research focuses on all-solid-state composites. Giant ME effects have been attained in some all-solid-state systems [4, 8–15]. However, the path towards the realization of a working ME device is still long. Indeed, although a high magnetic on/off ratio is certainly desirable, often it is attained at the expense of adequate reversibility, operating voltage, switching speed and working temperature.

Alternatively to all-solid-state devices, a very effective approach, yet largely uncharted, is offered by solid/liquid ME composites [6]. In the present work, the system of choice for studying ME coupling is represented by $La_{1-x}Sr_xMnO_3$ (LSMO) thin films electrically charged with an ionic liquid (IL) electrolyte.

LSMO belongs to the class of magnetic perovskite manganites exhibiting strong coupling between spin, orbit and lattice parameters [16]. This complex oxide features a variety of magnetic states sensitive to the charge state, bond length and angle between Mn–O–Mn chains, which can be affected in different ways by an external electric field. In addition, depending on the Sr doping concentration, LSMO can have a Curie point above room temperature, which is desirable in the perspective of possible device applications.

The charging agent, i.e. DEME-TFSI ionic liquid, belongs to the category of non-aqueous electrolytes [17]. IL electrolytes can be used to induce accumulation of charge carrier densities up to 10^{14}-10^{15} cm^{-2}, which is well beyond the values achievable with the best ferroelectrics. Whether the high values of charge carrier doping (and thus also capacitance) are due to purely-electrostatic or electrochemical charging is often debatable [18, 19]. However, it has already been proven that fascinating phenomena, such as metal-to-insulator transition [19], para-to-ferromagnetic transition [20] or superconductivity [21, 22] can be controlled via electrolyte gating.

1.2 Scope and outline of the thesis

This thesis presents results of the comprehensive investigation of the ME coupling at the interface between LSMO films and an IL electrolyte (DEME-TFSI). Upon application of an external voltage the induced accumulation/depletion of surface charge carriers allows to reversibly manipulate the double-exchange (DE) and superexchange (SE) magnetic interactions, or, in other words, to explore different areas of the LSMO magnetoelectronic phase diagram.

The initial task was to grow epitaxial, atomically-smooth thin films of LSMO over large surface areas on top of single-crystalline $SrTiO_3$ substrates. Large-Distance Magnetron Sputtering (LDMS), featuring an unconventional large target-substrate separation, proved to be a suitable and reliable deposition method to attain excellent structural and magnetic properties. The thickness of the LSMO films was kept in the 3 - 15 nm range in order to preserve a high surface-to-volume ratio, which is preferable considering the interfacial nature of the ME effect. Microstructure and magnetic properties of the LSMO samples have been extensively analyzed with a variety of characterization methods.

The second step was to perform *in situ* tuning measurements of LSMO magnetic response while charging its surface via IL gating. In this regard, the combination of Superconducting Quantum Interference Device (SQUID) magnetometry and Cyclic Voltammetry (CV) provided powerful tools to concurrently and quantitatively track magnetic and charge signals, respectively. The ME coupling was studied on thin films of LSMO with a thickness of about 13 nm at different temperatures ($200\,\mathrm{K} < T < 340\,\mathrm{K}$), applied voltages ($0.2\,\mathrm{V} < \Delta V < 3.7\,\mathrm{V}$) and voltage ramp rates ($3\,\mathrm{mV\,s^{-1}} < \mathrm{d}V/\mathrm{d}t < 300\,\mathrm{mV\,s^{-1}}$).

Finally, the performance of the solid/liquid ME devices was put to test in terms of the magnitude of the magnetic tuning effect, cycling stability, power consumption and speed response in case of ultrathin LSMO films with an optimized thickness of about 3 nm.

The present dissertation is organized in the following chapters:

Chapter 1 is a survey of the ME effect, starting from a brief historical background, until reaching the current state-of-the-art on MFs, all-solid-state and solid-liquid composite MEs. Strengths and weaknesses of the various approaches and their relationship will be discussed. Since the thesis embraces in particular ME effect at solid/liquid interfaces, the fundamental charging/discharging mechanisms using electrolytes, namely electric double layer capacitance, pseudocapacitance and electrochemical intercalation, will be discussed as well.

Chapter 2 summarizes the key features of the employed materials, the LDMS deposition method and the characterization techniques. Details about structural and magnetic properties of LSMO and strongly-correlated manganites and the main characteristics of the employed IL electrolyte (DEME-TFSI) will be given. Afterwards, the experimental setup implemented for carrying out *in situ* ME measurements, including the ME tuning cell used to host the LSMO/IL devices, will be described.

Chapter 3 elaborates on the optimization of the growth conditions of LSMO films and the resulting microstructural and magnetic properties. Special attention is paid to the influence of post-deposition annealing and different growth temperatures on the LSMO characteristics.

Chapter 4 illustrates the outcomes of the *in situ* ME tuning experiments. Thorough analysis of both magnetic and charging/discharging responses under different conditions of temperature, applied voltage and voltage ramp rate will be presented. Interpretation of the interfacial ME coupling mechanisms will be done taking into account the bulk magnetic phase diagram of LSMO and the quantitative values of ME coupling coefficient $\alpha = \Delta M/\Delta Q$.

Chapter 5 shows the investigation of the ME effect in case of ultrathin LSMO films with an optimized thickness of only ≈ 3 nm. The experimental results will be critically compared with the recent advances established in ME systems.

Chapter 6 contains some concluding remarks and an outlook on possible future work in the field of solid/liquid composite MEs.

1.3 The magnetoelectric effect

In its most general definition, the ME effect[1] refers to the coupling between electric and magnetic properties in matter. More specifically, the *direct* ME effect occurs when an electric polarization P is induced by application of a magnetic field H according to:

$$\Delta P = \alpha_{\mathrm{D}}\,\Delta H \tag{1.1}$$

where α_{D} is the so-called direct, linear[2] ME coupling coefficient[3].

The *converse* ME effect implies the electric field control of magnetism and follows the relation:

$$\Delta M = \alpha_{\mathrm{C}}\,\Delta E \tag{1.2}$$

where M, E and α_{C} are the induced magnetization, the applied electric field and the converse ME coupling coefficient, respectively.

Historically, the initial studies on the ME effect go back to 1888, when Roentgen [37] discovered that a dielectric material moved in an electric field can be magnetized. A few years later also the reverse effect [38] was demonstrated: by moving a dielectric in a magnetic field, an electric polarization can be induced. Curie [39] was the first in 1894 who suggested the possibility of a static ME effect intrinsic in non-moving systems on the basis of symmetry considerations.

---

[1] To further deepen into the topic of ME coupling, the reader may also refer to the abundant amount of very comprehensive reviews in the literature [2, 8, 23–36].

[2] The majority of research on ME coupling is devoted to the linear ME effect and it is generally acceptable to omit such prefix. In the following we will adhere to this convention. Nonetheless, it should be noticed that for a formal description of the ME effect, higher order coefficients should be included as well.

[3] A discussion on the variant definitions of ME coupling coefficient present in the literature is developed in the Appendix (Section A.1.1).

During the next decades, apart from a few unsuccessful experiments [40, 41], there was a gap in the experimental research until in 1959 Dzyaloshinskii [42] theoretically predicted the occurrence of ME effect in the antiferromagnetic compound Cr_2O_3. Just a few years later an electric-field-induced magnetization [43] and a magnetic-field-induced polarization [44] of Cr_2O_3 were experimentally proved. These pioneering experiments triggered the search for new ME systems. Already in 1973 about 80 single-phase compounds were classified [45] as MEs and more were added afterwards. For instance, ME coupling was found in Ti_2O_3 [46], $GaFeO_3$ [47], $PbFe_{0.5}Nb_{0.5}O_3$ [48], $Y_3Fe_5O_{12}$ [49], and $TbPO_4$ [50].

Despite the flurry of new discovered ME materials, it became clear already after the first experiments that the magnitude of the ME effect in single-phase MEs is intrinsically small. As an example, considering the maximum value obtained by Rado *et al.* [51], the ME effect in Cr_2O_3 corresponds to the flipping of only five ferromagnetically-coupled spins in a lattice of 10^6 antiferromagnetically-coupled spins upon application of an electric field of $10^6\,\mathrm{V\,cm^{-1}}$. It has been established [52] that the size of the ME effect is limited by:

$$\alpha^2 < \varepsilon\mu \tag{1.3}$$

where ε and μ indicate the dielectric permittivity and the magnetic permeability, respectively, or more rigorously [53]:

$$\alpha^2 < \chi^e \chi^m \tag{1.4}$$

where χ^e and χ^m denote the electric and magnetic susceptibilities, respectively.

Therefore, aiming at larger ME effects, the attention was brought to ferroelectric and ferromagnetic materials, which possess the highest values of permittivity and permeability. In this regard, there was great excitement once it was discovered that a certain class of materials – the so-called multiferroics (MFs) – possess both ferroelectricity and ferromagnetism (often, but not always) intrinsically coupled to each other in one single-phase compound.

As a parallel stream of research to single-phase ME systems, the idea was developed of combining electric/magnetic materials in which the ME effect is not inherently manifested, but originates as a product property between the constituents [54]. Interestingly, already in the

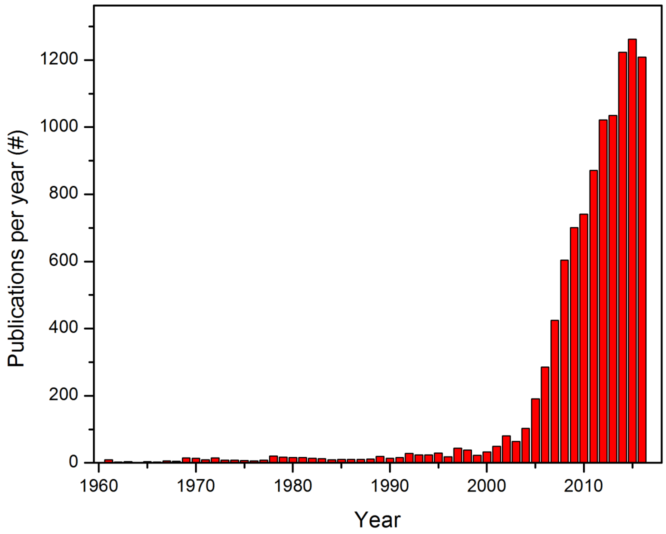

Figure 1.1: Chronological number of publications per year based on statistical data according to THOMSON REUTERS *Web of Knowledge*, as returned for the search criterion 'Multiferroic' or 'Magnetoelectric'.

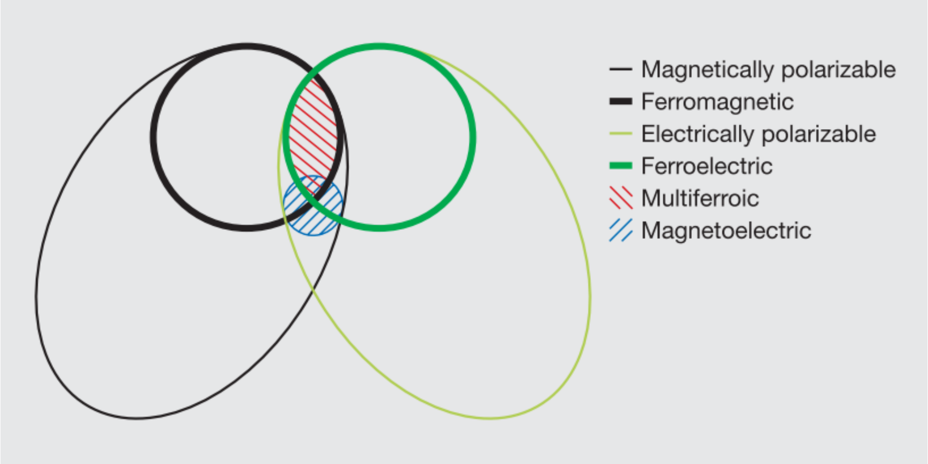

Figure 1.2.: Classification of ME materials. The ME effect is a phenomenon that can, but not necessarily, arise by the coupling between magnetically and electrically polarizable materials (and their subsets). To notice that the area of MFs is given by the intersecting set of ferromagnets and ferroelectrics, which only partially overlaps with the sector of MEs. (Reprinted by permission from MACMILLAN PUBLISHERS LTD: *Nature* [25], ©2006)

initial experiments [55, 56], the ME coupling in composite MEs was stronger than in single-phase MEs and controllable near room temperature.

The early studies on MFs and MEs had to face non-trivial obstacles hampering the investigation of the ME effect. On the one hand, there was scarcity of reliable experimental techniques to properly control the growth of good quality crystals and compounds. On the other hand, both theoretical and experimental methods for the analysis of the ME effect were still in a germinal phase.

Thanks to the development and improvement in experimental and theoretical physics, including techniques capable of controlling matter at the nanoscale, the last two decades witnessed a revived interest on the topic, as confirmed by the increased number of publications per year in the fields of MEs and MFs (see Fig. 1.1).

A classification of the systems presenting ME effect is depicted in the diagram of Fig. 1.2. In the next sections the most common ME systems (single phase MFs and composite MEs) and approaches (strain, electrostatic charge doping and ionic migration) that can be used to realize ME effect will be described. Since the results presented in the current dissertation focus on electric field control of magnetism, more details on the converse rather than direct ME effect will be given. The attributes 'direct' or 'converse' will be tacitly omitted when clearly understandable from the context, whereas they will be specified in case they are required to avoid ambiguity.

1.4 Single-phase multiferroic magnetoelectrics

According to the definition of Schmid [57], multiferroics are single-phase materials possessing two or more primary ferroic properties, i.e. ferromagnetism, ferroelectricity, ferroelasticity and ferrotorodoicity. A more generalized definition includes also the antiferroic counterparts [58]. In the past also expressions like *ferroelectromagnets* [23] were used in the case of (anti)ferromagnetic (anti)ferroelectrics.

A MF material is considered to be also ME when it displays simultaneously ferromagnetism and ferroelectricity and the two properties are coupled to each other[4]. In some cases ferromagnetism and ferroelectricity are not macroscopically coupled due to symmetry restrictions[5], but ME interactions may still be active on a microscopic level [2].

The discovery of the first multiferroic material in the early 1960s is attributed to a group of Leningrad physicists [60, 61] who prepared the first ferroelectromagnet $Pb(Fe_{2/3}W_{1/3})O_3$, which combined ferroelectric and antiferromagnetic properties. Moreover, they synthesized the first ferroelectric ferromagnetic solid solution $(1\text{-}x)Pb(Fe_{2/3}W_{1/3})O_3 + xPb(Mg_{1/2}W_{1/2})O_3$ [62, 63].

In nature only two crystals, the congolite $Fe_3B_7O_{13}Cl$ [64] and the chambersite $Mn_3B_7O_{13}Cl$ [65], are known to be MF. The nearly remaining 80 systems which exhibit multiferroicity are artificial.

Classification of MFs can be done according to structural features [2, 23]:

- **perovskite-type compounds** with chemical formula ABO_3 or $A_2B'B''O_6$. Typically the unit cells do not have an ideal cubic symmetry, but are slightly deformed. A variety of MF compounds can be obtained by chemical substitution. Examples of such perovskite-type MFs are $Pb(Fe_{2/3}W_{1/3})O_3$, $Pb(Fe_{1/2}Nb_{1/2})O_3$, $Pb(B_{1/2}Re_{1/2})O_3$ (with B = Fe, Mn, Ni, Co), and $BiFeO_3$ [62].
- **hexagonal-type compounds** where the main group is formed by the ferroelectric antiferromagnetic manganites RMnO$_3$ with R = Sc, Y, In, Ho, Er, Tm, Yb, Lu.
- **boracites compounds** with general formula $M_3B_7O_{13}X$ where M = Cr, Mn, Fe, Co, Cu, Ni and X = Cl, Br, I, respectively.
- **orthorhombic $BaMF_4$ compounds** with M = Mg, Fe, Mn, Co, Ni,Zn.

MF materials with coexistence of ferroelectricity and ferromagnetism are very appealing from a technological point of view. The combination of the two properties is considered a sort of *holy grail* in the field of information technology because the currently-used magnetic random access memories may be replaced by non-volatile counterparts in which an information bit could be written with a low-power electric field and read by detecting a magnetic field [66]. Unluckily, theoretical studies have shown that, in general, the presence of transition metal d electrons, which are essential for ferromagnetism, reduce the tendency for off-center unit cell distortion, which is a necessary condition for ferroelectricity [66]. Thus, the already not very ample class of MFs shrinks even further when the attention is restricted to the ones presenting both ferromagnetism and ferroelectricity.

The first experimental observation of cross-correlation between magnetic and electric domains in MF was achieved in 2002 when Fiebig *et al.* [69] investigated the coupling between antiferromagnetic and ferroelectric domains in $YMnO_3$ by imaging with optical second harmonic generation. One year later Kimura *et al.* [70] reported on gigantic ME effect in $TbMnO_3$ in which ferroelectricity was induced on application of a magnetic field. Afterwards, in 2004 highly reproducible electric polarization reversal and permanent polarization imprint in $TbMn_2O_5$ were actuated using a magnetic field [67] (see Fig. 1.3(a)). The same year Lottermoser *et al.* [71] reported on the converse effect with on and off switching of ferromagnetic ordering in $HoMnO_3$

---

[4] Vice versa, notice that often single-phase MEs do not present multiferroicity: for example Cr_2O_3 is a single-phase ME with coupled antiferromagnetism and electric polarizability, thus lacking of a ferroic electrical counterpart. Nonetheless, in the literature the disambiguation between MFs and MEs is not always strict: in some cases Cr_2O_3 is referred as a single-phase MF [59].

[5] ME effect is allowed only in systems were both spatial and time reversal symmetry are broken [2].

by application of an external electric field. In 2012 Tokunaga *et al.* [68] proved reversible switching of magnetization in a bulk single crystal of $Dy_{0.7}Tb_{0.3}FeO_3$ using electric field pulses (see Fig. 1.3(b)). To date, the manipulation of coupled electric and magnetic domains using external fields is still under intense investigation [72]. Despite the fascinating physical phenomena discovered in single-phase MFs, a persistent crucial constraint against device applications is related to the electric and magnetic ordering temperatures that are often far below room temperature [23].

Among the panorama of MFs, $BiFeO_3$ is probably the most investigated system of the last years [73]. Bulk $BiFeO_3$ is one of the few robust room-temperature ME MFs with antiferromagnetic Néel temperature around 650 K and ferroelectric Curie temperature around 1100 K. Antiferromagnetism is manifested as short-range ordering with each Fe^{3+} spin surrounded by six antiparallel spins on the nearest Fe neighbors and a long-range order with a cycloidal-like shape [74] over tens of $BiFeO_3$ unit cells. Weak ferromagnetism ($\approx 0.02\ \mu_B\,Fe^{-1}$) is detected in $BiFeO_3$ due to canting of the antiferromagnetically aligned spins by the Dzyaloshinskii–Moriya (DM) interaction [75, 76]. The electric polarization of $BiFeO_3$ can be as high as 150 $\mu C\,cm^{-2}$ [77], which exceeds the values reachable in Pb-based ferroelectrics [78] (and with the non-trivial advantage of being non toxic). However, the fabrication of high quality crystals with low leakage current is a challenging task [79].

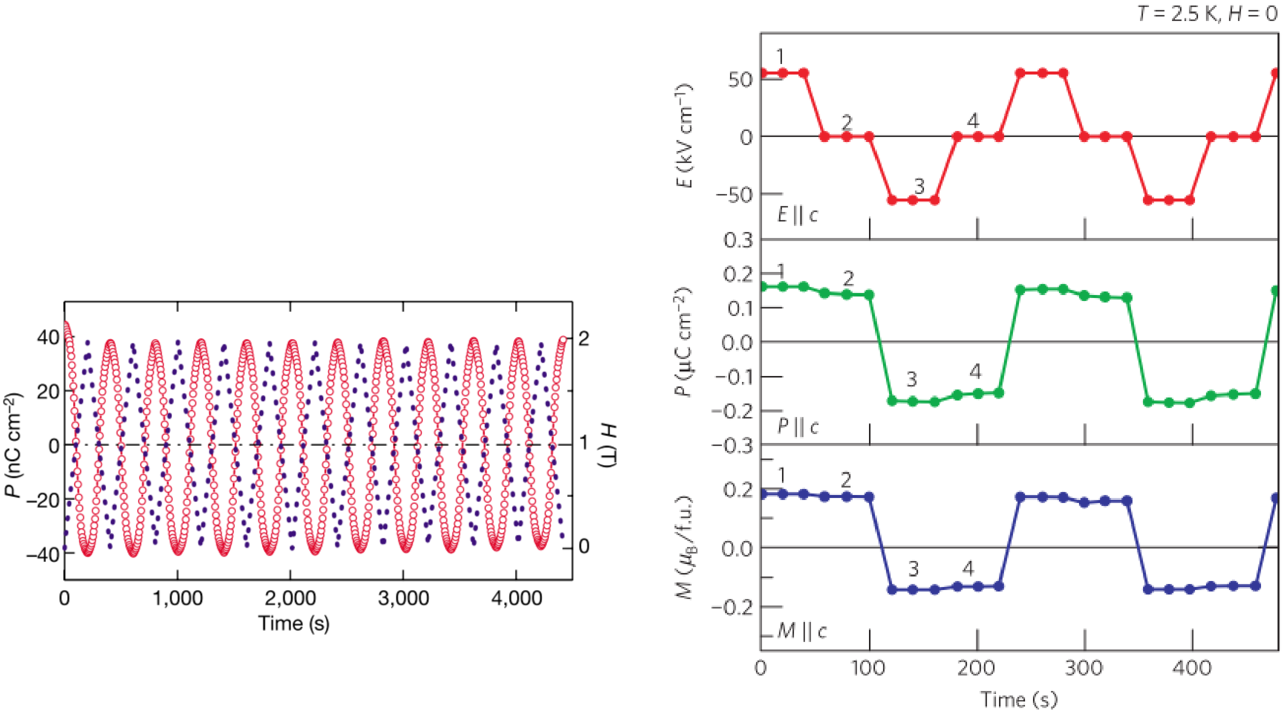

(a) Direct ME effect in $TbMn_2O_5$

(b) Converse ME effect in $Dy_{0.7}Tb_{0.3}FeO_3$

Figure 1.3.: Magnetoelectric effect in single-phase multiferroics. (a): Reversible electric polarization flipping at 3 K by linearly varying magnetic field from 0 to 2 T in multiferroic $TbMn_2O_5$. (b): Reversal of magnetization in multiferroic $Dy_{0.7}Tb_{0.3}FeO_3$ at 2.5 K due to reversal of electric polarization with an electric field. (Adapted by permission from MACMILLAN PUBLISHERS LTD: *Nature* [67], ©2004; *Nature Physics* [68], ©2012)

In 2003 there was great excitement when a group [80] reported that strained $BiFeO_3$ films epitaxially grown on $SrTiO_3$ substrates possessed a high polarization of 90 $\mu C\,cm^{-2}$ together with an unexpectedly high magnetization of 1 $\mu_B\,Fe^{-1}$. Nonetheless, the results were not reproducible and another group [81] ascribed the enhanced magnetization to oxygen off-stoichiometry. Despite the lack of robust ferromagnetism, $BiFeO_3$ provides an ideal playground for studying the coupling between magnetic and electric order parameters. For instance, antiferromagnetic domain switching was induced upon ferroelectric domain switching at room temperature [82]. Examples of how such control has been exploited in more complex composite systems shall be given in the next section.

Recently, another example of a room temperature multiferroic system was provided by Henrichs *et al.* [83] who discovered a novel relaxor ferroelectric single-phase material, $(BiFe_{0.9}Co_{0.1}O_3)_{0.4}$–$(Bi_{1/2}K_{1/2}TiO_3)_{0.6}$, featuring MF clusters in which ME coupling was locally controlled using both piezoresponse and magnetic force microscopies.

1.5 ME effect in all-solid-state composite devices

Comparing to the rather limited families of single phase MEs and MF MEs, composite MEs offered an unprecedented flexibility in terms of involved materials, stoichiometries and microstructures. Indeed, in principle, any combination of magnetic polarizable (e.g. paramagnets or ferromagnets) and electric polarizable (e.g. paraelectrics or ferroelectrics) materials may give rise to ME coupling. The spread of the composite ME approach went along with the development of nanotechnology, which allowed for careful adjustment of the materials control parameters and of the quality of interfaces down to the atomic level. In addition, in the course of the studies it was discovered that various phenomena can be exploited to realize interfacial ME effects. For example, strain is the source of the ME coupling at the interfaces between magnetostrictive and piezoelectric materials. Alternatively, following the same principles governing a field-effect transistor or a battery, electrostatic charge doping or electrochemical ionic diffusion can be used to control magnetism via application of an external voltage.

1.5.1 ME coupling via strain

Experiments on composite ME systems started with the utilization of strain acting as mediator between electric and magnetic order parameters in bulk macroscopic constituents. Indeed, when magnetostrictive and piezoelectric materials are put in contact with each other, either an electric or a magnetic field can be used to influence the mutual counterparts, i.e. magnetic or electric polarizabilities, respectively. The first successful composite ME was realized in 1972 and consisted of ferroelectric piezoelectric $BaTiO_3$ and ferromagnetic magnetostrictive $CoFe_2O_4$ solidified in the form of particles from the liquid phase [55, 84]. Thereafter, several other material combinations were investigated: $PbZr_{1-x}Ti_xO_3$ (PZT)/ ferrites [85–87], PZT/$Tb_{1-x}Dy_xFe_2$(Terfenol-D) [24, 88], PZT/LSMO [89], PZT/$Fe_{0.5}Co_{0.5}$ [56] and Terfenol-D/polyvinylidenefluorid [90]. Soon the attention was brought from particulate to laminate composites, which allowed to overcome some of the negative side effects occurring during the preparation of particles, such as the formation of chemically impure phases, mechanical defects and non-homogeneous particle dispersion. For instance Ryu *et al.* demonstrated that using a laminar geometry the ME effect could be enhanced reaching values of ME coupling coefficient two orders of magnitude higher than in single phase

MEs [88]. Further studies aimed at improving the size of the ME effect by investigating different thickness ratios between piezoelectric and magnetostrictive units [90, 91], number of stacking layers [89] and kind of bonding between the layers [92]. The ME effect was also studied as a function of the direction of the external field with respect to the stacking layers: it was found that the transverse ME response is more pronounced, but of the same order of magnitude, compared to the longitudinal ME response [92]. Interestingly, an intensified ME effect was observed when the frequency of the external field was set in resonance with the vibrational mechanical modes of the layered structure. Under conditions of resonance frequency Laletsin *et al.* [56] attained in $Fe_{0.5}Co_{0.5}$/PZT/$Fe_{0.5}Co_{0.5}$ trilayers an increase in ME effect exceeding more than three orders of magnitude the values of single phase MEs. Alternative geometries with vertical PZT pillars embedded in a Terfenol-D/epoxy matrix were also put to test [93].

The abundant amount of experimental research was accompanied by an as much ample number of theoretical works which helped to disentangle the complex physics underlying the ME coupling [94–98].

In the last 15-20 years, the results attained in bulk composites together with the substantial progress in growth and characterization techniques has triggered the interest in the topic of ME coupling looking from a nanoscale perspective. The control of matter down to the atomic level allows for precise adjustment of composition, size and morphology of the involved species [28].

Regarding strain-mediated ME coupling, several kinds of magnetic thin films have been grown on single crystal piezoelectric substrates. Manganese-based oxides (also called manganites), due to their intrinsic strong correlation [99] between spin, orbit, lattice degrees of freedom, which binds together magnetic, electric and elastic properties, are often chosen as prototypical systems[6]. Lee *et al.* [100] studied the influence on the electrical transport and magnetic properties of thin films ($\approx$ 50 nm) of $La_{0.67}Sr_{0.33}MnO_3$ epitaxially grown on $BaTiO_3$ substrates as a function of the structural phase transitions occurring in the substrate at different temperatures. In proximity of the BTO phase transitions jumps of up to 12% and 70% in electrical resistivity and low-field magnetization of LSMO were found, respectively. Nonetheless, rather than modification of temperature, the usage of an external voltage to control the strain state (and so magnetization) is technologically more appealing. In the light of this idea, Eerenstein *et al.* [9] analyzed the behavior of magnetization in LSMO/BTO heterostructures by application of an external voltage to control the substrate strain. The authors reported on giant sharp and persistent switching of magnetization of up to 65% (in particular in the vicinity of the BTO phase transitions) driven by an external voltage (see Fig. 1.4(a)). The increase, removal or reversal of the voltage did not modify anymore the magnetization. The ME effect was giant and exceeded the values achieved by Ryu *et al.* [88] in bulk composites. Electric field effects related to electrostatic charge carrier doping were assumed to be absent. The influence of dynamic modification of strain via electric fields was also studied on LSMO and $La_{1-x}Ca_xMnO_3$ (LCMO) thin films grown on piezoelectric $Pb(Mg_{1/3}Nb_{2/3})_{0.72}Ti_{0.28}O_3$ substrate [101].

In other studies, ferromagnetic metals were combined with piezoelectric substrates. Changes in the magnetic coercivity of up to 40% were observed in Fe thin films deposited on BTO substrates [102, 103]. The out-of-plane magnetization of a Cu/Ni multilayer was switched to in-plane using the voltage-induced strain of a BTO substrate [104]. Enhanced ferromagnetic resonance tunability and non-volatile, bistable magnetization switching with a change of up to 60% was attained in FeGaB/PZN-PT heterostructures via strain mediated ME coupling [105].

---

[6] A more specific introduction to manganites shall be given under Materials and Methods.

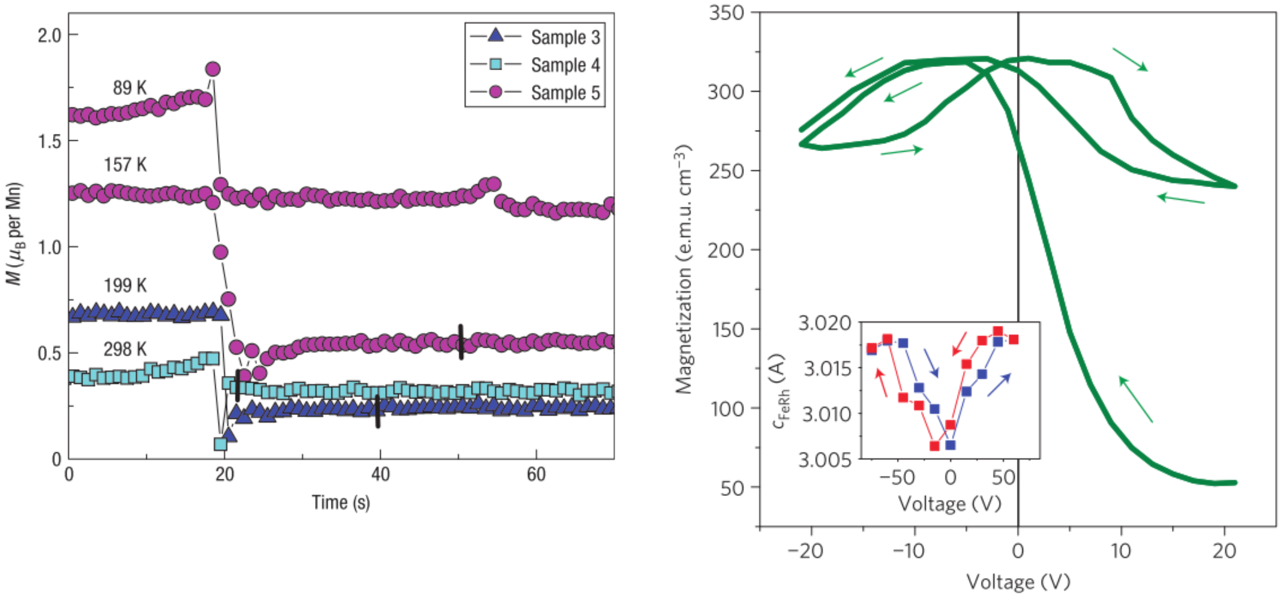

(a) Strain-mediated ME effect in LSMO/BTO **(b)** Strain-mediated ME effect in FeRh/BTO

Figure 1.4.: Strain-mediated ME effect in solid-state nanocomposites. (a): Large and sharp magnetic switching in LSMO/BTO heterostructures due to an applied electric field. The switching persisted after the electric field was abruptly switched off (vertical black lines). The data were recorded at 4 $\mathrm{kV\,cm^{-1}}$ (sample 3), 10 $\mathrm{kV\,cm^{-1}}$ (sample 4) and 6 $\mathrm{kV\,cm^{-1}}$ (sample 5 at both 89 K and 157 K). (b): Voltage-induced magnetic variation at 385 K in epitaxial FeRh films on top of BTO substrates. The initial large irreversible change in magnetization is followed by a smaller reversible magnetic modulation. The inset shows the voltage dependence of the out-of-plane lattice parameter of FeRh at 390 K. (Reprinted by permission from MACMILLAN PUBLISHERS LTD: *Nature Materials* [9], ©2007; *Nature Materials* [14], ©2014)

A giant strain-mediated ME effect was reported by Cherifi *et al.* [14] in FeRh/BTO heterostructures. Changes in the magnetization of FeRh thin films of up to $\approx 550\,\mathrm{emu\,cm^{-3}}$ - corresponding to a shift of $T_C \approx 25$ K - were produced using an external voltage of about ± 20 V above room temperature. Nonetheless, it should be pointed out that the variation in magnetization featured only a minor reversible part of about $\approx 70\,\mathrm{emu\,cm^{-3}}$ (see Fig. 1.4(b)). The butterfly-like shape of the magnetic response on changing the voltage confirmed that strain was the main driving force of the ME coupling. The slight asymmetry in the observed loop could be ascribed to asymmetry in the strain or to a "secondary" electric field effect, namely electrostatic charge carrier doping at the substrate/film interface.

Although in the previous examples also giant ME effects were obtained, the practical usage of strain to control the ME effect is often hampered by some non-trivial aspects. For example, strain, in order to be effective, requires thicknesses of the piezoelectric material markedly larger than the magnetic layers. This is the reason why in most of the circumstances bulk macroscopic piezoelectric substrates are chosen rather than thin films. Indeed, if a piezoelectric material were chosen in the form of a thin film, the inevitable presence of an underlying substrate would block the propagation of strain. In this respect, a workaround to reduce substrate clamping effects have been proposed by growing vertically-aligned rather than planar ME composites [106, 107].

Anyhow, the typically-employed large size of the piezo-ferroelectric does not facilitate integration in modern microelectronics. Furthermore, another factor that should not be underestimated is the endurance of strain-based devices, which can be limited by cracking during poling, sparking and contact loosening [9]. Aging effects may also be accelerated by orientation of intrinsic defects [2] or ionic diffusion (e.g. oxygen anions) at large electric fields [13].

1.5.2 ME coupling via electrostatic charge doping

The same principle governing the "workhorse" [108] of modern microelectronics - the field effect transistor (FET) - offer attractive means to realize the ME effect. Fig. 1.5 shows a simplified[7] FET configuration, where a "gate" dielectric of thickness d is put in contact with a "channel" composed of a magnetic material. By application of an external voltage ΔV the formation of an electric field $E = \Delta V/d$ polarizes the dielectric material. The polarization charge induced at the dielectric extremes is compensated by the accumulation of opposite charge carriers in the channel counterpart. The phenomenon is known as *electrostatic charge doping* and allows for reversible modulation of the charge carrier density of the channel [3, 108]. If the latter is composed of a magnetic material, the modification of the electronic structure affects not only the electric transport but also the magnetic properties. In a classical scenario[8], the reason is due to the change in the number of elementary charge carriers, each one contributing with one spin (and so one Bohr magneton μ_B) to the magnetization.

The choice of channel and gate materials plays a crucial role in the control of the ME coupling. The magnitude of the magnetic tuning effect is directly related to the amount of charge carriers that can be accumulated/depleted at the interface [8, 109]. In this regard an important figure of merit is the *capacitance*:

$$C = \frac{Q}{V} \tag{1.5}$$

---

[7] Notice that in this way the structure is analogous to a regular dielectric capacitor.

[8] In the next chapters it will be described why in the case of LSMO it is not possible to invoke a simple classical scenario to explain the origin of ME coupling [16].

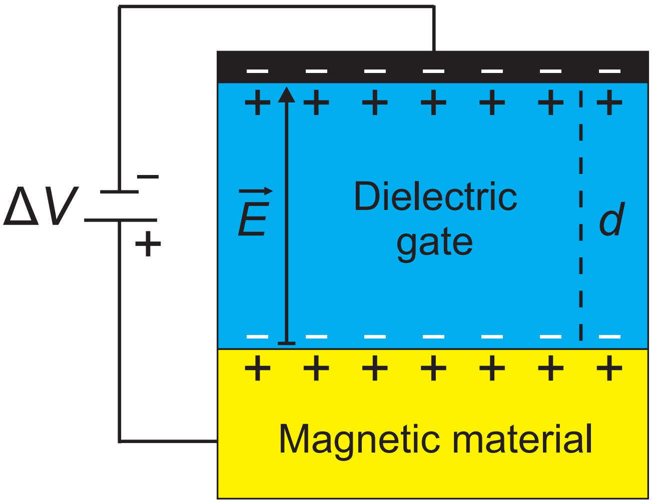

Figure 1.5: Principle of electrostatic charge doping for the control of magnetism. By exploiting the polarization of a dielectric, the charge carrier density of a magnetic material can be varied and therefore also its magnetoelectronic configuration. In the schematic ΔV, E and d correspond to the applied external voltage, the electric field and the thickness of the dielectric, respectively.

defined as the ratio between the total amount of charge induced at the interface and the applied voltage. A large capacitance signifies a large surface charge carrier density via application of low voltage. Considering a parallel-plate capacitor structure, C is also given by:

$$C = \varepsilon_0 \kappa \cdot \frac{A}{d} \tag{1.6}$$

where $\varepsilon_0 = 8.85 \cdot 10^{-12}\,\mathrm{F\,m^{-1}}$ is the dielectric permittivity of vacuum, κ is the relative permittivity of the dielectric material, A is the surface area of the capacitor and d is the thickness of the dielectric material. The implementation of high-κ dielectrics or ferroelectrics, large surface areas and a small thickness of the gate material are helpful to attain high values of capacitance. By using high-κ dielectrics a charge carrier doping of up to about $10^{13}\,\mathrm{cm^{-2}}$ can be achieved, whereas ferroelectrics can reach up to $10^{14}\,\mathrm{cm^{-2}}$. Table 1.1 summarizes the main parameters of commonly-used high-κ dielectrics and ferroelectrics. Apart high values of capacitance and surface charge, the channel/gate chemical compatibility and the quality of interfaces and microstructures are of primary importance as well. Indeed, defects such as dislocations [110, 111] can act as preferential conduction paths for the charge carriers thus causing leakage current and, in the worst scenario, dielectric breakdown.

Table 1.1.: Typical values of dielectric constant κ, surface capacitance C and surface charge density modulation ΔQ of commonly-used dielectrics and ferroelectrics. The surface capacitance C has been calculated using Eq. 1.6 on the basis of dielectric constants κ reported in the literature and assuming a dielectric thickness of 300 nm.

Material	κ	C ($\mu\mathrm{F\,cm^{-2}}$)	ΔQ ($\mu\mathrm{C\,cm^{-2}}$)	Reference
SiO_2	3.9	0.01	1 - 3	[108, 112, 113]
Al_2O_3	8 - 9	0.02	1.1	[112, 114, 115]
HfO_2	22 - 25	0.07	1.3	[112, 116]
ZrO_2	22 - 25	0.07	0.8 - 9.6	[112, 116, 117]
TiO_2	50 - 80	0.2	1 - 2	[112, 118]
$SrTiO_3$	200 - 400	0.9	8 - 13	[119–121]
$BaTiO_3$	3800	11.2	50 - 70	[77, 122, 123]
$PbZrTiO_3$	5000	14.7	80 - 100	[78, 101]

The electronic nature of the magnetic channel material is another crucial factor to be considered. On the one hand, if the magnetic material is a metal, the applied electric field is screened by the high concentration of free charge carriers (e.g. Fe has a free electron density of $n \approx 10^{22}\,\mathrm{cm^{-3}}$ [124]) at the very proximity of the surface, which leads to a Thomas-Fermi screening length of the order of about one-two Angstrom. On the other hand, magnetic semiconductors have a lower charge density ($n < 10^{20}\,\mathrm{cm^{-3}}$ [20]), and thus the electric field can penetrate several nanometers into it with a bigger portion of the magnetic volume being affected. Consequently, in

Figure 1.6: ME effect in a magnetic semiconductor film of (In,Mn)As gated with an insulating polymide layer. The sheet Hall resistivity is plotted as a function of different applied voltages. For V_G = +125 V the sample is in a paramagnetic state. A clear magnetic hysteresis loop, fingerprint of ferromagnetism, is observed for V_G = -125 V. By removing the external voltage, the sample goes back to its initial magnetic configuration. The inset shows the same curves at higher magnetic fields. (Reprinted by permission from MACMILLAN PUBLISHERS LTD: *Nature* [4], ©2000)

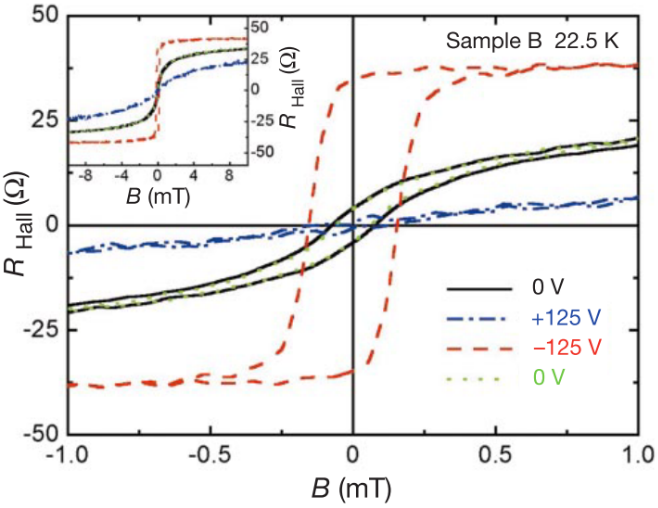

order to achieve large electric field effects, an appropriate adjustment of the surface-to-volume ratio of the channel material is required.

Several combinations of channel/gate materials have been put to test for the electric field tuning of magnetism. Some of the most remarkable achievements have been attained in magnetic semiconductors gated with dielectrics.

In 2000 Ohno *et al.* [4] switched a magnetic semiconductor thin film (5 nm) of (In,Mn)As covered with a thick (800 nm) insulating polymide layer from a ferromagnetic to a paramagnetic state using an external voltage of ± 125 V at 20 K (see Fig. 1.6). The estimated shift of T_C was ≈ ± 1 K. Afterwards, Chiba *et al.* [125] reversed the magnetization of similar (In,Mn)As films using SiO_2 as gate material by exploiting the change in magnetic coercive field H_c due to charge carrier doping (with a surface charge doping of $\approx 2.7 \cdot 10^{12}\,\text{cm}^{-2}$). The shift of T_C was about ± 2 K. The same author manipulated the magnetic anisotropy, which determines the magnetization direction, of (Ga,Mn)As thin films using ZrO_2 as dielectric material [117]. Another group [126] covered (Ga,Mn)As with a P(VDF-TrFe) ferroelectric polymer and demonstrated an overall shift in T_C of ≈ 4 K. In this case the usage of a ferroelectric as gate material presented the advantage of non-volatile control of magnetism. Other works analyzed the electric manipulation of magnetism in semiconductor nanodots of (Ga,Mn)As [127] and quantum dots of ($Mn_{0.05}Ge_{0.95}$) [114] gated with HfO_2 and Al_2O_3, respectively. Despite the remarkable results, the main limiting factor undermining the usage of magnetic semiconductors in practical applications is represented by the low temperature ferromagnetism, which is typically below 100 K.

As alternative channel materials, magnetic transition metals (e.g. Fe, Co, Ni) benefit of a higher Curie temperature than magnetic semiconductors, but are characterized by a lower penetration depth of the electric field. For this reason ultrathin films with a thickness even below 1 nm are generally chosen for electric field induced manipulation of magnetization. Maruyama *et al.* [10] managed to produce a magnetic anisotropy change of up to 40% in ultrathin films (about four monolayers) of Fe covered with a MgO(10 nm)/polymide(1500 nm) dielectric structure under application of ± 200 V (see Fig. 1.7). A similar study was performed by Chiba *et al.* [128] on ultrathin (0.4 nm) Co films using a MgO(2 nm)/HfO_2(50 nm) bilayer as gate dielectric. The overall change in the Curie temperature of Co was about 12 K at room temperature by applying

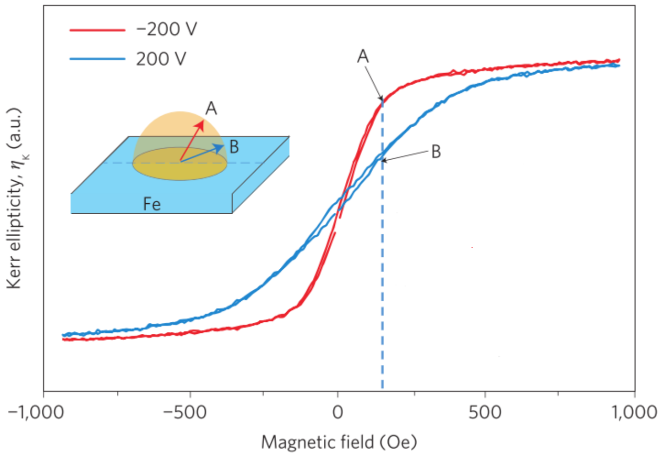

Figure 1.7: ME effect in an ultrathin film of Fe electrically charged using a dielectric bilayer of MgO/polymide. The change in the shape of the hysteresis curve indicate a change in perpendicular magnetic anisotropy of Fe on application of the bias voltage $V_G = \pm 200$ V. The inset shows the magnetization direction at points A and B in the hysteresis curves. (Adapted by permission from MACMILLAN PUBLISHERS LTD: *Nature Nanotechnology* [10], ©2009)

a gate voltage of about ± 10 V. Afterwards, the electric field control of magnetic domain wall velocity in ultrathin Co films was studied by different groups [129, 130]. Electric field effect has also been used in combination with tunneling magnetoresistance (TMR) devices. For example, the ability to reverse magnetization in ultrathin $Fe_{80}Co_{20}$ films by sending voltage pulses [12] was exploited for electric field manipulation of the TMR effect in $Fe_{80}Co_{20}$(0.7 nm)/MgO(1.5 nm)/Fe(10 nm) trilayers. Other electric field assisted TMR studies focused on $Co_{40}Fe_{40}B_{20}$(1.2 nm)/MgO(2 nm)/$Co_{40}Fe_{40}B_{20}$(1.6 nm) magnetic tunnel junctions [131]. It should be noticed that the reported examples of magnetic metal/dielectric heterostructures are characterized by the presence of a metal/oxide interface. As a drawback, often the very reactive surfaces of ultrathin films of Fe, Co, Ni and related alloys, which may be altered already during the growth process of the oxide layer [132] or due to oxygen ions migration during application of an external voltage [13, 103, 133], hampers the endurance of metal/oxide devices.

The problem of channel/gate compatibility can be circumvented to a great extent when both materials are composed of oxides. In this regard, a possible good choice of channel material is represented by the class of conducting manganese-based oxides, which typically features an intermediate charge carrier density ($n \approx 10^{21}\,\mathrm{cm}^{-3}$) between semiconductors and metals. Several manganites possess crystal structure (i.e. perovskite) and lattice parameter ($a \approx 0.39$ nm) compatible with some of the mostly-used dielectrics and ferroelectrics, such as STO, BTO and PZT, thus facilitating the growth of high quality epitaxial heterostructures with sharp interfaces [28]. These characteristics substantially help to improve the interfacial chemical stability and reducing the leakage current during application of an external voltage [78].

As already mentioned, several manganites[9] feature an intriguing correlation between electronic transport and magnetic properties, which gives rise to complex phase diagrams where insulator-to-metal transitions are associated with para-to-ferromagnetic transitions [134, 135]. Due to the strong link between electric and magnetic degrees of freedom, it is not a surprise that the electric field effect has been widely used as a probe for manipulating both resistivity and magnetization[10].

In a pioneering experiment performed in 1997, Mathews *et al.* [5] grew an epitaxial heterostructure of $La_{0.7}Ca_{0.3}MnO_3$ (≈ 30 nm)/PZT (≈ 300 nm) on top of a (001)-oriented $LaAlO_3$

---

[9] A more specific introduction to manganites shall be given under Materials and Methods.

[10] The interest in resistivity is related to the fact that some manganites show the phenomenon of colossal magnetoresistance. For this reason several studies focused on the electric field tuning of resistivity rather than magnetism.

single crystal substrate with a field effect transistor configuration. By poling the gate ferroelectric with a voltage of ≈ ± 7 V a 300% modulation in channel resistance was attained.

Magnetotransport measurements were performed in manganite/dielectric composite heterostructures by several groups. Hong *et al.* reported on a shift of 35 K [136] and 50 K [137] in the metal-to-insulator transition T_{MI} (reflecting an equal change in T_{C}) in LSMO films with a thickness of 4 nm. Besides, it was concluded that the LSMO layer became electrically "dead"[11] for thicknesses ≤ 3.7 nm with the whole heterostructure being insulating, regardless of the polarization state of the PZT layer. Due to the very different resistive behavior of heterostructures with slightly thicker LSMO films, an electric field screening length of the order of 0.2 nm was estimated. Afterwards, Kanki *et al.* [138] simultaneously tracked magnetization and conductivity in a field effect transistor device where $La_{0.85}Ba_{0.15}MnO_3$ and PZT were employed as channel and gate materials, respectively. In this case, a shift T_{MI} of only about 1.5 K was shown, but differently from the previous works the effect was realized at room temperature.

In other studies STO was used as gate dielectric in combination with thin films of LSMO. Pallecchi *et al.* [120] observed a maximum shift in T_{MI} of 43 K and a resistivity modulation of up to 250% in 7 unit cells (≈ 2.8 nm) LSMO samples. Thinner LSMO films became insulating and almost insensitive to field effect modulation. Similar heterostructures were grown by Brivio *et al.* [119] in back-gated (Ag/LSMO/STO/STO:Nb substrate) and top-gated (Au/STO/LSMO/STO substrate) geometries. Upon charge carrier doping the former configuration did not produce any sizable variation in T_{C}, while the latter displayed a shift of 5 K at room temperature. The reason for the different behavior was ascribed to the direct contact between STO and the LSMO electric dead layer in the back-gated setup.

A deeper understanding of the ME coupling in LSMO/PZT heterostructures was reached when quantitative magnetometry techniques such as superconducting quantum interference device (SQUID) magnetometry and (calibrated) magneto-optic Kerr effect (MOKE) were implemented to respectively probe macroscopic and local magnetism as a function of interfacial charge accumulation. Temperature dependence analyses upon PZT poling [11, 139] revealed a increase

---

[11] The concept of magnetic and electric dead layers will be described in Section 3.3.4.

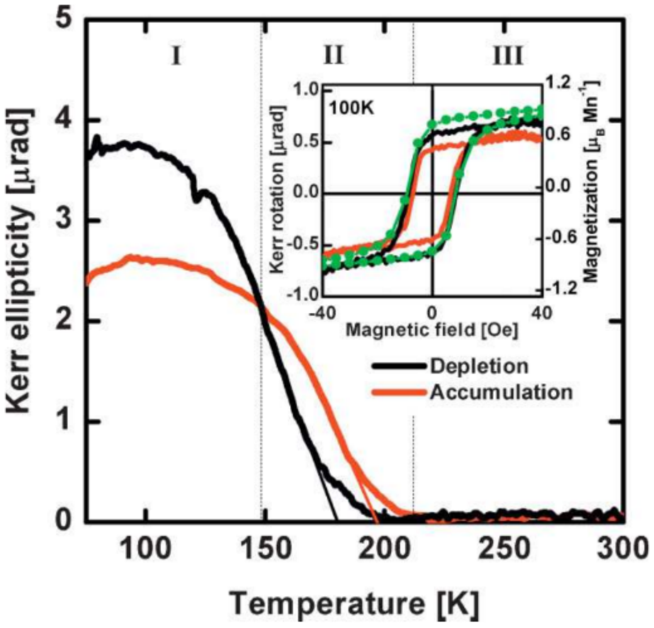

Figure 1.8: ME effect in a LSMO/PZT composite heterostructures. The temperature dependence of LSMO magnetization shows that T_{C} increases whereas the low-temperature magnetization decreases when LSMO is in a hole accumulation state due to poling with PZT (vice versa on hole depletion). In the inset the black and red curves are magnetic hysteresis loops measured via MOKE; the green curve is a SQUID measurement for the hole depletion state, which is used to calibrate the MOKE signal. (Reprinted by permission from John Wiley and Sons: *Advanced Materials* [11], ©2009)

in critical temperature[12] of $T_C \approx 20$ K in LSMO films with a thickness of about 4 nm and a drop in saturation magnetization when switching from depletion to accumulation of holes (see Fig. 1.8). The opposite behavior was encountered when switching from accumulation to depletion of holes. The competition between these effects manifested itself in a reversed sign[13] of the magnetic modulation, and thus also of the ME effect $\alpha = \Delta M/\Delta E$, when electrostatic charging was performed close to or far from T_C. The outcomes are consistent with a subsequent quantitative SQUID study performed by Leufke *et al.* [109] who found a T_C shift of nearly 10 K and reversed tuning effect in LSMO/PZT epitaxial bilayers with a LSMO thickness of nearly 7 nm. Interestingly, Lu *et al.* [59] found that thicker LSMO films in the range of 10 - 50 nm poled with BTO did not reveal any significant shift in T_C or any reversed tuning effect. In addition, the authors estimated a maximum relative variation of LSMO magnetization of about 27% for the thinnest (10 nm) LSMO sample, and, in contrast with previous reports [137], a penetration depth of the electric field of up to 3 nm. The latter value corresponded to the expected LSMO thickness required to completely suppress magnetization via BTO ferroelectric polarization.

It is worth to mention that the electronic - rather than strain - origin of the ME effect present in LSMO/PZT heterostructures was elucidated by X-ray absorption spectroscopy studies [140], which confirmed a shift in Mn valence state due to electrostatic charge carrier doping.

1.5.3 ME coupling via ionic diffusion

As previously stated, metal/insulator composite devices are sensitive to interfacial ionic diffusion on application of external voltages. Generally, the ionic diffusion leads to undesirable irreversible changes in one (or both) materials [141], which are detrimental for practical usage. Nonetheless, in the last years there has been a flourishing of activities aiming at the control of ionic migration to reversibly imprint material properties. For example the effect has triggered the interest for potential realization of nanoionics-based resistive switching memories, which should combine the advantages of flash and dynamic random access memories [142].

Regarding ME coupling, the idea of controlling magnetism via voltage-induced ionic migration opened the path for the emerging field of *magnetoionics*. Promising results have been attained in ultrathin films of Co ($\approx$ 2 u.c.) covered with a GdO layer. The latter is a rare-earth oxide with a high O^{2-} mobility [143, 144]. It has been shown [15, 144] that using an external voltage it is possible to reversibly control the oxidation front at the Co/GdO interface, which in turn allows for changing the magnetic anisotropy of Co from out-of-plane to in-plane. Although the ME effect was large, the migration of oxygen ions required the application of voltages (about 5 - 10 V) for prolonged time (several minutes), unless high temperatures (> 100 °C) or laser-assisted heating were used.

Zhu *et al.* [145] performed *in situ* studies on the local evolution of individual magnetic domains and domain wall motion during Li^+ ionic migration in $LiFe_5O_{8-x}$. It has been found that the local magnetization of the domains can be reversibly modulated up to 100% by sending fast voltage pulses.

---

[12] It is interesting to notice that the effect is remarkably smaller than the 50 K shift reported a few years earlier by the same group for magnetotransport measurements on similar LSMO/PZT samples.

[13] Notice that this behavior is consistent with the results later discussed in Section 4.4.

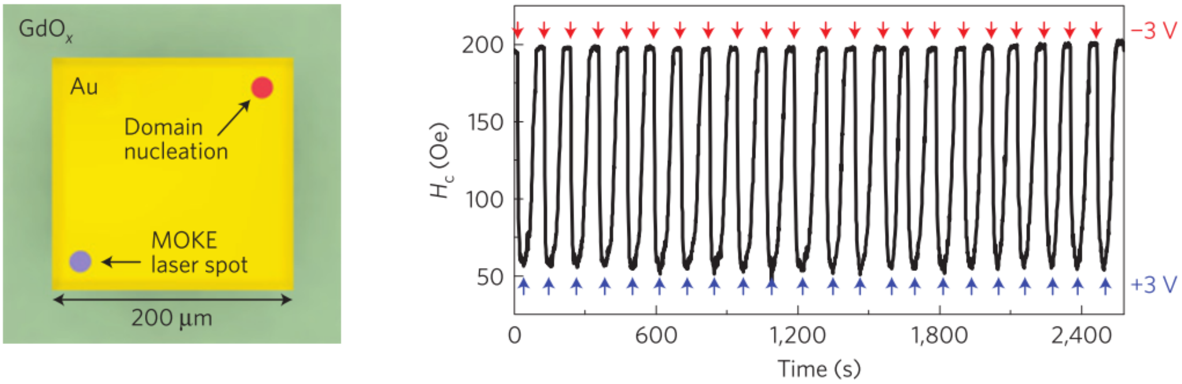

Figure 1.9.: ME effect via ionic diffusion in Co/GdO$_x$ heterostructures. The magnetic coercivity H_C of an ultrathin (0.9 nm) film of Co can be varied by migration of oxygen ions from a GdO$_x$ layer upon application of an external voltage. Domain nucleation via laser assisted heating facilitates the change in H_C (see schematic on the left). Right panel: H_C of Co is repeatedly toggled as the voltage is cycled between ±3 V. (Reprinted by permission from Macmillan Publishers Ltd: *Nature Materials* [15], ©2015)

1.5.4 Other studies on ME coupling

In the previous sections it has been described that strain, charge carrier doping and electrochemical ionic migration are powerful tools to control magnetism. The rather broad and constantly-expanding ME community is currently exploring also other phenomena associated with ME coupling. Here, we only mention - without any claim for completeness - some other interesting research areas.

It has been shown [146, 147] that magnetic exchange bias can be controlled by means of an electric field in composite multiferroic/ferromagnetic heterostructures. For example the strong coupling between antiferromagnetism and ferroelectricity in BFO was used to shift the ferromagnetic hysteresis loop of LSMO films up to 125 Oe at 5.5 K by sending ±60 V voltage pulses [147]. More recently, Gilbert *et al.* [148] proposed that also electric field induced oxygen migration may enable the tuning of magnetic exchange bias.

Other forms of coupling between electric and magnetic order parameters were achieved by combining multiferroics and ferromagnets. In 2008 Chu *et al.* [149] grew CoFe/BFO layers and observed that the average magnetization of the ferromagnet rotates by 90° on application of an electric field; by switching the BFO once again, the initial magnetization direction of CoFe was restored. These preliminary results were afterwards further examined by the same group in similar CoFe/BFO heterostructures, where 180° domain switching in CoFe was proven upon switching of the BFO ferroelectric polarization [13]. The origin of the ME coupling was attributed to the deterministic reversal of the weak ferromagnetism in BFO, which acts as mediator between BFO ferroelectricity and CoFe ferromagnetism. The switching was exploited for energy-efficient control of a BFO/$Co_{0.9}Fe_{0.1}$/Cu/$Co_{0.9}Fe_{0.1}$ spin valve devices at room temperature.

Another emerging area that is worth pointing out is the electric field control of magnetic skyrmions, which may bring about the development of recently envisaged skyrmion race-track type memories [150, 151]. Hsu *et al.* [152] showed that whereas a magnetic field can adjust the energy levels between skyrmionic and ferromagnetic state on a global scale, reversible activation of magnetic skyrmions can be realized locally by using an electric field.

1.6 ME effect in solid/liquid composite devices

To date, electric manipulation of magnetism has been achieved across a number of ME systems. Several of the ME coupling phenomena described in the previous sections on all-solid-state composite MEs are to a great extent also valid in solid/liquid devices. The main difference between the two approaches is in the nature of the gate material: if solid-state ME composites make use of dielectrics or ferroelectrics, solid/liquid MEs exploit *electrolytes*. In general, an electrolyte[14] is a substance containing mobile ions (e.g. Na^+, K^+, Li^+, Cl^-, OH^-, SO_4^{2-}) dissolved in a solvent (e.g. water, propylene carbonate, acetonitrile or ethyl acetate). ME effect can be realized between a magnetic electrode and an electrolyte by controlling the ionic motion via application of an external voltage (see below for an in-depth discussion).

The current ongoing research on all-solid-state MEs largely overshadows the later-born field of solid/liquid MEs. This is confirmed by the fact that in several highly-cited reviews on the topic of ME coupling, liquid-gating approaches are only briefly mentioned (if not neglected at all) [2, 8, 24–27, 29–31, 33, 34, 36].

There is indeed a series of reasons why the research on solid/liquid MEs, albeit rapidly expanding, is still in a germinal phase comparing to solid-state MEs.

First of all, it should be remembered that although the first experiments on ME coupling were conducted already about 50 - 70 years ago, a revived flurry of activities on the topic goes back more recently to the last 15-20 years. Thus, it is reasonable that the so-called *renaissance* of ME effect [1] started with single-phase MFs and solid-state composite MEs on the basis of the knowledge previously acquired in bulk solid materials and combined with the modern means of nanotechnology.

From an experimental perspective, there are some non-trivial aspects that undermine the development of the field of ME coupling by using liquid-gating techniques. For instance, standard aqueous electrolytes allow for usage of low external voltages of about ± 1.2 V [154] in order to avoid water electrolysis and a limited range of accessible temperatures due to the freezing[15] and boiling points of water. The replacement of water with a non-aqueous solvent helps to enlarge the operating potential window and temperature range [155]. Nonetheless, in general, the application of higher voltages and temperatures facilitate the onset of irreversible electrochemical reactions [141], which alter the initial electrolyte and/or electrode characteristics. Apart from voltage and temperature, other parameters such as the electrode/electrolyte chemical compatibility and the amount of impurities present in the electrolyte have to be considered. Altogether they determine the predominance of either electrostatic or electrochemical interfacial charging/discharging processes, which are not always easily distinguishable [18, 19, 156–158].

For practical purposes, concerns in the usage of certain liquid electrolytes are related to safety, environmental impact and costs. Indeed some non-aqueous solvents are flammable and reactive with the charged electrodes [159], while others are highly toxic [160]. Nonetheless, it should be noticed that several electrolytes, for instance ILs [161], are known for being

---

[14] It may be in the liquid or solid phase (as for solid polymer electrolytes [153]). Here we focus on liquid electrolytes.

[15] Nonetheless, there are examples where electrolytes in a frozen state where useful to study superconductivity induced by charge carrier doping [21, 22].

environmental friendly and practically non-flammable. Substantial costs for processing the electrolyte components and the requirement for an appropriate (yet often cumbersome) housing against contamination during operation under ambient conditions still pose problems.

More specifically, as already mentioned, one of the main practical envisions of ME effect is the fabrication of non-volatile and fast ME memories. In this regard, gating using solid-state ferroelectrics is preferable over electrolytes for controlling magnetism. It is challenging to concurrently fulfill non-volatility and fast switching speed with liquid-gating approaches. Solid/liquid devices behaving as electrolytic capacitors feature relatively-fast charging/discharging processes, but lack preservation of the stored charge when the external voltage is removed; on the contrary, when electrochemical reactions (such as Li^+ intercalation) are exploited, non-volatility is gained at the expense of slow charging speeds.

Although it is still necessary to overcome some evident obstacles that hinder the study and practical utilization of solid/liquid ME devices, they feature certain superior characteristics comparing to all-solid-state systems. Electrolytes allow for accumulation of surface charge densities (up to $10^{15}\,\mathrm{cm}^{-2}$) appreciably higher than high-κ dielectrics and ferroelectrics. By exploiting their unrivaled values of charge carrier density modulation, fascinating phenomena such as the induction of insulator-to-superconductor [21, 22] or metal-to-insulator [162] transitions were observed. In addition, elevated surface charge densities are achieved by applying rather low external voltages, which result in much higher capacitances than in polarizable solids. For example a capacitance of about 1000 $\mu\mathrm{F\,cm}^{-2}$ was found for MnO_2 electrodes charged in aqueous electrolyte [163] (compare with Table 1.1). As a consequence, also the energy consumption for charging an electrode via an electrolyte is also comparatively low: it is indeed not a coincidence that electrochemical batteries, supercapacitors and electrolytic capacitors are at the forefront of modern energy storage and delivery.

Another strength of the solid/liquid approach is represented by an extraordinary stability upon repetitive charge/discharge cycling (under appropriate conditions). Contrarily, in several cases all-solid-state devices lack an adequate endurance [13] or feature predominant irreversible contributions [9, 14].

A practical advantage of liquid gating methods is given by the possibility to easily fabricate large surface area devices by simply pouring the desired amount of electrolyte onto the specimen. On the contrary, the growth of high quality dielectrics or ferroelectrics over large surface areas keeping a low level of leakage current can be very demanding [78]. In fact, despite advanced physical vapor deposition techniques enabling the control of epitaxial layers at the atomic level, defects are intrinsically inevitable due to the lattice misfit between the materials, off-stoichiometry, interdiffusion during growth, and other effects [28].

Liquid gating methods offer another noteworthy feature comparing to ferroelectrics. On application of an external voltage, the hysteretic behavior of ferroelectrics permits them to be in only two well-defined polarization state ("up" or "down") and so only two discrete values of polarization are easily accessible[16]. In the case of a liquid electrolyte the surface charge can be quasi-continuously monitored while the voltage polarity is being swept. This allows for a more precise determination of the specimen response, also in terms of other physical quantities such as magnetism, during the process of charge carrier doping.

---

[16] Even by performing minor hysteresis loops, the switching process is non-linear and implies two discrete values of polarization.

In the following, an in-depth description of the charging/discharging processes occurring in solid/liquid systems will be provided. Afterwards, it will be shown how ME coupling can be realized at solid/liquid interfaces.

1.6.1 Charging mechanisms with electrolytes

The complex interplay of physical and chemical phenomena occurring at the interface between an electrode and an electrolyte has been addressed in a variety of theories and experimental systems. Depending on the nature of interfacial charging processes, three main device categories - electric double layer (EDL) capacitors, pseudocapacitors and electrochemical batteries - can be distinguished.

Hermann von Helmholtz in 1879 was the first one who set the basis for the development of the EDL theory at solid/liquid interfaces. He suggested that during application of a positive (negative) external voltage to an electrode, electrolyte ions with negative (positive) charge experience an electric field, which drives them onto the electrode's surface until interfacial charge neutrality is reached. The nature of the charging process is electrostatic with no exchange of electrons at the interface, and thus it is defined as non-faradaic. The final configuration is similar to an ultrathin dielectric capacitor where the potential drops from its starting value at the electrode's surface to zero over a tiny distance, which is equal to the thickness of the layer of counter ions (see Fig. 1.10(a)).

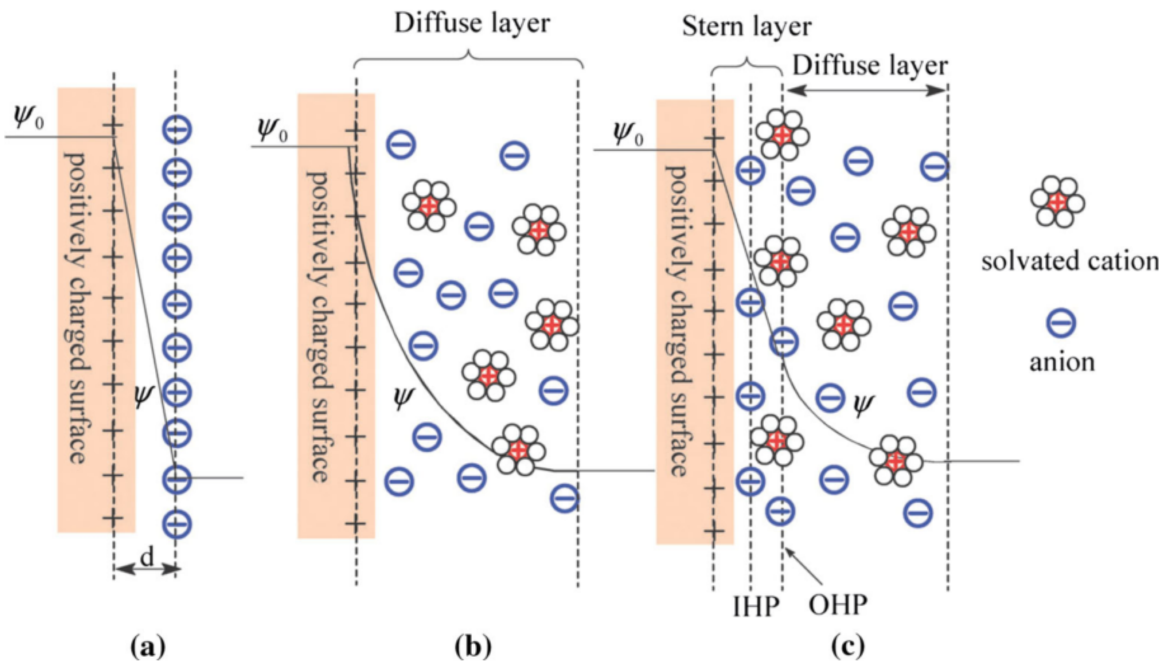

Figure 1.10.: Models of electric double layer. (a) Helmholtz, (b) Gouy-Chapman and (c) Stern-Grahame models for a positively charged electrode in contact with a liquid electrolyte. ψ_0 and ψ are respectively the potentials at the surface of the electrode and in the electrolyte; *d* is the thickness of the double layer in the Helmholtz model; IHP and OHP indicate the inner and outer Helmholtz planes, respectively. (Reprinted by permission from Springer: *Journal of Materials Science* [164], ©2015)

Subsequently, Gouy and Chapmann suggested that due to thermal agitation a rigid layer of counter ions cannot be formed onto the electrode surface but rather a diffuse layer, which extends several nanometers into the electrolyte (see Fig. 1.10(b)). Consequently, the potential decays more gradually over larger distances starting from the electrode surface.

A more realistic representation of the interfacial processes is given by the Stern model, which combines a Helmholtz plane and a diffuse layer. Afterwards, the model was further expanded by Grahame who considered the role of solvent molecules attached to the electrolyte ions (see Fig. 1.10(c)). Some ions may lose their solvation shell (e.g. composed of water molecules) while approaching the electrode; those ions directly in contact with the electrode are referred as *specifically-adsorbed* ions and form the inner Helmholtz plane. The distance of closest approach of ions that still possess a solvation shell delimits the outer Helmholtz layer. Beyond this region there is the diffuse layer where the ions can move more freely.

Thus, the term *electric double layer* is used to describe the thin layer of adsorbed ions anchored to the electrode surface and the more loose layer of ions electrostatically screening the former. Most of the applied potential drops at a distance of the order of one nm from the surface of the electrode and consequently a very strong interfacial electric field can be produced by applying just a few volts. The EDL formed on top of an electrode enables the formation of a subnanometer gap capacitor with a high capacitance of up to about 5 - 20 $\mu\mathrm{F\,cm^{-2}}$ [17, 113, 164], that is much larger than conventional dielectric-based capacitors (compare with Table 1.1).

Since the nature of the charging processes is electrostatic (in the ideal case no electrochemistry is involved), EDL capacitors possess a high level of reversibility with a working lifetime that can extend to a few decades [165] under standard working conditions. For instance, it has been statistically estimated a device failure after 10^7 hours of operations at 85 °C in tantalum-based EDL capacitors [166] and one failing device out of 1000 components after 10^6 hours of operations at 40 °C in aluminum-based EDL capacitors [167]. In addition, the fact that charging occurs at the surface of the electrode (and not in the bulk as for electrochemical batteries) allows for remarkable switching speeds. It has been reported that EDL field-effect transistors can reach operating frequencies of several kHz [113, 164, 168, 169].

Electrostatic charge carrier doping via electrolytes has been exploited to manipulate properties of matter in a versatile way. Just to give a few examples it has been used in a variety of materials, such as C, Fe, Au, $InSnO_2$, ZnO, $SrTiO_3$, $LaCaMnO_3$, for the control of resistivity [170], magnetism [6, 20, 171–173], superconductivity [21, 22] and strain [174, 175].

The phenomenon of *pseudocapacitance* [176–178] was discovered by B. E. Conway [179, 180] who in the years between 1975-1980 performed systematic studies on the charge storage mechanisms of RuO_2 electrodes immersed in aqueous electrolytes. He observed that although the charging processes had some similarities to EDL capacitors, much higher values of capacitance of up to 2000 $\mu\mathrm{F\,cm^{-2}}$ were achievable concurrently with considerable cycling stability and switching speed. Pseudocapacitance involves redox reactions at the electrode/electrolyte interface accompanied by exchange of charge carriers (i.e. faradaic process) according to three possible mechanisms (see Fig. 1.11):

- **Underpotential deposition** is manifested as the chemisorption of ions on the surface of noble-metal electrodes. An example is the electrosorption of Pb ions on Au according to: $\mathrm{Au} + x\mathrm{Pb}^{2+} + 2x\mathrm{e}^- \leftrightarrows \mathrm{Au}{\cdot}x\mathrm{Pb}_{ads}$
- **Redox pseudocapacitance** occurs when electrolyte ions are adsorbed onto the surface or near the surface of an electrode and charge carriers are exchanged at the interface via redox

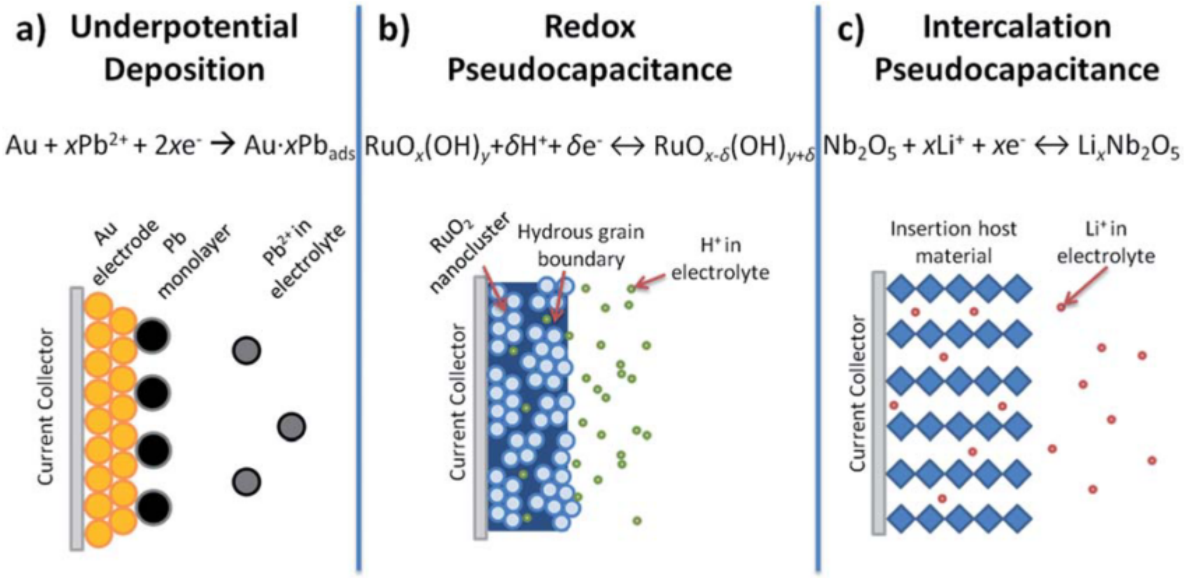

Figure 1.11.: Mechanisms of pseudocapacitance: (a) underpotential deposition, (b) redox pseudocapacitance, (c) intercalation pseudocapacitance. (Reprinted by permission from ROYAL SOCIETY OF CHEMISTRY: *Energy & Environmental Science* [177], ©2014)

reactions. Hydrous RuO_2 belongs to this group with the pseudocapacitive reaction: $RuO_2 + xH^+ + xe^- \leftrightarrows RuO_{2-x}(OH)_x$

- **Intercalation pseudocapacitance** takes place via ionic diffusion through tunnels or layers (typically in proximity of the surface) of a redox active material. The process involves faradaic charge transfer with no crystallographic phase change of the hosting material. An example is the intercalation of Li^+ ions in Nb_2O_5 with redox reaction: $Nb_2O_5 + xLi^+ + xe^- \leftrightarrows Li_xNb_2O_5$

Despite the superior charge storage properties discovered in RuO_2, its technological viability was hampered by the high costs of ruthenium. In the course of the studies new materials were discovered to be prone to pseudocapacitive reactions: VN [181], MoO_2 [182], MoN [183], MnO_2 [163, 184–190], Fe_2O_3 [191, 192], CoO_x [193], NiO [194], Nb_2O_5 [195].

It is interesting to notice that some of the pseudocapacitive materials on the list are composed of transition metals, whose presence is a prerequisite for the occurrence of magnetism. Recently, pseudocapacitive redox reactions were found also in $LaMnO_3$ [196], which is end member compound of the already-mentioned class of manganese-based oxides (e.g. LSMO, LCMO or $La_{1-x}Ba_xMnO_3$) known for displaying colossal magnetoresistance, Mott transitions and intrinsic spin polarization. Consequently, in principle, not only electrostatic doping via EDL charging but also pseudocapacitance may be exploited to control various properties of manganites. This idea is at the base of the interpretation of some of the experimental results attained on LSMO/IL devices that will be discussed in the next chapters.

Another remark worth mentioning is that the term *supercapacitor* was coined [179] to underline the high amounts of charge attainable by pseudocapacitors. Nonetheless, in the course of the years the definition acquired a more general connotation, including not only pseudocapacitors but also high-surface-area EDL capacitors (typically made of carbon) [180].

Electrochemical batteries [197–201] are charge storage systems that exploit the insertion of ions of small size (such as H^+ or Li^+) into the bulk of a host electrode[17]. The portion of affected volume is much larger than in EDL capacitors and pseudocapacitors. During the discharging process, a conventional battery produces a faradaic current due to redox reactions between the electrodes and the electrolyte ions. Such current can be used to generate useful work in an external electric circuit (chemical energy is transformed into electrical energy). In certain kinds of batteries the process of ionic insertion is reversible: by applying an external voltage with reversed polarity, the ions previously inserted into the electrode during discharging can be extracted out from it, thus regenerating (to a certain extent) the original chemical configuration. Reversibility is typically limited to 500-1000 cycles due to progressive loss of the active material in both electrode and electrolyte.

In general, batteries accumulate higher amounts of energy (charge) than EDL capacitors and pseudocapacitors, because a larger portion (not just the surface) of the electrode is affected. Nonetheless, as a drawback the process of ionic migration shows much slower kinetics, and so also the specific power is smaller.

Currently, many efforts are directed towards the optimization of batteries performance by investigating new materials. In case of Li-ion batteries the typical materials[18] employed as positive electrodes are $LiCoO_2$, $LiMnO_2$, $LiNiO_2$, $LiFePO_4$, whereas $Li_{3-x}Co_xN$ and Li alloys are used as negative electrodes.

When envisioning the future of energy storage and delivery, hybrid systems are very compelling [178, 199], because by appropriately combining different electrode and electrolyte materials a smart balance of performance between EDL capacitors, pseudocapacitors and batteries should be possible.

Although the aim of this brief overview is to summarize the main features of the different charging mechanisms at solid/liquid interfaces (see also Table 1.2), it should be stressed that, practically, the distinction between electrostatic and electrochemical charging is not always straightforward. In particular, it is sometimes challenging to clearly separate[19] between EDL capacitance and pseudocapacitance. Identifying the nature of the interfacial charging processes is a complex task comprising several involved parameters, such as temperature, local strength of the electric field and electrode/electrolyte chemical compatibility. Often it is under debate [18, 19, 156–158] whether upon application of an external voltage the electrolyte ions are simply in contact (physisorption), form chemical bonds (chemisorption) with the electrode surface, or both mechanisms concurrently occur. Anyhow, it should be underlined that similar difficulties arise also in all-solid-state ME devices, since several effects (strain, charge and ionic diffusion) may simultaneously occur when applying an external voltage.

Some useful criteria to distinguish between the charging regimes of EDL capacitors, pseudocapacitors and electrochemical batteries can be defined from the analysis of their different current-voltage responses. This can for example be done using an experimental technique called *Cyclic Voltammetry*, which will be described under Materials and Methods.

---

[17] Notice that there are several kinds of batteries, such as Li-ion, lead-acid or nickel-metal hydride batteries.

[18] Notice again that transition metals are involved.

[19] The tendency is to invoke electrostatic doping even if appropriate precautions to exclude redox pseudocapacitance are not taken into account [6, 20].

Table 1.2.: Comparison of the charge storage characteristics of EDL capacitors, supercapacitors and batteries. Data from Ref. [202] and [179].

System	Energy ($\mathrm{Wh\,kg^{-1}}$)	Power ($\mathrm{W\,kg^{-1}}$)	Charging/discharging time (s)	N° of Life Cycles
EDL capacitor	< 0.1	$\gg 10000$	10^{-6}–10^{-3}	$\gg 10^6$
Supercapacitor	1 – 10	500 – 10000	1 – 100	10^4–10^6
Battery	10 – 100	< 1000	10^3–10^4	~ 1000

1.6.2 Control of magnetism via electrolytes

The same means previously described in all-solid-state ME devices, namely strain, electrostatic charging and electrochemical intercalation, can also be exploited in solid/liquid systems to reversibly control magnetic properties.

In 2003 Weissmüller *et al.* [174] demonstrated that charging with an electrolyte produces a remarkable strain[20] modification of the order of 0.1% in porous Pt, that is comparable to the magnitude reachable with commercial piezoceramics. The origin of strain was attributed to the electrostatic pressure exerted by EDL charging (with surface charge densities of up to 500 $\mu\mathrm{C\,cm^{-2}}$) within the interior of the crystallites. From an atomistic perspective, the effect is related to the modification of the electronic population via band filling, which affects the equilibrium interatomic spacing.

Regarding ME coupling, a change of about 1% in magnetic susceptibility was attained in electrolyte-gated nanocrystalline Pd [203]. Similar studies were conducted also on NiPd [204] and $\mathrm{Pd}_{1-x}\mathrm{Co}_x$ [205] nanoporous alloys, with the latter study reporting on a maximum value of 3% in relative magnetic change. The dominant microscopic mechanism driving the magnetic response was attributed to surface-induced pressure in the crystal lattice rather than filling of the d-band by extra charge carriers. A change of 0.2% in ferromagnetism and 2.5% in electrical conductivity was observed in electrolyte-gated nanoporous AuFe [206]. In this case, the effect on magnetism was explained in terms of Coulombic pressure, while the modification in electrical transport properties was attributed to the change in carrier concentration due to electrostatic doping.

In general, strain-induced ME effect using electrolytes is primarily investigated in porous materials and powders rather than thin films, because the former have a high surface-to-volume ratio with the nanoparticles being free to expand in between the pores without limitations due to substrate clamping. Nonetheless, the tendency of sintering of the nanoparticles during their expansion hampers the cycling stability. In addition, to date, the obtained changes in magnetization are significantly smaller than the giant ME effects reported on all-solid-state MEs [9, 14]. For these reasons, strain-induced ME coupling by means of electrolytes holds a side role within the panorama of possible routes to realize ME effect.

---

[20] However, hints of electrochemical reactions can be easily recognized from the reported current-voltage characteristics.

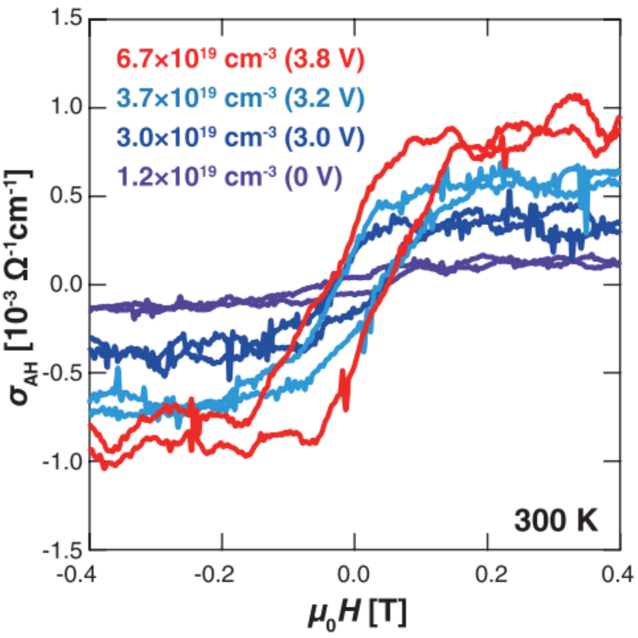

Figure 1.12: Voltage-induced para-to-ferromagnetic transition in electrolyte-gated magnetic semiconductor films of (Ti,Co)O_2. Behavior of the Anomalous Hall conductivity using different gate voltages at a temperature of 300 K. (Reprinted by permission from AAAS: *Science* [20], ©2011)

Electrostatic charge doping using electrolytes has been established as a powerful method to manipulate magnetism. In 2007 Weisheit *et al.* [6] demonstrated a modification of 4.5% in the magnetic coercivity of FePt ultrathin films (≈ 2 nm) above room temperature by application of low voltages of about 0.6 V. The work opened up the path for investigation of other magnetic thin films systems via EDL charging.

One of the most remarkable examples of voltage-driven control of magnetism via electrolytes was realized by Yamada *et al.* [20], who successfully triggered a low-carrier paramagnetic state into a high-carrier ferromagnetic state in magnetic oxide semiconductor films (thickness of 33 nm) of (Ti,Co)O_2 using just ≈ 4 V above room temperature (see Fig. 1.12). Although the work does not provide quantitative information about the shift in transition temperature T_C, it underlines the possibility of inducing magnetic phase transitions by application of small voltages. Considering other EDL gating studies on magnetic semiconductors, a shift of $T_C \approx 14$ K was attained in (Ga,Mn)As films [207] by applying voltages ranging from -1 to 3 V, although irreversible effects beyond 2 V were observed.

An impressive shift in T_C of about 100 K has been reported in Co ultrathin films (0.4 nm) charged with an IL electrolyte [172] by applying ± 2 V (corresponding to ± 0.084 electrons per Co atom). The integrity of Co was guaranteed by covering it with a 2 nm protective layer of MgO. Nonetheless, it was not clearly stated to which extent the giant modifications were reversible. In addition, although the effect was attributed to EDL charging, the fact that the SQUID measurements were performed after prolonged application of ± 2 V for about 30 - 60 min gives a strong indication that oxygen ions diffusion may contribute to alter the magnetism of Co (compare also with the results in Ref. [15]).

Recently, Zhao *et al.* [208] investigated the ME coupling under electrostatic and electrochemical charging regimes at the interface between an ultrathin (2.2 nm) film of Co and an IL electrolyte. It was found that electrostatic doping dominates the magnetic tuning process within a potential window of about ± 1.5 V. On increasing the external voltage irreversible chemical reactions contribute to the erosion of Co with significant loss of the magnetic signal.

Apart from pure transition metals and magnetic semiconductors, EDL gating has been widely explored in strongly-correlated magnetic oxides. In 2013 Mishra *et al.* [173] reversibly tuned up to 2.5% the magnetization of a LSMO nanopowder by an electrostatic surface charge modulation of 22 μC cm^{-2} using a potential window of less than 1 V at 325 K. Interestingly, it was found that the sign of the magnetic response was reversed with respect to the surface charge modulation when a strong magnetic field of 9 T (instead of 0.1 T) was applied (in other words, the sign of ME effect was inverted). Subsequent studies were carried out on LSMO with porous [209] (with a peak-to-peak magnetic change of 6%) and epitaxial [210] film geometries. Electrostatic control of magnetism was proven also in other electrolyte-charged manganites. In LCMO$_3$ a magnetic variation of up to 8.5% was reached in porous films [170], while a 30 K shift in T_C was estimated by resistivity measurements in 5 nm epitaxial films [156]. In $Pr_{0.65}(Ca_{0.75}Sr_{0.25})_{0.35}MnO_3$ a 250% resistance change was observed, equivalent to an increase in ferromagnetic phase fraction of 0.51% [211]. It was found [158] that $La_{1-x}Sr_xCoO_3$ films are sensitive to the voltage polarity, with irreversible electrochemical reactions kicking in for gate voltages > 0, while a reversible variation of 12 K in T_C occurred via electrostatic doping for negative gate voltages.

In the examples described up to now electrostatic doping represents the predominant mechanism constituting ME coupling, in accordance with the EDL theory. Anyway, it is worth noticing that often the possible influence of reversible electrochemical reactions are not taken into account, and actually they are rather quickly dismissed on the rather vague ground that "the involved materials are chemically stable" [6, 20].

There are some works in which redox pseudocapacitance has been recognized as the main contributor to the ME coupling. Reversible variations in magnetization of up to 10% were observed in γ-Fe_2O_3 nanopowders immersed in KOH aqueous electrolyte [212, 213]. Although a contribution from strain magnetoelastic coupling was not ruled out, the magnetic tuning effect was predominantly ascribed to pseudocapacitive charging via electrochemical adsorption and desorption of ions on the electrode's surface.

Pseudocapacitance was exploited to control the magnetic properties of some transition metal thin films. Via formation and dissolution of a chemisorbed oxygen surface layer it was possible to modify the magnetic susceptibility ($\approx 1\%$) and the electrical resistance ($\approx 6\%$) of porous nanocrystalline Pt gated with KOH electrolyte [214]. Supercapacitive behavior was claimed in 2 nm Fe films charged with KOH electrolyte [215] with a 64% change in anomalous Hall resistance, albeit no information about the current-voltage characteristics was provided. The same group showed that slightly thicker (10 nm) Fe electrodes in KOH present pronounced and clear features of electrochemical intercalation [216]. Leistner *et al.* [217–219] studied FePt films with different thicknesses gated by $LiPF_6$ and $LiClO_4$ electrolytes and reported on a 25% change in magnetic coercivity and 4% change in saturation magnetization in ultrathin films with a thickness of 2 nm. Similar studies on ultrathin CoPt films immersed in $LiClO_4$ displayed a change in magnetic coercivity of 200% and saturation magnetization of 4%, but the redox processes were mainly irreversible [220]. In most of the described examples the poor longevity of the devices on repetitive cycling calls for further improvements.

ME coupling via electrochemical ionic intercalation is an effective route to manipulate a larger portion of material volume comparing to the more restricted interfacial effects achievable with EDL and pseudocapacitive charging. Probably, the first example of electrochemical ionic intercalation to control magnetism was shown in 1996 by Itoh *et al.* [7] who modified the ferromagnetic transition temperature of a $La_{1-x}Mn_xO_3$ powder by means of lithium intercalation with an impressive shift of $T_C \approx 100$ K. The effect was assigned to modification of the crystal

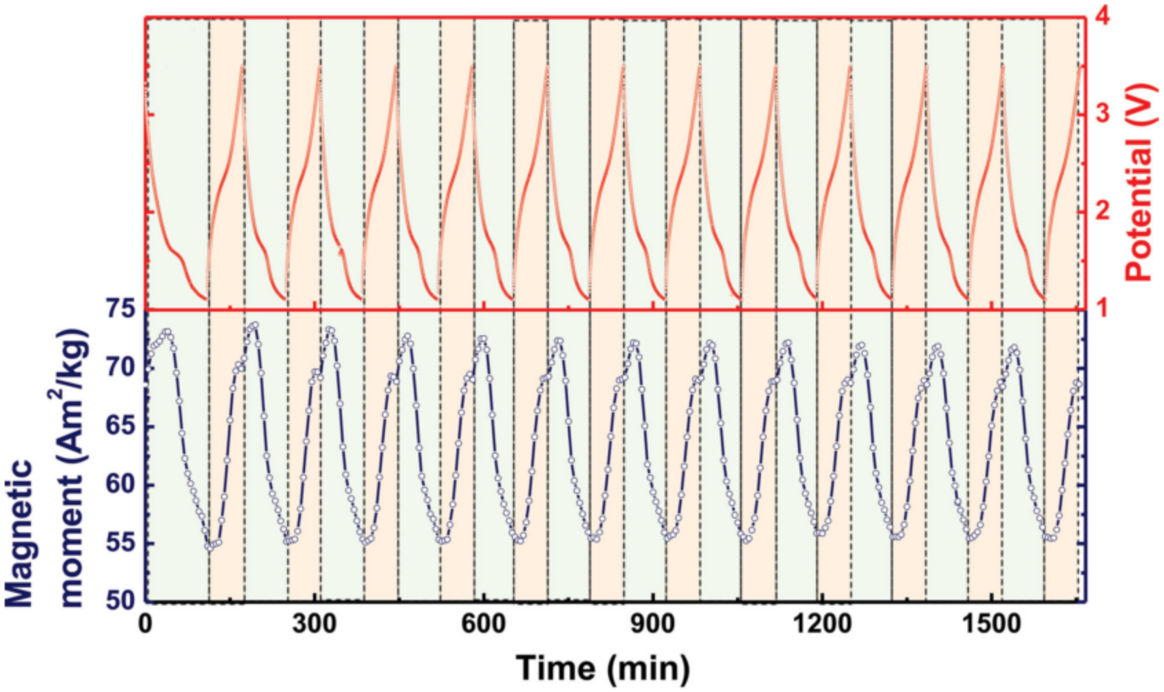

Figure 1.13.: Reversible variation of magnetization in γ-Fe_2O_3 nanopowders via electrochemical lithiation at room temperature in presence of a magnetic field of 1 T. Lithiation (discharging, light blue areas) and delithiation (charging, light red areas) are carried out with a potentiometric constant current of 115 mA g^{-1} and respective cut-off potentials set at 1.1 V and 3.5 V vs. Li^+ /Li. (Reprinted by permission from JOHN WILEY AND SONS: *Advanced Materials* [221], ©2014)

structure and not to the valence state of the manganese ions. Unluckily no details about the degree of reversibility were given.

Recently, after a period of almost total silence on the topic, probably also due to the more urgent demand for improving the energy (rather than magnetic) performance of batteries, a revival of new research activities flourished in the area of *magnetoionics*. In 2014 Dasgupta *et al.* [221] made use of Li^+ intercalation to reversibly change up to 30% the magnetization of γ-Fe_2O_3 nanopowders at room temperature (see Fig. 1.13). Almost contemporarily, Yamada *et al.* [222] exploited the same principle to tune the magnetic signal of Fe_3O_4 nanoparticles with a 13% change. In both works it was underlined the importance of the application of an appropriate operating potential window in order to avoid the onset of irreversible electrochemical processes. Soon after, giant room-temperature ME effects pointing towards reversible on-off switching of magnetism were attained in α-Fe_2O_3 [223], $CuFe_2O_4$ and $ZnFe_2O_4$ [224] nanopowders. The research carried on by testing different electrode's geometries and kind of electrolytes, such as mesoporous films of α-$LiFe_5O_8$ gated with LiTFSI-based electrolyte [225], thin films of Fe_3O_4 gated with $Li_{1.5}Al_{0.5}Ge_{1.5}P_3O_{12}$ solid-state electrolyte [226] and commercial Fe_3O_4 nanoparticles gated with $LiPF_6$ electrolyte [227]. In all these instances the reachable magnetic modulation was below 12%.

Apart from lithiation approaches, oxygen ions and oxygen vacancies migration was used as another means to tune magnetic properties [228]. It was found that the prolonged application of constant voltages (for 30 - 90 min) in LSMO films gated with ILs brings about the migration of oxygen centers within a thickness of about 12 nm [229]. An enhancement of the effect was noticed when high amounts of residuals of water contamination were present in the IL.

So far electric-field ionic diffusion studies have focused on control of single ionic species. Nonetheless, recently, reversible dual-ion (oxygen and hydrogen) phase transformations were shown in IL-gated epitaxial thin films of $SrCoO_{2.5}$ (an antiferromagnetic insulator), which turned into $SrCoO_{3-\delta}$ (a ferromagnetic metal) upon oxidation and $HSrCoO_{2.5}$ (a weakly ferromagnetic insulator) upon hydrogenation [230]. These results on electric-field control of multistate phase transformations may greatly enrich materials functionality.

1.7 Applications of the ME effect

Since the initial studies on ME coupling, the idea of mutually controlling electric or magnetic properties with magnetic or electric fields, respectively, has always attracted great attention for the variety of applications, which could be envisioned. Already in 1974, when the magnitude of the ME effect was still far too low to be useful for any practical application, Wood and Austin [231] discussed the utilization of the ME effect to realize devices for (i) modulation of amplitudes, polarizations and phases, (ii) ME data storage and switching, (iii) optical diodes, (iv) spin-wave generation, (v) amplification and (vi) frequency conversion.

In the light of novel findings and better understanding of the phenomenon of ME coupling, a variety of technological applications have been proposed and put to test.

The direct ME effect is a potential candidate to implement highly sensitive sensors of AC or DC magnetic fields by outputting electric signals[21]. This may be useful to complement ordinary magnetic measurement systems such as SQUID magnetometers and Hall sensors [24]. So far, it has been achieved a low-magnetic field detection limit down to 10^{-12} T at room temperature [232], although reduction of environmental noise (thermal, acoustic, electric) is still an issue [233]. The sensitivity is lower than SQUID magnetometry, but the costs of the final working device are expected to be much lower. It has also been suggested that the ability of sensing magnetic fields could be used in information technology to read the ’bits’ of recording media by using miniaturized, energy-efficient ME heads in replacement of traditional cumbersome, current-consuming magnetoresistance heads [234, 235]. In a completely different scenario, *in vivo* medical applications have been proposed for the detection of magnetoencephalographic and magnetocardiographic signals [236].

Due to its very nature, ME coupling implies the transduction of electrical energy into magnetic energy (and vice versa) [237]. In this regard, another intriguing and challenging area is represented by energy conversion and harvesting via ME effect. For instance, O’Handley *et al.* [238] utilized AC magnetic fields to remotely transmit electric power to a ME receiver device. Such a technology could be useful to wirelessly activate a therapeutic device implanted into a body thus avoiding inconveniences related to potentially-risky surgeries. From a different perspective, it has been suggested that electromagnetic and mechanical noise (for example coming from the environment) could be collected to produce useful electrical energy: preliminary results from Dong *et al.* [239] demonstrated that the summation of magnetic and mechanical vibrations can generate an open circuit output voltage of up to 8 V.

---

[21] Typically, experiments on direct ME effect are performed using a magnetic field with superimposed dc and ac magnetic signals and then measuring the output voltage. Thus, if one of the two magnetic components is known, by detecting the output voltage, the unknown magnetic contribution can be estimated.

The conversion efficiency of magnetic fields into electric fields (and vice versa) can be enhanced when ME coupling occurs under mechanical or magnetic resonance conditions [56, 240]. The fact that the resonance frequency typically operates in a microwave regime and can be shifted in presence of a static magnetic or electric field, indicates the possibility to create various tunable sub-THz and THz signal processing devices [241] such as filters [242], resonators [240] and phase shifters [243].

In general, the converse ME effect offers some fundamental advantages comparing to the direct ME effect, because the application of electric rather than magnetic fields allows for lower power consumption, less noise (e.g. due to joule heating) and faster parameter control. It is widely considered that usage of electric fields to control magnetism may lead to a revolution in memory storage technologies. Indeed, if it were possible to completely and reversibly switch on/off magnetization by simply applying an electric field alone, then ME coupling could enable the rapid development of novel electric-writing and magnetic-reading hard disk drives[22]. Even in the case that electric field lacked the ability of completely suppressing and restoring magnetism, it could still assist the magnetization switching, thus leading to an improvement in energy performance. In addition, considering that magnetic and spintronic degrees of freedom are intrinsically coupled to each other, electric field effect opens up new opportunities for the progress of emerging spintronic technologies. In a theoretical work Rondinelli *et al.* [246] defined the concept of *spin capacitance*: when a spin-polarized metal is in contact with a dielectric material, the polarization of the latter brings to accumulation of spin-polarized carriers at the interface. Such heterostructure corresponds to the spintronic analogue of a regular capacitor and therefore could find application for filtering spin-polarized currents or as an element of spin-logic circuitry.

---

[22] In the same line of thinking, also ME random access memories could be realized. They would combine the advantages of ferroelectric and magnetic random access memories for non-volatile magnetic storage of bits controlled via an electric field [244, 245].

2 Materials and Methods

Purpose of this chapter is to provide details about the materials used in the present study and the experimental techniques employed for their fabrication and characterization. In particular, the main characteristics of $La_{1-x}Sr_xMnO_3$ (LSMO) perovskite manganites and of the DEME-TFSI ionic liquid (IL) will be discussed. Information about the experimental setup used to perform *in situ* magnetoelectric (ME) measurements will be given as well.

2.1 Perovskite oxides

Perovskite oxides belong to a class of materials with ABO_3 crystal structure, where the A-site is occupied by an alkaline earth or rare-earth element (e.g. Ba, Sr, Ca, La, Pr) and the B-site is taken by a transition metal (e.g. Ti, Mn, Fe, Cu, Co). The rather simple and at the same time stable crystal structure and the various possible combinations of elements give rise to a series of compounds with fascinating physical and chemical properties. Just to give a few examples, perovskite oxides can display phenomena such as superconductivity [21, 22], ferroelectricity [5, 78, 247, 248], ferromagnetism [11, 109, 249], magnetoresistance [108, 120, 250], ionic conductivity [251–253] and photovoltaic effect [105, 254–256].

Although at some stages of the PhD work the author had the opportunity to investigate different perovskite systems[1], such as $Ba_{1-x}Sr_xTiO_3$ and $BaFeO_3$, the functional perovskite material in the focus of the current dissertation is LSMO.

In the following section the attention shall be brought to the structural, magnetic and electronic features of LSMO and the reasons for their intrinsic correlation, which is at the base of the phenomena of colossal magnetoresistance, metal-to-insulator and para-to-ferromagnetic transitions.

2.1.1 $La_{1-x}Sr_xMnO_3$ and related manganites

$La_{1-x}Sr_xMnO_3$ is a perovskite manganite belonging to the class of so-called *strongly-correlated* systems. In the last 15-20 years such materials have attracted great scientific attention thanks to their intriguing relation between structural, magnetic and electronic degrees of freedom.

Considering a pseudocubic structure (lattice parameter $a_{pc} \approx 3.9\,\text{Å}$) as a simplified[2] representation of the LSMO unit cell (see Fig. 2.1(a)), the A-sites are occupied either by La or Sr cations, whereas in the B-site it is located a Mn cation surrounded by an oxygen octahedron. Mn cations of adjacent unit cells are connected to each other along Mn–O–Mn chains mediated by oxygen anions. Magnetic and transport properties of LSMO depend on the mutual coupling between Mn cations, which is directly related to the Mn oxidation state and the Mn–O–Mn bond lengths

---

[1] See Appendix for a summary of the studies performed on $Ba_{1-x}Sr_xTiO_3$ and $BaFeO_3$ (Sections A.2.1 and A.2.2, respectively).

[2] Although strictly speaking LSMO is not a perfect cubic perovskite in the bulk form, the generally small degree of distortion allows to consider a pseudocubic representation with a good approximation.

and angles. These parameters can be modified by adjusting the Sr doping concentration. Indeed, owing to the different ionic radii of Sr and La, Sr doping affects the interatomic distance and bond angles between the atoms constituting the unit cell. Furthermore, by replacing La^{3+} with Sr^{2+}, the oxidation state of the manganese ions shifts from 3+ to 4+, which corresponds to doping with an electron hole (h^+). In other words, by tailoring the Sr concentration in LSMO, the band filling (charge doping level) and the bandwidth (electron hopping interaction) can be controlled to a considerable extent [257].

The intrinsic complex relation between structural, magnetic and electronic parameters is reflected by a rich variety of crystalline structures and magnetoelectronic states present in the bulk phase diagram[3] of LSMO (see Fig. 2.1(b)). It is worth pointing out that both endmembers, namely $La^{3+}Mn^{3+}O_3^{2-}$ and $Sr^{2+}Mn^{4+}O_3^{2-}$, are antiferromagnetic (AF) insulators. Nonetheless,

---

[3] Details about the experiments performed for the compilation of the LSMO bulk phase diagram can be found in [134, 258, 259].

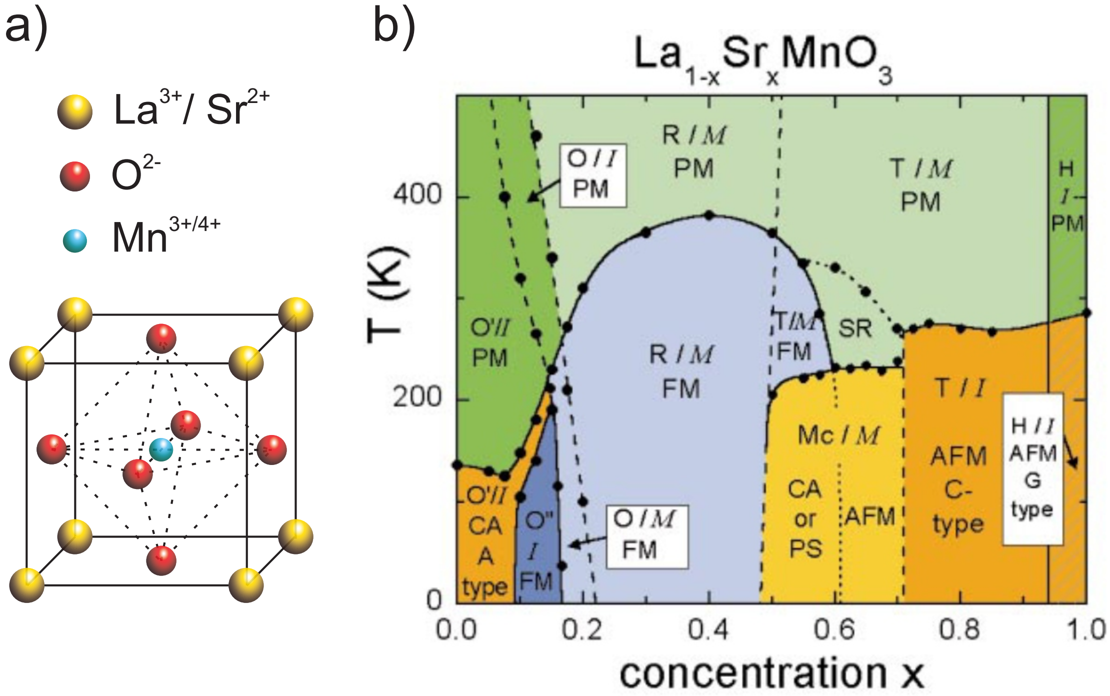

Figure 2.1.: a) Crystal structure of LSMO perovskite. For the sake of clarity, the sketch depicts the pseudocubic representation of the LSMO unit cell. The lattice parameter is $a_{\mathrm{pc}} \approx 3.9\,\text{Å}$. The A-site cations ($La^{3+}$ and Sr^{2+}) are located at the vertices of the pseudocubic structure, while the B-site cation ($Mn^{3+/4+}$) is at the center and surrounded by an oxygen octahedron (dashed lines). b) Structural and magnetoelectronic phase diagram of bulk $La_{1-x}Sr_xMnO_3$. The crystal structures (Jahn-Teller distorted orthorhombic: O', orthorhombic O; orbital-ordered orthorhombic: O", rhombohedral: R, tetragonal: T, monoclinic: Mc, and hexagonal: H) are indicated as well as the magnetic structures (paramagnetic: PM (green), short-range order (SR), canted (CA), *A*-type antiferromagnetic structure: AFM (yellow), ferromagnetic: FM (blue), phase separated (PS), and AFM *C*-type structure) and the electronic states (insulating: I (dark), metallic: M (light). (Figure (b) reprinted by permission from American Physical Society: *Phys. Rev. B* [135], ©2002)

within the doping region of about $0.2 < \mathrm{Sr} < 0.55$, LSMO is a ferromagnetic (FM) metal with Curie point in proximity of room temperature. These remarkable features, together with the fact that Sr doping corresponds to doping with holes, are at the base of the description of the ME coupling phenomena investigated in the present work.

Understanding of the mechanisms governing structural, magnetic and transport properties in strongly-correlated manganites and more specifically in LSMO requires delving deeper into their microscopic origins.

An important figure of merit which determines the distortion of the perovskite structure from an ideal cubic geometry is the so-called tolerance factor Γ [260], defined as:

$$\Gamma = \frac{d_{\mathrm{A-O}}}{\sqrt{2} \cdot d_{\mathrm{Mn-O}}} \tag{2.1}$$

where $d_{\mathrm{A-O}}$ and $d_{\mathrm{Mn-O}}$ correspond to the distance between the A-cation and Mn to the nearest oxygen anion, respectively. An alternative representation of the pseudocubic structure in Fig. 2.1(a) consists of the Mn cations and the respective oxygen octahedra being placed at the vertices of a pseudocube, whereas the A-site cation is at the center of the structure. From this point of view, it becomes clear that $\Gamma = 1$ with a 180° bond angle between the Mn–O–Mn chains only in the ideal case of a perfect cube. The more the radius of the A-site cations differs from the one of Mn, the more the tolerance factor deviates from unity. As a consequence, the Mn–O–Mn bond angle also varies from 180°. In a three-dimensional perspective this translates to the tilting of the oxygen octahedra.

Apart from structural considerations, the importance of the tolerance factor stems from the fact that it directly affects the hopping probability[4] of the conducting charge carriers between the manganese d-orbitals and the oxygen p-orbitals. As Γ deviates from the value of 1, the tendencies to charge localization increase due to the reduction in the mobility of the carriers [260].

As pointed out by Tokura *et al.* [257] a large deviation from $\Gamma = 1$ does not only signifies a decrease in conductivity but also in para-to-ferromagnetic transition temperature. The fact that Γ of LSMO is close to 1 is consistent with the fact that LSMO possesses one of the highest T_C of the entire class of perovskite manganites. Nonetheless other factors have to be considered in order to provide a more precise interpretation of the mechanisms underlying magnetic and transport properties.

The peculiar perovskite configuration with the Mn cation being surround by an oxygen octahedron has a deep impact on the orbital ordering of Mn (see Fig. 2.2). Indeed the electrostatic field produced by the oxygen octahedron - the so-called *crystal field* [262] - is responsible for splitting the 3d electron orbital states of manganese from a classical 5-fold degeneracy into a lower-lying triplet (t_{2g}) and a higher-lying doublet (e_g). Thus, the d_{xy}, d_{xz} and d_{yz} orbitals are at a lower energy than the d_{z^2} and $\mathrm{d}_{x^2-y^2}$ orbitals, because the former group is farther from the oxygen ligands than the latter and therefore experience less coulombic repulsion[5].

An additional effect, that further lifts and stabilizes the energy levels occupied by the d electrons, is given by the Jahn-Teller distortion, which is related to the spontaneous uniaxial deformation of the $\mathrm{MnO_6}$ octahedron [257]. This electron-lattice interaction helps stabilizing the

---

[4] Notice that in general the hopping probability pertains only Mn–O–Mn chains, because for a 90° bond the hopping involving a p-orbital at the oxygen simply cancels [260]. This is also at the origin of the interplane AF coupling along the c-axis in cubic perovskites [261].

[5] For visualizing the shape of the orbitals the reader may refer to ref. [261].

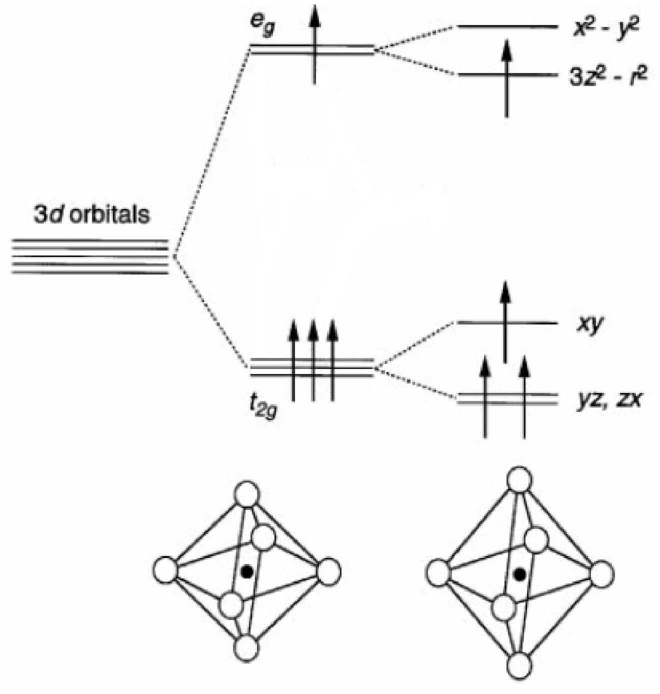

Figure 2.2: Degeneracy of manganese orbitals in LSMO. The five-fold degenerate electronic 3-d levels of manganese undergo a splitting in a low-energy triplet (t_{2g}) and a high-energy doublet (e_g) due to the electrostatic field induced by the surrounding oxygen octahedron (the crystal field). The Jahn-Teller effect brings about a further lift in degeneracy. The four electrons of Mn^{3+} are in a high-spin configuration. (Adapted by permission from ELSEVIER: *J. Magn. Magn. Mater.* [257], ©1999)

electronic configuration of Mn^{3+}, which otherwise would tend to disproportionate into a mixture of Mn^{2+} and Mn^{4+} [16].

Despite the splitting of energy levels induced by the crystal field and the Jahn-Teller effect, the not so large energy gap between t_{2g} and e_g states allows the electrons to fill the orbitals with a high spin configuration, in accordance with the Hund's rules.

The t_{2g} electrons, not highly hybridized with the 2p-orbitals of oxygen, are always localized. The e_g electrons, strongly hybridized with the 2p-orbitals of oxygen, may be either localized or itinerant.

The theoretical models proposed by Anderson [263] (the superexchange (SE) interaction) and Zener [264] (the double-exchange (DE) interaction) take into account spin, orbit and lattice parameters and explain to a great extent the strong correlation between magnetic and transport properties of LSMO and related perovskite manganites (see Fig. 2.3).

Both mechanisms are of indirect exchange type because the Mn ions are too far from each other to directly affect their spin configuration. Therefore magnetic exchange interactions between Mn

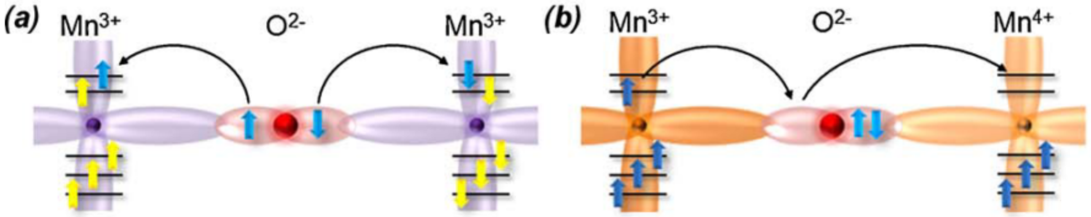

Figure 2.3.: Magnetic coupling mechanisms in strongly-correlated manganites. Schematic representation of (a) superexchange (antiferromagnetic and insulating behavior) and double-exchange (ferromagnetic and metallic behavior) interactions. (Adapted by permission from ELSEVIER: *Mater. Sci. Eng. R-Rep.* [28], ©2010)

ions are mediated by the (non-magnetic) oxygen anions. In the ground state, SE interaction is manifested by AF alignment of the Mn spins and insulating behavior, while DE interaction leads to FM coupling and metallic behavior.

Let us consider the case of the AF insulator $La^{3+}Mn^{3+}O_3^{2-}$ (Sr = 0). SE interactions are driven by the fact that the spins in the p-outer shells of the oxygen ions interconnecting the Mn cations have an antiparallel alignment. Due to the hybridization with the d-outer shell of Mn^{3+} and the strong intra-atomic Hund rule exchange, the spins in the t_{2g} and e_g electronic states of adjacent Mn ions are forced to be in an antiparallel AF alignment. In addition, carrier conductivity is suppressed because the e_g electrons of Mn are localized due to the lack of free available electronic states to move into. Indeed O^{2-} has a complete p-orbital configuration and so "jumping" of electrons is prevented by the electron-electron coulombic repulsion. In this context, the insulating behavior of $LaMnO_3$ can be inferred as a prototypical example of Mott-insulator[6].

By doping $LaMnO_3$ with strontium, the coupling progressively moves from SE to DE. Sr doping implies the insertion of holes and so the removal of some e_g electrons from the d-orbitals of Mn. Thus, Mn progressively shifts from 3+ to 4+ oxidation state and some new electronic d-states become accessible. Via a simultaneous double step process (which is necessary since the O^{2-} orbitals are complete) electronic hopping occurs from Mn^{3+} $3d^4$ to O^{2-} $2p^6$ and from O^{2-} $2p^6$ to Mn^{4+} $3d^3$ states. Overall, this translates in the conduction of an electron - the so-called Zener electron - from a Mn^{3+} to a Mn^{4+} cation. Zener [264] showed that the electron hopping process is energetically favorable only if the conduction electrons carry along their own spin unchanged and they move in an environment of spins pointing in the same direction. These remarkable features explain why LSMO in the $0.2 < \mathrm{Sr} < 0.55$ doping range is ferromagnetic, metallic[7] and spin-polarized[8].

At larger doping concentrations (Sr > 0.55) DE interactions become progressively weaker until the excessive emptying of electrons from e_g energy levels leads to carrier localization and AF coupling between adjacent Mn^{4+} cations.

The theories of DE and SE interactions reveal also other peculiarities of the LSMO phase diagram.

As predicted by Goodenough [265], the optimum strontium doping to enhance DE in a random lattice of Mn^{3+} and Mn^{4+} cations occurs for Sr = 0.31. In this way the largest number of Mn^{3+} cations have one, and only one, Mn^{4+} cation as near neighbor[9]. This is in accordance with the maximum $T_C \approx 360$ K experimentally observed for a strontium doping of ≈ 0.3 [266].

Another remarkable aspect is the good agreement [259, 267] between theory and experiments on the value of the average ground state magnetization per unit cell (or analogously per Mn atom):

$$m_{\mathrm{Mn}} = (1-x)\cdot 4\mu_{\mathrm{B}} + x\cdot 3\mu_{\mathrm{B}} = (4-x)\mu_{\mathrm{B}} \tag{2.2}$$

where x is the strontium doping and μ_B is the Bohr magneton. The formula is a direct consequence of the fact that each Mn^{3+} contributes with four electrons (and therefore four

---

[6] Conducting charge carriers are present, but no free electronic states are available, therefore conductivity is suppressed.

[7] It is worth to notice that although the LSMO charge carrier density of about $\approx 10^{21}\,\mathrm{cm}^{-3}$ is lower than in metals ($n \approx 10^{22}\,\mathrm{cm}^{-3}$), the hopping mobility is enough to bring to metallic behavior.

[8] LSMO is a so-called half-metal.

[9] In a perfectly ordered lattice this would occur for Sr = 0.25. Nonetheless, in general double exchange mechanism requires a disordered arrangement.

aligned spins, each one bringing one μ_B), whereas Mn^{4+} has only three electrons with spins aligned. As an example, the experimentally measured magnetization is close[10] to 3.7 $\mu_B Mn^{-1}$ for Sr = 0.3 [266].

Notably, the magnetic exchange interactions of LSMO and related manganites render them nearly-ideal spin polarized systems (see Fig. 2.4). Hwang et al. [268] and subsequently Park *et al.* [269] reported on 100% spin polarization of $La_{2/3}Sr_{1/3}MnO_3$. As a comparison, the degree of spin polarization of conduction electrons at the Fermi energy in elemental ferromagnetic 3d metals is $P = (n_{up} - n_{down})/(n_{up} + n_{down}) < 50\%$ [99].

The mechanisms underlying the DE interaction also explain why the para-to-ferromagnetic transition temperature (T_C) corresponds to the metal-to-insulator transition temperature (T_{MI}). Above T_C the disorder induced by thermal energy does not allow the spins for staying in a parallel configuration. Hence, neither ferromagnetism nor carrier conductivity (due to spin dependent scattering) can take place. On decreasing temperature, both spin alignment along a preferred direction and carrier hopping become favorable.

Interestingly, it has been found that if an external magnetic field is applied during cooling, the further promotion of spins alignment brings to a decrease in resistivity of several orders of magnitude. After the thousandfold change in resistivity measured in $LaCaMnO_3$ films by Jin *et al.* [250], the term *colossal* magnetoresistance (CMR) was coined in order to distinguish the phenomenon from standard magnetoresistance and giant magnetoresistance.

Since the DE model alone is not enough to justify the magnitude of the CMR effect, new alternative theories, involving spin canting [270] and Jahn-Teller polaron [271], were put under discussion.

After years of debate on the origin of CMR, theoretical and experimental works converged to a unified picture pointing toward a physics of manganites dominated by intrinsic inhomogeneities in the form of coexisting phases, which compete against each other [260]. In a completely homogeneous material one would expect a sharp transition from a low-temperature ferromagnetic metallic phase to a high-temperature paramagnetic insulating phase. Nonetheless, computational [260, 272, 274, 275] and experimental [211, 273, 276–278] studies revealed the compresence of metallic and insulating domains below T_C/T_{MI} transition temperatures in manganites. The phenomenon is called *magnetoelectronic phase separation* (see Fig. 2.5) and it is considered to be

---

[10] Nonetheless in the next chapters it will be explained why generally it is not possible to reach such high values of magnetic moment in LSMO thin films.

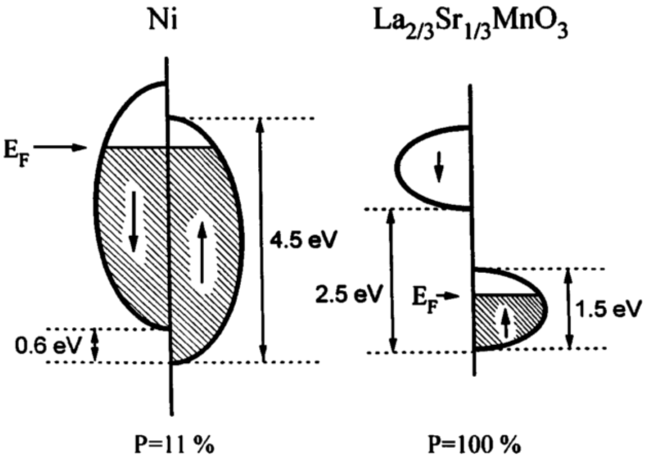

Figure 2.4: Energy level diagrams of Ni and $La_{2/3}Sr_{1/3}MnO_3$. Differently from Ni, $La_{2/3}Sr_{1/3}MnO_3$ features only one spin band accessible for the conduction carriers at the Fermi energy. (Reprinted by permission from AMERICAN PHYSICAL SOCIETY: *Phys. Rev. Lett.* [268], ©1996)

an intrinsic feature of single crystals, unrelated to grain boundary effects of polycrystals [260] or chemical inhomogeneities [272]. Moreo proposed that even at the ground state, where the magnetic state is supposed to be entirely FM or AF, phase separation tendencies, rather than of electronic origin, may occur in the vicinity of phase transitions due to the *disorder* induced by the different ionic radii of the various elements composing the manganite [272]. Experimental studies showed that the size of non-FM insulating and FM metallic clusters can extend from a few tens of nanometers [273, 276] up to microns [277–280].

In a phase-separated scenario, the essence of the CMR effect can be explained as follows. At temperatures slightly above T_C the manganite sample consists of a predominant network of insulating phases and a minor population of metallic domains. Carrier conductivity is hampered by the lack of macroscopic conduction paths. However, by decreasing temperature below T_C, the size of the metallic domains starts to increase at the expense of the insulating ones. Progressively, an interconnected network of conducting domains within an insulating surrounding matrix is formed. The consequent creation of percolative paths, which act as sort of conducting filaments, is consistent with the drastic reduction of resistivity observed in the CMR effect.

After this brief survey on strongly-correlated manganites, it becomes evident that providing an adequate interpretation of the coupling mechanisms between structural, magnetic and transport properties in such systems is a non-trivial task that requires the consideration of manifold factors such as the tolerance factor Γ, the crystal field splitting, the Jahn-Teller effect, indirect exchange couplings and phase separation.

Figure 2.5: Phase separation in CMR manganites. (a) Monte Carlo simulation on a doped manganite. Dark regions have spins up in case of zero magnetic field, grey regions are previously-spins down that have flipped to up on application of an external magnetic field. White regions have spins down with and without magnetic field. Arrows mark the areas that became interconnected after spin flipping, thus enhancing percolative-like features. (b-d) Current-voltage conductance maps (500 × 500 nm^2) in LSMO performed via Scanning Tunneling Microscopy at different temperatures (black = insulating, white = metallic). The density of coexisting phases changes on modification of the temperature. (Figures (a) and (b-d) reprinted by permission from American Physical Society: *Phys. Rev. Lett.* [272], ©2000 and *Phys. Rev. Lett.* [273], ©2002, respectively.)

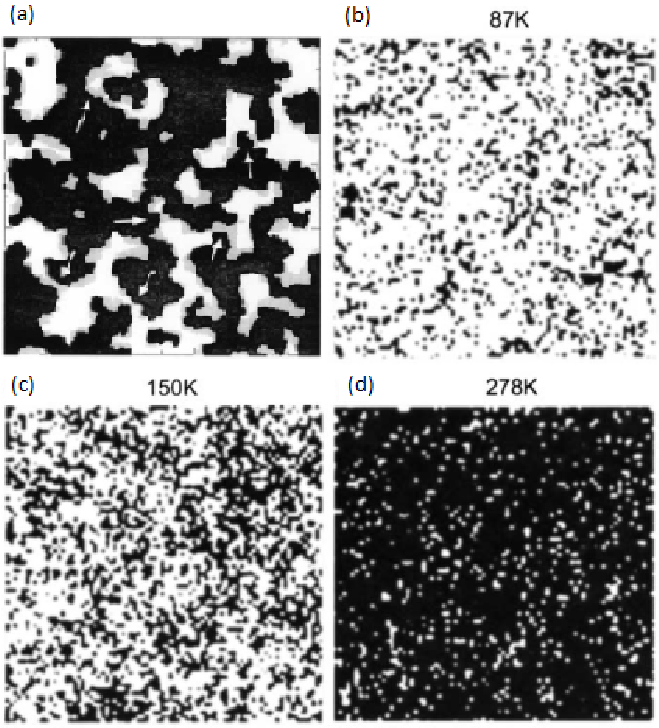

2.1.2 $La_{1-x}Sr_xMnO_3$ films and $SrTiO_3$ substrates

The results presented in the current work focus on $La_{0.74}Sr_{0.26}MnO_3$ films with a thickness between 3 - 15 nm. The specific composition of Sr = 26 has been chosen because, as can be seen in the phase diagram (see Fig. 2.1(b)), it lies in the region between $0.15 < Sr < 0.3$ where magnetic and transport properties change steeply upon a relatively little modification of the doping level. At the same time the Curie point is still above room temperature. As a comparison, although the highest T_C of ≈ 360 K occurs at Sr = 0.33, in the vicinity of such value the phase diagram is almost plateau-like, signifying less sensitivity towards modification of the doping level.

The thickness of the LSMO films was kept at rather small values in order to maintain a high surface-to-volume ratio. Indeed, as already discussed in the Introduction, tuning of the magnetic properties of conducting materials using an external voltage is constrained by the limited penetration depth of the electric field. Therefore, due to the mainly interfacial nature of ME coupling, a biggest relative change in the magnetism is expected for a thin film geometry.

LSMO was grown in the form of epitaxial films on $SrTiO_3$ (STO) substrates[11] (size of 10 mm × 10 mm × 0.5 mm, (001) oriented, epi-polished, 0.3° of miscut angle, purchased from SurfaceNet GmbH). The combination of the two materials is widely used in the literature [59, 266, 281–290], because STO has a cubic perovskite structure (lattice parameter $a = 3.905$ Å) [291] and a low lattice misfit with LSMO. In addition, if necessary, it is possible to adjust the surface quality of STO down to the atomic level via chemical etching and high-temperature annealing processes [292–294]. These features facilitate the growth of highest quality epitaxial LSMO films.

Other two characteristics of STO that come at a hand are its diamagnetic and insulating nature. The former results in a negligible influence of STO on the magnetic signal coming from LSMO (although the substrate is macroscopically bigger than the films, its diamagnetic contribution can easily be subtracted). The latter ensures that only the conductive LSMO films participate in the interfacial charging/discharging processes with the ionic liquid electrolyte (LSMO is the active electrode).

As a final remark, which will be further elaborated in Chapter 3, it should be noticed that the properties of LSMO films may substantially deviate from their bulk form. Indeed, at the nanoscale several factors, such as substrate-induced strain effects, oxygen stoichiometry, or interdiffusion at the substrate/film interface, can have a deep influence on the structural and magnetic characteristics of LSMO. The presence of so-called electric and magnetic dead layers [120, 266, 275, 281, 282, 295–297] at the LSMO/STO interface is a clear example of the new complexities emerging at the nanoscale, where the bulk phase diagram can be used only in first approximation [298].

2.2 DEME–TFSI ionic liquid and related electrolytes

As a general definition, an electrolyte is a chemical solution containing ionic species dissolved in a solvent. Electrolytes display large ionic and poor electronic conductivity; ionic motion can be controlled via application of an external voltage. They can be classified in solid electrolytes,

---

[11] At some stages of the work of thesis also other substrates, such as Nb-doped STO, MgO, $(La_{0.3}Sr_{0.7})(Al_{0.65}Ta_{0.35})O_3$ and $NdGaO_3$, have been tested. Here we focus on the characteristics of STO.

when ions move within a polymeric [153, 299–301], ceramic [302, 303] or glass [304] medium, or liquid electrolytes, when water [154, 196] or a non-aqueous liquid [155] are used as solvent.

In the current study we are interested in a special class of non-aqueous liquid electrolytes called *ionic liquids* (ILs) [17, 113, 305, 306]. ILs can be defined as salts with a very low melting point. They consist of a solvent-free solution composed of only ions, typically being in the liquid phase in a relatively large range of temperatures, including room temperature. Comparing to other electrolytes, ILs present some unique properties that are of critical importance for the realization of high-performance charge-accumulation devices with enhanced energy efficiency and safety.

ILs are known for being non-volatile, which signifies a high thermal stability (low vapor pressure) and non-flammability. Most of ILs are stable enough for ordinary use up to 200 - 300 °C. Thanks to the large number of ions ($n\,e$) and remarkable ionic mobility μ, ILs feature a large ionic conductivity $\sigma = n\,e\,\mu \approx 10^{-2}\,\mathrm{S\,cm^{-1}}$, which is desirable for fast charging/discharging applications. ILs allow to achieve larger energy densities than standard water-based electrolytes, due to the possibility to enlarge the operating potential window beyond the limits imposed by water decomposition reactions [154].

Table 2.1.: Properties of commonly used ILs. T_g and T_d stand for the glass and decomposition temperatures, respectively. Values of potential window and conductivity refer to a temperature of 25 °C. A more comprehensive database of the physico-chemical properties of ILs can be found in Zhang *et al.* [306].

Ionic Liquid	$T_\mathrm{g} - T_\mathrm{d}$ range (°C)	Potential window (V)	Conductivity ($\mathrm{mS\,cm^{-1}}$)	Density ($\mathrm{g\,cm^{-3}}$)	Reference
DEME–TFSI	-91, +383	-3, +2.5	3.5	1.42	[305]
DEME–$\mathrm{BF_4}$	-100, +318	-3, +3	4.8	1.18	[305, 307]
EMI–$\mathrm{BF_4}$	-87, +391	-2, +2.5	12.3	1.24	[17, 305]
EMI–TFSI	-98, +420	-1.8, +2.5	8.6	1.52	[306]

The electric double layer (EDL) capacitance of ILs is typically around 10 $\mu\mathrm{F\,cm^{-1}}$ [17, 113] and its value was found to be nearly unchanged on different conducting electrodes such as Hg or C [308].

Utilization of ILs requires attention with respect to the amount of dissolved impurities, which are detrimental for the electrochemical properties. The main sources of contamination are represented by water and oxygen, which can be easily absorbed from air.

The specific ionic liquid employed in the current study is DEME–TFSI (diethylmethyl(2-methoxyethyl)ammonium bis(trifluoromethylsulfonyl)imid, purchased from SIGMA ALDRICH). Both storage and utilization of the IL took place under inert atmosphere (either Ar gas inside a glovebox or He gas inside a magnetometer). Prior to utilization, the DEME-TFSI ionic liquid was purified under vacuum (10^{-3} mbar) and high temperature (100 °C) for about 24 h in order to decrease the amount of contamination residuals below 50 ppm. Details about the structure and physico-chemical features of the DEME–TFSI ionic liquid can be found in Fig. 2.6 and Table 2.1.

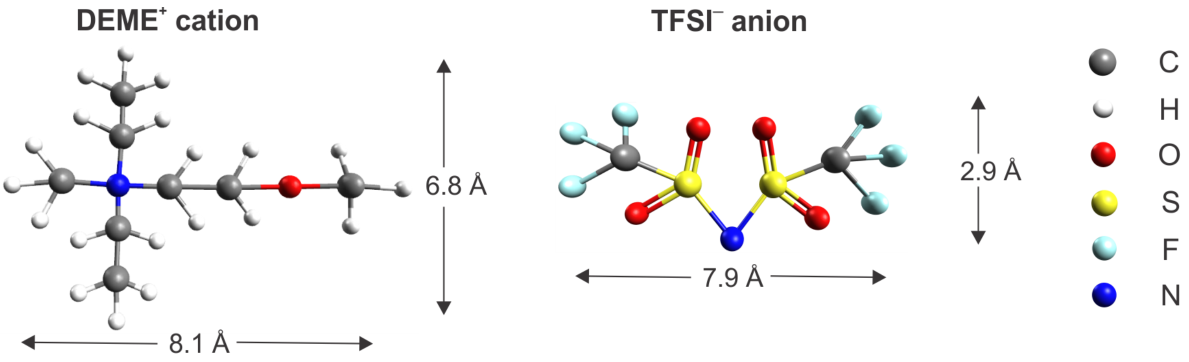

Figure 2.6.: DEME-TFSI ionic liquid. Structure and size of DEME cation [309] and TFSI anion [310] modeled with *Avogadro* molecule editor.

2.3 LSMO samples preparation method

2.3.1 Large-Distance Magnetron Sputtering

Large-Distance Magnetron Sputtering (LDMS) belongs to the family of physical vapor deposition (PVD) methods, consisting in the controlled transfer of atoms in the gas phase from a source to a substrate where film formation and growth proceed atomistically [311].

To a large extent, nanotechnologies owe their birth and development to the precise adjustment of material's control parameters offered by PVD techniques.

Pulsed laser deposition, molecular beam epitaxy and sputtering are perhaps the most well-known and widely-spread PVD methods. The choice of which deposition technique is the most appropriate for preparation of samples is not always obvious. Several factors, such as quality, purity and size of the final samples as well as required processing time and equipment costs, have to be considered in order to identify the optimal deposition tool.

In the current section, the main features of conventional sputtering and of the LDMS technique used for fabrication of LSMO films shall be discussed[12].

Essentially, a sputtering apparatus is composed of a vacuum chamber, a target acting as source material and a substrate onto which the evaporated atoms are deposited.

During deposition the chamber is filled with an inert gas (typically Ar) with a pressure between 1–10^{-3} mbar. The source-target is in direct contact with a cathode which is set at a certain negative voltage with respect to a positive anode. According to the kind of target material, a constant (DC) voltage is applied for the deposition of conducting metals, whereas an alternating (RF) voltage is more suitable for the sputtering of insulating materials[13]. By using an ionization current, neutral Ar atoms are ionized and then accelerated towards the source-cathode. Due to momentum transfer, atoms are ejected from the target and "fly" through the chamber until reaching the substrate. The mixture of neutral gas atoms, Ar^+ ions and secondary electrons released by the bombarded cathode produce a lighting plasma referred as *glow discharge*.

---

[12] A more detailed description of the sputtering mechanism can be found in ref. [311].

[13] In DC mode an exceedingly large voltage should be supplied to sputter an insulating target, because not enough current is driven to the cathode. In RF mode (13.56 MHz is the typical frequency) the target *self*-biases to a negative voltage due to the different mobility of electrons and ionic species. In this way reasonable deposition rates are achieved applying relatively low voltages (more details in ref. [311]).

In case of *magnetron* sputtering a magnet is inserted underneath the cathode-target assembly. The generated magnetic field act as a trap for the electrons of the plasma near to the target, thus producing two advantageous effects. On the one hand, it increases the ionization rate of Ar atoms in proximity of the target and therefore also the sputtering rate (the typical ring-like track left on the target due to erosion is a direct consequence of such effect). On the other hand, electron trapping driven by the magnetic field drastically reduces electron bombardment against the sample and so also its possible damaging. Indeed, all the negatively charged particles that manage to escape from the plasma will accelerate towards the inner parts of the chamber that are at ground potential.

The growth of good quality compounds (such as alloys or oxides) is somewhat more complicated than the case of single-elemental metals. If the target is composed of different materials, the sputtering yield, defined as the number of atoms released by the target surface per incident Ar ion, can substantially differ for the various elements (each one has specific adhesive forces). Although sputtering is considered as a self-stabilizing process[14], it is recommended to investigate the stoichiometry of the deposited films, because it may diverge from the target composition.

Apart from the different sputtering yield, a common problematic regarding the growth of oxides is related to the formation of oxygen deficiencies in the deposited films. A way to circumvent - at least to a certain extent - the reduction in oxygen stoichiometry is to add oxygen gas during the growth process. Anyhow, the ability to adequately control the rate of oxygen incorporation into the film is a complex task, which depends on the oxygen partial pressure, the substrate temperature (the higher the temperature, the stronger the film oxidation) and the growth rate. In most cases, it is necessary to find an appropriate trade-off between these parameters in order to obtain high quality epitaxial oxides. Aiming at improving the degree of oxidation of the films, after deposition it is a common practice to perform a slow cooling down process in pure oxygen gas, often also followed by an *ex situ* high-temperature post-annealing step in ambient atmosphere (or with flowing oxygen). Considering the specific case of LSMO, careful control of the oxygen stoichiometry is important because it directly affects the perovskite structure and therefore also the magnetic and transport properties [281, 290].

It should be noticed that the addition of oxygen gas during sputtering deposition introduces new complexities to the growth process. One of the major drawbacks is the fact that negative ionized oxygen ions accelerate and possibly damage the film during growth. A way to mitigate this problem is to set target and substrate to an off-axis geometry (the so-called off-axis sputtering). As a negative side effect both film uniformity and deposition rate decrease.

An alternative is to increase the target-substrate separation distance. Indeed, if the mean-free-path of the accelerated oxygen ions becomes comparable to the target-substrate separation, then, thanks to particle scattering, less damage takes place in the sample. This is exactly the advantage offered by LDMS, which feature a distance of about 30 cm between target and substrate, whereas it is around 5 - 10 cm in conventional sputtering. The large distance helps also to improve film uniformity over large surface areas, but as a disadvantage the deposition rate is decreased. Further, during preparation of a compound the sample stoichiometry may significantly diverge from the target due to different scattering lengths of involved elemental species.

---

[14] If an element *A* has a larger sputtering yield than an element *B*, initially the surface of the target will eject more *A* species. But once the density of *B* species increases at the target surface, more of them will be sputtered.

LDMS chamber specifications

After an introduction on the general features of sputtering and LDMS, technical specifications of the employed LDMS chamber shall now be described (see cross section drawing in Fig. 2.7).

The custom-made LDMS chamber (from Createc Fischer & Co. GmbH) is equipped with eight 3" magnetrons arranged in an octagonal geometry. The multiple source-target assembly enables concurrent deposition from different target materials[15], which is useful for the preparation of alloys and compounds or, in case the same target material is used in different sources, for increasing the deposition rate. Alternatively, multilayer samples can be prepared by sequentially closing/opening target shutters.

The stainless-steel sample holder is lodged in a manipulator at the center of the chamber at a distance of about 28.5 cm and an incident angle of 37.5° with respect to the magnetron targets. During deposition the manipulator can be rotated (typically with a speed of 8 rpm) to improve film uniformity. In addition, the manipulator hosts four 250 W halogen lamps, which allow for heating the samples up to a maximum temperature of about 850 °C. The temperature is monitored using a type-K thermocouple mounted close to the lamps. In order to more precisely

---

[15] As a good common practice, it is recommended to sputter clean the targets for about 30 min before setting up a new deposition in order to rule out possible sample contamination due to partial material cross deposition between neighboring sources.

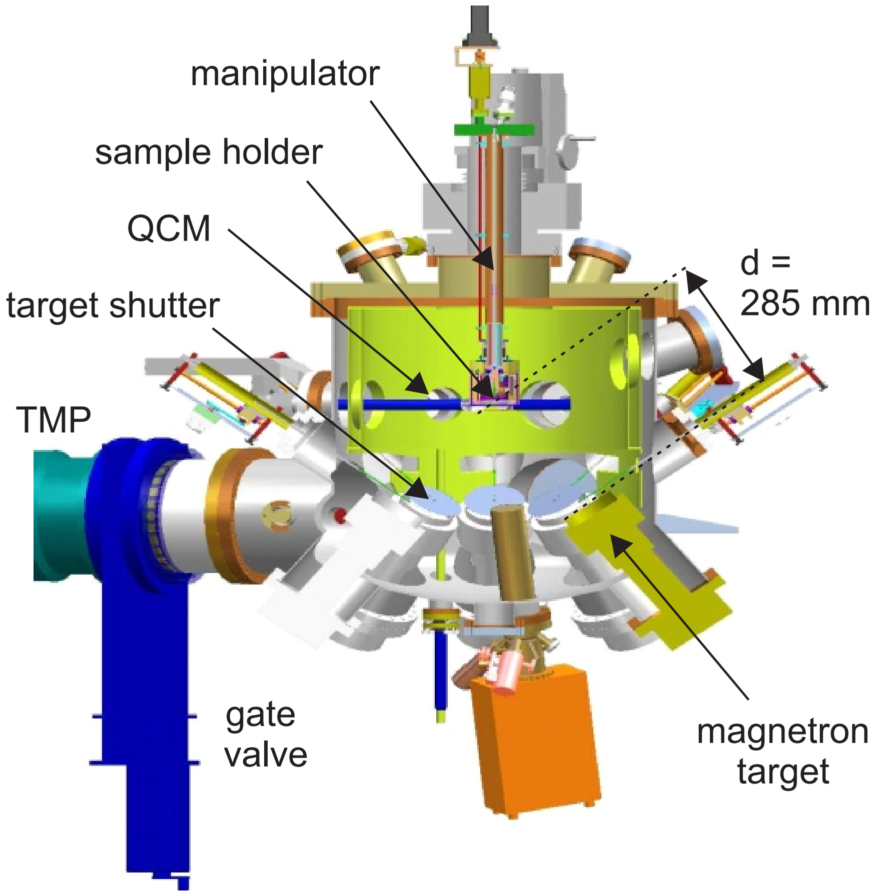

Figure 2.7.: Schematic cross section of the Large-Distance Magnetron Sputtering chamber.

track the actual sample temperature, a temperature calibration was performed by comparing the values of the thermocouple with another one mounted directly on top of a sample holder[16]. It is worth noticing that after any maintenance session requiring the venting of the whole sputtering system, the heating lamps came at a hand for baking the chamber from the inside, thus allowing to promptly reach the base pressure (as low as 10^{-9} mbar) thanks to a facilitated removal of adsorbate contaminants.

In the proximity of the sample manipulator, a quartz crystal microbalance (QCM) displays the growth rate and film thickness. The QCM deposition rate, which may substantially vary when different growth parameters are used, was calibrated via X-ray Reflectometry (XRR) measurements carried out on tooling samples.

During deposition the chamber pressure is monitored with a capacitive vacuum gauge (Baratron, MKS INSTRUMENTS). An adjustable gate valve placed in front of the turbo molecular pump permits to control the deposition pressure in a wide range (1–10^{-3} mbar). The gas mixture (Ar/O_2) can be set via two distinguished flow meters connected to separated gas bottles (O_2: 99,998%, Ar: 99,9999%).

The purity of the final samples depends on the chamber base pressure and the quality of substrates, sample holders, sputtering gases and targets. The functional thin films of LSMO employed in the current work were deposited from a commercially available sputtering target with chemical composition $La_{0.65}Sr_{0.35}MnO_3$ and 99.9% purity (from KURT J. LESKER). Details about the optimization of structural and magnetic properties of LSMO as a function of different growth parameters will be addressed in Section 3.

2.4 LSMO samples characterization methods

In this work a variety of experimental techniques has been utilized to analyze the microstructure, chemical composition and magnetic properties of LSMO thin films and to carry out *in situ* ME measurements on LSMO/IL devices.

2.4.1 X-ray Diffraction

X-ray Diffraction (XRD) has been widely used to investigate the degree of epitaxial quality of LSMO films grown on STO substrates.

XRD [312, 313] is an experimental technique where an incident X-ray beam impinges on a sample and scatters along specific directions according to the Bragg law:

$$2\,d\,\sin\theta = \mathrm{m}\,\lambda \tag{2.3}$$

where θ is the incident angle, m is an integer number, λ is the wavelength of the X-ray radiation. The parameter d represents the size of the periodic structure, such as a certain family of crystallographic lattice planes, responsible for coherently scattering the X-rays.

For the study of LSMO films, XRD measurements were performed using a BRUKER D8 *Discover* diffractometer in a high-resolution set up (HRXRD). The X-ray source is composed of an X-ray tube with a copper anode against which electrons are accelerated with a voltage of 40 kV. The generated radiation is composed of Cu-K_α and Cu-K_β characteristic lines and Bremsstrahlung

---

[16] See also Appendix (Section A.2.3)

background. The primary beam is first reflected by a Göbel mirror, which converts it into a parallel beam with a width of 1.2 mm and removes the Cu-K_β radiation, and then by a four-bounce Ge(022) monochromator, which generates a well-defined Cu-$K_{\alpha1}$ beam with $\lambda = 1.54\,\text{Å}$. The X-ray beam intensity can be tuned by means of an absorber composed of Cu sheets placed in series. Afterwards, the beam is scattered by the sample (which is mounted on a vacuum chuck) and proceeds his path through an anti-scattering slit with a 0.5° opening until reaching the NaI:Tl scintillation counter detector.

The X-ray setup presents a four-circle goniometer, which allows for fine adjustment of sample and detector alignment positions[17]. This feature is essential for the investigation of epitaxial thin films. In order to analyze the degree of epitaxial quality of LSMO films grown on top of (001)-oriented STO substrates, θ-2θ scans, rocking curves and two-dimensional Reciprocal Space Maps[18] (RSM) were carried out. Information regarding the film thickness (including the analysis of tooling samples) and interface roughness was extracted by means of X-ray Reflectometry (XRR).

HRXRD data analysis was done using *EVA* and *Leptos* program software from BRUKER-AXS GMBH.

2.4.2 Transmission Electron Microscopy

If HRXRD provides a macroscopic information on the structural characteristics of thin film samples, Transmission Electron Microscopy (TEM) is a perfect complementary technique to investigate microstructures from a local perspective. Similarly to XRD, TEM is based on the coherent diffraction of a probe which scatters against a periodic structure within a specimen. In case of TEM the probe is represented by high-energy electrons which pass through a thin sample (thickness < 100 nm). Selected LSMO samples were prepared for TEM and Scanning TEM (STEM) analyses by extracting a thin lamellae using a Focused Ion Beam (FIB). TEM studies[19] were carried out in a FEI Titan 80-300 electron microscope operated at 300 kV.

2.4.3 Atomic Force Microscopy

Atomic Force Microscopy (AFM) is a surface science technique belonging to the wider class of Scanning Probe Microscopies (SPM). The analysis of the surface morphology of LSMO films was investigated by tapping-mode AFM. The measurement principle is related to the interaction via Van der Waals or electrostatic forces between the sample surface and a sharp Si tip mounted on a cantilever. The cantilever is put in oscillation at its resonance frequency with a certain amplitude. On approaching the sample, the interaction with the surface becomes stronger and the tip undergoes a change in oscillation amplitude. An external feedback loop system acts to restore the initial value by adjusting the sample-tip distance. In this way a roughness profile along the z-direction can be obtained while scanning the AFM tip along the x-y plane.

---

[17] Four angles define the alignment of the sample: 2θ is the angle between the incident and diffracted beam, ω defines the angle between the incident beam and the sample plane ($\omega = \theta$ in a standard Bragg-Brentano geometry), φ characterizes the angle of rotation around the normal to the sample plane, χ describes the eucentric tilting of the sample normal out of the diffraction plane.

[18] RSM scans were performed only on a few selected samples. RSM studies were performed by Dr. Ralf Witte at the Institute of Nanotechnology (KIT).

[19] TEM investigations were performed by Dr. Houari Amari at the Institute of Nanotechnology (KIT).

Tapping-mode AFM studies were carried out on LSMO films using a a VEECO / DIGITAL INSTRUMENTS MultiMode AFM. The AFM tip (HQ:NSC15 / Al BS from μmasch) featured a 8 nm radius and a resonance frequency of ≈325 kHz. The measurements were performed *ex situ* under ambient conditions thanks to the stability of oxides in air.

2.4.4 Elemental analysis techniques

During STEM analysis, Energy Dispersive X-ray (EDX) spectroscopy allowed to extract elemental distribution profiles of the LSMO films grown on STO substrate.

EDX spectroscopy is based on the emission of characteristic X-ray radiation lines which are the fingerprint of a specific element. When high-energy electrons are accelerated towards a specimen, some of the core electrons may be excited from the ground state and escape from their shell. The empty shell can be filled by an electron from an outer, higher energy shell. The difference in energy between outer and inner shell may be released in the form of characteristic X-rays.

Complementarily to EDX, quantitative (with an accuracy of about 2%) and macroscopic information on the samples stoichiometry was attained via Rutherford Backscattering Spectroscopy[20] (RBS). The RBS setup employed a beam of high-energy α particles (i.e. $^4He^+$ ions with energy of 2 MeV) accelerated by a Van de Graaff generator, which hit a LSMO specimen perpendicularly. In first approximation, the scattering process can be described as an elastic, hard-sphere collision event between the α particles and the nuclei of the sample-target. The energy loss of the backscattered ions is measured with a detector at a backscattering angle of 152°. The target composition can be estimated on the basis of element-specific scattering angles and energies of the incident α particles.

For RBS studies, a LSMO film was intentionally grown on a MgO substrate (following the same deposition parameters used with STO substrate) in order to avoid the overlap of the strontium signals.

2.4.5 Superconducting Quantum Interference Device magnetometry

SQUID magnetometry [314–316], thanks to its extraordinary sensitivity capable to detect ultra small magnetic moments down to 10^{-8} emu, is one the most-established techniques to investigate the magnetic properties of thin and ultrathin films film with highest accuracy.

A SQUID magnetometer can be referred to as a very precise magnetic flux-current-voltage converter. The main features of a DC-SQUID magnetometer, that represents one of the most commonly-used SQUID variants, can be summarized as follows.

A "bare" DC-SQUID sensor consists of a superconducting loop with two Josephson junctions[21] connected in parallel (see Fig. 2.8(a)). A superconducting current flows through the ring in such a way that equal currents pass through the two Josephson junctions. Afterwards the two branches converge again into a unique superconducting current. No significant resistance arises from the tunneling of charge carriers (Cooper pairs) through the junctions and therefore *no* voltage drop is measured at the two extremes of the sensor between the points A and B.

---

[20] RBS analysis was performed by A. Beck at the Institute for Solid State Physics (KIT).

[21] A Josephson junction consists of two superconductors separated by a "weak" link, represented for example by a thin insulating barrier. In a superconducting state electron-electron Cooper pairs can tunnel through the barrier without any voltage drop at the junction extremes.

If the DC-SQUID sensor experiences a change in magnetic flux, for example due to a probe-magnet moving perpendicularly to the sensor's plane, then, in accordance with Faraday's law, the induced current adds to the superconducting current in one branch and subtracts in the other. In this case a measurable voltage arises between the A-B extremes.

In real devices, in order to achieve highest sensitivity, the probe-magnet (i.e. the sample) is not moved in the direct proximity of the DC-SQUID sensor, but rather inside a separated superconducting pick up loop wire with a much larger flux capture area (see Fig. 2.8(b)). The superconducting wire is then coupled to the DC-SQUID sensor via a multi-turn spiral (a flux transformer) surrounding the latter. The final SQUID output consists of a voltage signal expressed as a function of the sample position along the superconducting input coil.

Further improvements of the measurements quality can be attained via the Reciprocating Sample Option (RSO). RSO makes use of smoothly operating transport mechanism to apply a small sinusoidal motion to the sample in the region of maximum sensitivity of the SQUID sensor, that occurs in correspondence with the highest slope of the SQUID output signal.

DC-SQUID sensor and superconducting pick up coils, which represent the core of the SQUID magnetometer, are hosted in a Magnetic Properties Measurement System (MPMS) that allows for setting different magnetic fields (up to 7 T) and temperatures (in the 1.8 - 400 K range).

Although SQUID magnetometry provides highest accuracy and flexibility for investigation of magnetic properties, it must be kept in mind that the final output SQUID signal is a superposition of all contributing magnetic moments. Hence, the sheer magnetic signal of the sample has to be separated from spurious contributions of substrate and/or sample fixtures. In most circumstances, substrates are macroscopically bigger in size than the magnetic thin films of interest. Therefore,

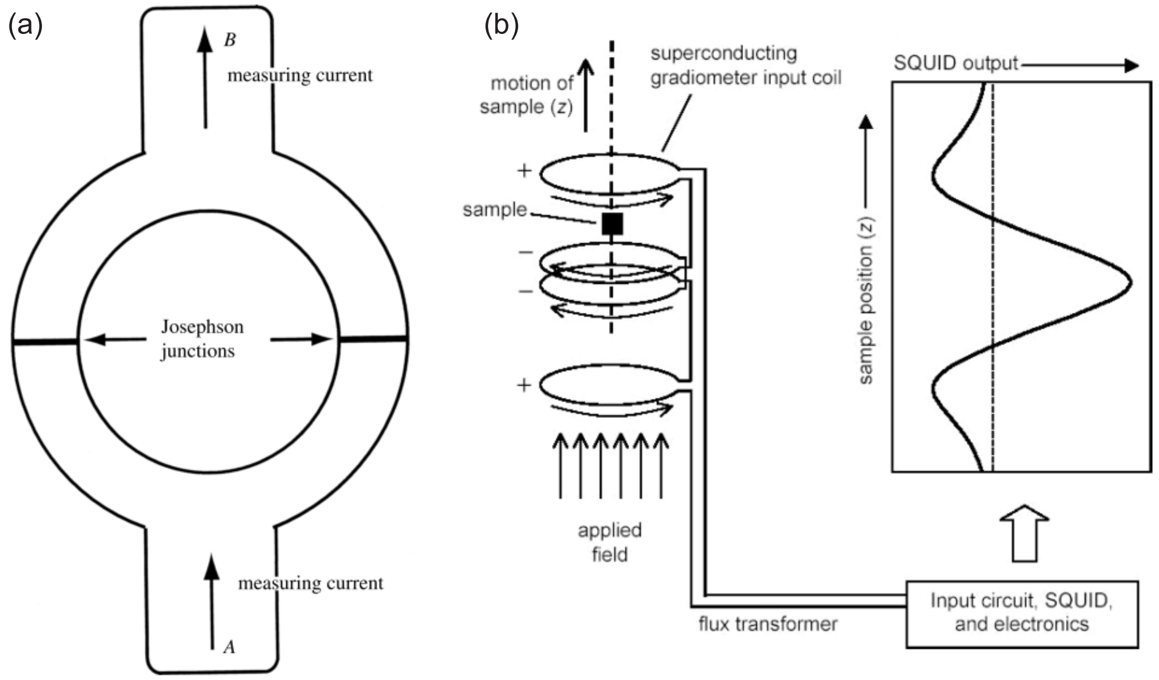

Figure 2.8.: (a) Schematic of a DC-SQUID sensor. (b) Illustration of the SQUID magnetometry measurement principle. (Figures (a) and (b) reprinted by permission from John Wiley and Sons, Ref. [316], ©2008, and Ref. [315], ©2006, respectively.)

the choice of an appropriate substrate material should be done not only on the basis of crystal structure and lattice parameter but also in terms of its magnetic characteristics (substrates with weak diamagnetism and low-level of magnetic impurities are generally preferred).

In the current work, the magnetic properties of LSMO thin films have been characterized via a QUANTUM DESIGN MPMSXL5 SQUID magnetometer equipped with a M130 RSO measurement head.

The temperature behavior of LSMO, including information on the para-ferromagnetic transition and the low-temperature magnetization, was studied via field-cooled (FC) measurements typically performed in the 10 - 400 K temperature range with a magnetic field of 100 Oe applied parallel to the plane of the film.

The saturation magnetization of LSMO was estimated via magnetization versus field ($M(H)$) measurements at low temperature. STO represented a good substrate choice since its diamagnetic signal could easily be subtracted from the one of LSMO by extrapolating a linear fit at high magnetic fields after LSMO magnetization reached saturation.

Apart from the initial characterization of the LSMO samples, SQUID magnetometry served as a fundamental technique to track the LSMO magnetic response during ME measurements. The modifications applied to the standard SQUID setup in order to carry out ME experiments will be described below. But first, we shall introduce the experimental technique – Cyclic Voltammetry – used to analyze the charging/discharging processes of LSMO films gated with DEME-TFSI IL electrolyte.

2.4.6 Cyclic Voltammetry

Cyclic Voltammetry (CV) is a potentiodynamic technique useful to investigate the interfacial charging/discharging processes occurring in electrochemical cells. The possible charging mechanisms taking place at an electrode/electrolyte interface during application of an external voltage - EDL capacitance, redox pseudocapacitance or ionic intercalation - have already been discussed in Section 1.6.1.

Electrochemical cells may have a three-electrode configuration in case they are composed of working, counter and reference electrodes. In case of a two-electrode setup (see Fig. 2.9(a)), only working and counter electrodes are used.

The working electrode is the one where the electrochemical charging/discharging processes of interest take place. The counter electrode (e.g. graphite or platinum), attached to the same external power supply of the working electrode, but to the opposite terminal, completes the current path of the electrochemical cell. In other words currents with the same magnitude but opposite sign flow through working and counter electrodes. Purpose of the reference electrode is to provide a well-defined reference value for the potential of the working electrode. Reference electrodes (e.g. Ag/AgCl) are generally grounded to 0 V and no current flows through them.

During a CV experiment, the working electrode is set to a desired potential with a certain voltage ramp rate ($\mathrm{d}V/\mathrm{d}t$). Concurrently, the current flowing to the working electrode is monitored. Once the peak potential is reached, the voltage ramp is reversed in the opposite direction to a new set potential. The whole process can be repeated as many cycles as needed. The plot of the recorded current versus applied potential is called *cyclovoltammogram*. By integration of the charging current, the charge accumulated at the working electrode/electrolyte interface can be calculated. Wealth of information on the interfacial charging/discharging processes can be extracted from the analysis of the CV characteristics (see later discussion).

Fig. 2.9(b) depicts the equivalent circuit of an electrochemical cell, which comprises capacitive (C^{EDL}) and pseudocapacitive (Z) elements and the electrolyte resistance (R^{EL}) (see Fig. 2.9(b)). The advantage of a three-electrode configuration is that the measurements refer only to the half of the cell with the working electrode, without being affected of possible changes that may occur at the counter electrode. Therefore the usage of a reference electrode permits to accurately study the electrochemical processes (e.g. redox reactions) taking place at the surface of the working electrode.

On the contrary, in a two-electrode setup the charging/discharging characteristics describe the behavior of the whole cell (including counter electrode and electrolyte). Nonetheless, an elegant workaround which allows to "observe" mainly the charging effects at the working electrode is to choose a counter electrode made of a chemically-stable material and with a much larger surface area than the working electrode. In this way neither potential drifts nor limitations in the amount of accumulated charge should be caused by the counter electrode, but rather due to the processes happening at the working electrode/electrolyte interface. This translates to a simplified equivalent circuit (see Fig. 2.9(c)): in good approximation the effective total capacitance is given solely by the working electrode (C_{WE}) since the capacitance of the counter electrode is much larger ($C_{CE} >> C_{WE}$) and the two capacitors are in series. The major source of resistance R is given by the electrolyte.

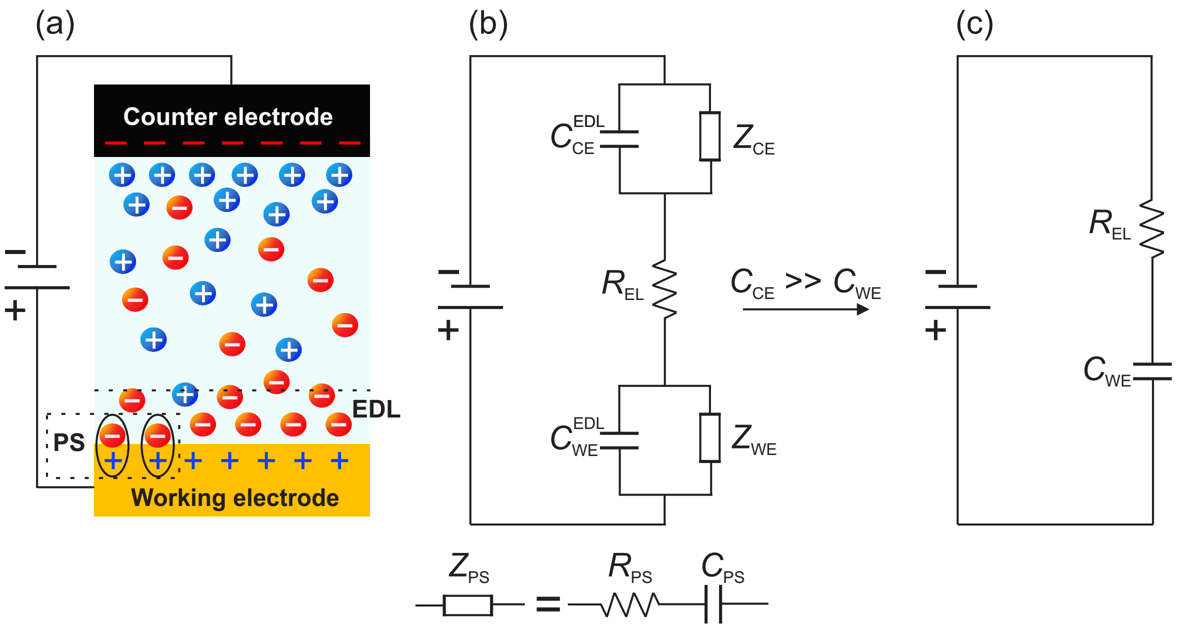

Figure 2.9.: (a) Schematic of a two-electrode electrochemical cell. EDL and PS represent the interfacial charge accumulation via electric double layer capacitance or pseudocapacitance, respectively. (b) Equivalent circuit of an electrochemical cell. The Z elements correspond to the contribution due to pseudocapacitance, defined as a resistor and a capacitor in series. (c) Approximated equivalent circuit in case the capacitance at the counter electrode/electrolyte interface is much larger than the capacitance at the working electrode/electrolyte interface. (Figures (b) and (c) inspired by Ref. [317].)

If a reference electrode is not used, it is common practice to start the CV measurements with respect to the value of open circuit potential (OCP). OCP by definition is the potential built up in the cell in conditions of open circuit, i.e. when no current flows.

At this point, we shall now provide some guidelines useful for the interpretation and analysis of CV plots (see Fig. 2.10).

Already at a quick glance the shape of the current-voltage curves elucidates whether the charging/discharging processes are due to EDL capacitance, pseudocapacitance or ionic intercalation.

The CV plot of an EDL capacitor presents a nearly perfect rectangular shape (see Fig. 2.10(a)). This stems from the fundamental nature of capacitive charging, which undergoes virtually-instantaneous[22] charge separation (polarization) under application of an external electric field [178]. The fact that the value of current density J is constant while increasing the potential at a fixed voltage ramp rate $\frac{\delta V}{\delta t}$ indicates that also the value of the capacitance is constant. This is in accordance with Eq. 1.5, with the capacitance defined as $C = \frac{\delta Q}{\delta V} = \frac{\delta Q}{\delta t} \cdot \frac{\delta t}{\delta V} = J \cdot \frac{\delta t}{\delta V}$. In case of EDL capacitors expected values of capacitance are in the range of 5-15 $\mu\mathrm{F\,cm^{-1}}$ [17, 113].

It is also worth pointing out that when an IL is used as charging medium, the value of capacitance tends to decrease upon substantial increase of the external voltage ($C \sim V^{-1/2}$). This behavior has been tentatively interpreted in terms of the theories of *overscreening* and *crowding* (see Fig. 2.11). It was suggested that at moderate voltages the first layer of ions delivers more counter-charge than the one present at the electrode's surface (overscreening); this disproportion is corrected by an excess of counter-ions in the second ionic layer. At higher voltages the crowding of ions extends across two monolayers and dominates overscreening, which now leads to accumulation of counter-ions in the third monolayer.

---

[22] In real devices, the polarization response is limited according to the *RC* time constant of the circuit.

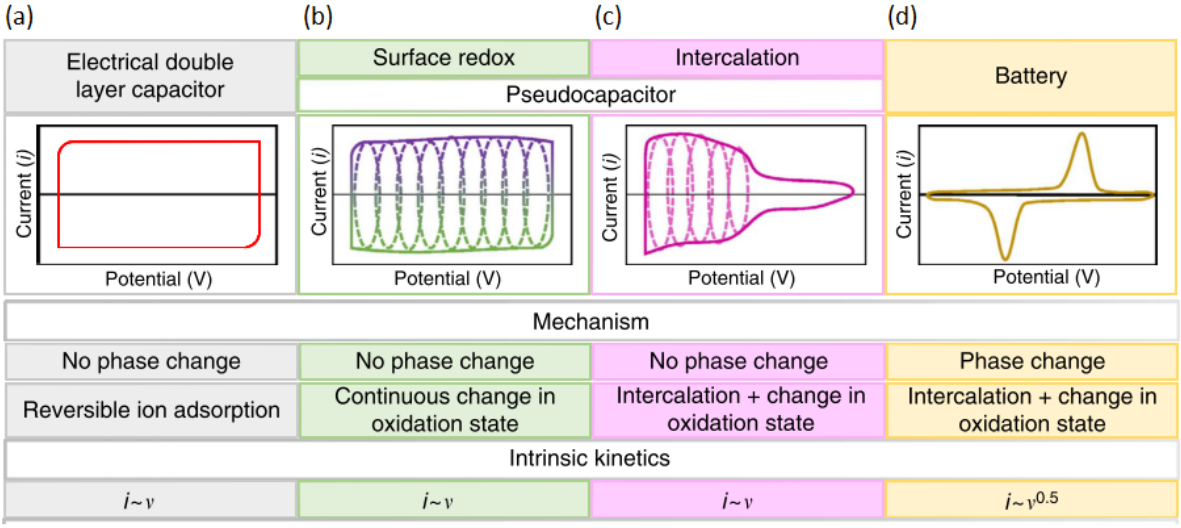

Figure 2.10.: Charging characteristics in EDL capacitors (a), pseudocapacitors (b,c) and batteries (d). The current-voltage plots display the typical responses measured via cyclic voltammetry. The parameter ν represents the voltage ramp rate. (Adapted from *Nature Communications* [178] (2016) under Creative Commons CC-BY license)

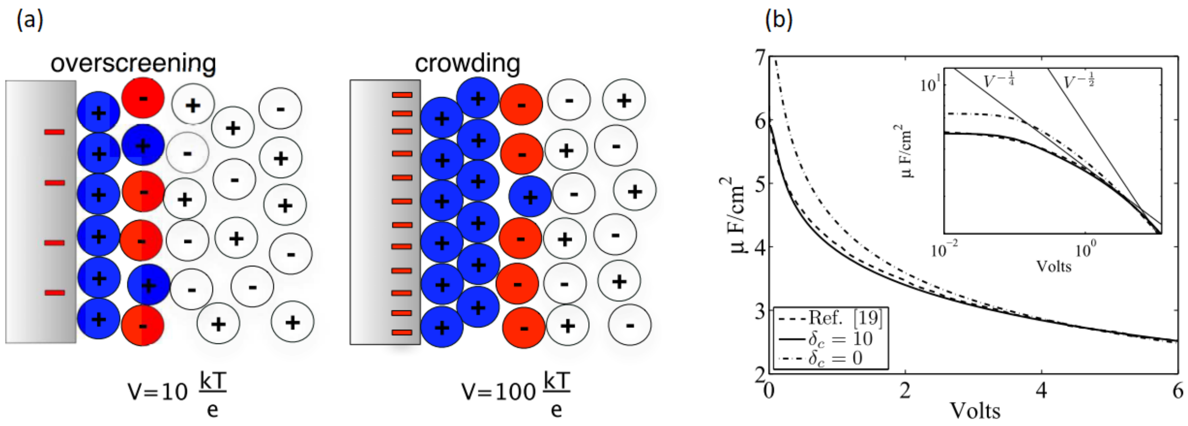

Figure 2.11.: EDL capacitance as a function of applied voltage in IL gated systems. (a) EDL structure at the electrode/IL interface. The surface charge is overscreened by a monolayer of counter-ions located in the second monolayer for moderate voltages (overscreening) and in the third monolayer at larger voltages (crowding). (b) Behavior of ionic liquid EDL capacitance as a function of the applied voltage according to overscreening-crowding theoretical model (solid), simulations (dashed), mean-field theory (dash-dot), and asymptotic scalings (inset). (Reprinted by permission from American Physical Society [318] (2010), ©2010)

Another important feature of EDL charging is that on repetitive cycling the $J(V)$ curves match almost perfectly on top of each other since the charging/discharging processes are highly-reversible.

Electrochemical batteries display completely different CV characteristics. The fingerprint of ionic intercalation materials is the presence of pronounced peaks in the current at certain threshold voltages where electrochemical reactions occur (see Fig. 2.10(d)). Typically, yet after a limited number of cycles, the $J(V)$ curves do not overlap anymore, signifying the onset of irreversible electrochemical processes.

Intermediate behavior between EDL capacitors and electrochemical batteries is manifested in pseudocapacitors. Depending on whether pseudocapacitance is mainly driven by near-surface or surface redox reactions, the CV plots present more or less pronounced "bumps" comparing to the symmetric rectangular response of an EDL capacitor (see Fig. 2.10(b,c)). The increase in charging current is accompanied with larger values of capacitance of the order of 100 - 1000 $\mu\mathrm{F\,cm^{-2}}$ [163, 179, 180]. Interestingly, and with the opposite trend as compared to EDL capacitors, on progressive expansion of the potential window the capacitance tends to increase [180, 190, 319]. This is related to the fact that ionic chemisorption is facilitated as the interfacial electric field is increased. Of course, at excessively high voltages irreversible electrochemical reactions kick in, resulting in electrode-electrolyte decomposition and consequently lead to a decrease in capacitance and a reduction in cycling reversibility.

CV measurements are also useful to analyze the kinetics of electrochemical processes [177]. The charging current increases linearly on increasing the voltage ramp rate in case of EDL capacitors and pseudocapacitors, whereas it shows a square root trend in the case of batteries (intercalation slows ionic diffusion). This behavior is reflected by the nature of the charging process, taking place either at the surface or in the bulk of the electrode.

In the current study, careful and comprehensive investigations of the charging/discharging mechanisms of LSMO films electrically charged with a DEME-TFSI ionic liquid electrolyte have been performed.

LSMO films with a surface area of ≈ 0.4 cm^2 and high-surface area carbon fiber cloth ($S_{BET} \approx$ 2400 m^2 g^{-1}, from WHATMAN) were respectively used as working and counter electrodes in a two-electrode setup. A borosilicate glass fiber filter with a nominal thickness of 260 μm (GF/A, from WHATMAN) was used as insulating separator between counter and working electrodes. Thin metallic wires in contact with working and counter electrodes were connected to a potentiostat (μAUTOLAB Type3), which was used to carry out CV experiments.

2.4.7 *In situ* magnetoelectric setup

Ultimate aim of this work is the investigation of the ME effect in LSMO films charged with an IL electrolyte. The combination of SQUID magnetometry and CV provided powerful tools to concurrently and quantitatively track magnetic and charge correlations.

In order to synchronize the two experimental techniques a few modifications to the standard measurement setups were made. In particular, since a conventional SQUID sample holder (i.e. a plastic straw) is not meant for lodging neither liquids (as electrolytes) nor electrical wires, both necessary to perform CV measurements, a custom-made *electrochemical tuning cell*[23] was employed (see Fig. 2.12). The cell is made of Polyether Ether Ketone (PEEK), which allowed for easy machining of the required grooves to host sample and wiring[24]. One branch of the cell mounts the LSMO/STO sample (the working electrode) with a thin gold wire (99.99 % purity, 0.127 mm in diameter) in direct contact with the LSMO surface. On the opposite side a carbon cloth (the counter electrode) is put on top of a gold pad, in turn connected to a Cu wire (0.21 mm in diameter). An insulating glass fiber cloth inserted between counter and working electrodes prevents short circuiting. The electrochemical cell is completed once a few drops of DEME-TFSI ionic liquid are poured onto the LSMO surface.

---

[23] In the following we may also refer to it as "ME tuning cell". Details about fabrication materials and measurement procedures inside a SQUID magnetometer can also be found in Ref. [320].

[24] A few drops of insulating and chemically-stable epoxy were used to fix the wires in the respective grooves. In general, all employed materials, such as PEEK, Kapton and various epoxies were tested for compatibility with low-temperature and vacuum conditions.

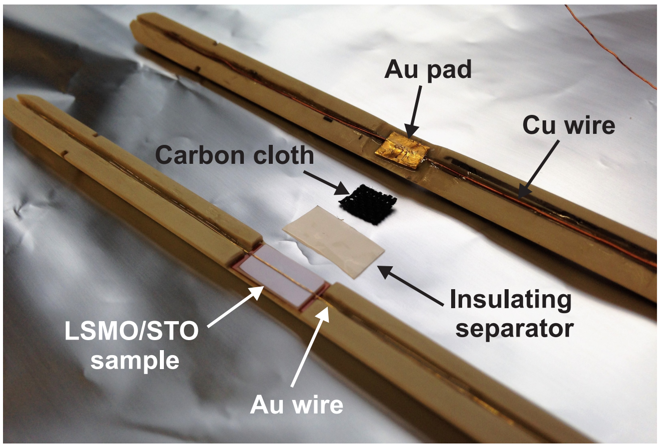

Figure 2.12: Photograph of the parts composing the electrochemical tuning cell employed to perform *in situ* ME measurements. To estimate the size of the components, notice that the surface of the STO substrate is 1 × 0.5 cm^2.

The process of cell assembly is done under glove box conditions (with $[O_2] < 1$ ppm and $[H_2O] < 1$ ppm) in order to limit moisture contamination. Afterwards, the tuning cell is quickly transferred into the SQUID magnetometer. The Au and Cu wires are attached to a connector positioned at the lower end of the SQUID rod. From there, other conducting wires reach the upper end of the SQUID rod and pass through a PMMA plug used as feed-through. Hereafter, the cables are connected to the crocodile clips of the μAutolab potentiostat.

Voltage and current outputs of the potentiostat are sent to two multimeters (KEITHLEY 2001), which then transmit the signals to the SQUID magnetometer by means of GPIB ports. Finally, a software script (Delphi) allows for real-time control and detection of magnetization, voltage and current signals.

As already mentioned, care should be taken when analyzing SQUID data in order to avoid falling into pitfalls related to spurious magnetic signal. In this regard, it should be kept in mind that the utilization of an electrochemical cells may produce different artifacts [320].

For instance, extra contributions to the total magnetization may come from impurities present in the materials constituting the macroscopic chemical cell and wiring. Thus, it is important to choose materials with good purity level. A way to eliminate spurious magnetic signals is to compare magnetization measurements (such as FC curves) performed with the whole tuning cell and with the bare sample. Artificial contributions are revealed by an off-set that can be removed by subtracting the two curves. Such factorization works only if the sample magnetization is clearly distinguishable from the spurious signal. When possible, the application of low magnetic fields comes at a hand as well. Indeed, since LSMO is a soft ferromagnetic material, typically only a few hundreds Oe are applied and thus, para or diamagnetic contributions coming from the cell are kept low.

Another major concern during an *in situ* charging experiment is represented by the current flowing through the wires for it may be high enough to be detected by the very-sensitive SQUID magnetometer or to influence the sample magnetization. By making a few assumptions, the magnitude of the two artifacts can be estimated. If we consider a current loop $I = 10\ \mu$A with an enclosed area of $A = 1\ \text{mm}^2$, a magnetic moment $m = A \cdot I = 10^{-11}\ \text{A m}^2 = 10^{-8}$ emu [316] is produced, corresponding yet to the lower detection limit of the SQUID. Now, if we assume the same current to flow in a straight wire, at a distance of 1 nm a magnetic field $H = \frac{2I}{R} = 200$ Oe is generated [316]. Although the considered distance is quite conservative, such value of magnetic field is already enough to produce remarkable changes in a magnetic material.

There are a few decisive factors in the ME measurement procedure to be considered in order to overcome the described issues. On the one hand, it is useful to keep the charging current as low as possible: spurious contributions become negligible if the current is in a nA regime. In addition, there is an easy and fundamental test to rule out the presence of current-induced magnetization effects. Indeed, one can do charging experiments for two orientations of the magnetization by simply changing the direction of the applied magnetic field. Hence, the genuine ME effect changes its sign together with the changed magnetization (following the external magnetic field). But any artificial contribution to magnetization coming from the charging current does not change its direction at all (the direction of the current is always the same).

Finally, the design of the tuning cell should be symmetric with the metallic wires stretching through the cell in accordance with the extension of sample motion within the superconducting coil circuit (see Fig. 2.12 and Fig. 2.8(b)).

With these guidelines in mind, it is possible to extract precise and reliable quantitative information of ME coupling in IL-gated thin films of LSMO via *in situ* SQUID-CV measurements.

3 Growth and characterization of epitaxial thin films of LSMO

In this chapter detailed information about the structural, chemical and magnetic characteristics of epitaxial thin films of $La_{0.74}Sr_{0.26}MnO_3$ (LSMO) grown on $SrTiO_3$ (STO) substrate are presented. The optimization steps required for fabrication of LSMO films with quality comparable to the state-of-the-art will be described.

3.1 Background

Aiming at the realization of ME coupling in LSMO/ionic liquid (IL) systems, the choice of using LSMO in the form of smooth epitaxial thin films brings several advantages.

First, having LSMO as a single crystal with a well-defined crystallographic orientation allows for easier interpretation of the experimental results. Indeed, single-crystalline LSMO provides the opportunity to work as close as possible on an ideal system where eventual influences of microstructure on magnetism, for example coming from different grain orientations and grain boundaries, are kept at minimum.

The ME effect takes place at the electrode/electrolyte interface. Therefore, an atomically flat LSMO surface is of importance because it implies a uniform distribution of the electric field and, more importantly, enables a quantitative assessment of the amount of accumulated/depleted charge per unit surface area.

As already mentioned, the usage of thin films offers an enhanced surface-to-volume ratio, which in turn is expected to increase the magnitude of ME effect. Nonetheless, as the thickness is progressively reduced, interfacial effects become more and more pronounced and so structural and magnetic properties may substantially deviate from the standard bulk behavior.

The fabrication of LSMO films with the desired epitaxial quality, thickness, surface smoothness and composition can pose a formidable task. Fulfillment of such requirements demands for optimization of multiple involved parameters. In this regard, the vast literature [59, 266, 281–290] about LSMO films grown onto STO substrate supplies plenty of valuable information.

In a previous work by Leufke *et al.* [281] the growth of LSMO thin films by means of Large-Distance Magnetron Sputtering (LDMS) method has been analyzed by considering the influence of different deposition conditions, including various Ar/O_2 gas pressures and ratios, deposition rates, sputtering modes (RF or DC) and cooling rates. Although the previous investigation was very comprehensive, further optimization of the LSMO characteristics is still feasible by taking into account parameters yet unexplored.

Before entering in details on the growth and characterization of LSMO films prepared via LDMS, we shall provide some information on the employed STO substrate.

3.2 STO substrate analysis

The substrate is the starting point where film nucleation and growth take place. For this reason, a fundamental prerequisite for the preparation of epitaxial thin films with highest quality is to choose a substrate with adequate crystalline structure and smooth surface.

STO represents one of the most common choices for the fabrication of LSMO films [59, 266, 281–290]. STO is a cubic perovskite with lattice parameter $a_{\mathrm{STO}} = 3.905\,\text{Å}$, whereas bulk LSMO (for Sr = 0.26) [134, 321] is a rhombohedral perovskite with pseudocubic lattice parameter $a_{\mathrm{LSMO}} \approx 3.899\,\text{Å}$. The low value of lattice misfit $\epsilon = (a_{\mathrm{STO}} - a_{\mathrm{LSMO}})/a_{\mathrm{LSMO}} = 0.15\%$ provides favorable conditions for epitaxial growth of LSMO. In order to accommodate to the slight tensile strain, the unit cells of LSMO thin films grown onto STO slightly elongate in-plane (a_{LSMO}) and shrink along the out of plane (c_{LSMO}) directions.

Apart from considerations concerning the crystalline nature of STO, analysis and preparation of the substrate surface prior to deposition is of crucial importance as well. As the aim is to produce thin and ultrathin films of LSMO with a thickness in the range of 3-15 nm, the surface of STO has to be atomically flat. Generally, after epi-polishing process[1] the STO surface has a very low roughness with only a minor amount of impurities (see Fig. 3.1(a)), which should be easily removed by a gentle annealing in vacuum conditions prior to deposition. Nonetheless, it may happen that residuals of big particles cover a remarkable portion of the STO surface (see Fig. 3.1(b)). In such case, it is recommended to perform a surface treatment procedure[2]

---

[1] STO substrates were purchased already in epi-polished conditions by SurfaceNet GmbH.

[2] See Appendix (Section A.3.1) and Ref. [292–294, 322] for more details.

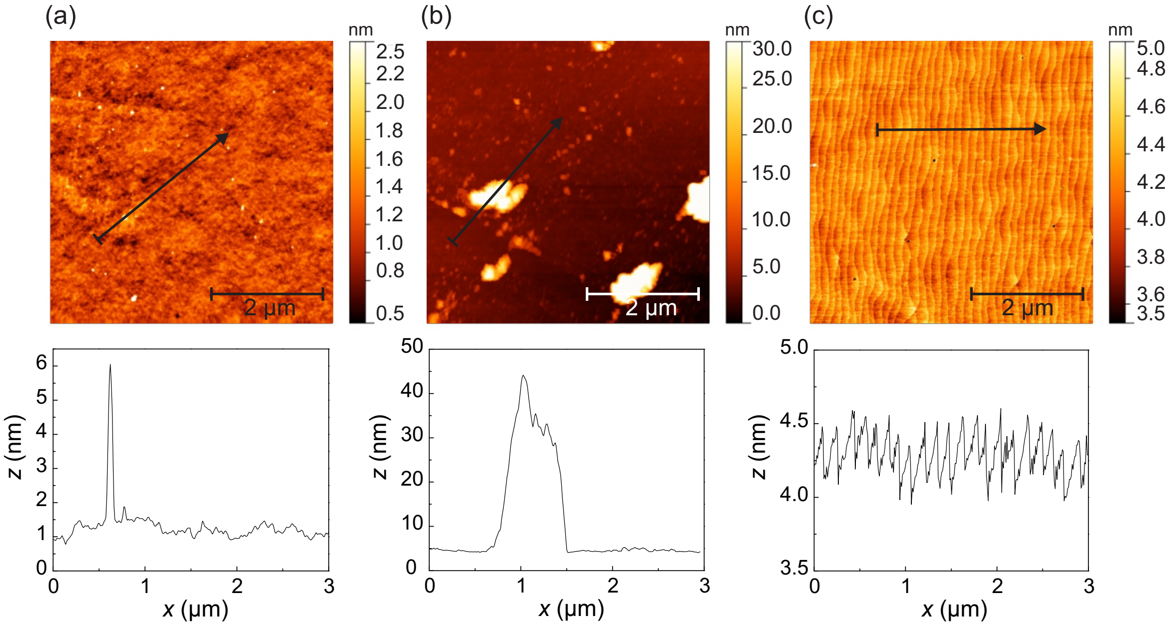

Figure 3.1.: Atomic force micrographs of the STO substrate surface. (a,b) As-received epi-polished STO substrates with low or high amount of residual particles, respectively. The root mean square (RMS) roughness is 0.2 nm in (a) and 6.5 nm in (b). (c) STO surface after chemical etching and high-temperature annealing in air. Atomically flat terraces are separated by one unit cell steps. The RMS roughness is 0.2 nm.

comprising chemical etching followed by high-temperature annealing in air. This method allows for a marked reduction of defect concentration and enables surface reconstruction with highly-ordered atomically flat terraces separated by one unit cell steps (see Fig. 3.1(c)). The presence of steps with a height of about 0.4 nm signifies that STO has a well-defined termination layer, i.e. TiO_2 as reported by several groups [292–294, 322].

Once verified that a STO substrate features a surface quality comparable to either Fig. 3.1(a) or (c), it can considered to be suitable for the growth of LSMO thin films[3].

A remark which concerns the quality of films deposited onto STO is that during the growth process, particularly in presence of reducing conditions such as high temperature and vacuum atmosphere, Sr atoms may diffuse from the bulk of the substrate and form islands on the film surface [323]. In this work attention has been paid to keep under control the phenomenon of Sr diffusion. As an example, after reaching the growth temperature of LSMO films the waiting time was just enough to reach thermal stability (not more than 5 - 10 min) before setting the desired Ar/O_2 pressure. In addition, it will be shown in Section 3.3.3 that by appropriately adjusting the deposition temperature it is possible to keep film surface roughening due to Sr diffusion at minimum.

3.3 Preparation of LSMO films via Large-Distance Magnetron Sputtering

The growth of high quality films of oxide materials (e.g. LSMO) using physical vapor deposition (PVD) methods is a challenging task whose complexity depends on the kind and amount of sample specifications that need to be fulfilled. Adjustment of a particular deposition parameter does not necessarily imply optimization of the overall film characteristics; for instance it may happen that an improvement in surface roughness is attained at the expense of poorer magnetic properties (or vice versa). In some cases a trade-off between the final desired features may be required.

One of the major issues related to the growth of an oxide material as LSMO using PVD methods is represented by the presence of oxygen deficiencies [59, 281–283, 288, 290]. Generally, a decrease in oxygen content in the deposited samples is connected to the fact that although most of elements evaporated from a target and reaching a substrate have a sticking coefficient close to unity, in the case oxygen the value is around 0.1 or below [311]. Improvement of oxygen uptake in LSMO films is essential, for it directly affects structural and magnetic properties of LSMO (see Section 2.1.1).

In this regard, increasing the oxygen pressure during deposition is a possible good strategy, but there are some non-trivial aspects that limit this approach. If the deposition pressure is exceedingly too high, the conditions for epitaxial growth are not met, because detrimental effects, including bulk-particles growth, surface roughening, phase segregation and reduction of deposition rate, take effect. Specifically concerning the LDMS technique, the study of the influence of various Ar/O_2 pressures and ratios leads to additional complications. Indeed, due to the large target-substrate separation, the on-flight scattering of the transferred elements may substantially vary when various deposition pressures are set, and so also the final LSMO sample stoichiometry may change.

A possible alternative is given by the careful adjustment of the deposition temperature. Deposition temperatures of a few hundred degrees are commonly used for the growth of epitaxial thin

---

[3] No remarkable differences in the final LSMO films quality were found when using either as-received or chemically-treated STO substrates.

films[4] because layer-by-layer or step-flow growth modes are facilitated, thanks to the diffusion of surface adatoms and ordered nucleation of staking layers [311]. Regarding the oxygen uptake, in general, by increasing the deposition temperature also the film oxidation rate increases. Nonetheless, if a too high temperature is set, then negative side effects, such as surface/substrate elemental interdiffusion and dewetting, may compromise the film quality.

In the current work, it was chosen to analyze the effect of various deposition temperatures (in the 500-800 °C range) on the growth of LSMO films while keeping a fixed gas pressure and mixture. The LDMS deposition parameters set for the growth of LSMO thin films are summarized in Table 3.1. At the end of the growth process the samples were cooled down to room temperature at a ramp rate of $10\,\mathrm{K\,min^{-1}}$ in pure oxygen atmosphere (0.08 mbar). After fabrication they were routinely characterized via High Resolution X-ray Diffraction (HRXRD), Atomic Force Microscopy (AFM) and Superconducting Quantum Interference Device (SQUID) magnetometry.

Table 3.1.: Deposition parameters of LSMO films grown onto STO substrate.

Temperature (°C)	Pressure (mbar)	Ar/O_2 ratio	Sputtering power ($\mathrm{W\,cm^{-2}}$)	Deposition Rate ($\mathrm{Å\,s^{-1}}$)	Thickness (nm)
500-800	0.018	3/2	4.4	0.044	3-15

In the course of the deposition studies, it was found that the issue related to the film oxygen uptake could be to a great extent overcome by performing high temperature (900 °C) annealing in air for 1 h after LSMO samples fabrication. In addition, by investigating the effect of using different deposition temperatures, an optimum balance between structural and magnetic features of thin and ultrathin LSMO films was obtained.

3.3.1 Preliminary test samples and characterization steps

Initial deposition tests of LSMO films were performed on both STO and MgO substrates. The deposition rate ($\approx 0.044\,\mathrm{Å\,s^{-1}}$) was calibrated by verifying the film thickness of tooling samples via X-ray Reflectometry (XRR) measurements (see Fig. 3.2). MgO substrate[5] allowed for an easier fitting procedure than STO because the finite-thickness fringes (the so-called *Kiessig* fringes) are more pronounced owing to a larger difference in density with LSMO. XRR provided also information on the interfacial roughness: low roughness values of the order of one unit cell were found at the film surface and at the film/substrate interface regardless of the substrate used.

The chemical composition of LSMO was analyzed by Rutherford Backscattering Spectroscopy (RBS). For this purpose a LSMO film with a thickness of 26 nm grown onto MgO substrate rather than STO was employed in order to avoid the overlap of Sr signals (see Fig. 3.3). Quantitative analysis with the Mn stoichiometry normalized to 1 revealed a Sr content of 0.26 within an accuracy of 2%. Therefore, it turned out that the composition of the films significantly differed from the employed $La_{0.65}Sr_{0.35}MnO_3$ target. The determination of the amount of strontium was

---

[4] This is valid for both oxides [281] and metals [324].

[5] Notice that MgO has a lattice misfit with LSMO of $\epsilon \approx 8\%$, which generally leads to worse structural and magnetic properties comparing to LSMO samples grown on STO [281].

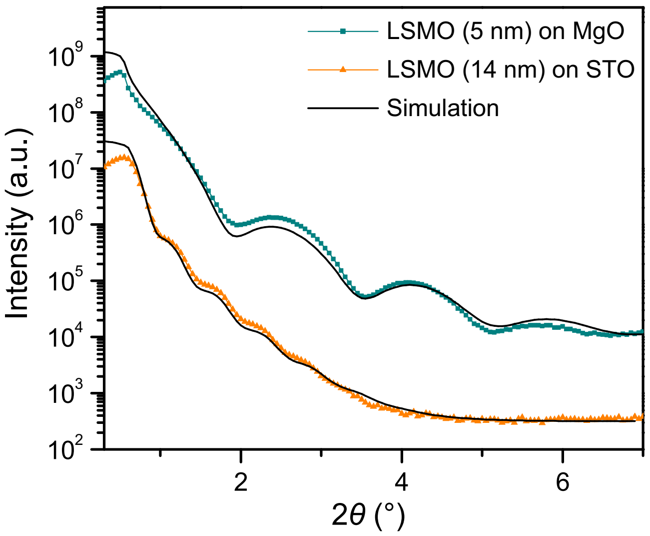

Figure 3.2: X-ray Reflectivity measurements of a LSMO film (5 nm thickness, 0.2 nm surface roughness) grown on MgO substrate (0.3 nm interfacial roughness) and a LSMO film (14 nm thickness, 0.3 nm surface roughness) grown on STO substrate (0.8 nm interfacial roughness). Intensity plots have been shifted for better clarity.

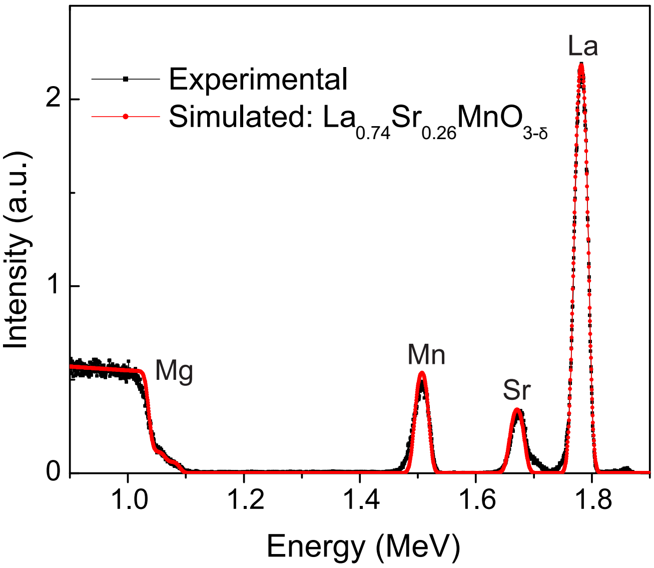

Figure 3.3: Rutherford backscattering spectrum of a 26 nm LSMO film grown on MgO substrate.

an important characterization step, because it allowed to identify the region of the LSMO phase diagram (see Section 2.1.1) where the films belong to. For the given composition, native bulk LSMO has a rhombohedral structure with a para-ferromagnetic transition temperature T_C of ≈ 340 K (see Fig. 2.1).

3.3.2 Comparison between as-prepared and post-annealed LSMO films

In order to identify the influence of annealing treatment on structural and magnetic properties of LSMO, the characteristics of as-prepared and post-deposition annealed (900 °C for 1 h in air) samples[6] have been compared.

Both as-prepared and post-annealed samples revealed that the lattice planes of the LSMO films have the same (00*l*) orientation of the STO substrate with the absence of any spurious phase in the whole 2θ range (see Fig. 3.4). Notably, small periodic oscillations - so-called *Laue* fringes - are visible close to the (001) and (002) reflections of LSMO. Akin to the Kiessig fringes observed

---

[6] For better confrontation, the results of the current section pertains LSMO films with a fixed thickness of about 13 nm deposited via LDMS at a temperature close to 600 °C.

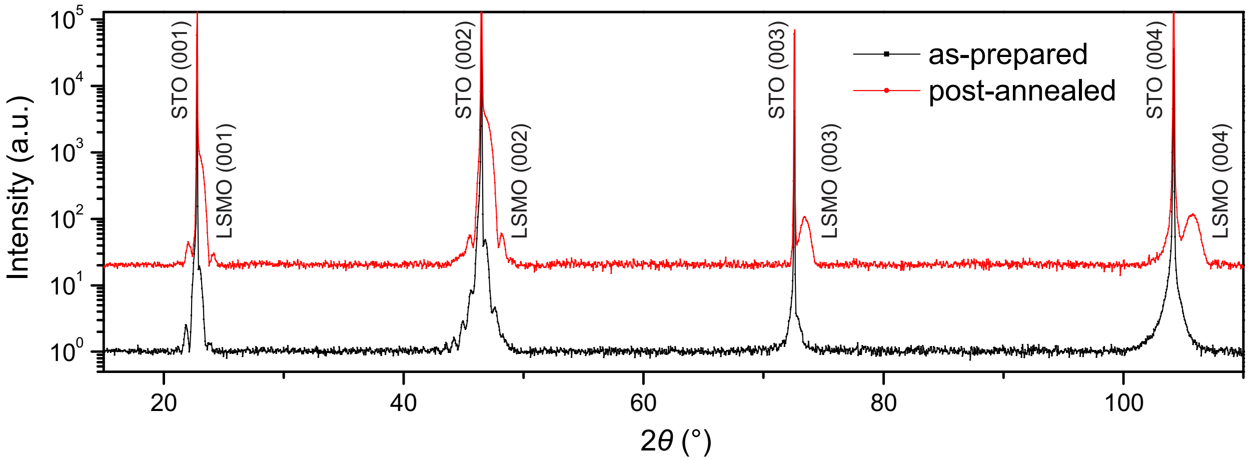

Figure 3.4.: HRXRD θ-2θ diffractograms of as-prepared ($T_{\mathrm{dep}} \approx 580$ °C) and post-annealed LSMO films (12.6 nm). The sharp and high-intensity peaks of the STO substrate are accompanied by lower-intensity LSMO reflections with Laue fringes visible close to the (001) and (002) reflections. The LSMO (00*l*) symmetric reflections shift towards higher angles upon post-annealing, indicating a decrease of the LSMO out-of-plane lattice parameter. For better clarity, the intensity of the post-annealed curve has been increased by 20 times.

by XRR, Laue fringes provide information on the film thickness. Nonetheless, in case of XRR the periodic oscillations are related to the scattering of X-rays at interfaces (the film surface and the film/substrate interface) with different densities. Thus, the intensity of Kiessig fringes depend on the smoothness and density variation of interfaces, but the specific crystal structure of the film (e.g. polycrystalline or amorphous) is not involved. On the contrary, the presence of Laue fringes is the fingerprint of crystalline coherence and homogeneity of the unit cells composing the film along the growth direction. Since the thickness calculated from Laue and Kiessig fringes matches, it can be concluded that the LSMO unit cells are coherently-ordered along the film growth direction.

The main difference between the as-prepared and post-annealed HRXRD curves is represented by the shift of LSMO reflections towards higher angles. The effect is clearly visible at the (003) and (004) higher order reflections, with the LSMO peaks basically overlapping with STO for the as-grown case, whereas small "shoulders" appear after post-annealing. The resulting out-of-plane lattice parameter is $c_{\mathrm{LSMO}} \approx 3.9\,\text{Å}$ and $\approx 3.86\,\text{Å}$ for the as-prepared and post-annealed samples, respectively. In the literature it is known that a shrinkage of the LSMO unit cell along the *c*-axis is related to an increase of oxygen content in the film [281, 290].

AFM micrographs displayed a smooth surface morphology for both as-prepared and post-annealed LSMO samples (see Fig. 3.5). In particular, the latter featured the presence of atomically flat terraces separated by periodic steps with a height of about one LSMO unit cell[7], with a quality comparable to the surface of STO substrates after high temperature annealing (see Fig. 3.1).

Interestingly, the biggest effect of post-deposition treatment regarded the magnetic properties (see Fig. 3.6). LSMO samples deposited at around 600 °C displayed a low para/ferromagnetic transition temperature[8] ($T_{\mathrm{C}} \approx 120$ °C) and poor magnetic moment per unit cell (1 μ_{B} u.c.$^{-1}$), both

---

[7] In some samples the terraces were separated by half unit cells steps.

[8] The value of T_{C} was estimated according to the derivative method [325].

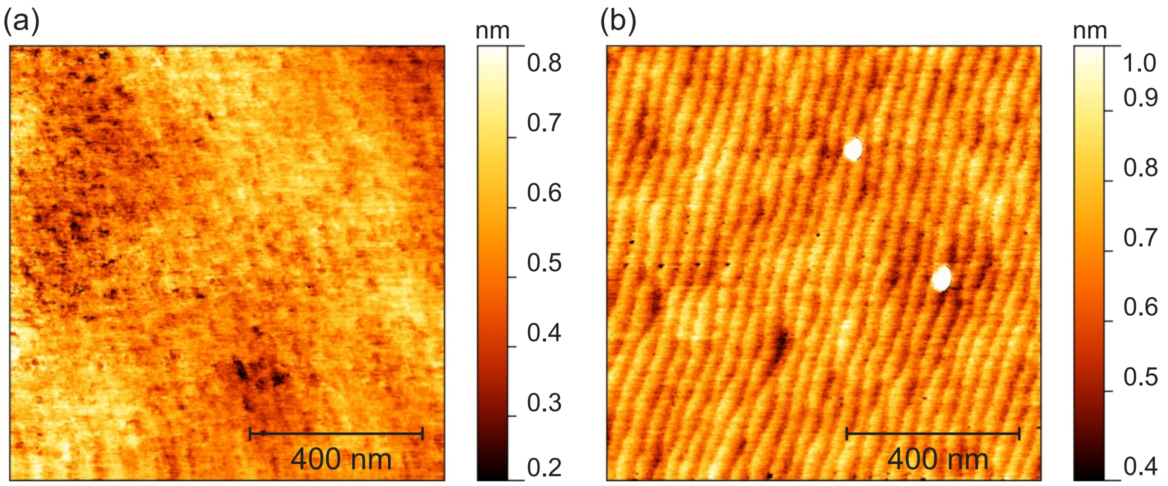

Figure 3.5.: Atomic force micrographs of (a) as-prepared ($T_{\mathrm{dep}} \approx 620$ °C) and (b) post-annealed LSMO thin films (13.2 nm). RMS roughness is 0.1 nm (a) and 0.15 nm (b).

values being way off from bulk $La_{0.74}Sr_{0.24}MnO_3$. Nonetheless, after high-temperature annealing, T_C increased above room temperature (around 325 °C) with an impressive shift of about 200 K. In addition, the low-temperature magnetization increased to about 2.5 μ_B u.c.$^{-1}$. The latter value is compatible with the majority of literature reports on LSMO films [120, 266, 275, 281, 282, 295–297], since the bulk saturation magnetization of $M_{\mathrm{sat}} \approx 3.7\,\mu_B$ u.c.$^{-1}$ is generally not reachable. The remarkable improvement in magnetic properties provides a strong indication that subsequent to high-temperature annealing the oxygen content of the films increased, as also corroborated by the aforementioned decrease in the *c* lattice parameter measured by HRXRD.

As a result, it turned out that post-annealing was beneficial for the LSMO characteristics, particularly concerning the magnetic properties. Therefore, it was decided to perform post-deposition annealing treatment on all the LSMO samples fabricated next.

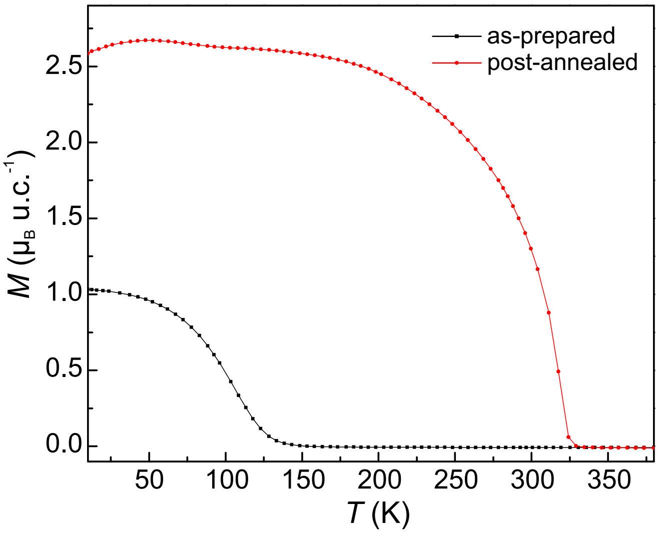

Figure 3.6: Field-cooled magnetization curves of as-prepared ($T_{\mathrm{dep}} \approx 580$ °C) and post-annealed LSMO thin films (12.6 nm). Measurement performed using a magnetic field of 100 Oe applied parallel to the in-plane film direction.

3.3.3 Effect of different deposition temperatures

The effect of different deposition temperatures T_{dep} on the properties of LSMO films[9] was investigated in the 500-800 °C temperature range. It has been found that the best characteristics in terms of epitaxial growth, film flatness and robustness of the magnetic properties were reached for $540\ ^\circ\mathrm{C} < T_{\mathrm{dep}} < 700\ ^\circ\mathrm{C}$.

In such temperature regime no remarkable variations in the HRXRD plots were observed: all the samples presented (001)-oriented growth with a lattice parameter $c_{\mathrm{LSMO}} \approx 3.86\,\text{Å}$ and pronounced Laue fringes (see Fig. 3.7).

The analysis of the rocking curves (RCs, corresponding to ω scans) provided additional information on the crystalline quality (see Fig. 3.8). In general, a sharp RC signifies that the film is in good registry with the underlying substrate, whereas a broadening along ω is caused by slight film misorientation or, in other words, to the presence of so-called *mosaicity* [326]. The RC curve of the (002) reflection of the LSMO sample grown at 700 °C has a full-width at half maximum (FWHM) close to 0.06°, which is comparable to the best values reported in the literature for LSMO films grown via pulsed laser deposition [283] or molecular beam epitaxy [327]. By decreasing the deposition temperature a systematic broadening of the RC was observed. For the lower temperature $T_{\mathrm{dep}} \approx 540$ °C the FWHM of the LSMO (002) reflection enlarged[10] to 0.11° (see Fig. 3.8).

Further insights into the crystalline quality of LSMO samples were gained by performing two-dimensional reciprocal space maps (2D-RSMs) and φ-scans of asymmetric (204) reflection on a representative sample deposited at 540 °C. RSM analysis revealed that film and substrate have nearly identical in-plane h component (see Fig. 3.9(a)). This denotes fully-strained growth with the unit cells of LSMO adapting pseudomorphically to the substrate. The φ-scans showed

---

[9] For a better comparison, only the results concerning LSMO films with a fixed thickness of about 13 nm are considered.

[10] This is still a quite good value comparing to the literature [328].

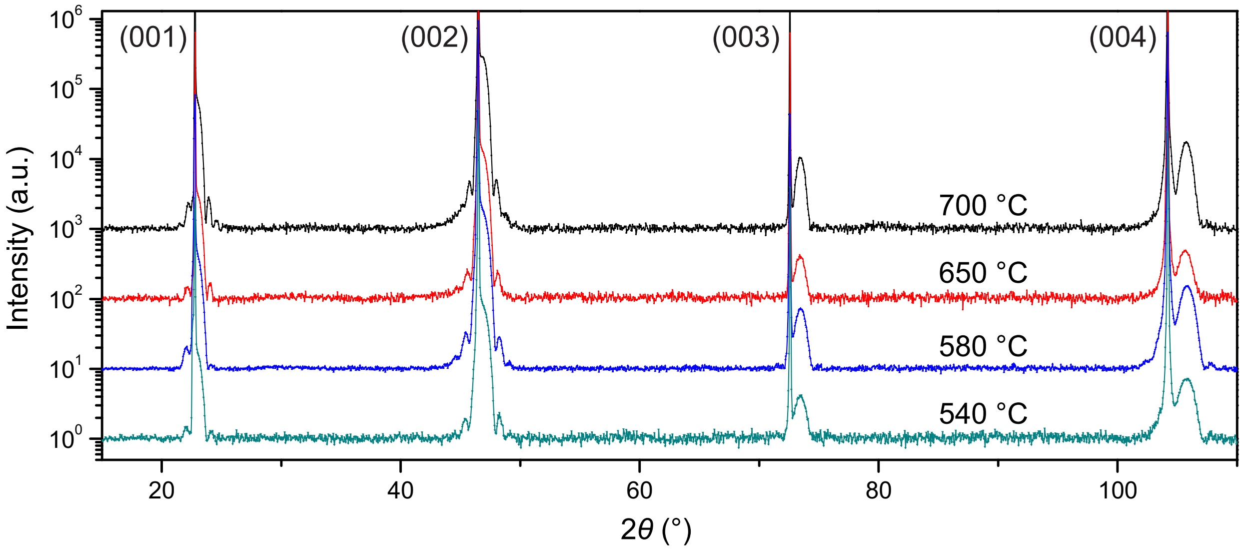

Figure 3.7.: HRXRD θ-2θ diffractograms of LSMO films grown at different deposition temperatures. The curves have been shifted for better clarity.

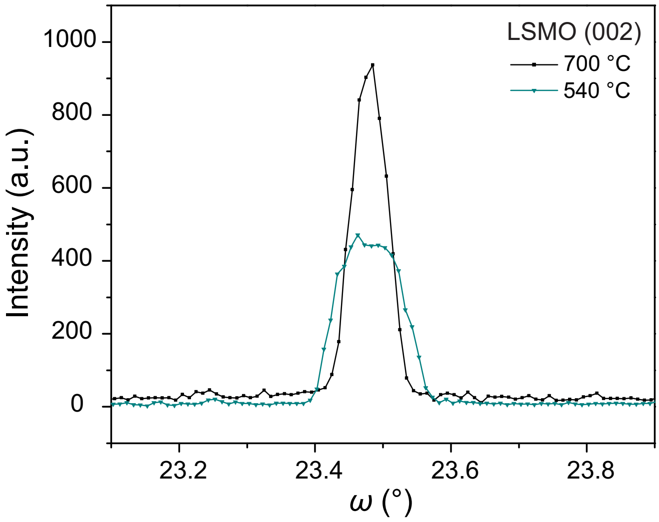

Figure 3.8: Rocking curves of LSMO (002) reflection for the samples grown at 540 °C and 700 °C.

that upon sample rotation, the (204) LSMO peaks periodically occur every 90° (see Fig. 3.9(b)), thus demonstrating the four-fold symmetry of LSMO.

By combining the whole set of XRD data, it can be concluded that for the investigated deposition conditions LSMO films grow epitaxially onto STO with a tetragonal structure. The in-plane and out-of-plane lattice parameters are $a_{\mathrm{LSMO}} \approx 3.9\,\text{Å}$ and $c_{\mathrm{LSMO}} \approx 3.86\,\text{Å}$, respectively. It should be noticed that the deviation from the bulk crystal structure[11] is known to be caused by substrate-induced strain effect [281, 289].

The results of HRXRD analysis were confirmed by Scanning Transmission Electron Microscopy (STEM) carried out on a selected sample grown at a temperature of 585 °C (see Fig. 3.10(a)). The nearly perfect cube-on-cube structure of LSMO onto STO is a confirmation of high quality epitaxial and fully-strained growth with the film and substrate sharing the same in-plane lat-

---

[11] For Sr = 0.26 LSMO is expected to have a rhombohedral structure (see Section 2.1.1).

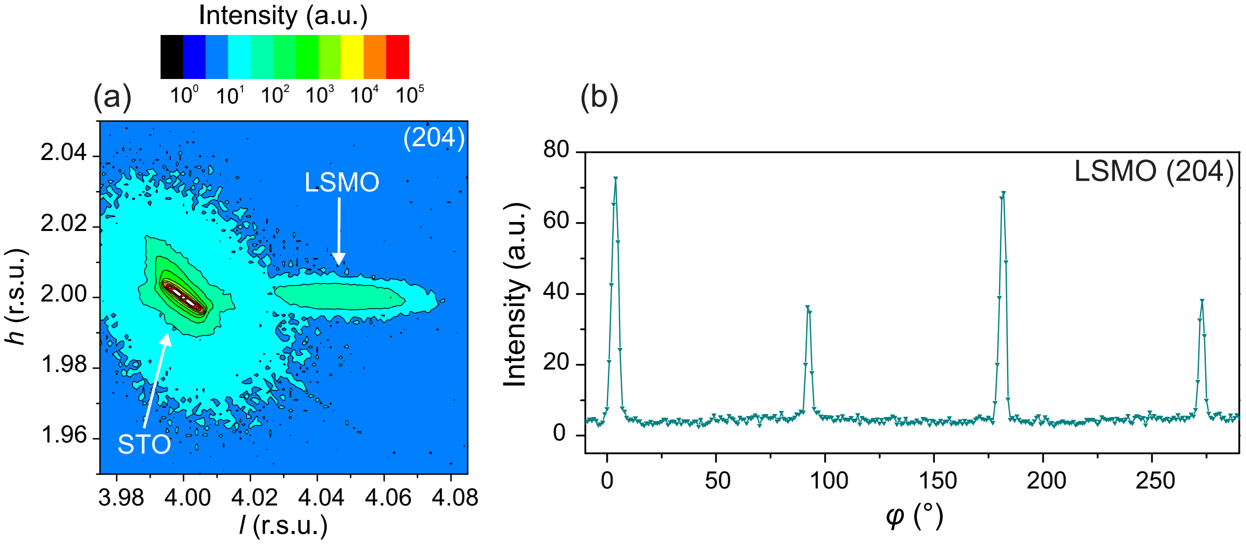

Figure 3.9.: XRD analysis of asymmetric (204) reflection of a LSMO sample grown at 540 °C. (a) 2D-RSM revealing that film and substrate possess nearly coincident in-plane *h* component (*h* and *l* stand for reciprocal space units). (b) φ-scan indicating four fold symmetry of LSMO.

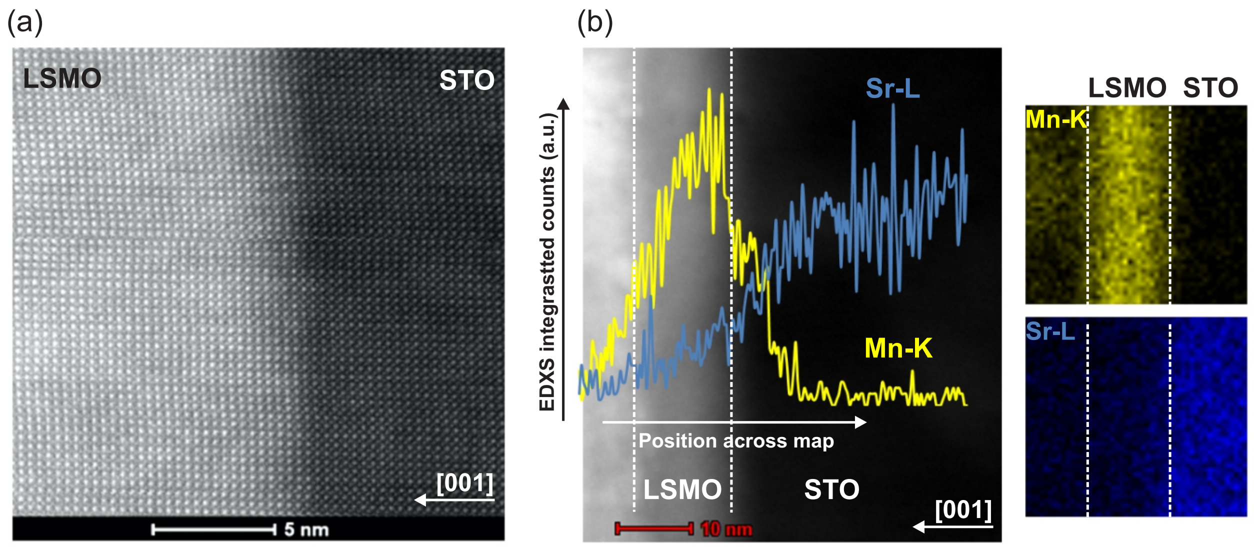

Figure 3.10.: (a) Scanning transmission electron micrograph of a LSMO film grown on STO. The cube-on-cube growth denotes almost perfect epitaxy. (b) Energy Dispersive X-ray (EDX) analysis of a LSMO film grown on STO. EDX spectra of Sr and Mn signals are displayed for a line scan (left panel) and two-dimensional mapping (right panels).

tice parameter. Additionally to STEM, Energy Dispersive X-ray (EDX) spectroscopy offered a qualitative assessment of the elemental distribution (see Fig. 3.10(b)). The energy spectra of Mn revealed negligible interdiffusion of such element from LSMO, whereas the Sr-signal was homogeneously distributed in both film and substrate, although more pronounced in the latter (as expected).

Concerning the surface morphology, AFM analysis confirmed that the surface of the LSMO films is atomically flat with one or half unit cell steps over large areas. Nonetheless, the surface roughness systematically increases when using higher growth temperatures. For $T_{\mathrm{dep}} \approx 700$ °C, atomically flat terraces are sporadically covered with particles with a height of about 10-15 nm (see Fig. 3.11(a)). At a lower deposition temperature of 650 °C, the particles are smaller and more evenly spread on the LSMO surface (see Fig. 3.11(b)). By further decreasing growth temperature, the surface becomes progressively smoother and smoother (see Fig. 3.11(c,d)).

The behavior may be explained as a consequence of Sr diffusion from the STO substrate [296, 323, 329, 330]. Indeed, at high T_{dep} strontium atoms that from the substrate reach the LSMO surface have enough energy to further diffuse and nucleate into large islands. For lower deposition temperatures the minor strontium diffusion towards the LSMO surface and the reduced thermal energy cause the formation of smaller particles that are not able to move and merge into bigger ones. On further decreasing the growth temperature, no significant macroscopic Sr diffusion takes place from the STO substrate.

It is anyway worth noticing that the formed islands cover only a minor portion of the atomically flat surface of LSMO. Concerning the utilization of high temperature deposited LSMO films for *in situ* magnetoelectric (ME) measurements via IL charging, the islands are not expected to provide any relevant contribution to the ME coupling. Indeed, strontium, which oxidizes under oxygen conditions (as during film fabrication or after air exposure), is non-magnetic and insulating.

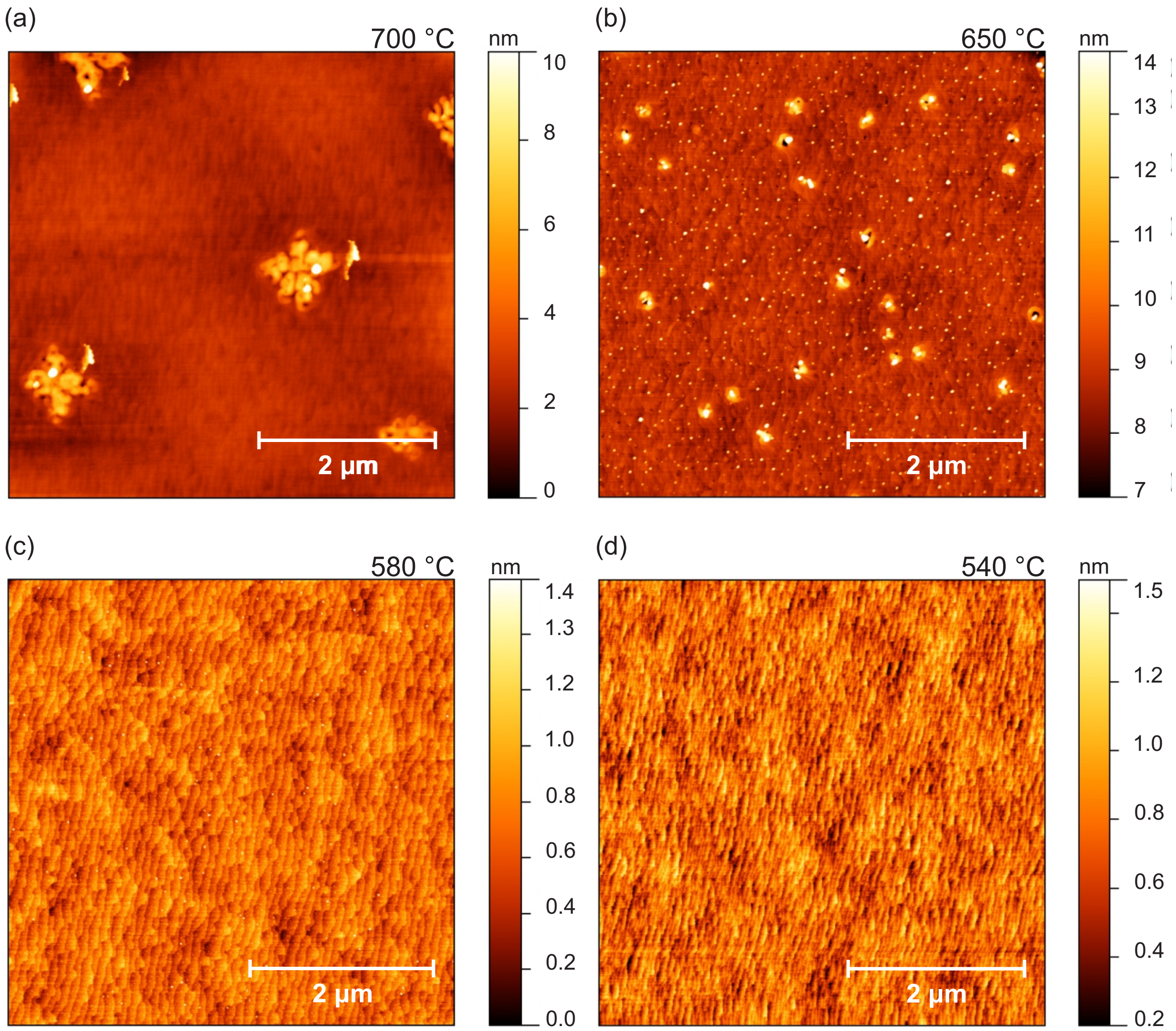

Figure 3.11.: Atomic force micrographs of LSMO films grown at different temperatures. The respective RMS roughness is 1.8 nm (a), 0.8 nm (b), 0.2 nm (c) and 0.2 nm (d).

Thus, the SrO islands are not expected to affect the overall magnetic response of the sample or to significantly participate into the charging/discharging processes with the IL[12].

The magnetic properties of LSMO were studied as a function of various deposition temperatures by analyzing field-cooled (FC) magnetization curves (see Fig. 3.12). All the LSMO samples displayed a Curie point above room temperature, typically with higher values (T_C up to 326 K) and sharper para/ferromagnetic transitions (FWHM ≈ 11 K for the first derivative of the FC curve) for the films deposited at higher temperatures. A possible explanation for this behavior may be related to a slightly enhanced oxygen stoichiometry and better epitaxial quality (sharper RCs) observed for the samples grown at higher temperatures, both factors facilitating double-exchange magnetic interactions (see Section 2.1.1). The bump in magnetization at around 105 K is attributed to the magnetostriction in LSMO induced by the structural phase transition of STO from cubic to tetragonal, which underlines once again the excellent substrate-film adhesion

---

[12] This is also one of the advantages of using IL gating rather than solid-state gating. Indeed, the presence of the islands would be detrimental for the growth of a dielectric or ferroelectric gate material, because the inevitable formation of defects would substantially contribute to increase the leakage current.

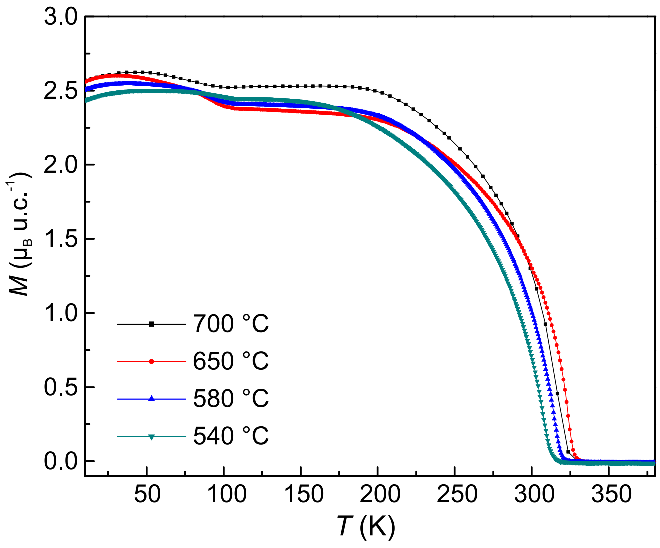

Figure 3.12: Field-cooled magnetization curves of LSMO films prepared at different deposition temperatures. T_C is 324, 326, 318 and 312 K, whereas the FWHM of the derivative of the FC curves is 26, 11, 20 and 20 K, for the LSMO films grown at 700, 650, 580 and 540 °C, respectively. All measurements performed applying a magnetic field of 100 Oe parallel to the in-plane film direction.

[281]. Additional remarks concerning the saturation magnetization of LSMO and the role of magnetic dead layers will be discussed in the following section.

On the basis of the findings acquired with the survey on different growth temperatures, it can be concluded that a good trade-off between structural and magnetic properties of LSMO was accomplished for the samples deposited in the range between 540 °C and 700 °C. Higher growth temperatures (above 800 °C) were found to be detrimental because they led to the loss of epitaxial growth with the onset of spurious phases, pronounced dewetting and islands growth on the film surface together with suppressed magnetic properties. Usage of lower deposition temperatures (below 500 °C) implied a progressive reduction in T_C, broader para/ferromagnetic transition and worse crystalline quality (broader RCs).

3.3.4 Magnetism in thin and ultrathin films: role of the magnetic dead layer

In general, a reduction of LSMO film thickness allows to enhance the surface-to-volume ratio, and thus also all correlated interfacial phenomena (including ME coupling). However, as a drawback, thin films experience a reduction in saturation magnetization M_{sat} and transition temperature T_C as compared to bulk LSMO [109, 281, 288, 289, 298, 331]. The weakening of ferromagnetism is particularly pronounced when the thickness is reduced to just a few unit cells.

Fig. 3.13(a) shows the FC magnetization curves of three LSMO samples with different thicknesses. In the case of ultrathin LSMO films of 3 nm (i.e. about 8 unit cells) T_C decreases down to 240 K and the para-ferromagnetic transition conspicuously broadens. Other insights on the change of magnetic behavior with the LSMO thickness can be observed from the analysis of the magnetic hysteresis loops $M(H)$ (see Fig. 3.13(b)). When the thickness is diminished from 12 nm to 3 nm the saturation magnetization M_{sat} drops from $\approx 2.8\,\mu_B\,\mathrm{u.c.}^{-1}$ to $\approx 1.7\,\mu_B\,\mathrm{u.c.}^{-1}$, whereas the coercivity H_C enlarges, signifying that LSMO tends to become a slightly harder magnetic material. It is worth to notice that the values of M_{sat} are significantly below the maximum theoretical value of $\approx 3.7\,\mu_B\,\mathrm{u.c.}^{-1}$ (for Sr ≈ 0.26).

The prominent reduction of magnetic properties in thin and ultrathin films of LSMO as compared to bulk has been widely investigated, though a unique and clear picture of the phenomenon has not been found yet. Boschker *et al.* [298] assigned the exotic magnetic and conducting properties of ultrathin films of LSMO to the strain-induced tilting of the oxygen

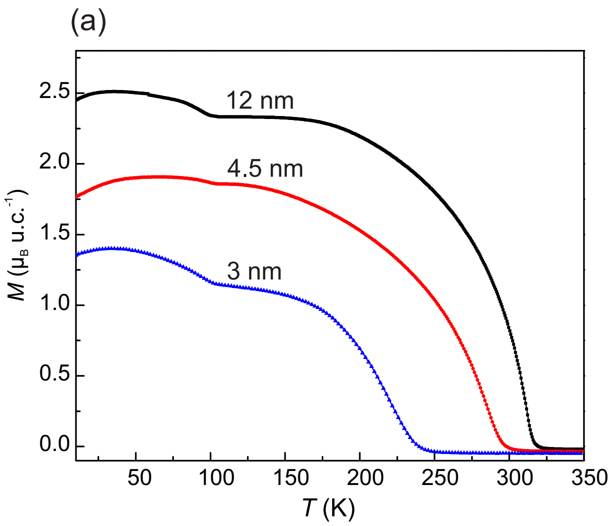

Figure 3.13.: (a) Field-cooled magnetization curves of LSMO films grown at 540 °C with different thickness values. T_C is 314, 294 and 240 K, whereas the FWHM of the derivative of the FC curves is 18, 40 and 55 K, for a LSMO thickness of 12, 4.5 and 3 nm, respectively. Measurements performed at 10 K applying a magnetic field of 100 Oe parallel to the in-plane film direction. (b) Magnetic hysteresis loops carried out at 10 K for different LSMO thicknesses.

octahedra at the film/substrate interface. In addition, on the basis of the results of a thickness-dependence study, the author proposed an alternative magnetoelectronic phase diagram for ultrathin films of LSMO, which significantly deviates from standard bulk LSMO.

Apart this noteworthy example, the large majority of theoretical and experimental studies ascribe the anomalies of ultrathin films to the formation of a so-called magnetic dead layer (MDL) at the film/substrate interface. Some works attributed the origin of the MDL to oxygen deficiencies [282, 332] or substrate/film elemental interdiffusion [296, 329, 333] during the growth process. In other reports [297, 334] it was found a preferential occupation of e_g electrons in ($3z^2$ - r^2) rather than (x^2 - y^2) orbitals at the LSMO/STO interface, with consequent promotion of double-exchange (ferromagnetic) interactions in the out-of-plane instead of the in-plane direction. Another possibility is given by the already-mentioned phenomenon of magnetic phase separation [272, 273, 275, 288, 335, 336]. For instance it has been proposed [275] that a separation between ferromagnetic-metallic and antiferromagnetic-insulating phases can occur at the interface between a half-metallic manganite and an insulator due to the lack of charge carriers.

It should anyway be noticed that not necessarily only one single phenomenon may cause the formation of MDLs. The definition of a common consistent scenario is also complicated by the very different experimental conditions and experimental techniques reported in the literature. For instance, Herger *et al.* [329] suggested that Sr segregation towards the film surface leads to a lower concentration of e_g electrons (and so to a higher hole concentration), thus affecting the interplay between double and superexchange magnetic interactions. According to our results, this idea is consistent with LSMO samples prepared at high temperatures (around 700 °C) where prominent Sr diffusion and islands formation occur, but it is not compatible with the atomically flat LSMO surfaces attained at lower deposition temperatures. In this case, the reduced

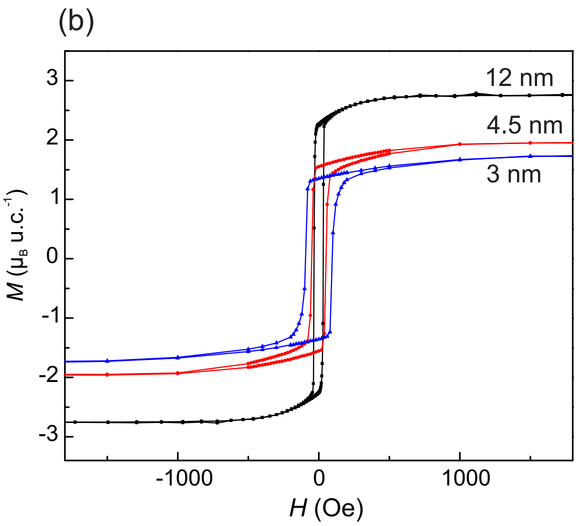

crystallinity (broader RCs) and larger oxygen deficiencies (oxygen vancancies correspond to electron doping) may be a possible explanation.

The presence of MDL was not only observed in LSMO films grown on STO substrate, but also in other manganite systems deposited on various substrates. Moreover, owing to the intrinsic relation between magnetism and conductivity in strongly-correlated manganites, not only MDLs but also electric dead layers have been discovered. The latter are generally thicker than the former in accordance with the percolative nature of conducting/insulating domains (see Section 2.1.1). For instance the electric dead layer thickness of LSMO films grown on STO, $NdGaO_3$ and $LaAlO_3$ was estimated to be in the range between 3-8 nm [282], whereas for LSMO/STO heterostructures the MDL is typically in the range between 1.2 and 4 nm [288].

Considering the values of M_{sat} attained in the thickness-dependence study (see Fig. 3.13(b)) and their deviation from the expected bulk theoretical value of $\approx 3.7\,\mu_B\,\text{u.c.}^{-1}$ (for Sr ≈ 0.26), it is possible to estimate the size of the magnetically active material contributing to ferromagnetism. For LSMO films grown at 540 °C with a thickness of 12, 4.5 and 3 nm the resulting MDL is 3.2, 2.1 and 1.6 nm, respectively. The reason why the size of the MDL significantly varies in LSMO films with different thicknesses grown under same deposition conditions may be related to a different oxygen uptake during postannealing process. It is possible that during postannealing the oxidation front formed at the film's surface prevents (or hinders) further oxygen diffusion towards deeper LSMO atomic layers closer to the substrate. The progressive strain-relaxation taking place in LSMO on increasing the film thickness may also play a role. In addition, it cannot be also excluded that different amounts of Sr diffusion towards the surface may occur on varying the thickness, simply because of different deposition times (e.g. 750 s for 3 nm LSMO films, whereas 3000 s for 12 nm LSMO films).

3.4 Summary

In this chapter the optimization steps required to fabricate $La_{0.74}Sr_{0.26}MnO_3$ thin films (3 - 15 nm) with highest quality in terms of epitaxial growth, surface smoothness and magnetic properties have been described.

Prior to deposition the STO substrates were examined to verify whether they were suitable for the preparation of thin films or not. In case of abundant surface contamination a chemical etching process followed by high-temperature annealing was performed in order to significantly decrease the surface roughness.

The common issue related to the abundance of oxygen deficiencies in PVD-prepared films has been tackled by carrying out high-temperature post-deposition annealing, which was found to be particularly beneficial for increasing the value of T_C.

The effect of different growth temperatures has been extensively investigated with a variety of characterization techniques. The best compromise between optimum structural and magnetic characteristics of LSMO was found in the 540 - 700 °C range. In this temperature region LSMO films grown at higher temperature displayed higher T_C and better crystallographic orientation with respect to the substrate (sharper RCs), although the formation of islands at the surface, probably due to Sr diffusion from STO, resulted in an increase in surface roughness. On the other hand, LSMO films grown at lower temperatures showed an atomically flat surface with nearly absence of particles at the expense of a slight decrease of T_C.

Magnetic properties have been analyzed as a function of the LSMO film thickness. In accordance with the literature, a systematic reduction of T_C and M_{sat} as compared to bulk LSMO takes place on diminishing the film thickness. This indicates that the bulk phase diagram of LSMO can be used only in first approximation to describe the properties of thin films and that new interfacial phenomena, such as MDLs, emerge at the nanoscale.

With the fabrication of LSMO films with a quality comparable to the state-of-the art, the stage for the inspection of ME coupling at the LSMO/IL interface was finally set up.

4 Magnetoelectric coupling in LSMO thin films gated with DEME-TFSI ionic liquid

Selected parts of this chapter are also published in [337] within the framework of this thesis. The respective paragraphs – with minor adjustments included – are indicated by a vertical gray bar at the inner page margin[1].

With the fabrication of $La_{0.74}Sr_{0.26}MnO_3$ (LSMO) films featuring excellent characteristics in terms of microstructure and magnetic properties, a solid foundation for the investigation of the phenomenon of magnetoelectric (ME) coupling at the LSMO/ionic liquid (IL) interface was laid. This chapter deals with the results of voltage-induced tuning of magnetism in LSMO films with a thickness of about 13 nm. First, the attention is focused on the nature of the charging/discharging processes taking place at the LSMO/IL interface. It is shown that electrostatic doping (electric double layer (EDL) capacitance) is progressively supplanted by surface electrochemical redox reactions (pseudocapacitance (PS)) upon enlarging the applied potential window. Afterwards, it is demonstrated that interfacial charge doping is intimately related to the reversible control of LSMO magnetization. ME coupling is quantitatively analyzed as a function of different temperatures and voltage-driven surface charge densities by means of *in situ* synchronized Superconducting Quantum Interference Device (SQUID) magnetometry and Cyclic Voltammetry (CV). Eventually, a consistent scenario linking experimental results and theory is proposed by invoking the phenomenon of magnetic phase separation at the LSMO surface.

4.1 Background

Manipulation of the electronic structure of a magnetic material upon voltage-induced charge doping is a common and direct approach to realize ME effect [8]. Typically, two possible charging mechanisms may occur at solid/solid or solid/liquid interfaces. The first involves non-faradaic electrostatic doping, where the charge carriers are electrostatically separated at the interface between a magnetic material and a ferroelectric [11, 109, 139], a dielectric [119] or an electrolyte [170, 173], in analogy to a parallel plate capacitor. The second implies faradaic electrochemical doping, where redox reactions with exchange of charge carriers [15, 221, 223] occur across the interface between a magnetic material and a different chemical species, resembling the behavior of an electrochemical cell.

It has been experimentally shown that the strength of the ME effect at the interface is directly related to the electric capacitance [8, 109]. In this regard, supercapacitors (SCs), so far primarily utilized for energy storage and delivery, provide attractive tools to reversibly and robustly control magnetism. They can accumulate charge electrostatically (as in EDL capacitors [202, 338]), electrochemically (as in metal-oxide pseudocapacitors [163, 177, 179, 180]) or by a combination of both (as in hybrid supercapacitors [339, 340]). In particular, pseudocapacitors can reach

---

[1] Reprinted from [337] under Creative Common CC-BY license.

values of capacitance [163] as high as $\sim 1000\,\mu\mathrm{F\,cm^{-2}}$, which allows for surface charge densities appreciably beyond ferroelectrics (e.g. $\sim 150\,\mu\mathrm{C\,cm^{-2}}$ for $BiFeO_3$ [77]). Further, they feature an exceptional degree of reversibility upon charge/discharge cycling [184, 187].

To date, intensive efforts have been aimed at improving the SCs performance in terms of energy storage-capacity and delivery, but the idea of utilizing a pseudocapacitor or a hybrid supercapacitor, per se, to control magnetism has been hardly explored yet. In view of the recent discovery [196] of pseudocapacitive reactions in $LaMnO_3$, the class of magnetic manganese-based perovskite oxides naturally qualifies as a system of interest for modulation of magnetic properties via both electrostatic and electrochemical stimuli. In particular, $La_{1-x}Sr_xMnO_3$, owing to its high Curie temperature, can certainly be considered as a technologically relevant prototype system. This strongly-correlated oxide features a rich magnetoelectronic phase diagram [134, 258, 259] encompassing a variety of magnetic states[31] that are determined by the charge state of the manganese ions ($Mn^{3+/4+}$).

In the following, ME effect is extensively studied in supercapacitors of LSMO thin films electrically charged with an IL electrolyte examining the correlation between the interfacial charging/discharging processes and the respective magnetic response.

4.2 Sample preparation and experimental details

LSMO films were epitaxially grown onto $SrTiO_3$ (STO) substrates via Large-Distance Magnetron Sputtering in accordance with the optimized conditions discussed in Section 3. A LSMO thickness of 13 nm was chosen for it guaranteed a robust magnetic signal easily detectable via SQUID in a wide temperature range, including room temperature.

An electrochemical tuning cell (see schematic in Fig. 4.1(a)), composed of a LSMO film (working electrode), a high-surface-area carbon cloth (counter electrode) separated by an insulating porous glass fiber soaked in ionic liquid (diethylmethyl(2-methoxyethyl)ammonium bis(trifluoromethylsulfonyl)imid, DEME–TFSI), was inserted into a SQUID magnetometer and connected to a potentiostat. The setup allowed for quantitative and quasi-continuous *in situ* measurements of the magnetization response upon modulation of the interface charge density (see also Section 2.4.7). For the measurement of the magnetic moment measured via SQUID an external magnetic field of 100 Oe was applied parallel the plane of the film in order to align the spins along a well-defined direction. Since the ME tuning cell featured a two-electrode configuration, all the potential windows were set with respect to open circuit potential[2] (≈ -150 mV).

During *in situ* tuning experiments, while the external potential $V(t)$ was being ramped, the current density $J(t)$ flowing towards the LSMO electrode was monitored, and upon integrating it, the surface charge $Q(t)$ at the LSMO/IL interface was calculated. Simultaneously, the magnetic response $M(t)$ was measured. An illustrative example of a typical tuning experiment performed at 323 K, revealing the high degree of reversibility achieved above room temperature, is provided in Fig. 4.1(b). In the initial state (before t_0), the magnetization is constant. Afterwards, during CV cycling (from t_0 to t_f), the magnetic signal follows the surface charge modulation in a highly reproducible *zigzag–like* fashion with low noise fluctuations. After t_f, the magnetization recovers its initial value.

---

[2] All voltage data here reported are represented using the value of open circuit potential as starting point.

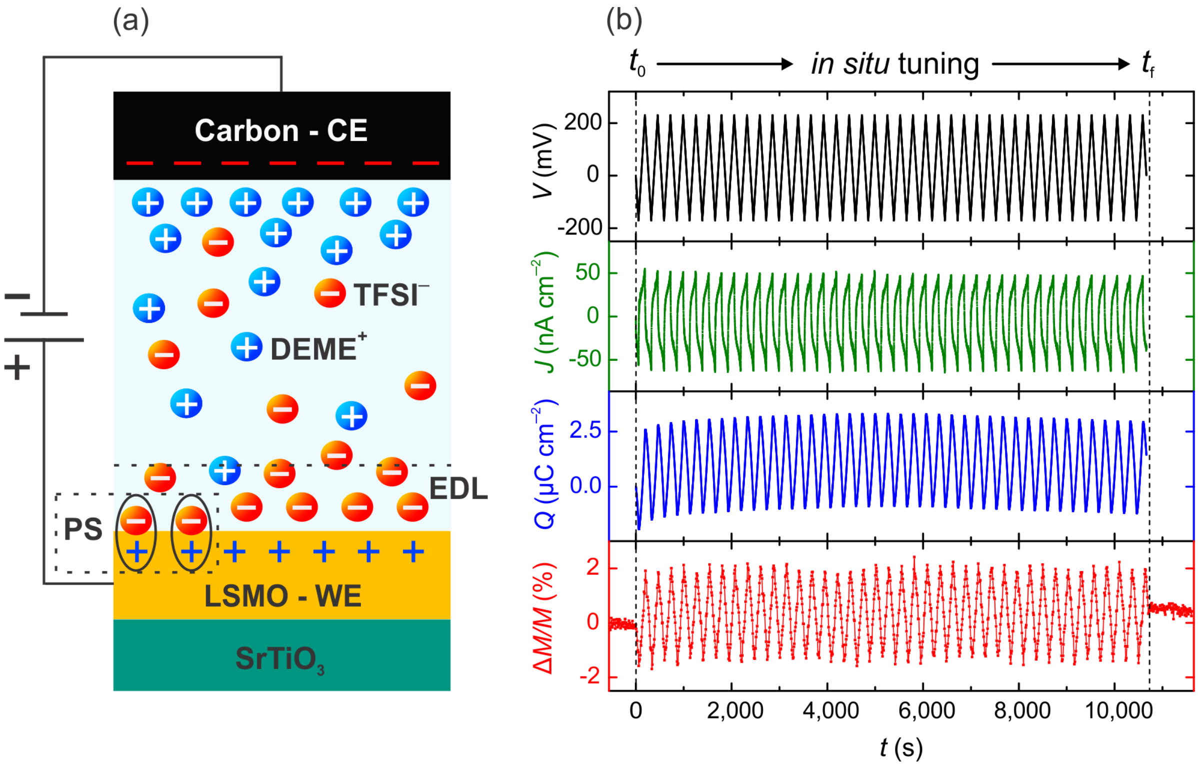

Figure 4.1.: Sketch of the ME setup and *in situ* measurement principle. (a) Schematic of the electrochemical tuning cell: a LSMO single crystalline thin film (≈ 13 nm) grown on STO substrate and a high-surface-area carbon cloth serve as working (WE) and counter (CE) electrodes, respectively. On application of an external voltage, the ions of the ionic liquid (DEME-TFSI) approach the LSMO surface inducing charge carrier accumulation in the LSMO electrode either through electrostatic (electric double layer (EDL) capacitance) or electrochemical (pseudocapacitance (PS)) doping. Both mechanisms allow for manipulating the magnetic state of LSMO. (b) Example of *in situ* tuning experiment performed at 323 K: the magnetic response (in red) reversibly follows the surface charge modulation (in blue), calculated by integrating the measured current density (in green), on repetitive cycling of the external potential (in black). (Published in *Nature Communications* 2017 [337])

4.3 Capacitive and Pseudocapacitive charging regimes

One of the most important figures of merit in CV experiments is the capacitance, defined as $C = \Delta Q / \Delta V_{Q_{\mathrm{max}}}$, where ΔQ is the difference between positive and negative maximum surface charge and $\Delta V_{Q_{\mathrm{max}}}$ is the difference in the respective voltages. Alternatively, the current density $J = \mathrm{d}Q/\mathrm{d}t$ and the ramp rate $a = \mathrm{d}V/\mathrm{d}t$ can be used to express the capacitance as $C = J/a$. High values of capacitance are certainly desirable for tuning the magnetization because they directly result in large modulations of interface charge density ΔQ. Thus, the higher the charge carrier accumulation at the LSMO electrode is, the larger the number of Mn ions to undergo a change in oxidation state will be. This, in turn, enables a wider portion of the LSMO magnetoelectronic phase diagram to be probed in a full voltage sweep.

Owing to a number of very sensitive control parameters, such as temperature, applied voltage and electrode/electrolyte chemical compatibility, a clear determination of whether the capacitance

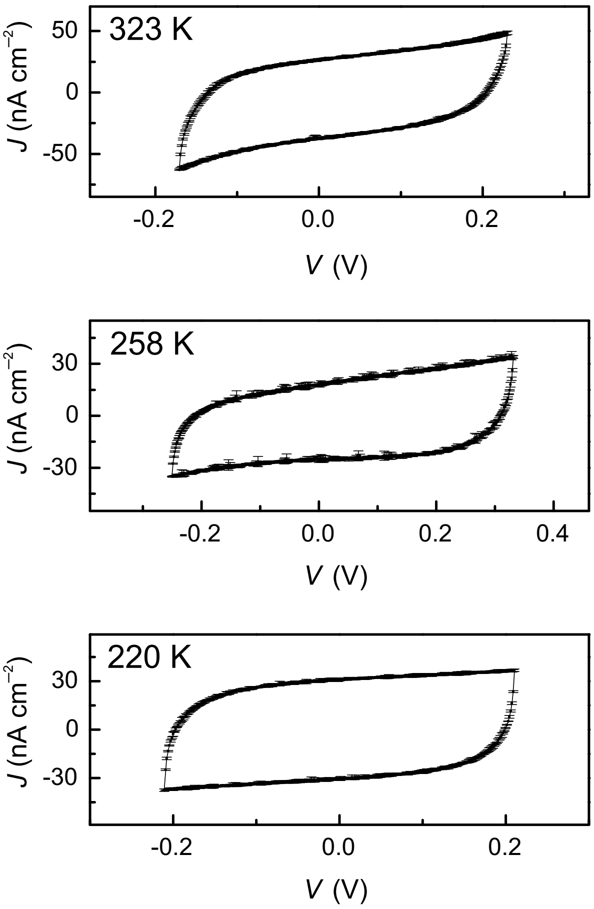

Figure 4.2: Current-voltage characteristics at different temperatures for a constant $\Delta Q \approx 4\,\mu\mathrm{C\,cm^{-2}}$. The curves feature a high level of reversibility and rectangular-like shapes, as expected for a traditional EDL capacitor. The curves are constructed by averaging several consecutive measurements (40 cycles at 323 and 220 K, and 10 cycles at 258 K). (Published in *Nature Communications* 2017 [337])

originates from electrostatic, electrochemical charging or a combination of both, is a non-trivial task [18, 19, 156]. In this work, in order to reliably discern between faradaic and non-faradaic charging regimes, a series of systematic CV measurements was conducted for different temperatures, potential windows and voltage sweep rates.

Initially, a temperature-dependence survey was carried out from 330 K to 220 K, that is, slightly above the LSMO Curie point down to the DEME–TFSI glass transition [305]. The surface charge modulation was intentionally kept at the small value of $\Delta Q \approx 4\,\mu\mathrm{C\,cm^{-2}}$ using a working potential window of $\Delta V \approx 400\,\mathrm{mV}$. Thus, electrochemical reactions at the LSMO/IL interface were hindered. Throughout the whole investigated temperature range, the $J(V)$ characteristics featured the behavior of an ideal capacitor with symmetric and nearly-rectangular shape of the charging/discharging processes and a remarkable reversibility upon cycling (see Fig. 4.2). The calculated capacitance $C \approx 10\,\mu\mathrm{F\,cm^{-2}}$ was virtually constant (see also Table A.1 in Appendix A.4 for more details) and consistent with the expected EDL capacitance values reported for metallic conductive electrodes in ILs [17, 310, 318, 341]. These findings give a strong indication that under application of small external voltages the CV measurements were performed within a regime dominated by electrostatic doping.

Afterwards, an isothermal charge-dependence study (see Fig. 4.3(a)), with progressive expansion of the potential window ΔV from 0.2 V up to 3.7 V, was carried out at the lowest temperature of 220 K, where electrochemical reactions are expected to be hampered [143]. Interestingly, up to ~2.4 V, the $J(V)$ characteristics still exhibited a high level of reversibility with a nearly perfect rectangular shape. However, a systematic increase in current density, and therefore capacitance, was observed. These features represent the fingerprint of ideal PS [179, 180, 190], denoting

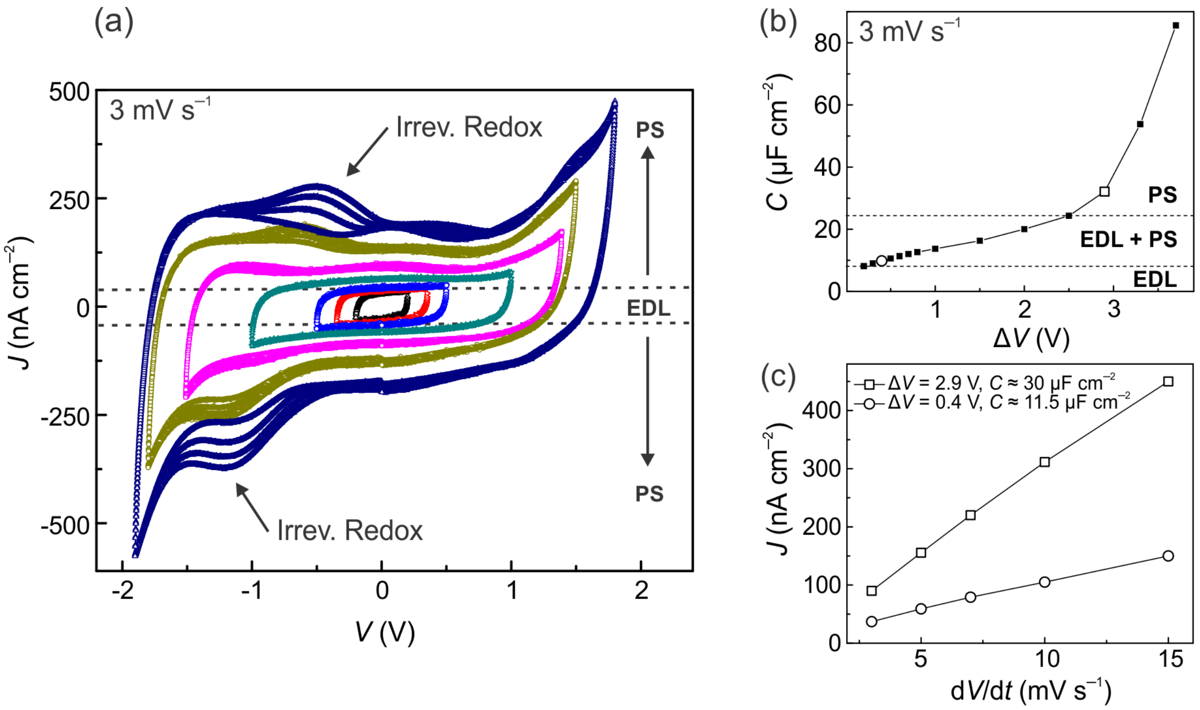

Figure 4.3.: Transition from capacitive to pseudocapacitive charging at 220 K. (a) Current density - voltage characteristics upon expansion of the potential window ($0.2\,\mathrm{V} < \Delta V < 3.7\,\mathrm{V}$) with a constant scan rate of 3 $\mathrm{mV\,s^{-1}}$. Each curve corresponds to four consecutive CV cycles. The dashed lines qualitatively delimit the operative region expected for an ideal EDL capacitor. The increment in current density upon increasing the applied ΔV indicates a progressive pseudocapacitive (PS) behavior. The arrows indicate the points where irreversible redox reactions start to appear. (b) Calculated capacitance versus applied voltage for a scan rate of 3 $\mathrm{mV\,s^{-1}}$. The trend of *C* indicates a gradual transition from EDL capacitance to PS up to $\Delta V \sim$ 2.4 V. Beyond this value, the steep increase in *C* denotes the predominance of PS. (c) Voltage ramp rate dependence of the current density for a particular potential window of 0.4 V and 2.9 V. In (b) and (c) the experimental errors are within a 5% accuracy. (Published in *Nat. Comm.* 2017 [337])

that electrode charging/discharging is driven also by interfacial electrochemical reactions. At a certain limit, when ΔV was considerably expanded up to 3.7 V, the $J(V)$ curves displayed more pronounced electrochemical features.

The trend of the calculated capacitance, which increases from $\approx 10\,\mu\mathrm{F\,cm^{-2}}$ up to $\approx 85\,\mu\mathrm{F\,cm^{-2}}$, is illustrated in Fig. 4.3(b). The onset of PS seems to develop already at low voltages since the EDL capacitance of standard metallic electrodes gated via ILs exhibits exactly the opposite behavior[3] [318]. Beyond a threshold value of $\Delta V \sim$ 2.4 V, the steeper increase in *C* heralds a transition to a pseudocapacitive-dominated regime. Notably, at the biggest applied potential window of 3.7 V, the surface charge modulation reached a value of $\approx 270\,\mu\mathrm{C\,cm^{-2}}$.

It is known [177, 179, 180, 196] that PS involves redox reactions with faradaic charge transfer occurring at the surface and/or in the bulk of the electrode. Here, ionic intercalation into LSMO is unlikely as the DEME [342] and TFSI [310] ions are nearly twice the size of the LSMO unit

---

[3] As already discussed in Section 2.4.6, the EDL capacitance of IL-gated devices decreases on increase of the external voltage.

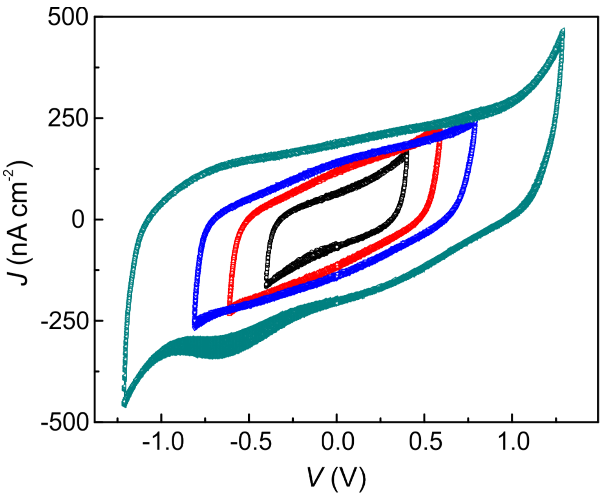

Figure 4.4: Current density - voltage characteristics upon expansion of the potential window ($0.8\,\mathrm{V} < \Delta V < 2.5\,\mathrm{V}$) at 270 K. More pronounced PS features are visible as compared to the behavior encountered at the lower temperature of 220 K. Each curve corresponds to four consecutive CV cycles. (Published in *Nat. Comm.* 2017 [337])

cell [134, 258, 259]. A minor contribution due to oxygen ions migration into LSMO may be attributed to the decomposition of residual traces of water [229] present in the ionic liquid[4]. This is compatible with the appearance of small irreversible redox peaks upon expansion of the potential window up to 3.7 V (see arrows in Fig. 4.3(a)). The interpretation that surface PS plays a major role in the electrochemical doping of LSMO is corroborated by a voltage ramp rate study performed at the fixed potential windows of 0.4 V and 2.9 V (Fig. 4.3(c)). On the one hand, the linear behavior of the current density indicates the presence of fast surface charging/discharging processes [177, 182], resembling the charge-transfer kinetics of a capacitor rather than of an electrochemical cell. On the other hand, the calculated slopes confirm the radical increase in capacitance upon expansion of the potential window.

These findings imply that the LSMO/IL system behaves as an archetypal hybrid supercapacitor. A plausible scenario is that the electric field driven attraction of DEME and TFSI ions to the LSMO surface changes from physisorption to chemisorption upon increasing the potential window. Consequently, the charging processes move from electrostatic (EDL capacitance) to electrochemical (surface redox PS) doping.

The behavior of C upon isothermal increase of the applied voltage was also studied at higher temperatures. Considering the results attained at 270 K (see Fig. 4.4), the shape and reversibility of the $J(V)$ characteristics and the values of calculated capacitance corroborate the idea that the charging/discharging processes in the LSMO/IL system are due to a combination of EDL capacitance and surface PS. In general, at higher temperatures the thermally activated nature of electrochemical reactions [143] precipitated the occurrence of PS. The highest value of $C \approx 180\,\mu\mathrm{F\,cm^{-2}}$ was achieved at around 320 K under the application of 1.8 V, leading to a surface charge density of $\Delta Q \approx 200\,\mu\mathrm{C\,cm^{-2}}$.

4.4 Control of magnetism via voltage-induced surface charge doping

After describing the nature of the charging/discharging processes at the LSMO/IL interface, we shall now focus on the voltage-induced response of LSMO magnetization.

As a starting point, a magnetic field-cooled (FC) measurement was carried out prior to *in situ* tuning experiments (Fig. 4.5(a)), which revealed a Curie temperature $T_C \approx 323$ K. Afterwards,

---

[4] Although the preparation of the ME tuning cell is done under glove box conditions and the *in situ* SQUID-CV measurements are carried out in He atmosphere, little amounts of H_2O residuals are inevitable.

the effect of a nearly constant surface charge modulation $\Delta Q \approx 4\,\mu\mathrm{C\,cm^{-2}}$ – corresponding to an EDL charging regime – on the LSMO magnetic response was investigated from above T_C down to 220 K. The peak-to-peak variation in magnetization was defined as $\Delta M = M_\mathrm{acc}^{h^+} - M_\mathrm{depl}^{h^+}$, that is, the difference between the maximum magnetization in hole accumulation and depletion states.

Fig. 4.5(b) represents the behavior of ΔM_σ, determined by normalizing ΔM with respect to the LSMO surface unit cell area (u.c.^{2}). The definition accounts for the interfacial nature of the tuning effect by assuming in first approximation a Thomas-Fermi screening length [11, 109] for the electric field of ∼0.2–0.4 nm. The trend of $\Delta M/M$ that gives the overall tuning effect compared to the untuned LSMO magnetization is depicted in Fig. 4.5(c).

The study of the temperature dependence revealed that above T_C the magnetic response $M(t)$ was negligible while sweeping the surface charge $Q(t)$. On reaching T_C, a steep tuning effect with $M(t)$ changing in-phase with $Q(t)$ (Fig. 4.5(d)) was observed. After reaching a maximum magnetic modulation of ≈ 4.5%, a further decrease in temperature brought about a gradual reduction of the magnetic signal until it virtually vanished at $T_\mathrm{cross} \approx 258\,\mathrm{K}$ (Fig. 4.5(e)). Below this threshold, a crossover with a reverse in sign of the magnetic modulation was observed,

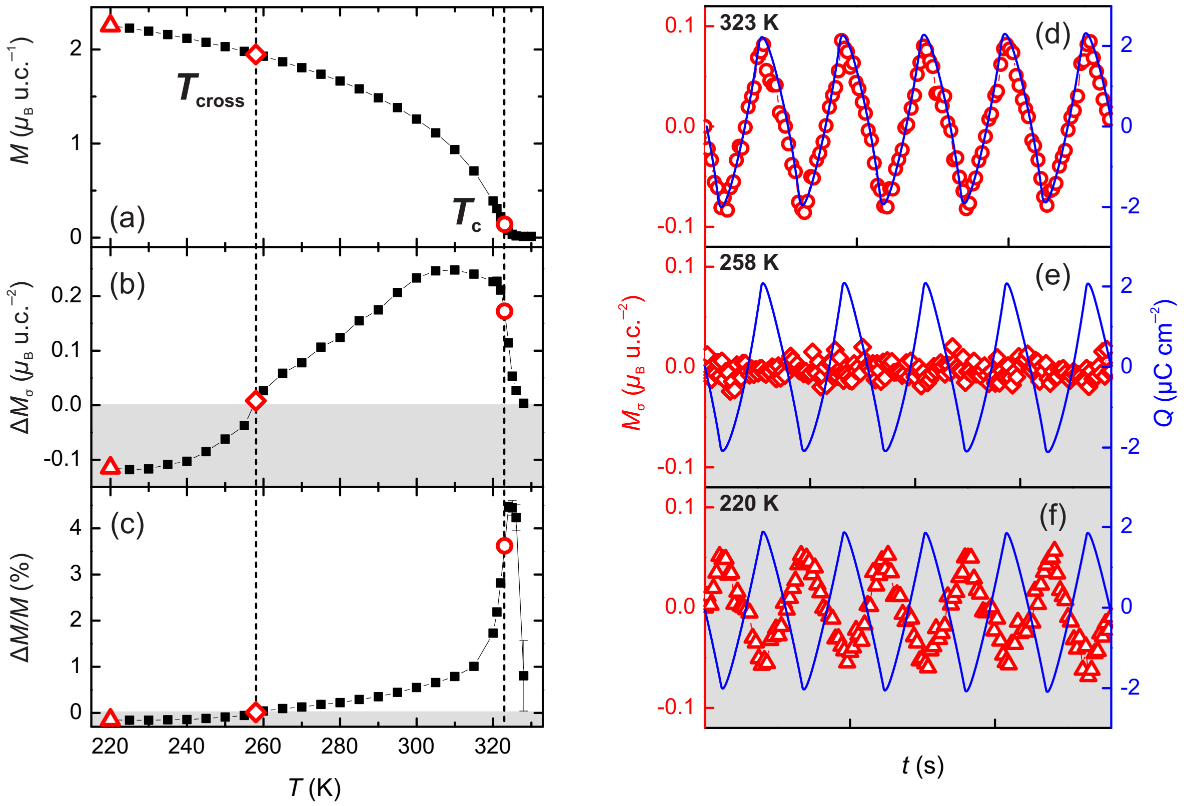

Figure 4.5.: Temperature-dependence magnetic response of LSMO/IL for $\Delta Q \approx 4\,\mu\mathrm{C\,cm^{-2}}$. (a) Magnetic field-cooled curve performed before *in situ* tuning revealing a $T_\mathrm{C} \approx 323$ K. (b,c) Response of the magnetic modulation normalized per LSMO surface unit cell (b) and with respect to the film volume magnetization (c). A crossover temperature $T_\mathrm{cross} \approx 258$ K separates in-phase (white area) and anti-phase (gray area) magnetic responses with respect to the surface charge modulation (see text for more details). (d-f), Time–resolved magnetic response respectively at T_C (d), T_cross (e) and 220 K (f). Each time step in (d-f) on the abscissa corresponds to 500 seconds. (Published in *Nat. Comm.* 2017 [337])

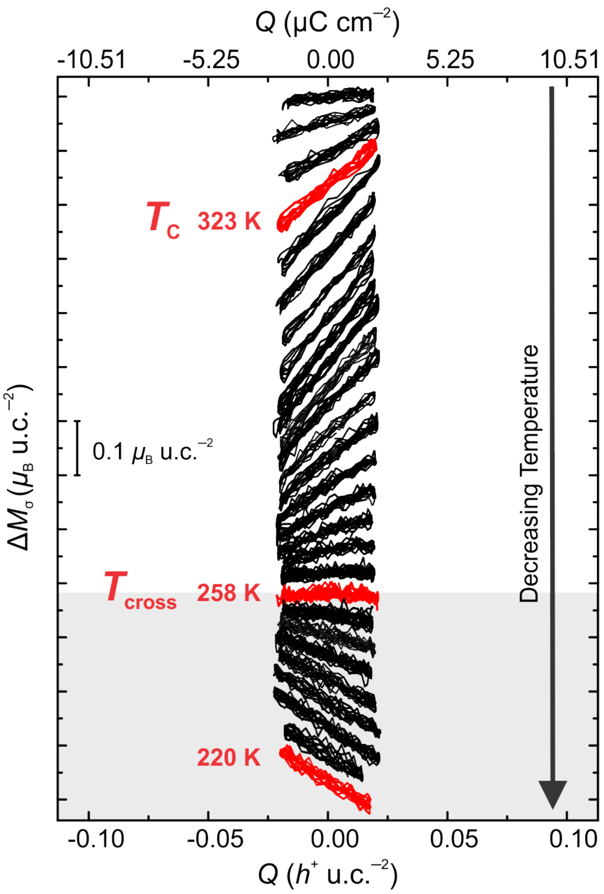

Figure 4.6: Alternative representation of the temperature-dependence survey: magnetic response as a function of the induced surface charge ($\Delta Q \approx 4\,\mu\mathrm{C\,cm^{-2}}$). The slope of the curves provides the ME coupling coefficient α. Each curve consists of at least 10 consecutive CV cycles. Notice that above (white area) or below (gray area) $T_{\mathrm{cross}} \approx$ 258 K the sign of the slopes is positive or negative (and so also α), respectively. The curves at 323 K, 258 K and 220 K belong to the same set of data already shown in Fig. 4.5(d-f), respectively. (Published in *Nat. Comm.* 2017 [337])

i.e. $M(t)$ changed to anti-phase with respect to $Q(t)$ (Fig. 4.5(f)). The existence of a crossover point has already been shown in other LSMO-tuning studies [11, 109, 139, 173], but here T_{cross} reaches the highest temperature reported[5].

Another useful way to represent the results of the temperature-dependence survey is to plot the LSMO magnetic response directly as a function of the induced surface charge (referred to as $M(Q)$ curves, see Fig. 4.6). At a quick glance it is evident that T_{cross} delimits the regions with in-phase/anti-phase tuning effect according to the positive/negative sign of the slope of the $M(Q)$ curves. Furthermore, the values of the slopes come at a hand to evaluate the strength of the interfacial ME effect by defining the ME coupling coefficient $\alpha = \Delta M/\Delta Q$. The introduction of this definition of α as a figure of merit directly stems from the access to reliable, quantitative data on surface charge density and magnetization as given by the potentiostat and the SQUID magnetometer. The values ranged between $+6.4\ \mu_{\mathrm{B}}/h^{+}$ (in proximity of T_{C}) and -3.2 μ_{B}/h^{+} (at the lowest T of 220 K). A deeper analysis of the values of α is postponed to the discussion in Section 4.5.

A broader inspection of the effect of surface charge doping on the LSMO magnetization started with tracking down the magnetic response during isothermal progressive expansion of the applied potential window. It turned out that the high value of T_{cross} together with the achievable surface charge modulation of up to $\Delta Q \approx 270\,\mu\mathrm{C\,cm^{-2}}$ had a deep influence on the magnetism.

Fig. 4.7 reports the results of an isothermal charge-dependence study (with 0.2 V$< \Delta V <$ 3.7 V) performed at 220 K. It was found that from small applied potential windows up to ∼2.9 V

---

[5] After performing *in situ* ME experiments on various LSMO/IL samples it was found that the value of T_{cross} depends on T_{C} and on the sharpness of the para-ferromagnetic transition. General trends are similar for samples with different T_{cross}. Here, for the sake of clarity, we focus on the results attained for a device with $T_{\mathrm{cross}} \approx 258\,\mathrm{K}$.

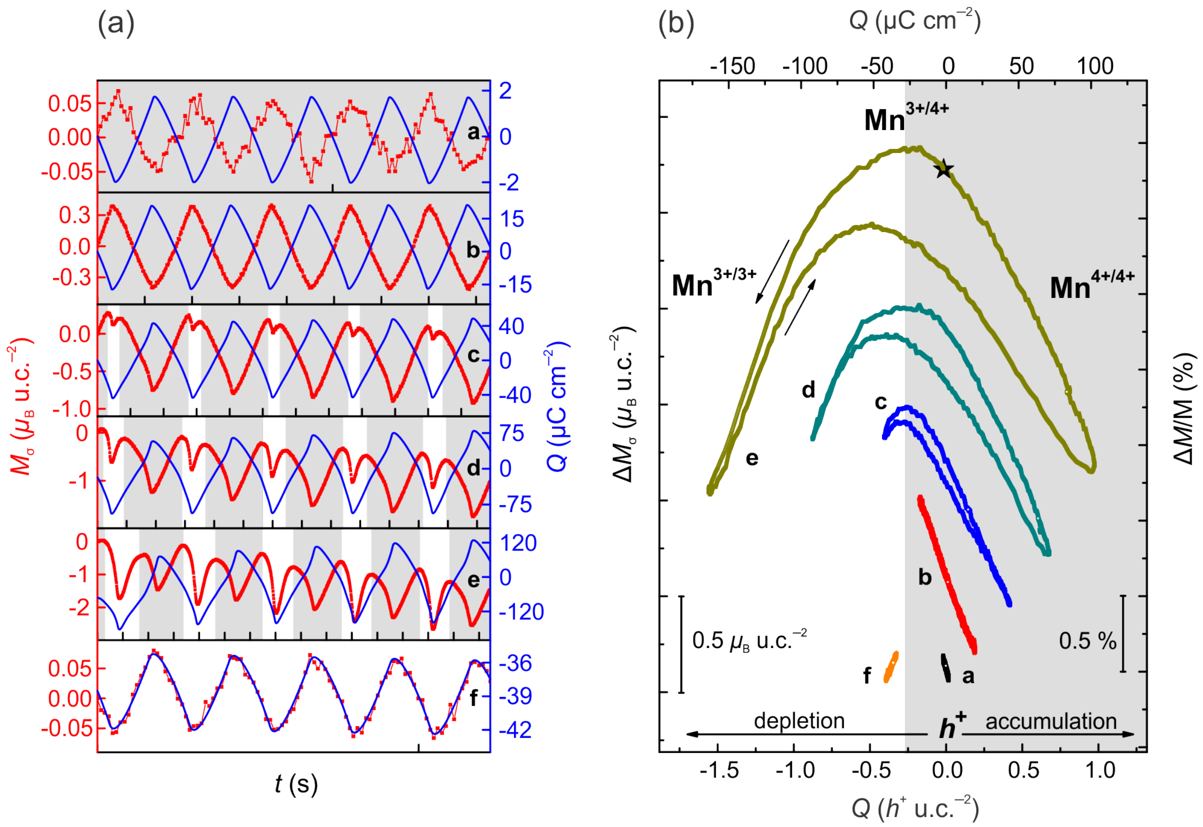

Figure 4.7.: Isothermal charge-dependence ME response at 220 K. (a) Time-resolved magnetic responses upon sequential increase of the surface charge modulation ΔQ from $\approx 1.5\,\mu\mathrm{C\,cm^{-2}}$ up to $\approx 270\,\mu\mathrm{C\,cm^{-2}}$. The expected anti-phase response (plots **a**,**b**) reveals an in-phase splitting of the *M*(*t*) curve (plots **c**-**e**) upon progressive electron doping, like the behavior observed *above* T_{cross} for a small potential window. The application of a bias voltage $V_{\mathrm{b}} \approx -1.3\,\mathrm{V}$ yielded an in-phase response (plot **f**). Each time step on the abscissa corresponds to 800 seconds. (b) Behavior of the magnetization as a function of the surface charge doping. The slope of the *M*(*Q*) curves provides the ME coupling coefficients α. The small variation in $|\Delta M/M|$ underlines the interfacial nature of the magnetic tuning effect at low temperature. In (a,b) the white and gray areas qualitatively separate the data with the LSMO magnetization responding to the applied surface charge as above or below T_{cross}, respectively. (Published in *Nat. Comm.* 2017 [337])

the magnetic signal was in anti-phase with respect to the surface charge modulation (plots **a**,**b** in Fig. 4.7(a)), in agreement with the results of temperature dependence (Fig. 4.5(f)). One of the main findings is that above this threshold voltage, the $M(t)$ curve manifested a splitting on the electron accumulation side (plot **c** in Fig. 4.7(a)) with the distinctive in-phase characteristic observed *above* T_{cross} for a small potential window. As the potential window was further increased (plots **d**,**e** in Fig. 4.7(a)), this trend became more and more pronounced. Notably, by setting a negative bias $V_{\mathrm{b}} \approx -1.3\,\mathrm{V}$ as starting point, the magnetic signal became immediately in-phase with the charge modulation (plot **f** in Fig. 4.7(a)). The analysis of the slopes of the $M(Q)$ plots (see Fig. 4.7(b)) indicated that the sign of the magnetic tuning effect was reversed from negative to positive on increasing the external potential towards larger negative values (higher electron

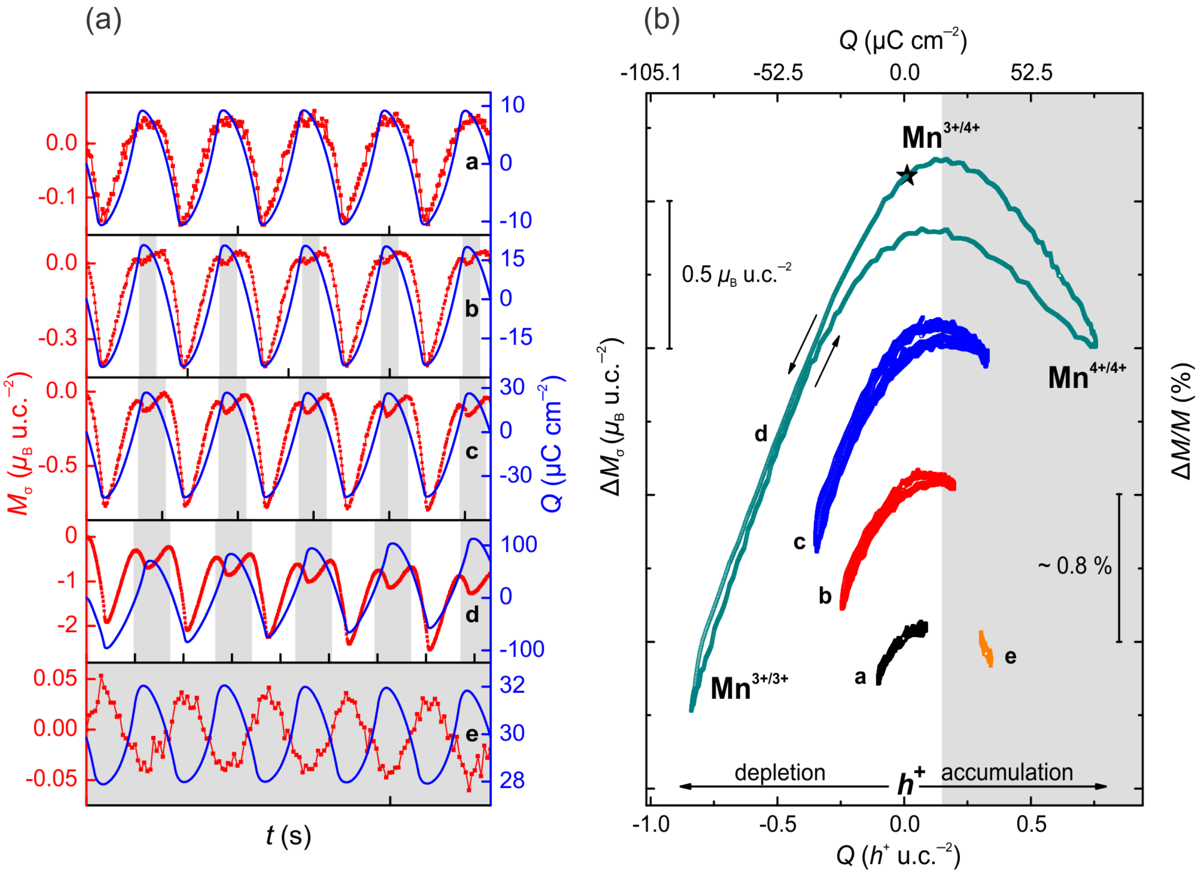

Figure 4.8.: Isothermal charge-dependence ME response at 270 K. (a) Time-resolved magnetic responses upon sequential increase of the surface charge modulation. The expected in-phase response (plot **a**) reveals an in-phase splitting of the $M(t)$ curve (plots **b**-**d**) upon progressive hole doping, like the behavior observed *below* T_{cross} for a small potential window. The application of a bias voltage $V_b \approx +0.9\,\mathrm{V}$ yielded an anti-phase response (plot **e**). Each time step on the abscissa corresponds to 1000 seconds. (b) Behavior of the magnetization as a function of the surface charge doping. The slope of the $M(Q)$ curves provides the ME coupling coefficients α. In (a,b) the white and gray areas qualitatively separate the data with the LSMO magnetization responding to the applied surface charge as above or below T_{cross}, respectively. (Published in *Nat. Comm.* 2017 [337])

doping). The values of α moved between $\alpha \sim -3\,\mu_B/h^+$ and $\alpha \sim +2.2\,\mu_B/h^+$ with respect to a plateau region where a maximum magnetization was reached.

The ME response was also investigated for an analogous isothermal charge-dependence study carried out at a higher temperature of 270 K, that is above T_{cross} (see Fig. 4.8(a)). For potential windows below ~0.8 V, the magnetic signal was in-phase with respect to the surface charge modulation (plot **a** in Fig. 4.8(a)), in agreement with the temperature-dependence study (Fig. 4.5(d)). Beyond this threshold voltage, the $M(t)$ curve manifested a splitting on the hole accumulation side (plot **b** in Fig. 4.8(a)) with the distinctive anti-phase characteristic with respect to $Q(t)$, as observed *below* T_{cross}. As the potential window was further increased (plots **c**,**d** in Fig. 4.8(a)), this behavior became more and more pronounced. Upon application of a positive bias $V_b \approx +0.9\,\mathrm{V}$, the magnetic signal turned out to be directly anti-phase with the interface charge modulation (plot **e** in Fig. 4.8(a)). In this case the slope of the $M(Q)$ plots (see Fig. 4.8(b))

Figure 4.9: Tuning of magnetism in proximity of $T_C \approx 323$ K. A relative variation in LSMO magnetization of 33% is achieved upon reversibly modulating a surface charge density $\Delta Q \approx 200\,\mu\mathrm{C\,cm^{-2}}$. White and gray areas qualitatively separate the data with the LSMO magnetization responding to the surface charge as above or below T_{cross}, respectively. (Published in *Nat. Comm.* 2017 [337])

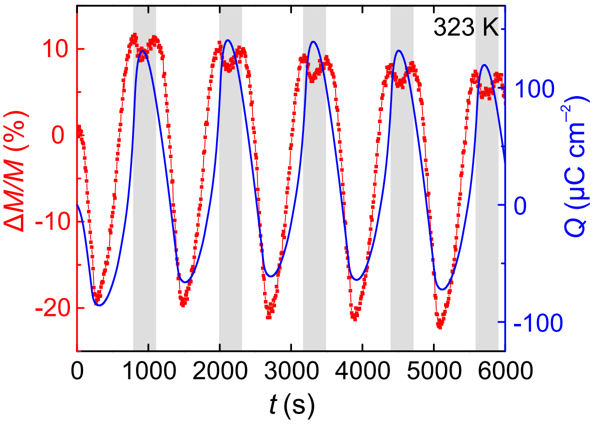

moved from positive to negative on increasing the external voltage towards larger positive values (higher hole doping) with α ranging between $\pm 2\,\mu_B/h^+$.

The isothermal charge-dependence experiments carried out at 220 K and 270 K demonstrate an outstanding flexibility in tuning the LSMO magnetic response. Tuning of magnetism occurs as if the system were toggled above and below T_{cross} by simply adjusting the external voltage. It is interesting to notice that for $T < T_{\text{cross}}$ the standard anti-phase modulation becomes in-phase on increasing the voltage towards negative values (i.e. higher electron doping), whereas for $T > T_{\text{cross}}$ the standard in-phase modulation becomes anti-phase on increasing the voltage towards positive values (i.e. higher hole doping). These facts indicate that not only the total amount of charge, but also the specific kind of charge carriers, either holes or electrons, accumulated at the interface play a main role in determining the ME response.

The results of the ME coupling investigation at the LSMO/IL interface leads to another interesting observation: after testing a variety of temperatures and surface charge modulations in most of the circumstances $|\Delta M/M|$ ratios of only a few per cent are measured. The overall tendency is that even if remarkable amounts of surface charge doping are applied (see Fig. 4.7), the relative variation in magnetic tuning effect becomes smaller and smaller as the temperature is decreased. This corroborates the idea that ME coupling is predominantly an interfacial effect with a penetration depth of the electric field of only about 0.2-0.4 nm, in agreement with other literature reports [137]. Nonetheless, as can also be observed from the trend of Fig. 4.5(c), a considerable enhancement in the magnitude of $|\Delta M/M|$ occurs in proximity of the para/ferromagnetic transition, as also confirmed by prominently larger values of α up to $\approx +6.4\,\mu_B/h^+$. For this reason, the sensitivity of the system to surface charge modulation was further probed at the immediate proximity of T_C. A remarkable magnetic modulation $|\Delta M/M| \approx 33\%$ was reached using a potential window of only $\Delta V \approx 1.8$ V (Fig. 4.9). A reasonable explanation for the increased magnitude of magnetic modulation is possibly related to a deeper penetration depth of the interfacial electric field close to T_C. This is consistent with the results of Dhoot *et al.* [156] who proved that in electrolyte-gated $La_{1-x}Ca_xMnO_3$ films an electrostatic charge doping layer can extend up to 5 nm into the electrode material.

To visualize the full set of experimental data, including the values of potential window, surface charge modulation, capacitance and α attained in the temperature and charge-dependence studies, the reader may refer to Tables A.1, A.2, A.3 in Appendix A.4.

4.5 Interpretation of the interfacial ME coupling

A tentative approach [11, 109, 139] to interpret the interfacial ME phenomena starts with the $La_{1-x}Sr_xMnO_3$ bulk phase diagram [134, 258, 259]. As previously discussed in Section 2.1.1, an increase of Sr content in LSMO translates to doping the system with holes. Considering as starting point the doping region close to Sr ≈ 0.26, each hole (electron) introduced at the LSMO/IL interface via either electrochemical or electrostatic charging results in a shift of T_C towards higher (lower) temperatures. Concurrently (and with the opposite trend), the ground state magnetization ($M_{Mn} = (4-x)\,\mu_B\,\mathrm{u.c.}^{-1}$) decreases (increases) upon hole (electron) doping in accordance with a band filling model where each introduced positive (negative) carrier contributes with a magnetic moment of –(+)1 μ_B due to the removal (addition) of one spin. The competition between these two effects, with the former prevailing in proximity of T_C and the latter at low temperatures, is consistent with the results of the temperature-dependence survey, which evidenced the presence of a crossover point T_{cross} separating the in-phase and anti-phase regimes of $M(t)$ over $Q(t)$.

From a qualitative perspective, this behavior can be illustrated by considering the effect of charge carrier doping on the *virgin* (prior to *in situ* tuning) magnetic FC curve (see Fig. 4.10). In such a simplified scenario (see Fig. 4.10(a)), the original magnetic FC curve ($M(T)$) shifts to higher T_C and concurrently to a reduced low-temperature magnetization when LSMO is doped with holes (vice versa in the case of electron doping). This trend is consistent with the temperature-dependence study performed under a moderate surface charge modulation $\Delta Q \approx 4\,\mu\mathrm{C\,cm}^{-2}$. However, by further increasing the amount of charge carrier doping the shift of the initial magnetic FC curve becomes more and more pronounced.

Fig. 4.10(b) elucidates the results of the isothermal charge-dependence study carried out at 220 K. The black arrow is a guide to the eye: initially for low h^+ depletion the magnetization is enhanced. Afterwards, on progressively increasing h^+ depletion the shift in T_C, which normally does not play a major role at low temperatures, becomes predominant and causes a decrease of the LSMO magnetization. Similar considerations are also valid for the isothermal charge-

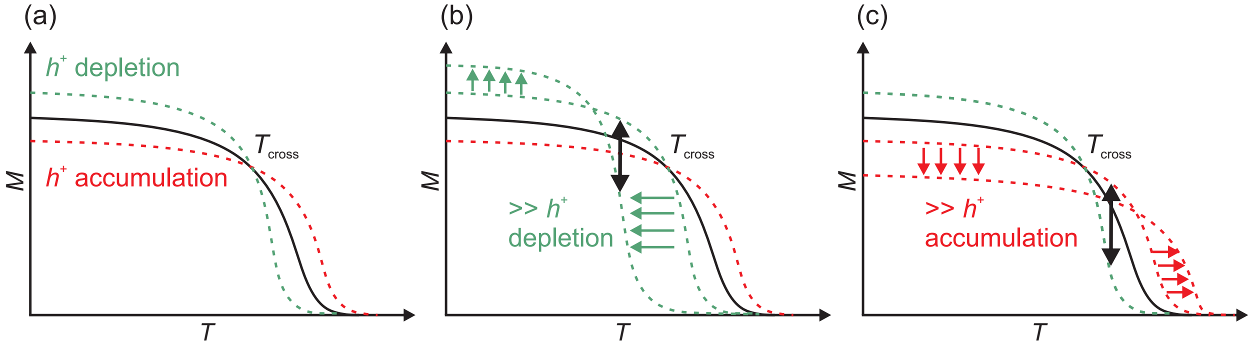

Figure 4.10.: Qualitative model of interfacial ME coupling. The black lines represent the *untuned* magnetic field-cooled (FC) curve of LSMO. The dashed green and red lines represent the magnetic FC curves of LSMO upon h^+ depletion and accumulation. (a-c) depict the behavior for moderate doping, large h^+ depletion and large h^+ accumulation, respectively. The black arrows in (b) and (c) are guides to the eye to follow the magnetic responses encountered at $T = 220\,\mathrm{K} < T_{cross}$ and $T = 270\,\mathrm{K} > T_{cross}$.

dependence study performed at 270 K. In this case, in the beginning of the process of h^+ accumulation the increase in T_C is beneficial for the LSMO magnetization, but beyond a certain threshold the excessive removal of electrons (and so spins) brings about a progressive reduction of magnetization.

There are anyway some non-trivial aspects that constrain the described model to be purely phenomenological[6]. For instance, it should be considered that ME coupling is mainly an interface effect due to the low penetration depth of the electric field of about 0.2-0.4 nm into LSMO[7]. Therefore, the *bulk* untuned $M(T)$ curve can be used to analyze the effect of charge carrier doping only as a first rough approximation, since the majority of affected unit cells are located at the LSMO surface. This point is also confirmed by the small $|\Delta M/M|$ values attained for the charge-dependence experiments carried out at 220 K and 270 K.

Apart from this criticism, the major failure of the phenomenological model comes from the analyses of the quantitative values of α. As previously mentioned, in accordance with a band filling model each introduced/removed carrier brings one (and only one) spin, which is expected to imply $\alpha = \pm 1\,\mu_B/h^+$. However, all the tuning experiments via IL charging revealed *always* values of α considerably beyond unity. This is particularly relevant if we consider the results at the lowest temperature of 220 K, that is far from possible critical effects occurring close to T_C. Indeed, already for a relatively-tiny amount of surface charge doping $\Delta Q \approx 4\,\mu\mathrm{C\,cm^{-2}} \approx 0.04\,h^+\,\mathrm{u.c.}^{-2}$, which signifies a little perturbation of the initial magnetoelectronic configuration of LSMO, the ME coupling coefficient is $\alpha \sim -3\,\mu_B/h^+$ (plot **a** in Fig. 4.7(b)). Interestingly, the latter value is markedly close to the variation of magnetization expected if a single charge carrier were able to completely switch on/off the magnetic moment carried by one LSMO unit cell ($m_{\mathrm{Mn}} \approx 3.7\,\mu_B\,\mathrm{u.c.}^{-1}$).

To capture the essence of a plausible microscopic picture, one should bear in mind the following considerations based on the experimental findings at 220 K.

First, the interfacial nature of the magnetic tuning effect together with charge density modulations of up to $\Delta Q \approx 270\,\mu\mathrm{C\,cm^{-2}}$ (corresponding to about $\pm 1\,h^+\,\mathrm{u.c.}^{-2}$) imply that the LSMO surface magnetoelectronic configuration can be virtually probed across the entire range of possible hole-doped states of the phase diagram. It is known [16] that the interaction between adjacent $\mathrm{Mn}^{3+/4+}$, $\mathrm{Mn}^{3+/3+}$ and $\mathrm{Mn}^{4+/4+}$ ions promotes ferromagnetic (FM), A-type and G-type antiferromagnetic (AF) ground states, respectively. Furthermore, at non-zero temperatures, paramagnetic (PM) states come into play as well.

Second, the absolute value of the ME coupling coefficient is $|\alpha| \sim 3\,\mu_B/h^+$. This is not in line with the $1\,\mu_B/h^+$ predicted by a band filling model, but rather points to the annihilation (creation) of an entire magnetic moment carried by one Mn ion ($M_{\mathrm{Mn}} \approx 3.7\,\mu_B\,\mathrm{u.c.}^{-1}$). Additionally, $|\alpha|$ is nearly constant over a broad range of investigated ΔQ, already when PS contributes to surface charging. This suggests that electrostatic and electrochemical doping, in spite of the different physical and chemical origin, have a similar functional role in the magnetic phase control.

These experimental facts indicate that a microscopic model still coherent with the major phenomenological features is conceivable only by incorporating a magnetoelectronic *phase separation* phenomenon [211, 273, 274] at the LSMO surface.

---

[6] Other works [11, 109, 139] already pointed out the inadequacy of such model in providing a consistent quantitative picture of the interfacial ME phenomenon.

[7] However, experimental evidence reveals that the penetration depth of the electric field may extend up to a few nm in proximity of T_C (see Ref. [156] and later discussion).

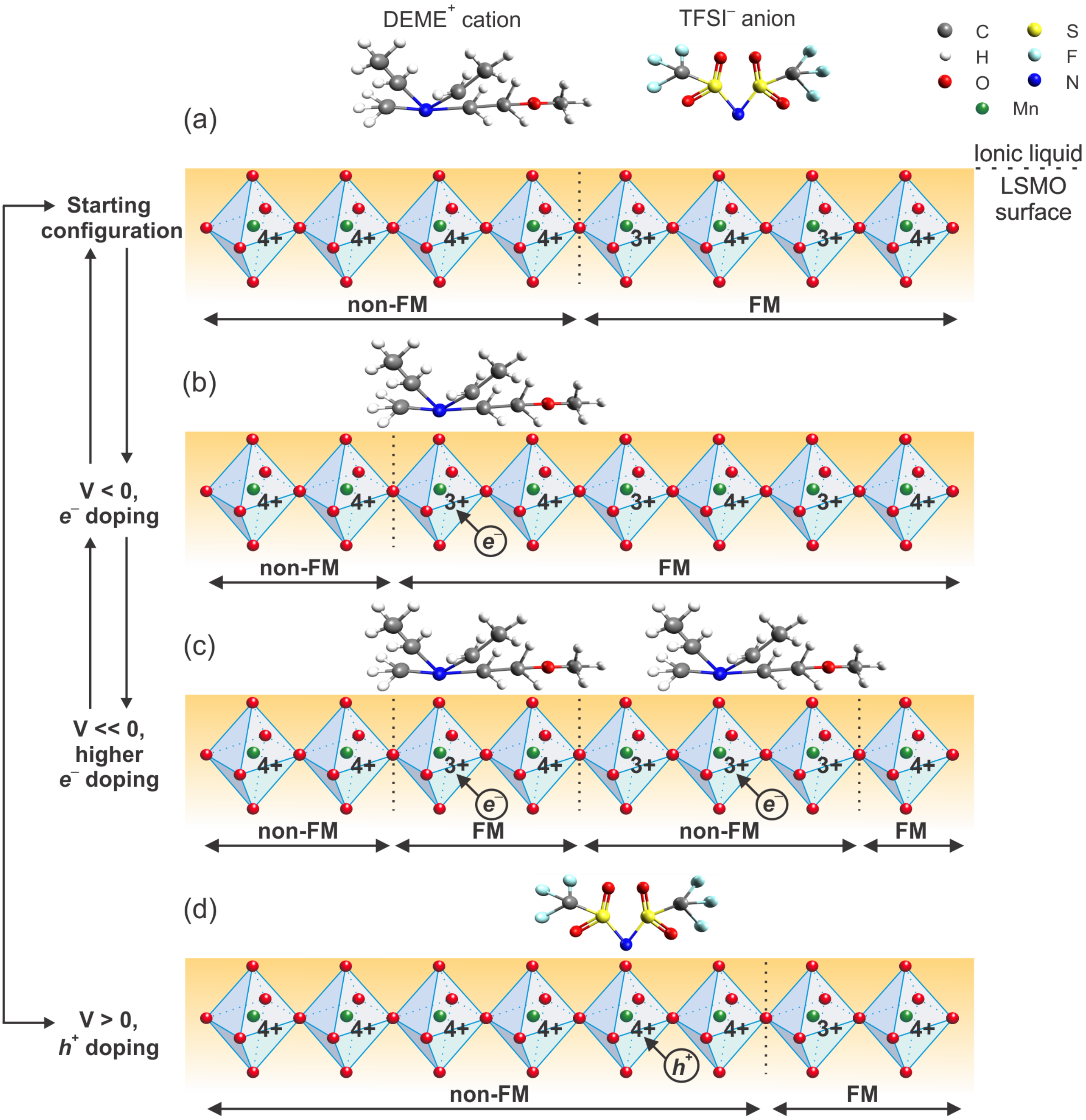

Figure 4.11.: Mechanism of electric field tuning of magnetoelectronic phase separation at the LSMO/IL interface. For the sake of clarity, not the entire perovskite unit cell of LSMO, but only the oxygen octahedron containing one Mn ion is shown. The sketches should be read together with the trend of the $M(Q)$ curves in Fig. 4.7(b). (a) Initial surface magnetoelectronic configuration of LSMO with two distinguished FM and non-FM domains. (b) Expansion of the FM domain upon electron doping (optimization of $\mathrm{Mn}^{3+/4+}$ balance). (c) Shrinkage of the FM domain upon further electron doping (increase in $\mathrm{Mn}^{3+/3+}$ balance). (d) Shrinkage of the FM domain upon hole doping (increase in $\mathrm{Mn}^{4+/4+}$ balance). (Published in *Nat. Comm.* 2017 [337])

In a simplified scenario (see Fig. 4.11), the local electric field at the electrode/IL interface induces the accumulation of charge carriers at the LSMO terminating layers. The consequent change in oxidation state of the Mn ions promotes either the expansion or shrinkage of FM and non-FM (PM or AF) domains, at the expense of each other. Considering the curves in Fig. 4.7(b), the initial increase in magnetization upon electron doping can be explained as a gradual optimization of the $\mathrm{Mn}^{3+/4+}$ ratio, hence fostering the growth of FM coupled domains (Fig. 4.11(b)). During sweeping to higher electron concentrations, the oxidation state of the surface manganese ions progressively shifts towards a $\mathrm{Mn}^{3+/3+}$ balance. Either AF or PM ordering is favored (Fig. 4.11(c)), thus decreasing the overall magnetization. By reversing the voltage sign, the magnetization recovers up to a maximum point due to the restored $\mathrm{Mn}^{3+/4+}$ interactions. By sweeping further along the hole accumulation side, the amount of $\mathrm{Mn}^{4+/4+}$ domains increases (Fig. 4.11(d)). Owing to the expansion of non-FM states, a decrease in the total magnetization is again observed.

The proposed microscopic model of electric field tuning of magnetoelectronic phase separation becomes more complex at higher temperatures when LSMO is far from a robust metallic/ferromagnetic state. As previously mentioned, close to T_C large values of α of up to $+6.4\ \mu_B/h^+$ (i.e. beyond the $+3.7\ \mu_B/h^+$ expected for switching on/off an entire LSMO unit cell), and magnetic modulations $|\Delta M/M|$ of up to $\approx 33\%$ are reached. Therefore, close to the para/ferromagnetic transition it is reasonable to envision that the phenomenon of expansion/shrinkage of FM and non-FM domains occur deeper into the LSMO film and not only at its surface.

4.6 Before and after ME tuning process: effect on LSMO characteristics

The ME measurements described so far evidence an outstanding level of reversibility regarding both magnetic and surface charge responses. As a consequence, no remarkable changes of the LSMO structural features are to be expected. Since ME coupling origins at the LSMO/IL interface, it is interesting to investigate whether the tuning process brings about any appreciable

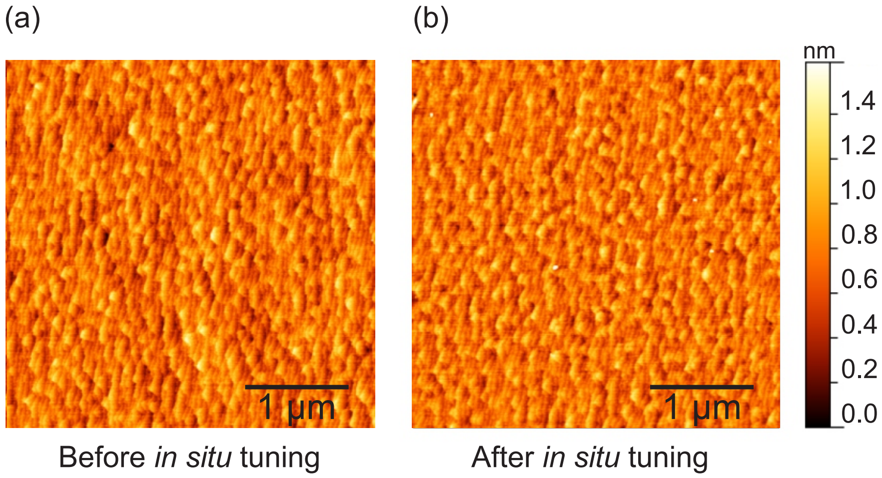

Before *in situ* tuning

After *in situ* tuning

Figure 4.12.: AFM micrographs of LSMO films before (a) and after (b) *in situ* ME tuning experiments performed under reversible conditions. In both pictures the RMS roughness is around 0.2 nm. (Published in *Nat. Comm.* 2017 [337])

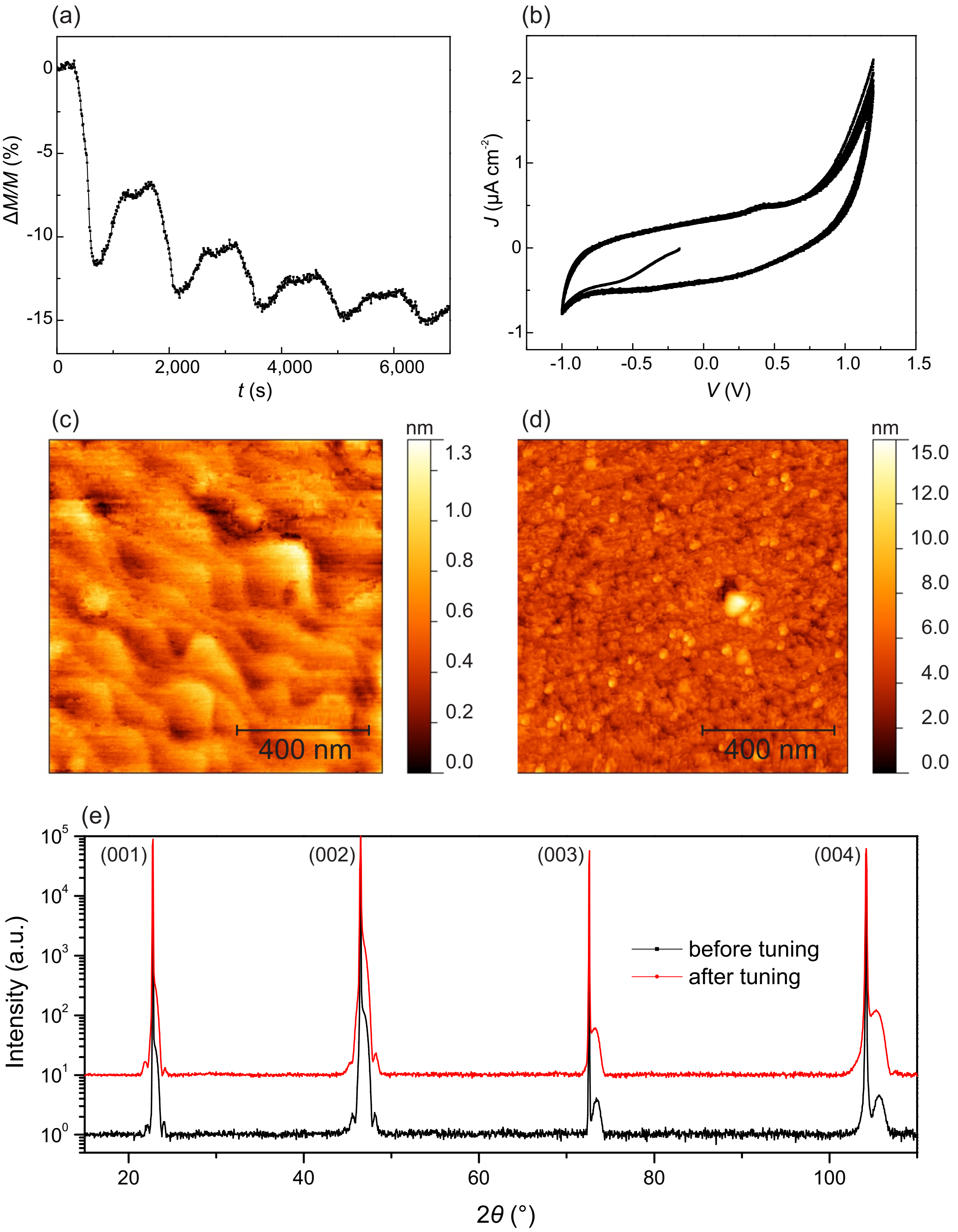

Figure 4.13.: Effect of irreversible interfacial charging processes on the LSMO characteristics. (a) Systematic decrease and loss of reversibility in the time-resolved magnetic response. (b) Current density-voltage characteristic in presence of pronounced interfacial electrochemical reactions. (c) Atomic force micrograph taken before *in situ* tuning experiment. The RMS roughness is 0.15 nm. (d) Atomic force micrograph taken after *in situ* tuning. The RMS roughness increases to 1.5 nm. (e) X-ray diffractograms of (00*l*) symmetric reflections before (in black) and after (in red) *in situ* ME tuning.

change in LSMO surface morphology[8]. Fig. 4.12(a) and (b) show atomic force micrographs of a representative LSMO film before and after performing more than 1000 CV cycles under different temperatures and applied voltages. In both cases, LSMO features an atomically smooth surface with one or half unit cell steps, thus demonstrating the non-destructive nature of EDL and PS charging.

In general, in order to achieve a high level of reversibility, the applied voltage was carefully adjusted at each temperature of interest. The procedure established to carry out ME coupling studies consisted in progressively expanding the potential window while monitoring magnetic and charging current signals.

Fig. 4.13 shows the consequences of application of exceedingly large voltage values. The onset of irreversible processes can be recognized from the shape of $M(t)$ and $J(V)$ characteristics. Irreversible electrochemical reactions cause a substantial loss of overall magnetization and are related to the presence of pronounced and increasingly-irreversible peaks in the $J(V)$ curves (see Fig. 4.13(a,b)). Regarding the structural features, a prominent roughening of the surface morphology occurs (see Fig. 4.13(c,d)), whereas most of the bulk integrity of the electrode remains unaffected, as confirmed by the absence of remarkable variations in the X-ray diffraction patterns (see Fig. 4.13(e)). Indeed, LSMO is still single-phase and epitaxial onto STO with well-defined *Laue* fringes, although a substantial expansion of the out-of-plane lattice parameter from $c_{\mathrm{LSMO}} \approx 3.86\,\text{Å}$ to $\approx 3.875\,\text{Å}$, possibly related to an increase of oxygen deficiencies, also happens.

4.7 Summary

In this chapter ME coupling at the interface between a magnetic thin film of LSMO ($\approx$ 13 nm) and an IL electrolyte (DEME-TFSI) was studied by means of *in situ* time-resolved SQUID-CV measurements. The analysis of the interfacial charging/discharging processes led to the conclusion that the LSMO/IL system behaves as a hybrid supercapacitor, where EDL capacitance ($C \approx 10\,\mu\mathrm{F\,cm^{-2}}$) is gradually substituted with surface pseudocapacitive reactions (C up to $\approx 180\,\mu\mathrm{F\,cm^{-2}}$) upon progressive expansion of the applied potential window. Voltage-induced charge carrier doping was exploited to modify the oxidation state of the Mn ions and thus the magnetic exchange interactions in LSMO. A temperature-dependence study carried out from above T_C down to 220 K using a constant charge carrier modulation $\Delta Q \approx 4\,\mu\mathrm{C\,cm^{-2}}$ revealed the presence of a characteristic threshold temperature $T_{\mathrm{cross}} \approx 258\,\mathrm{K}$. Above (below) T_{cross} the magnetic and surface charge modulations are in-phase (anti-phase) with respect to each other. Isothermal charge-dependence experiments performed below and above T_{cross} demonstrated that it is possible to freely control the sign of the magnetic tuning effect by appropriately adjusting the external voltage. Although ME coupling is predominantly an interfacial effect, in proximity of the para/ferromagnetic transition temperature a remarkable magnetic modulation $|\Delta M/M| \approx 33\%$ was attained thanks to an enhanced penetration depth of the electric field. The results of ME coupling have been qualitatively discussed on the basis of the bulk LSMO phase diagram. Values of ME coupling coefficient $\alpha = \Delta M/\Delta Q$ considerably off from unity indicated that a classical band filling model is inadequate to quantitatively describe the ME coupling phenomenon. A more consistent microscopic scenario was proposed in the framework of electric field tuning

---

[8] After *in situ* ME experiments the IL has been removed from the LSMO surface by ultrasonic cleaning for 10 min in methanol and 5 min in isopropanol.

of magnetoelectronic phase separation. Finally, the effect of *in situ* tuning experiments on the LSMO characteristics was discussed. In general, a high level of reversibility with absence of any appreciable modification of the starting LSMO films was achieved upon precise and careful regulation of the external voltage.

In the next chapter the attention is brought to the analysis of the ME effect in presence of ultrathin films of LSMO. By enhancing the surface-to-volume ratio, also the magnitude of the voltage-driven magnetic tuning effect is expected to increase.

5 Voltage-driven on/off switching of ferromagnetism in ultrathin LSMO films

Selected parts of this chapter are also published in [343] within the framework of this thesis. The respective paragraphs – with minor adjustments included – are indicated by a vertical gray bar at the inner page margin[1].

In this chapter we show that by optimizing the surface-to-volume of LSMO/ionic liquid (IL) devices, it is possible to completely suppress and restore the LSMO magnetization via IL gating. Apart from the magnitude of the magnetic tuning effect, other technologically-relevant parameters, including the cycling stability, the energy consumption and the device switching speed, are thoroughly discussed.

5.1 Background

To date, the realization of giant ME effects with either reversal or on/off switching of magnetism was successfully attained in some ME systems [8]. For instance, this was accomplished by using an external voltage to modify the strain [9, 14], charge [4, 10, 11] or chemical state [15, 144, 223, 224] of a magnetic component. Although a large magnetic on/off ratio is certainly appealing, a real working device must also fulfill other fundamental characteristics such as an appropriate reversibility, switching speed, operating voltage and working temperature.

Magnetic supercapacitors (SCs) have the potential to satisfy such requirements thanks to their innate ability to accumulate/deplete high amounts of charge in a fast and reversible manner at low energy cost.

In the previous chapter it was shown that a maximum variation of magnetization $|\Delta M/M| \approx 33\%$ could be attained in LSMO films with a thickness of 13 nm. Here, the strategy to increase the magnitude of the magnetic tuning effect consists in enhancing the surface-to-volume ratio of the LSMO/ionic liquid devices by decreasing the LSMO thickness down to 3 nm. The performance of the ME devices is critically discussed in reference to recent advances in the area of ME coupling.

5.2 Sample preparation and experimental details

Ultrathin films of LSMO with an optimized thickness of ≈ 3 nm and a surface area of ≈ 0.4 cm^2 were epitaxially grown on (001)-oriented $SrTiO_3$ (STO) substrates by Large-Distance Magnetron Sputtering. A thickness value of around 3 nm was chosen because it concurrently allowed to increase the surface-to-volume ratio and to preserve the Curie temperature T_C of LSMO above the freezing point of the IL. LSMO films thinner than 3 nm were not tested for *in situ* ME experiments, because the reduced T_C was too close (or below) with respect to the DEME-TFSI

---

[1] Reprinted with permission from [343]. ©2017, John Wiley and Sons.

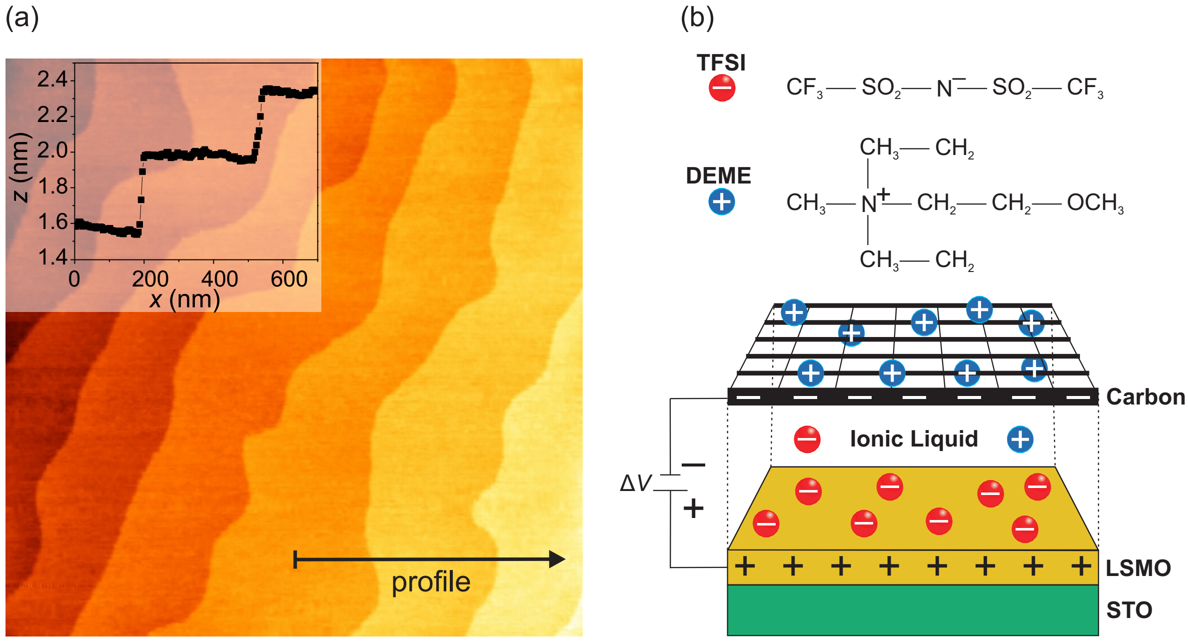

Figure 5.1.: (a) Atomic force micrograph of an ultrathin LSMO film (≈ 3 nm) featuring atomically smooth terraces separated by one (≈ 0.4 nm) LSMO unit cell steps (see height-profile in the inset). The root-mean-square roughness is below 0.1 nm. (b) Structural model of the DEME$^+$ and TFSI$^-$ ions (top) and schematic of the investigated ME devices (bottom). An ultrathin LSMO film grown on STO substrate and a high surface area carbon cloth serve as working and counter electrodes, respectively. A DEME-TFSI ionic liquid electrolyte is employed as charging/discharging medium. (Published in [343]. ©2017, John Wiley and Sons.)

glass transition. Below the glass transition temperature the ions are in a frozen state and so reversible charging/discharging processes are impossible.

The surface morphology of ultrathin LSMO films was analyzed by Atomic Force Microscopy (AFM), which showed flat and wide atomic terraces separated by one LSMO unit cell steps (see Fig. 5.1(a)). In general, a slight improvement in surface quality was attained in ultrathin films as compared to the thicker films described in Section 3.3.3.

The experimental setup for *in situ* ME measurements, which couples Superconducting Quantum Interference Device (SQUID) magnetometry and Cyclic Voltammetry (CV), is analogous to the one previously described (see Section 4). For the sake of clarity, a scheme of the implemented ME tuning cell, comprising a LSMO ultrathin film, a high-surface-area carbon cloth and a DEME-TFSI ionic liquid, is depicted in Fig. 5.1(b). Unless differently specified, the definitions introduced in the previous chapter (such as C and $\Delta M/M$) will be retained in the following.

5.3 Magnetoelectric coupling in case of an enhanced surface-to-volume ratio

At the beginning, a temperature dependent magnetic field-cooled (FC) measurement (see below in Fig. 5.4(a)), performed prior to *in situ* tuning experiments, revealed a $T_C \approx 246$ K. As already mentioned (see Section 3.3.4), the weakened magnetic properties in ultrathin films, as compared

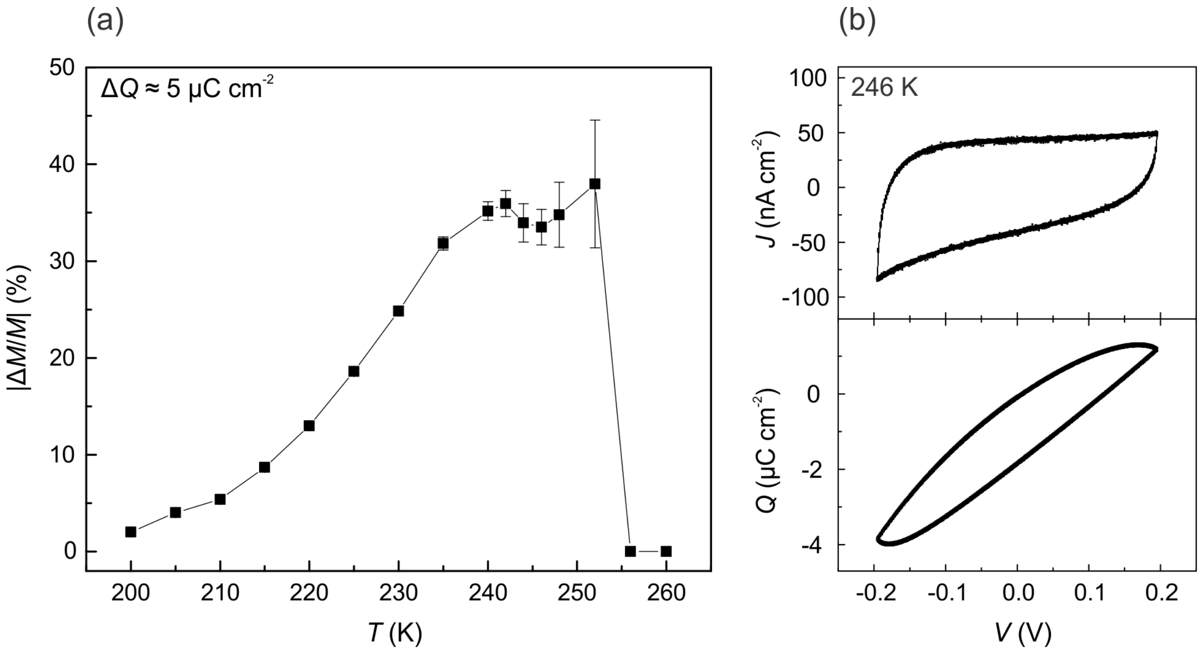

Figure 5.2.: Temperature dependence ME study in ultrathin LSMO films. (a) Magnitude of LSMO magnetic response as a function of temperature by application of a constant surface charge modulation $\Delta Q \approx 5\,\mu\mathrm{C\,cm}^{-2}$. Where not visible, the error bars are smaller than the symbol size. (b) Current density (top panel) and integrated surface charge (bottom panel) at 246 K for a potential window $\Delta V \approx 400\,\mathrm{mV}$. The curves represent 90 consecutive CV cycles. The voltage ramp rate is 3 mV s^{-1}. (Published in [343]. ©2017, John Wiley and Sons.)

to bulk LSMO, are commonly attributed to the presence of a magnetic dead layer (MDL) at the film/substrate interface[2].

The initial *in situ* ME experiments consisted of a temperature-dependence study in the 260 - 200 K temperature range, that is from above T_C down to the glass transition of the DEME-TFSI ionic liquid (see Fig. 5.2(a)). The surface charge density modulation was set to $\Delta Q \approx 5\,\mu\mathrm{C\,cm}^{-2}$ in order to probe the LSMO magnetic response in presence of a relatively-small amount of charge carrier doping. The surface charge modulation was obtained by the application of a potential window $\Delta V \approx 0.4\mathrm{V}$ with a voltage ramp rate of 3 mV s^{-1}; the only two exceptions occurred at 205 K and 200 K where potential windows of 700 mV and 900 mV were applied, respectively. The reason for the necessary increase of voltage is ascribed to the sluggish motion of the DEME-TFSI ions, and consequent reduced capacitance, in the very proximity of the glass transition of the IL.

As expected, above the Curie point, where LSMO is in the paramagnetic phase, no magnetic tuning effect was detectable with the SQUID magnetometer. At about 253 K a steep response in magnetic modulation was observed. The signal became less and less noisy as the temperature was decreased and ferromagnetism became more pronounced. An almost constant $|\Delta M/M| \approx 35\%$ remained unchanged until a temperature of 240 K. Below this threshold, the magnetic tuning effect systematically decreased until virtually vanishing in proximity of 200 K. The reduction in

---

[2] The possible contribution of a MDL was not subtracted from the results of the experiments reported below, because charge carrier doping may affect the MDL thickness and so also the portion of the magnetic active volume. Therefore, the reported values of voltage-induced magnetic response are rather conservative as they were calculated considering the whole LSMO volume.

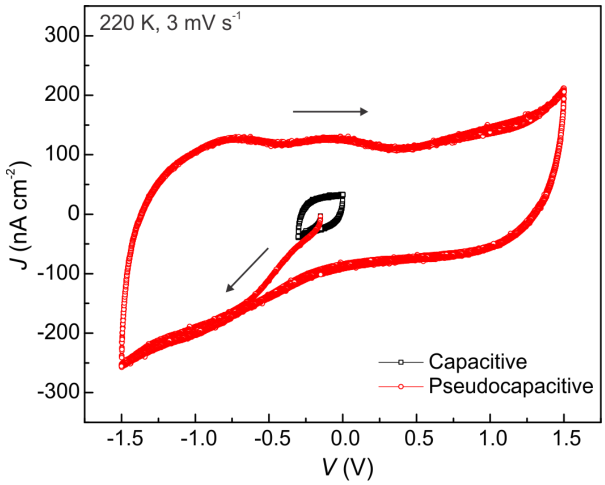

Figure 5.3: Capacitive and pseudocapacitive charging regimes. $J(V)$ characteristics upon expansion of the potential window. The nearly-ideal rectangular shape for ΔV = 0.4 V (black curve) represents the typical feature of a standard EDL capacitor. The slight deviation from a rectangular shape and the remarkable increase in current density for ΔV = 3 V (red curve) indicate the presence of pseudocapacitive charging. The calculated values of capacitance are $\approx 12\,\mu\mathrm{F\,cm^{-2}}$ and $\approx 45\,\mu\mathrm{F\,cm^{-2}}$ for the black and red curves, respectively. Both curves represent 7 consecutive CV cycles. The voltage ramp rate is 3 mV $\mathrm{s^{-1}}$. (Published in [343]. ©2017, JOHN WILEY AND SONS.)

magnetic response at low temperatures is consistent with the trend observed in thicker LSMO films described in Section 4.4, though in this case no magnetic crossover temperature T_{cross} - with the typical reversed sign of the magnetic tuning effect - was identified. This is probably to be ascribed to the combined effect of having T_{C} not far from the lower temperature limit of 200 K and a rather smeared out para-ferromagnetic transition (see also comments in Section 4.4).

Throughout the whole investigated temperature range the current density-voltage $J(V)$ characteristics of the LSMO/IL devices revealed a rectangular-like shape. Fig. 5.2(b) shows the current density (top panel) and integrated surface charge (bottom panel) as a function of the applied voltage for a typical experiment performed at 246 K. The curves correspond to 90 consecutive charging/discharging cycles: the nearly-perfect overlapping on repetitive cycling corroborates the observation that the process of LSMO tuning is highly reversible. The corresponding calculated capacitance of $\approx 12\,\mu\mathrm{F\,cm^{-2}}$ is consistent with the values attained in thicker LSMO films (see Section 4.3).

An important outcome of the temperature-dependence survey is the enhanced sensitivity of ultrathin films to the amount of surface charge induced with the IL. Indeed, a magnetic tuning effect of up to $|\Delta M/M| \approx 35\%$ was reached in ultrathin ($\approx$ 3 nm) films using a relatively-small $\Delta Q \approx 5\,\mu\mathrm{C\,cm^{-2}}$, whereas in case of thicker films ($\approx$ 13 nm) much larger surface charge densities ($\Delta Q \approx 200\,\mu\mathrm{C\,cm^{-2}}$) were required.

Afterwards, the effect of larger amount of surface charge doping was studied at various temperatures of interest.

On enlarging the applied potential window the $J(V)$ curves manifested a progressive increase in current density, and thus also in capacitance, with a slight deviation from the conventional rectangular-shape (see Fig. 5.3). For instance a CV experiment carried out at 220 K using ΔV = 3.0 V led to a capacitance of up to $\approx 45\,\mu\mathrm{F\,cm^{-2}}$; at the same time a high level of reversibility on repetitive cycling was still maintained. These features denote the presence of redox pseudocapacitive reactions at the LSMO/IL interface [178, 179]. These findings support the conclusion that the LSMO/IL devices behave as exemplary hybrid supercapacitors, where both EDL capacitance and pseudocapacitance take part in the interfacial charging/discharging processes.

The combination of large surface charge density modulations and high surface-to-volume ratio had a huge impact on the LSMO magnetic response. Fig. 5.4(b) presents the results attained at 235 K for $\Delta Q \approx 52\,\mu\mathrm{C\,cm}^{-2}$ under application of a potential window of 1.7 V (with -0.45 < V < 1.25 V).

The magnetization increases on electron doping and decreases on hole doping with a giant peak-to-peak magnetic tuning effect[3]. It is worth noticing that the $M(t)$ curve features a sharp peak on the electron accumulation side, whereas it is almost plateau-like when zero magnetization is approached at the highest hole doping concentration. Notably, the ferromagnetic signal of the ultrathin LSMO film is reversibly suppressed and restored with an overall variation in magnetization $\Delta M \approx 0.13\,\mu_B\,\mathrm{u.c.}^{-1}(\approx 21\,\mathrm{emu\,cm}^{-3})$ and an on/off ratio $|\Delta M/M| \approx 128\%$. Considering that the para-ferromagnetic transition of LSMO is at ≈ 246 K (see Fig. 5.4(a)), the resulting shift of T_C upon charging is about 14 K. Since in proximity of T_C magnetism is fully switched on and off, the interfacial electric field is expected to extend through the whole LSMO thickness[4] of 3 nm. This is consistent with the electric field penetration depth of up to 5 nm reported on electrolyte gated $La_{1-x}Ca_xMnO_3$ films [156].

An analogous experiment was carried out at the lower temperature of 220 K (see Fig. 5.4(c)) using a surface charge density modulation of about 120 $\mu\mathrm{C\,cm}^{-2}$ upon application of $\Delta V = 3.0$ V (with -1.5 < V < 1.5 V). In this case the maximum magnetic on/off ratio was ≈ 98.5% with $\Delta M \approx 0.34\,\mu_B\,\mathrm{u.c.}^{-1}$ ($\approx 54\,\mathrm{emu\,cm}^{-3}$). Furthermore, it is interesting to notice that a supplementary effect was achieved comparing to the steady *anti-phase* behavior between $M(t)$ and $Q(t)$ observed at 235 K. In fact, at 220 K the potential window has been deliberately enlarged towards bigger negative voltages in order to produce higher electron doping concentrations. This resulted in an steep variation of the sign of the magnetic modulation with $M(t)$ and $Q(t)$ behaving in-phase on the electron accumulation branch. These findings point out that not only the magnitude but also the sign of the ME coupling can be manipulated by a proper regulation of the external voltage.

Interestingly, although no magnetic crossover temperature was previously observed in the temperature-dependence study, its presence and its effects on the sign of ME effect evidently take effect when large carrier doping concentrations are induced (compare with the results of Section 4.4).

In order to evaluate the strength of the interfacial ME effect, the ME coupling coefficient[5] was defined as $\alpha = \Delta M/\Delta V$. The new formulation of α, which differs from the definition introduced

---

[3] The reader may notice that here $M(t)$ and $Q(t)$ are in anti-phase close to T_C, whereas in-phase behavior was observed in thicker LSMO films (see Section 4). It has been verified that the effect occurs systematically on different ultrathin samples and is not due to an error in the experimental setup, such as swapping of voltage polarities. A possible explanation of the reversed sign of magnetic tuning may be ascribed to a slight enrichment in Sr content within the 0.3 - 0.55 range in ultrathin films, as may occur in the proximity of the LSMO/STO interface [296, 323, 329, 330] (consider also the LSMO bulk phase diagram in Section 2.1.1). Nonetheless, the influence of other possible effects related to the peculiar magnetic properties of ultrathin films, such as the presence of an interfacial dead layer, cannot be ruled out as well (see also comments in Section 3.3.4).

[4] Similar *in situ* tuning experiments were also performed on LSMO films with a thickness of ≈ 4 nm, which gave a maximum magnetic modulation $|\Delta M/M| \approx 60\%$ (see also Appendix A.5).

[5] Notice that the conversion factor between different magnetic units is 1 emu $\mathrm{cm}^{-3} = 10^3\ \mathrm{A\,m}^{-1} = 4\,\pi$ Oe.

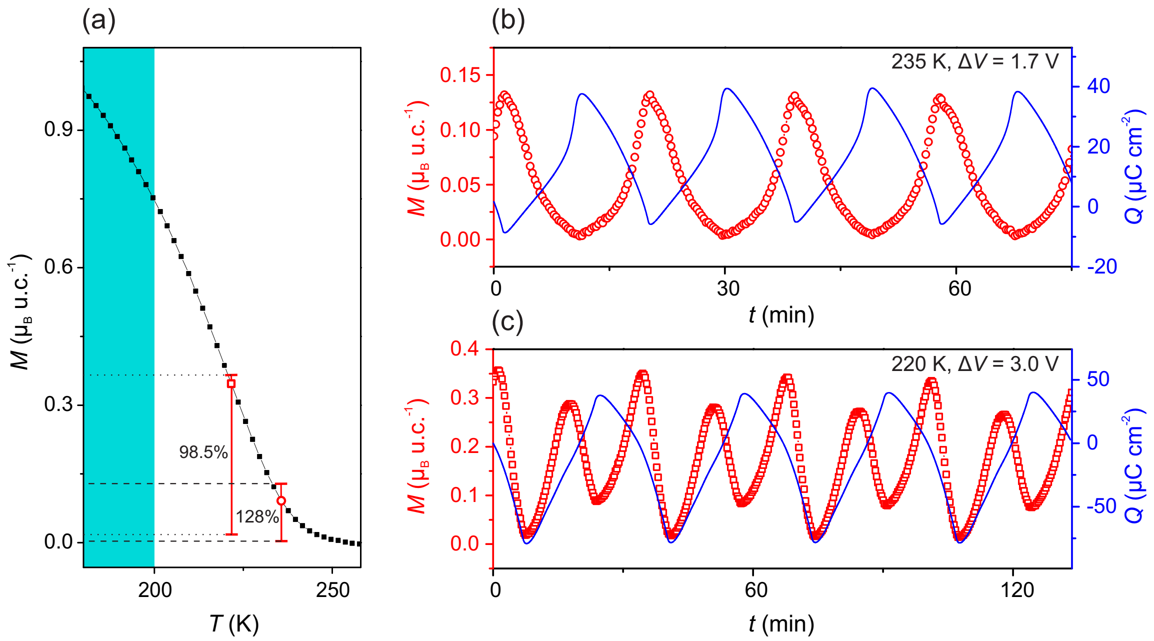

Figure 5.4.: On/off switching of ferromagnetism in ultrathin LSMO films (3 nm). (a) LSMO magnetization as a function of temperature measured before *in situ* ME tuning experiments. The red lines delimit the range of magnetization values measured during surface charging with the IL in the experiments shown in (b) and (c), where relative changes in LSMO magnetization $|\Delta M/M| \approx 128\%$ and $\approx 98.5\%$ were found at 235 K and 220 K, respectively. The colored area below 200 K defines the glass phase of the IL. (b,c) Time-resolved magnetic response during surface charging by application of a potential window of 1.7 V at 235 K (b) and 3.0 V at 220 K (c). In (b) $M(t)$ and $Q(t)$ are in anti-phase conditions. In (c) the in-phase splitting of the magnetic response indicates that the sign of the ME effect is reversed at large electron doping concentrations. The voltage ramp rate is 3 mV s^{-1} in both (b) and (c). (Published in [343]. ©2017, John Wiley and Sons.)

in the previous chapter (see Section 4.4), directly relates the overall change in magnetization to the applied external voltage, thus permitting an easier comparison with other ME systems[6].

The aforementioned experiments at 235 K and 220 K provide $\alpha \approx 155$ Oe V^{-1} and 226 Oe V^{-1}, respectively. These values of ME coupling coefficient are higher than the record of 146 Oe V^{-1} recently reported on ultrathin Co films gated with IL [208]. Furthermore, they exceed some of the best results reported in the literature on all-solid-state MEs. For instance, Cherifi *et al.* [14] by means of voltage-induced strain achieved an impressive change in magnetization of $\approx 550\,\mathrm{emu\,cm^{-3}}$ (with $\approx 70\,\mathrm{emu\,cm^{-3}}$ of reversible contribution) in FeRh thin films grown on $BaTiO_3$ substrate. Nonetheless, as a drawback, relatively-large voltages of ± 21 V were required, hence resulting in $\alpha \approx 164\,\mathrm{Oe\,V^{-1}}$ (and $21\,\mathrm{Oe\,V^{-1}}$ of reversible contribution). Following the same arguments, Molegraaf *et al.* [11] reached $\alpha \approx 14$ Oe V^{-1} (with $\Delta M \approx 22\,\mathrm{emu\,cm^{-3}}$ for ± 10 V) via electrostatic charge doping in LSMO/$Pb_{1-x}Zr_xTiO_3$ heterostructures, whereas Tokunaga *et al.* attained $\alpha \approx 2.1$ Oe V^{-1} (with $\Delta M \approx 58\,\mathrm{emu\,cm^{-3}}$ for ± 175 V) in single-phase multiferroics of $Dy_{0.70}Tb_{0.30}FeO_3$ (DTFO). In Table 5.1 the values of ΔM, ΔV and α are compared for some

---

[6] Further details about the choice of such definition of ME coupling coefficient can be found in the discussion of Appendix A.1.1.

Table 5.1.: Comparison of ME effect in all-solid-state and solid/liquid ME systems. Respective references are reported in square brackets.

	All-solid-state			**Solid/liquid**		
	FeRh/BTO [14]	LSMO/PZT [11]	DTFO [68]	Co/IL [208]	LSMO/IL [343]	Fe_2O_3/Li-el [223]
ΔM (emu cm^{-3})	70	32	58	17	54	31
ΔV (V)	42	20	350	1.5	3	3
$\alpha = \Delta M/\Delta V$ (Oe V^{-1})	21	14	2.1	146	226	130

all-solid-state and solid-liquid ME systems. In general, it results that the former category reaches slightly higher values of ΔM, but, owing to the necessary application of larger voltages, better values of ME coupling coefficient $\alpha = \Delta M/\Delta V$ are attained via solid/liquid approach.

The low-voltages required to charge/discharge the LSMO/IL supercapacitor do not only favor high values of α, but are also beneficial in terms of energy consumption. The ME efficiency can be computed considering the energy per unit area spent for every magnetic switching event (E $= \Delta Q \cdot \Delta V$), corresponding to the work done by the external voltage for charging the LSMO supercapacitor. On/off switching of ferromagnetism in the experiments performed at 235 K and 220 K required an energy cost of 90 μJ cm^{-2} and 360 μJ cm^{-2}, respectively. The values are remarkably lower than in several all-solid-state ME composites [4, 9–11, 13]. For instance, Heron *et al.* [13] estimated an energy loss of about 480 μJ cm^{-2} for switching ME spin-valve devices.

The reversibility and robustness of ME coupling was probed by performing more than 2000 CV cycles at different temperatures and applied potential windows. Fig. 5.5(a-c) demonstrates an excellent ME cycling stability with virtually zero losses and low noise fluctuations. As a comparison, it has been reported that metal/oxide composite MEs are prone to device failure already after a few switching cycles due to voltage-driven ionic diffusion at the interface [13]. In other cases, the gigantic ME effects shown in strain-mediated ME devices undergo persistent effects which hamper deterministic switching [9] or feature predominant irreversible contributions [14].

The ME switching speed of the LSMO/IL devices was put to test by systematically increasing the voltage ramp rate from 3 to 300 mV s^{-1} at 235 K. Since the measurement time of a SQUID magnetometer is of the order of a few seconds, it was not possible to concurrently follow the surface charge with magnetization measurements at high voltage scan rates. Nonetheless, it is known [11, 109, 337] that the magnetic response is directly related to the amount of surface charge accumulated at the interface. Thus, the evolution of the capacitance ($C = \Delta Q/\Delta V$) as a function of the voltage ramp rate ($a = dV/dt$) provides direct insights into the ME performance in terms of the device speed.

The current density ($J = C \cdot a$), monitored at different voltage scan rates for two distinguished potential windows of 0.3 and 1.4 V (see Fig. 5.6(a,b)), displayed the typical charging/discharging

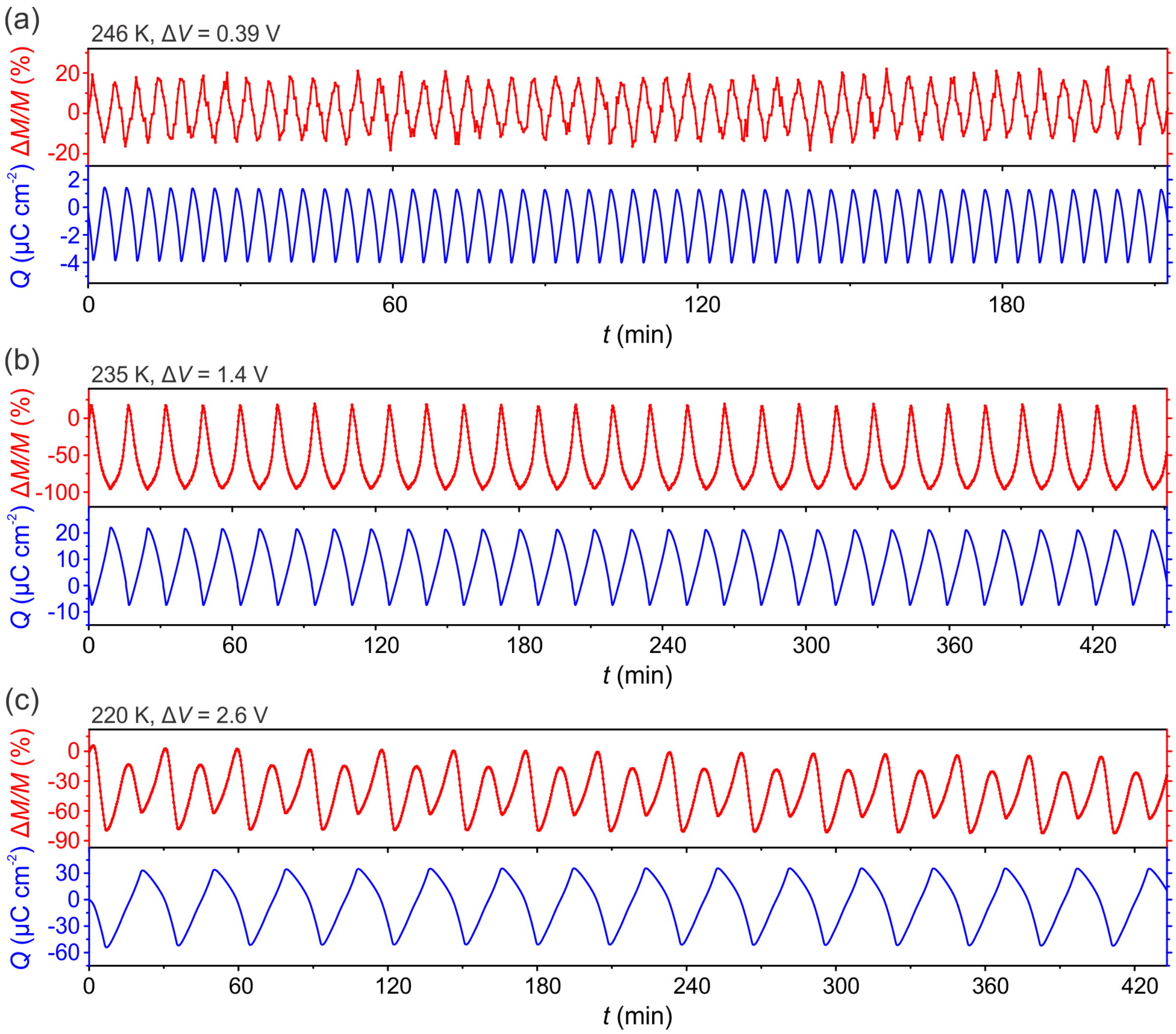

Figure 5.5.: Reversible control of LSMO magnetization at different temperatures and applied voltages. (a-c) Time-resolved magnetic response and surface charge density modulation obtained at T = 246 K, 235 K and 220 K on repetitive cycling of the external voltage using ΔV = 0.39 V, 1.4 V, and 2.6 V, respectively. The voltage ramp rate is 3 mV s^{-1}. (Published in [343]. ©2017, John Wiley and Sons.)

characteristics of an EDL capacitor [178]. Nonetheless, interestingly when the potential window was increased from 0.3 to 1.4 V the capacitance did not follow the decreasing trend expected for EDL capacitors [318] but almost doubled from $\approx 12\,\mu\mathrm{F\,cm^{-2}}$ to $\approx 21\,\mu\mathrm{F\,cm^{-2}}$ (see Fig. 5.6(c)). These results further support the idea that on increase of the external voltage surface pseudocapacitive redox reactions contribute to charge carrier doping of LSMO [337].

For both potential windows C follows a very similar trend with only a slight systematic decrease at high voltage ramp rates associated with incomplete charging of the electrodes [157]. Since C does not significantly change when the voltage ramp rate is spanned over two orders of magnitude, the LSMO magnetization is expected to respond accordingly fast. The combination of the results in Fig. 5.6(c) and Fig. 5.5(b) for ΔV = 1.4 V yields a maximum ME switching speed of about 0.1 Hz, that is so far the highest achieved in solid/liquid MEs. The switching time is

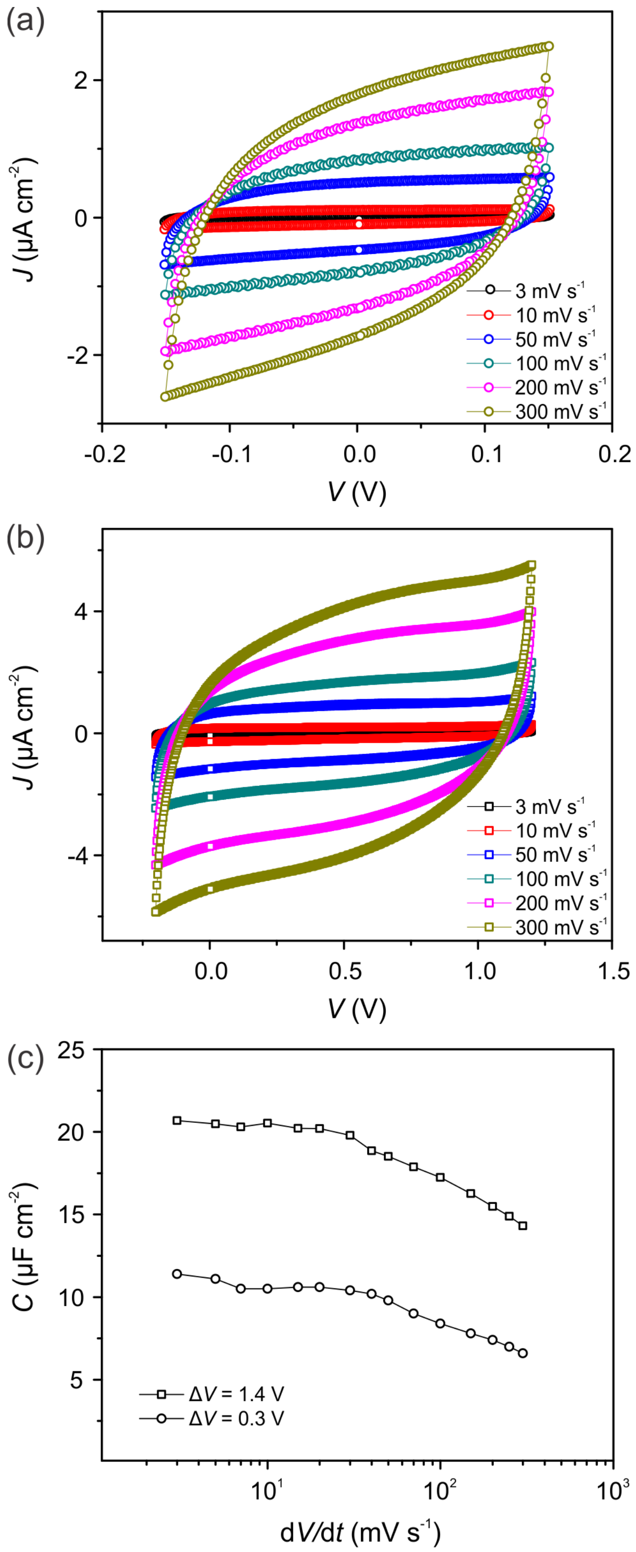

Figure 5.6.: Evolution of the capacitance on increasing the voltage ramp rate. (a,b) Current density-voltage characteristics at different voltage scan rates (3 - 300 mV s^{-1}) using a potential window of 0.3 V (a) and 1.4 V (b). (c) Calculated capacitance as a function of the voltage ramp rate. C is $\approx 12\,\mu\mathrm{F\,cm^{-2}}$ and $\approx 21\,\mu\mathrm{F\,cm^{-2}}$ for ΔV = 0.3 V and 1.4 V, respectively. Both experiments performed in (a,b) present similar trends with only a minor decrease of C at high voltage scan rates. All measurements performed at 235 K. (Published in [343]. ©2017, John Wiley and Sons.)

comparable to the results obtained in all-solid-state magnetoionics[7] [15, 144] or in single-phase multiferroics [68], but slower than the coherent magnetization switching reported on ultrathin films of FeCo/MgO/Fe trilayers [12].

Here, the main factor limiting the device switching speed is the sluggish ionic diffusion at temperatures close to the DEME-TFSI glass transition[8]. In order to estimate the maximum possible ME switching speed, a comparison with electrolyte-gated transistors seems appropriate, where ionic mobility is also an issue in terms of the device speed. In the case of gating via ILs, transistor frequencies beyond kHz have been reported [113, 168, 169].

To reinforce the idea that such speeds are in line of principle achievable in LSMO films gated with DEME-TFSI ionic liquid, it is useful to estimate the time constant $\tau = R \cdot C$ of the charging/discharging processes considering the simplified equivalent circuit of Fig. 2.9(c) (see Section 2.4.6). As already mentioned, the IL electrolyte provides the major source of resistance[9] $R = \rho \cdot \frac{l}{A} \approx 20\,\Omega$. Hence, taking into account a capacitance $C \approx 50\,\mu\text{F}$, it results $\tau \approx 10^{-3}$ s, corresponding to a frequency of 1 kHz.

Therefore, faster ME switching speeds may be possible by optimizing the device geometry [345], by implementing novel ILs with faster ionic conductivity or, alternatively, by replacing LSMO with another magnetic pseudocapacitor with higher T_C.

5.4 Summary

Purpose of this chapter was to analyze the ME performance of LSMO/IL supercapacitors with an optimized surface-to-volume ratio in terms of magnitude of the ME effect, cycling stability, energy consumption and switching speed.

On/off switching of ferromagnetism was realized with a giant magnetic tuning effect $|\Delta M/M|$ of up to 128% and a shift in T_C of up to 26 K by application of just a few volts. The resulting ME coupling coefficients $\alpha = \Delta M/\Delta V$ of up to $\approx 226\,\text{Oe}\,\text{V}^{-1}$ are comparable to the best values ever reported on the state-of-the-art MEs. In addition, the magnetic response could be flexibly modulated in-phase and/or anti-phase with respect to the voltage-induced surface charge density.

Thanks to the very nature of the interfacial charging processes of supercapacitors, toggling of magnetism was achieved in a highly-reversible manner and with low energy consumption.

It was proposed that the device switching speed may be further advanced by investigating novel device geometries and involved materials.

Although the *in situ* ME measurements were done not far from room temperature, the increase in the surface-to-volume ratio of LSMO brought about a significant reduction of T_C and thus also of operating temperature. However, it is believed that the path towards the investigation of other magnetic supercapacitors with higher para/ferromagnetic transition temperature has just been opened.

---

[7] ME switching speeds can drop down to ms in magnetoionics, but application of high temperatures ($\approx$ 120 °C) and voltages ($\approx$ 12 V) is required.

[8] DEME-TFSI ionic liquid is in the so-called *rubber* phase in the 200 - 230 K range [344].

[9] R is calculated considering that the DEME-TFSI conductivity is $\sigma = 3.5$ mS cm^{-1} *at room temperature* as reported in ref. [305], $l \approx 260\,\mu\text{m}$ corresponds to the thickness of the insulating glass fiber separating working and counter electrodes and $A \approx 0.4\,\text{cm}^2$ is the LSMO surface area.

6 Conclusions and future work

The aim of the presented thesis was to comprehensively and quantitatively investigate the phenomenon of magnetoelectric (ME) coupling at solid/liquid interfaces focusing on a representative system composed of LSMO (ultra)thin films gated with DEME-TFSI ionic liquid (IL) electrolyte.

Thin films of LSMO with a thickness in the range of 3 – 15 nm were epitaxially grown on (001)-oriented $SrTiO_3$ substrates by Large-Distance Magnetron Sputtering. Optimization of the LSMO characteristics concerning crystallinity, surface morphology and magnetic properties was done by testing the effect of different growth temperatures and post-deposition annealing treatment.

Systematic analysis of the ME coupling at the LSMO/IL interface was performed by combining *in situ* Superconducting Quantum Interference Device (SQUID) magnetometry and Cyclic Voltammetry (CV) under varied conditions of temperature, applied voltage and voltage ramp rate. It was found that not only electrostatic (electric double layer capacitance) but also electrochemical (redox pseudocapacitance) charging contributes to charge carrier doping of the LSMO films. Both charging mechanisms were exploited to extensively manipulate the LSMO magnetic response. Notably, a reversible magnetic modulation $\Delta M/M$ of up to 33% was achieved in LSMO films with a thickness of ≈ 13 nm, whereas ferromagnetism was switched on-and-off in ultrathin films (≈ 3 nm) thanks to the increased surface-to-volume ratio.

A physical model of the interfacial ME effect consistent with the precisely measured values of magnetization, surface charge and ME coupling coefficient α was proposed on the basis of the phenomenon of magnetic phase separation. In a microscopic scenario, the LSMO surface features competing ferromagnetic and non-ferromagnetic domains, which grow or shrink at the expense of each other due to charge carrier doping via IL gating.

The quantitative data extracted from SQUID and CV measurements offer a solid base for further theoretical modeling of the interfacial ME coupling phenomenon. Naturally, there are still some fundamental open questions that deserve deeper studies.

For example, concerning magnetism, although magnetic phase separation is to date the most widely-accepted theory to explain some of the complex behaviors of manganites, still little is known about the control of such phenomenon by means of an electric field. The results reported here strongly suggest that the penetration depth of the interfacial electric field is not constant but conspicuously increases in proximity of T_C. Therefore, also the process of shrinkage/expansion of competing magnetic domains may vary with temperature. An experimental strategy to shed some light on this topic would be to make use of polarized neutron reflectometry to analyze magnetic depth profiles during *in situ* charging.

Regarding the interfacial charging/discharging processes, pseudocapacitance is unequivocally identified via CV measurements. Nonetheless, the specific redox processes taking place at the LSMO/IL interface are yet to be investigated. Surface-sensitive spectroscopic techniques capable of penetrating the IL during *in situ* charging, such as X-ray Photoelectron Spectroscopy [346, 347], Infrared Spectroscopy [348, 349], Raman Spectroscopy [350], Atomic Force Microscopy [351, 352] and X-ray Absorption Spectroscopy [353], shall offer powerful means to better understand the interfacial charging mechanisms.

Possibly, also other physico-chemical effects and coupling phenomena may occur in the LSMO/IL system that are worth investigating.

As already mentioned, LSMO belongs to the class of colossal magneto-resistance (CMR) manganites. Hence, the significant magnetic modulations attained in ultrathin LSMO films upon surface charging are expected to have a huge impact also on the resistance of the films.

In this study, ME coupling was reached by means of charge carrier doping, which affected the oxidation state of the Mn ions (3+ or 4+), and thus, in turn, the double-exchange and superexchange interactions along Mn–O–Mn chains. Nonetheless, since oxygen acts as mediator of the magnetic exchange interactions, the ability to insert/extract reversibly oxygen ions from LSMO would provide an alternative effective route to control magnetism. The reader may recall that huge changes in T_C and M_{sat} were observed after post-annealing of oxygen-deficient LSMO films (see Section 3.3.2). A recent work of Mefford and co-workers [196] gives valuable hints about the kind of electrolytes and experimental conditions to be used in order to accomplish reversible oxygen intercalation into LSMO.

More details about the crossover temperature T_{cross} and the in-phase/anti-phase magnetic response of LSMO upon charging can be gained by using a different composition of LSMO. For instance, the sign of the ME tuning effect is expected to be reversed comparing to the results shown in Section 4 if the Sr content is tailored in the $0.3 < Sr < 0.5$ range.

From a more application-oriented perspective, we shall now briefly discuss on the technologically-relevant parameters of LSMO/IL devices as compared to more-established solid-state ME composites, which make use of dielectric or ferroelectric gating (see Table 6.1).

A substantial advantage of gating with an IL over high-κ dielectrics or ferroelectrics is represented by higher charge carrier densities ΔQ reached by application of lower voltages. This characteristic, which is a direct consequence of a higher capacitance C, offers two practical benefits. On the one hand, owing to more robust charge doping, the magnitude of magnetic response ΔM is enhanced. On the other hand, the energy spent for charging/discharging the magnetic material is remarkably lower.

Another experimental asset of LSMO/IL devices is the outstanding level of reversibility, which exceeds several thousand cycles if the external voltage is properly set in a way to avoid the onset of irreversible electrochemical reactions. As a comparison, in many cases the endurance of all-solid-state devices is limited to just a few cycles due to ionic diffusion at metal/oxide interfaces [13], or leakage currents caused by interfacial defects [79, 110, 111].

The attained ME switching speed of about 0.1 Hz is, to the best of the author's knowledge, the highest so far reported on solid/liquid devices, but still far from the nanosecond regime already established in all-solid-state systems such as ferroelectric/ferromagnetic heterostructures [354] or Fe/MgO/FeCo trilayers [12]. In this regard, improvement of the characteristic charging/discharging time constant $\tau = R \cdot C$ of LSMO/IL devices can be anticipated by reducing the electrolyte resistance, e.g. by optimizing the device geometry or replacing the involved materials to improve ionic conductivity.

Another issue to consider is the diminished operating temperature of ultrathin LSMO films as a consequence of the reduction in T_C. In this respect, other potential candidates for robust ME effect are double-perovskites, such as Sr_2FeMoO_6 which features a magnetic transition temperature of 410-450 K [355].

All-solid-state and solid/liquid MEs possess also other benefits/constraints that should be considered. Typically, the former systems enable for inspection of a broader temperature range, whereas the latter have a lower-temperature limit of about 200 K for reversibly accumulat-

Table 6.1.: Charge carrier doping as mediator of ME coupling: comparison between all-solid-state and solid/liquid ME composites. The acronyms DI, FE, EDL and PS stand for dielectric, ferroelectric, electric double layer and pseudocapacitance, respectively. References are in square brackets.

Parameter	Solid-state ME Composite	LSMO/IL
$\Delta Q\,(h^+\,\mathrm{cm}^{-2})$	DI: 10^{12-13} [120] FE: 10^{13-14} [11]	up to 10^{15}
ΔV (V)	10-100	1-5
$C\,(\mu F\,\mathrm{cm}^{-2})$	DI: 0.01-1 FE: 1-20	EDL: $\approx$ 10 PS: 10-200
ΔM (emu cm^{-3})	32 (LSMO/PZT) [11]	54
Reversibility	$<$ 10 cycles [13]	$>$ 1000 cycles
Speed response	down to ns [12, 354]	$\approx$ 10 s
Pros and Cons	Larger T range Complex sample fabrication Stable in air FE: two polarization states FE: non-volatile Q	Smaller T range Easier sample fabrication Non-stable in air IL: quasi-continuous control of Q IL: volatile Q

ing/depleting the charge caused by freezing of the electrolyte. Although this effect is generally seen as a drawback, the prevention of ionic diffusion permits the storage of large amounts of charge at low T. This was for example exploited to induce a superconducting transition in insulating $SrTiO_3$ and $KTaO_3$ gated with an electrolyte [21, 22].

To date, the best results in all-solid-state composite MEs are reached in single-crystalline epitaxial heterostructures, which require costly and not-easily-scalable fabrication methods. In contrast, in case of solid/liquid ME devices the surface of a magnetic electrode can be covered by simply adding an electrolyte onto it. Large-scale production of miniaturized devices may be possible by printing the electrolyte using, for instance, an inkjet printer [153, 345].

Stability of the gating materials under ambient conditions is another critical point to take into account. Solid-state dielectrics and ferroelectrics, generally made of oxides, are stable in air, whereas electrolytes have the tendency to absorb water or oxygen with consequent degradation of their initial characteristics. Thus, the latter approach requests a bulky sample packaging to protect the electrolyte against contamination. An interesting path would also be to study ME coupling using solid polymer electrolytes, known for being stable in air [153].

Differently from ferroelectrics, that allow for two well-defined and non-volatile polarization states, electrolytes accumulate quasi-continuously the surface charge, which is lost when the external voltage is removed. Deciding whether the former or the latter characteristics are more desirable depends on the specific application of interest: ferroelectrics/ferromagnetic composites may be more suitable for realization of fast, two-state memories, whereas electrolytes may be more impactful for transduction and actuation purposes.

Keeping in mind the current limits of LSMO/IL devices, a few possible future applications can be envisioned. Considering the experimental merits of the present work, LSMO/IL devices may be implemented as "electric field effect magnets", where ferromagnetism is easily switched to a non-magnetic state electrically to realize a low-power magnetic force generator [128]. The ability to control in-phase and/or anti-phase the magnetic response with respect to the voltage-induced surface charge opens up new opportunities for transduction and processing of ME signals. Another interesting possibility may be pursued in the ever-growing field of spintronics. Indeed, although electrolytic capacitors are basic components of modern computers, so far a spintronic analogue has not been fabricated yet. In this regard, the innate property of LSMO to be a half-metal, thus allowing only the conduction of electrons with a specific spin orientation, combined with the freedom in controlling magnetic phase transitions by means of an external voltage, may be exploited to design a "spin-polarized (super)capacitor" [246].

As a concluding remark, it is believed that one of the major contributions of this study was to include the phenomenon of psedocapacitance into the portfolio of tools, already comprising strain, electrostatic doping and electrochemical intercalation, to control magnetism. Further systems, such as transition metal oxides (e.g. CoO [193] or NiO [194]), double-perovskite oxides (e.g. Sr_2FeMoO_6) and strongly-correlated CMR oxides (e.g. $La_{1-x}Ba_xMnO_3$, $La_{1-x}Ca_xMnO_3$ and $La_{1-x}Sr_xCoO_3$) may be amenable to pseudocapacitive reactions. Hopefully, the results of ME coupling in LSMO/IL devices will pave the way for a broader, in-depth research in the hitherto uncharted area of ME supercapacitors.

Bibliography

[1] N. Spaldin and M. Fiebig, *Science* **309**, 391 (2005) `10.1126/science.1113357` (cit. on pp. 1, 18).

[2] M. Fiebig, *Journal of Physics D: Applied Physics* **38**, R123 (2005) `10.1088/0022-3727/38/8/R01` (cit. on pp. 1, 3, 6, 11, 18, 123).

[3] C. H. Ahn, A. Bhattacharya, M. Di Ventra, J. N. Eckstein, C. D. Frisbie, M. E. Gershenson, A. M. Goldman, I. H. Inoue, J. Mannhart, A. J. Millis, A. F. Morpurgo, D. Natelson, and J. M. Triscone, *Reviews of Modern Physics* **78**, 1185 (2006) `10.1103/RevModPhys.78.1185` (cit. on pp. 1, 11).

[4] H. Ohno, D. Chiba, F. Matsukura, T. Omiya, E. Abe, T. Dietl, Y. Ohno, and K. Ohtani, *Nature* **408**, 944 (2000) `10.1038/35050040` (cit. on pp. 1, 13, 87, 93).

[5] S. Mathews, *Science* **276**, 238 (1997) `10.1126/science.276.5310.238` (cit. on pp. 1, 14, 31).

[6] M. Weisheit, S. Fähler, A. Marty, Y. Souche, C. Poinsignon, and D. Givord, *Science (New York, N.Y.)* **315**, 349 (2007) `10.1126/science.1136629` (cit. on pp. 1, 21, 23, 25, 26).

[7] M. Itoh, T. Shimura, T. Hayashi, and Y. Inaguma, *Solid State Communications* **97**, 179 (1996) (cit. on pp. 1, 26).

[8] F. Matsukura, Y. Tokura, and H. Ohno, *Nature nanotechnology* **10**, 209 (2015) `10.1038/nnano.2015.22` (cit. on pp. 1, 3, 11, 18, 69, 87).

[9] W. Eerenstein, M. Wiora, J. L. Prieto, J. F. Scott, and N. D. Mathur, *Nature materials* **6**, 348 (2007) `10.1038/nmat1886` (cit. on pp. 1, 9–11, 19, 24, 87, 93, 123).

[10] T. Maruyama, Y. Shiota, T. Nozaki, K. Ohta, N. Toda, M. Mizuguchi, a. a. Tulapurkar, T. Shinjo, M. Shiraishi, S. Mizukami, Y. Ando, and Y. Suzuki, *Nature nanotechnology* **4**, 158 (2009) `10.1038/nnano.2008.406` (cit. on pp. 1, 13, 14, 87, 93).

[11] H. J. A. Molegraaf, J. Hoffman, C. A. F. Vaz, S. Gariglio, D. Van Der Morel, C. H. Ahn, and J. M. Triscone, *Advanced Materials* **21**, 1 (2009) `10.1002/adma.200900278` (cit. on pp. 1, 15, 31, 69, 75, 76, 80, 81, 87, 92, 93, 99, 124).

[12] Y. Shiota, T. Nozaki, F. Bonell, S. Murakami, T. Shinjo, and Y. Suzuki, *Nature materials* **11**, 39 (2012) `10.1038/nmat3172` (cit. on pp. 1, 14, 96, 98, 99).

[13] J. T. Heron, J. L. Bosse, Q. He, Y. Gao, M. Trassin, L. Ye, J. D. Clarkson, C. Wang, J. Liu, S. Salahuddin, D. C. Ralph, D. G. Schlom, J. Iñiguez, B. D. Huey, and R. Ramesh, *Nature* **516**, 370 (2014) `10.1038/nature14004` (cit. on pp. 1, 11, 14, 17, 19, 93, 98, 99, 123).

[14] R. O. Cherifi, V. Ivanovskaya, L. C. Phillips, A. Zobelli, I. C. Infante, E. Jacquet, V. Garcia, S. Fusil, P. R. Briddon, N. Guiblin, A. Mougin, A. A. Ünal, F. Kronast, S. Valencia, B. Dkhil, A. Barthélémy, and M. Bibes, *Nature materials* **13**, 345 (2014) `10.1038/nmat3870` (cit. on pp. 1, 10, 19, 24, 87, 92, 93, 124).

[15] U. Bauer, L. Yao, A. J. Tan, P. Agrawal, S. Emori, H. L. Tuller, S. van Dijken, and G. S. D. Beach, *Nature materials* **14**, 174 (2015) `10.1038/nmat4134` (cit. on pp. 1, 16, 17, 25, 69, 87, 96).

[16] J. Coey, M. Viret, and S. von Molnár, *Advances in Physics* **58**, 571 (2009) `10.1080/00018730903363184` (cit. on pp. 1, 11, 34, 81).

[17] H. Ohno, in *Electrochemical aspects of ionic liquids: second edition*, Vol. 125-126 (2011), pp. 1–3, `10.1002/9781118003350.ch1` (cit. on pp. 1, 21, 39, 49, 72).

[18] K. Ueno, H. Shimotani, Y. Iwasa, and M. Kawasaki, *Applied Physics Letters* **96**, 2010 (2010) `10.1063/1.3457785` (cit. on pp. 2, 18, 23, 72).

[19] J. Jeong, N. Aetukuri, T. Graf, T. D. Schladt, M. G. Samant, and S. S. P. Parkin, *Science* **339**, 1402 (2013) `10.1126/science.1230512` (cit. on pp. 2, 18, 23, 72).

[20] Y. Yamada, K. Ueno, T. Fukumura, H. T. Yuan, H. Shimotani, Y. Iwasa, L. Gu, S. Tsukimoto, Y. Ikuhara, and M. Kawasaki, *Science* **332**, 1065 (2011) `10.1126/science.1202152` (cit. on pp. 2, 12, 21, 23, 25, 26, 124).

[21] K. Ueno, S. Nakamura, H. Shimotani, A. Ohtomo, N. Kimura, T. Nojima, H. Aoki, Y. Iwasa, and M. Kawasaki, *Nature materials* **7**, 855 (2008) `10.1038/nmat2298` (cit. on pp. 2, 18, 19, 21, 31, 100).

[22] K. Ueno, S. Nakamura, H. Shimotani, H. T. Yuan, N. Kimura, T. Nojima, H. Aoki, Y. Iwasa, and M. Kawasaki, *Nature nanotechnology* **6**, 408 (2011) `10.1038/nnano.2011.78` (cit. on pp. 2, 18, 19, 21, 31, 100).

[23] G. A. Smolenskiĭ and I. E. Chupis, *Soviet Physics Uspekhi* **25**, 475 (1982) `10.1070/PU1982v025n07ABEH004570` (cit. on pp. 3, 5–7).

[24] J. Ryu, S. Priya, K. Uchino, and H. E. Kim, **8**, 107 (2002) `10.1023/A:1020599728432` (cit. on pp. 3, 8, 18, 28).

[25] W. Eerenstein, N. D. Mathur, and J. F. Scott, *Nature* **442**, 759 (2006) `10.1038/nature05023` (cit. on pp. 3, 5, 18).

[26] R. Ramesh and N. Spaldin, *Nature materials* **3**, 21 (2007), `http://www.nature.com/nmat/journal/v6/n1/abs/nmat1805.html` (cit. on pp. 3, 18).

[27] C. W. Nan, M. I. Bichurin, S. Dong, D. Viehland, and G. Srinivasan, *Journal of Applied Physics* **103** (2008) `10.1063/1.2836410` (cit. on pp. 3, 18).

[28] L. W. Martin, Y.-H. Chu, and R. Ramesh, *Materials Science and Engineering: R: Reports* **68**, 89 (2010) `10.1016/j.mser.2010.03.001` (cit. on pp. 3, 9, 14, 19, 34).

[29] G. Srinivasan, *Annual Review of Materials Research* **40**, 153 (2010) `10.1146/annurev-matsci-070909-104459` (cit. on pp. 3, 18).

[30] C. A. F. Vaz, J. Hoffman, C. H. Ahn, and R. Ramesh, *Advanced Materials* **22**, 2900 (2010) `10.1002/adma.200904326` (cit. on pp. 3, 18).

[31] J. Ma, J. Hu, Z. Li, and C. W. Nan, *Advanced Materials* **23**, 1062 (2011) `10.1002/adma.201003636` (cit. on pp. 3, 18, 123).

[32] S.-W. Cheong and M. Mostovoy, *Nature Materials* **6**, 13 (2007) `10.1038/nmat1804` (cit. on p. 3).

[33] L. W. Martin, S. P. Crane, Y.-H. Chu, M. B. Holcomb, M. Gajek, M. Huijben, C.-H. Yang, N. Balke, and R. Ramesh, *Journal of Physics: Condensed Matter* **20**, 434220 (2008) `10.1088/0953-8984/20/43/434220` (cit. on pp. 3, 18).

[34] J.-M. Hu, T. Nan, N. X. Sun, and L.-Q. Chen, *MRS Bulletin* **40**, 728 (2015) `10.1557/mrs.2015.195` (cit. on pp. 3, 18).

[35] D. Chen, X. Gao, and J.-M. Liu, *MRS Communications* **6**, 1 (2016) `10.1557/mrc.2016.39` (cit. on p. 3).

[36] J. M. Hu, L. Q. Chen, and C. W. Nan, *Advanced Materials* **28**, 15 (2016) `10.1002/adma.201502824` (cit. on pp. 3, 18).

[37] W. C. Röntgen, *Annalen der Physik* **271**, 264 (1888) `10.1002/andp.18882711003` (cit. on p. 3).

[38] H. Wilson, *Philosophical Transactions of the Royal Society A* **204**, 121 (1905) `10.1098/rsta.1905.0003` (cit. on p. 3).

[39] P. Curie, *Journal de Physique Théorique et Appliquée* **3**, 393 (1894) `10.1051/jphystap:018940030039300` (cit. on p. 3).

[40] A. J. S. A. Perrier, *Arch. Sci. Phys. Nat. (Geneva)* **4**, 373 (1922) (cit. on p. 4).

[41] A. J. S. A. Perrier, *Arch. Sci. Phys. Nat. (Geneva)* **5**, 333 (1923) (cit. on p. 4).

[42] I. Dzyaloshinskii, *Soviet Physics JETP* **10**, 628 (1960) (cit. on p. 4).

[43] D. N. Astrov, *Soviet Physics JETP* **13**, 729 (1961) (cit. on pp. 4, 125).

[44] V. J. Folen, G. T. Rado, and E. W. Stalder, *Physical Review Letters* **6**, 607 (1961) (cit. on p. 4).

[45] H. Schmid, *International Journal of Magnetism* **4**, 337 (1973) (cit. on p. 4).

[46] B. I. Alshin and D. N. Astrov, *Sov. Phys. JETP* **17**, 809 (1963) (cit. on p. 4).

[47] G. Rado, *Physical Review Letters* **l**, 335 (1964) (cit. on p. 4).

[48] T. Watanabe and K. Kohn, *Phase Transitions* **15**, 57 (1989) `10.1080/01411598908206837` (cit. on p. 4).

[49] B. B. Krichevtsov, V. V. Pavlov and R. V. Pisarev, *JETP Lett.* **49**, 535 (1989) (cit. on p. 4).

[50] G. T. Rado, J. M. Ferrari, and W. G. Maisch, *Physical Review B* **29**, 4041 (1984) `10.1103/PhysRevB.29.4041` (cit. on p. 4).

[51] G. T. Rado and V. J. Folen., *Physical Review Letters* **7**, 310 (1961) (cit. on pp. 4, 125).

[52] T. H. O'Dell, *Philosophical Magazine* **8**, 411 (1963) `10.1080/14786436308211142` (cit. on p. 4).

[53] W. F. Brown, R. M. Hornreich, and S. Shtrikman, *Physical Review* **168**, 574 (1968) `10.1103/PhysRev.168.574` (cit. on p. 4).

[54] B. D. H. Tellegen, *Phillips Research Reports* **3**, 81 (1948) (cit. on p. 4).

[55] V. S. J., *Philips Res. Rep.* **27**, 28 (1972) (cit. on pp. 5, 8).

[56] U. Laletsin, N. Padubnaya, G. Srinivasan, and C. P. Devreugd, *Applied Physics A: Materials Science and Processing* **78**, 33 (2004) `10.1007/s00339-003-2293-3` (cit. on pp. 5, 8, 9, 29).

[57] H. Schmid, *Ferroelectrics* **162**, 317 (1994) `10.1080/00150199408245120` (cit. on p. 5).

[58] M. Fiebig, V. V. Eremenko, and I. E. Chupis, *Proc. MEIPIC-5* **164**, 6221 (2004) `10.1007/978-1-4020-2707-9` (cit. on p. 5).

[59] H. Lu, T. A. George, Y. Wang, I. Ketsman, J. D. Burton, C.-W. Bark, S. Ryu, D. J. Kim, J. Wang, C. Binek, P. A. Dowben, A. Sokolov, C.-B. Eom, E. Y. Tsymbal, and A. Gruverman, *Applied Physics Letters* **100**, 232904 (2012) `10.1063/1.4726427` (cit. on pp. 6, 16, 38, 53–55).

[60] G. Smolenskii and A. Agranovskaya, *Zhur. Tekh. Fiz.* **28** (1958) (cit. on p. 6).

[61] G. Smolenskii, A. Agranovskaia, S. Popov, and V. Isupov, *Sov. Phys. Tech. Phys.* **3**, 1981 (1958) (cit. on p. 6).

[62] G. Smolenskii, V. Isupov, N. Krainik, and A. Agranovskaya, *Izvestiya Rossijskoj Akademii Nauk. Seriya Fizika Atmosfery i Okeana* **25**, 1333 (1961) (cit. on p. 6).

[63] G. Smolenskii and A. Andreev, *Bull. Russ. Acad. Sci. USSR Phys. Ser* **25**, 1405 (1961) (cit. on p. 6).

[64] R. H. E. Wendling and R. Kühn, *Kali und Steinsalz* **6**, 1 (1972) (cit. on p. 6).

[65] R. M. Honea and F. Beck, *Am. Mineralogist* **47**, 665 (1962) (cit. on p. 6).

[66] N. A. Hill, *J. Phys. Chem. B* **104**, 6694 (2000) `10.1021/jp000114x` (cit. on p. 6).

[67] N. Hur, S. Park, P. A. Sharma, J. S. Ahn, S. Guha, and S. W. Cheong, *Nature* **429**, 392 (2004) `10.1038/nature02572` (cit. on pp. 6, 7).

[68] Y. Tokunaga, Y. Taguchi, T.-H. Arima, and Y. Tokura, *Nature Physics* **8**, 838 (2012) `10.1038/nphys2405` (cit. on pp. 7, 93, 96).

[69] M. Fiebig, T. Lottermoser, D. Fröhlich, A. V. Goltsev, and R. V. Pisarev, *Nature* **419**, 818 (2002) `10.1038/nature01077` (cit. on p. 6).

[70] T. Kimura, T. Goto, H. Shintani, K. Ishizaka, T. Arima, and Y. Tokura, *Nature* **426**, 55 (2003) `10.1038/nature02018` (cit. on p. 6).

[71] T. Lottermoser, T. Lonkai, U. Amann, D. Hohlwein, J. Ihringer, and M. Fiebig, *Nature* **430**, 541 (2004) `10.1038/nature02673.` (cit. on p. 6).

[72] M. Matsubara, S. Manz, M. Mochizuki, T. Kubacka, A. Iyama, N. Aliouane, T. Kimura, S. L. Johnson, D. Meier, and M. Fiebig, *Science* **348**, 1112 (2015) `10.1126/science.1260561` (cit. on p. 7).

[73] G. Catalan and J. F. Scott, *Advanced Materials* **21**, 2463 (2009) `10.1002/adma.200802849` (cit. on p. 7).

[74] I. Sosnowska, T. P. Neumaier, and E. Steichele, *Journal of Physics C: Solid State Physics* **15**, 4835 (1982) `10.1088/0022-3719/15/23/020` (cit. on p. 7).

[75] I. A. Sergienko and E. Dagotto, *Physical Review B* **73**, 1 (2006) `10.1103/PhysRevB.73.094434` (cit. on p. 7).

[76] S.-W. Cheong and M. Mostovoy, *Nature Materials* **6**, 13 (2007) `10.1038/nmat1804` (cit. on p. 7).

[77] C. Ederer and N. A. Spaldin, *Physical Review Letters* **95**, 2 (2005) `10.1103/PhysRevLett.95.257601` (cit. on pp. 7, 12, 70).

[78] P. M. Leufke, R. Kruk, D. Wang, C. Kübel, and H. Hahn, *AIP Advances* **2**, 032184 (2012) `10.1063/1.4756997` (cit. on pp. 7, 12, 14, 19, 31).

[79] W. Eerenstein, F. D. Morrison, F. Sher, J. L. Prieto, J. P. Attfield, J. F. Scott, and N. D. Mathur, *Philosophical Magazine Letters* **87**, 249 (2007) `10.1080/09500830601173053` (cit. on pp. 7, 98).

[80] J. Wang, J. B. Neaton, H. Zheng, V. Nagarajan, S. B. Ogale, B. Liu, D. Viehland, V. Vaithyanathan, D. G. Schlom, U. V. Waghmare, N. A. Spaldin, K. M. Rabe, M. Wuttig, and R. Ramesh, *Science* **299**, 1719 (2003) `10.1126/science.1080615` (cit. on p. 8).

[81] W. Eerenstein, *Science* **307**, 1203a (2005) `10.1126/science.1105422` (cit. on p. 8).

[82] T. Zhao, A. Scholl, F. Zavaliche, K. Lee, M. Barry, A. Doran, M. P. Cruz, Y. H. Chu, C. Ederer, N. A. Spaldin, R. R. Das, D. M. Kim, S. H. Baek, C. B. Eom, and R. Ramesh, *Nature materials* **5**, 823 (2006) `10.1038/nmat1731` (cit. on p. 8).

[83] L. F. Henrichs, O. Cespedes, J. Bennett, J. Landers, S. Salamon, C. Heuser, T. Hansen, T. Helbig, O. Gutfleisch, D. C. Lupascu, H. Wende, W. Kleemann, and A. J. Bell, *Advanced Functional Materials* **26**, 2110 (2016) `10.1002/adfm.201670081` (cit. on pp. 8, 123, 125).

[84] J. Van den Boomgaard, D. Terrell, R. Born, and H. Giller, *Journal of Materials Science* **9**, 1705 (1974) (cit. on p. 8).

[85] Bunget, I. and V. Raetchi., *Revue Roumaine de Physique* **27**, 401 (1982) (cit. on p. 8).

[86] M. I. Bichurin, V. M. Petrov, R. V. Petrov, Y. V. Kiliba, F. I. Bukashev, A. Y. Smirnov, and D. N. Eliseev, *Ferroelectrics* **280**, 199 (2002) `10.1080/00150190214814` (cit. on p. 8).

[87] G. Srinivasan, E. Rasmussen, and R. Hayes, *Physical Review B* **67**, 1 (2003) `10.1103/PhysRevB.67.014418` (cit. on p. 8).

[88] J. Ryu, A. V. Carazo, K. Uchino, and H.-E. Kim, *Japanese Journal of Applied Physics* **40**, 4948 (2001) `10.1143/JJAP.40.4948` (cit. on pp. 8, 9).

[89] G. Srinivasan, E. T. Rasmussen, B. J. Levin, and R. Hayes, *Physical Review B* **65**, 134402 (2002) `10.1103/PhysRevB.66.029901` (cit. on pp. 8, 9).

[90] K. Mori and M. Wuttig, *Applied Physics Letters* **81**, 100 (2002) `10.1063/1.1491006` (cit. on pp. 8, 9).

[91] J. Wang, Z. Li, J. Wang, H. He, and C. Nan, *Journal of Applied Physics* **117**, 044101 (2015) `10.1063/1.4906407` (cit. on p. 9).

[92] N. Cai, C. W. Nan, J. Zhai, and Y. Lin, *Applied Physics Letters* **84**, 3516 (2004) `10.1063/1.1739277` (cit. on p. 9).

[93] Z. Shi, C. W. Nan, J. Zhang, N. Cai, and J. F. Li, *Appl. Phys. Lett.* **87**, 12503 (2005) `10.1063/1.1991983` (cit. on p. 9).

[94] C. W. Nan, *Physical Review B* **50**, 6082 (1994) `10.1103/PhysRevB.50.6082` (cit. on p. 9).

[95] C. Nan, M. Li, and J. Huang, *Physical Review B* **63**, 1 (2001) `10.1103/PhysRevB.63.144415` (cit. on p. 9).

[96] Z. Shi, C. W. Nan, J. M. Liu, D. A. Filippov, and M. I. Bichurin, *Physical Review B* **70**, 1 (2004) `10.1103/PhysRevB.70.134417` (cit. on p. 9).

[97] D. A. Filippov, M. I. Bichurin, V. M. Petrov, V. M. Laletin, and G. Srinivasan, *Physics of the Solid State* **46**, 1674 (2004) `10.1134/1.1799186` (cit. on p. 9).

[98] S. Srinivas, J. Y. Li, Y. C. Zhou, and A. K. Soh, *Journal of Applied Physics* **99** (2006) `10.1063/1.2173035` (cit. on p. 9).

[99] K. Dörr, *Journal of Physics D: Applied Physics* **39**, R125 (2006) `10.1088/0022-3727/39/7/R01` (cit. on pp. 9, 36).

[100] M. K. Lee, T. K. Nath, C. B. Eom, M. C. Smoak, and F. Tsui, *Applied Physics Letters* **77**, 3547 (2000) `10.1063/1.1328762` (cit. on p. 9).

[101] C. Thiele, K. Dörr, O. Bilani, J. Rödel, and L. Schultz, *Physical Review B* **75**, 1 (2007) `10.1103/PhysRevB.75.054408` (cit. on pp. 9, 12).

[102] S. Sahoo, S. Polisetty, C. G. Duan, S. S. Jaswal, E. Y. Tsymbal, and C. Binek, *Physical Review B* **76** (2007) `10.1103/PhysRevB.76.092108` (cit. on p. 9).

[103] S. Brivio, D. Petti, R. Bertacco, and J. C. Cezar, *Applied Physics Letters* **98**, 092505 (2011) `10.1063/1.3554432` (cit. on pp. 9, 14).

[104] Y. Shirahata, R. Shiina, D. L. González, K. J. a. Franke, E. Wada, M. Itoh, N. A. Pertsev, S. van Dijken, and T. Taniyama, *NPG Asia Materials* **7**, e198 (2015) `10.1038/am.2015.72` (cit. on p. 9).

[105] M. Liu, M. B. Johnston, and H. J. Snaith, *Nature* **501**, 395 (2013) `10.1038/nature12509` (cit. on pp. 9, 31).

[106] H. Zheng, J. Wang, S. E. Lofland, Z. Ma, L. Mohaddes-Ardabili, T. Zhao, L. Salamanca-Riba, S. R. Shinde, S. B. Ogale, F. Bai, D. Viehland, Y. Jia, D. G. Schlom, M. Wuttig, A. Roytburd, and R. Ramesh, *Science* **303**, 661 (2004) `10.1126/science.1094207` (cit. on p. 10).

[107] F. Zavaliche, H. Zheng, L. Mohaddes-Ardabili, S. Y. Yang, Q. Zhan, P. Shafer, E. Reilly, R. Chopdekar, Y. Jia, P. Wright, D. G. Schlom, Y. Suzuki, and R. Ramesh, *Nano Letters* **5**, 1793 (2005) `10.1021/nl051406i` (cit. on p. 10).

[108] C. H. Ahn, J.-M. Triscone, and J. Mannhart, *Nature* **424**, 1015 (2003) `10.1038/nature01878` (cit. on pp. 11, 12, 31).

[109] P. M. Leufke, R. Kruk, R. A. Brand, and H. Hahn, *Physical Review B* **87**, 094416 (2013) `10.1103/PhysRevB.87.094416` (cit. on pp. 11, 16, 31, 64, 69, 75, 76, 80, 81, 93, 123).

[110] E. J. Miller, E. T. Yu, P. Waltereit, and J. S. Speck, *Applied Physics Letters* **84**, 535 (2004) `10.1063/1.1644029` (cit. on pp. 12, 98).

[111] L. Pintilie, I. Vrejoiu, D. Hesse, G. LeRhun, and M. Alexe, *Physical Review B* **75**, 1 (2007) `10.1103/PhysRevB.75.104103` (cit. on pp. 12, 98).

[112] G. D. Wilk, R. M. Wallace, and J. M. Anthony, *Journal of Applied Physics* **89**, 5243 (2001) `10.1063/1.1361065` (cit. on p. 12).

[113] T. Fujimoto and K. Awaga, *Physical Chemistry Chemical Physics* **15**, 8983 (2013) `10.1039/c3cp50755f` (cit. on pp. 12, 21, 39, 49, 96).

[114] F. Xiu, Y. Wang, J. Kim, A. Hong, J. Tang, A. P. Jacob, J. Zou, and K. L. Wang, *Nature Materials* **9**, 337 (2010) `10.1038/nmat2716` (cit. on pp. 12, 13).

[115] M. Pawlik, J. P. Vilcot, M. Halbwax, D. Aureau, A. Etcheberry, A. Slaoui, T. Schutz-Kuchly, and R. Cabal, *Energy Procedia* **60**, 85 (2014) `10.1016/j.egypro.2014.12.347` (cit. on p. 12).

[116] N. P. Maity, R. Maity, R. K. Thapa, and S. Baishya, *Advances in Materials Science and Engineering* **2014** (2014) `10.1155/2014/497274` (cit. on p. 12).

[117] D. Chiba, M. Sawicki, Y. Nishitani, Y. Nakatani, F. Matsukura, and H. Ohno, *Nature* **455**, 515 (2008) `10.1038/nature07318` (cit. on pp. 12, 13).

[118] D. Wei, T. Hossain, N. Y. Garces, N. Nepal, H. M. Meyer, M. J. Kirkham, C. R. Eddy, and J. H. Edgar, *ECS Journal of Solid State Science and Technology* **2**, N110 (2013) `10.1149/2.010305jss` (cit. on p. 12).

[119] S. Brivio, M. Cantoni, D. Petti, and R. Bertacco, *Journal of Applied Physics* **108**, 113906 (2010) `10.1063/1.3516283` (cit. on pp. 12, 15, 69).

[120] I. Pallecchi, L. Pellegrino, E. Bellingeri, A. S. Siri, D. Marré, A. Tebano, and G. Balestrino, *Physical Review B* **78**, 1 (2008) `10.1103/PhysRevB.78.024411` (cit. on pp. 12, 15, 31, 38, 59, 99).

[121] H.-C. Li, W. Si, A. D. West, and X. X. Xi, *Applied Physics Letters* **73**, 464 (1998) `10.1063/1.121901` (cit. on p. 12).

[122] K. J. Choi, *Science* **306**, 1005 (2004) `10.1126/science.1103218` (cit. on p. 12).

[123] W. Luan, L. Gao, H. Kawaoka, T. Sekino, and K. Niihara, *Ceramics International* **30**, 405 (2004) `10.1016/S0272-8842(03)00124-X` (cit. on p. 12).

[124] N. Ashcroft and N. Mermin, *Solid state physics* (Cengage Learning, 2011), ISBN: 9788131500521, `https://books.google.de/books?id=x%5C_s%5C_YAAACAAJ` (cit. on p. 12).

[125] D. Chiba, *Science* **301**, 943 (2003) `10.1126/science.1086608` (cit. on p. 13).

[126] I. Stolichnov, S. W. E. Riester, H. J. Trodahl, N. Setter, A. W. Rushforth, K. W. Edmonds, R. P. Campion, C. T. Foxon, B. L. Gallagher, and T. Jungwirth, *Nature Materials* **7**, 464 (2008) `10.1038/nmat2185` (cit. on p. 13).

[127] D. Chiba, F. Matsukura, and H. Ohno, *Nano Letters* **10**, 4505 (2010) `10.1021/nl102379h` (cit. on p. 13).

[128] D. Chiba, S. Fukami, K. Shimamura, N. Ishiwata, K. Kobayashi, and T. Ono, *Nature Materials* **10**, 853 (2011) `10.1038/nmat3130` (cit. on pp. 13, 100).

[129] A. J. Schellekens, A. van den Brink, J. H. Franken, H. J. M. Swagten, and B. Koopmans, *Nature Communications* **3**, 847 (2012) `10.1038/ncomms1848` (cit. on p. 14).

[130] D. Chiba, M. Kawaguchi, S. Fukami, N. Ishiwata, K. Shimamura, K. Kobayashi, and T. Ono, *Nature Communications* **3**, 888 (2012) `10.1038/ncomms1888` (cit. on p. 14).

[131] W.-G. Wang, M. Li, S. Hageman, and C. L. Chien, *Nature Materials* **11**, 64 (2012) `10.1038/nmat3171` (cit. on p. 14).

[132] N. Cabrera and N. F. Mott, *Reports on Progress in Physics* **12**, 163 (1949) `10.1088/0034-4885/12/1/308` (cit. on p. 14).

[133] S. Couet, M. Bisht, M. Trekels, M. Menghini, C. Petermann, M. J. Van Bael, J. P. Locquet, R. Rüffer, A. Vantomme, and K. Temst, *Advanced Functional Materials* **24**, 71 (2014) `10.1002/adfm.201301160` (cit. on p. 14).

[134] A. Urushibara, Y. Moritomo, T. Arima, A. Asamitsu, G. Kido, and Y. Tokura, *Physical Review B* **51**, 14103 (1995) `10.1103/PhysRevB.51.14103` (cit. on pp. 14, 32, 54, 70, 74, 80).

[135] J. Hemberger, A. Krimmel, T. Kurz, H.-A. Krug von Nidda, V. Ivanov, A. Mukhin, A. Balbashov, and A. Loidl, *Physical Review B* **66**, 094410 (2002) `10.1103/PhysRevB.66.094410` (cit. on pp. 14, 32).

[136] X. Hong, A. Posadas, A. Lin, and C. Ahn, *Physical Review B* **68**, 1 (2003) `10.1103/PhysRevB.68.134415` (cit. on p. 15).

[137] X. Hong, A. Posadas, and C. H. Ahn, *Applied Physics Letters* **86**, 1 (2005) `10.1063/1.1897076` (cit. on pp. 15, 16, 79, 125).

[138] T. Kanki, H. Tanaka, and T. Kawai, *Applied Physics Letters* **89**, 242506 (2006) `10.1063/1.2405861` (cit. on p. 15).

[139] C. A. F. Vaz, Y. Segal, J. Hoffman, R. D. Grober, F. J. Walker, and C. H. Ahn, *Applied Physics Letters* **97**, 042506 (2010) `10.1063/1.3472259` (cit. on pp. 15, 69, 76, 80, 81).

[140] C. A. F. Vaz, J. Hoffman, Y. Segal, J. W. Reiner, R. D. Grober, Z. Zhang, C. H. Ahn, and F. J. Walker, *Physical Review Letters* **104**, 127202 (2010) `10.1103/PhysRevLett.104.127202` (cit. on p. 16).

[141] T. Grygar, *Journal of Solid State Electrochemistry* **2**, 127 (1998) `10.1007/s100080050077` (cit. on pp. 16, 18).

[142] R. Waser and M. Aono, *Nature Materials* **6**, 833 (2007) `10.1038/nmat2023` (cit. on p. 16).

[143] U. Bauer, S. Emori, and G. S. D. Beach, *Nature nanotechnology* **8**, 411 (2013) `10.1038/nnano.2013.96` (cit. on pp. 16, 72, 74).

[144] C. Bi, Y. Liu, T. Newhouse-Illige, M. Xu, M. Rosales, J. W. Freeland, O. Mryasov, S. Zhang, S. G. E. Te Velthuis, and W. G. Wang, *Physical Review Letters* **113**, 1 (2014) `10.1103/PhysRevLett.113.267202` (cit. on pp. 16, 87, 96).

[145] X. Zhu, J. Zhou, L. Chen, S. Guo, G. Liu, R.-W. Li, and W. D. Lu, *Advanced Materials*, 1 (2016) `10.1002/adma.201601425` (cit. on p. 16).

[146] V. Laukhin, V. Skumryev, X. Martí, D. Hrabovsky, F. Sánchez, M. García-Cuenca, C. Ferrater, M. Varela, U. Lüders, J. Bobo, and J. Fontcuberta, *Physical Review Letters* **97**, 227201 (2006) `10.1103/PhysRevLett.97.227201` (cit. on p. 17).

[147] S. M. Wu, S. Cybart, P. Yu, M. D. Rossell, J. X. Zhang, R. Ramesh, and R. C. Dynes, *Nature Materials* **9**, 756 (2010) `10.1038/nmat2803` (cit. on p. 17).

[148] D. A. Gilbert, J. Olamit, R. K. Dumas, B. J. Kirby, A. J. Grutter, B. B. Maranville, E. Arenholz, J. A. Borchers, and K. Liu, *Nature Communications* **7**, 11050 (2016) `10.1038/ncomms11050` (cit. on p. 17).

[149] Y.-H. Chu, L. W. Martin, M. B. Holcomb, M. Gajek, S.-J. Han, Q. He, N. Balke, C.-H. Yang, D. Lee, W. Hu, Q. Zhan, P.-L. Yang, A. Fraile-Rodriguez, A. Scholl, S. X. Wang, and R. Ramesh, *Nature Materials* **7**, 478 (2008) `10.1038/nmat2184` (cit. on p. 17).

[150] S. S. P. Parkin, M. Hayashi, and L. Thomas, *Science* **320**, 190 (2008) `10.1126/science.1145799` (cit. on p. 17).

[151] A. Fert, V. Cros, and J. Sampaio, *Nature Nanotechnology* **8**, 152 (2013) `10.1038/nnano.2013.29` (cit. on p. 17).

[152] P.-j. Hsu, A. Kubetzka, A. Finco, N. Romming, K. von Bergmann, and R. Wiesendanger, *Nature Nanotechnology* **12**, 123 (2016) `10.1038/nnano.2016.234` (cit. on p. 17).

[153] F. Von Seggern, I. Keskin, E. Koos, R. Kruk, H. Hahn, and S. Dasgupta, *ACS Applied Materials and Interfaces* **8**, 31757 (2016) `10.1021/acsami.6b10939` (cit. on pp. 18, 39, 100).

[154] L. Suo, O. Borodin, T. Gao, M. Olguin, J. Ho, X. Fan, C. Luo, C. Wang, and K. Xu, **350** (2015) `10.1126/science.aab1595` (cit. on pp. 18, 39).

[155] K. Xu, *Chemical Reviews* **104**, 4303 (2004) `10.1021/cr030203g` (cit. on pp. 18, 39).

[156] A. S. Dhoot, C. Israel, X. Moya, N. D. Mathur, and R. H. Friend, *Physical Review Letters* **102**, 1 (2009) `10.1103/PhysRevLett.102.136402` (cit. on pp. 18, 23, 26, 72, 79, 81, 91).

[157] H. Yuan, H. Shimotani, J. Ye, and S. Yoon, *Journal of the American Chemical Society* **132**, 18402 (2010), `http://dx.doi.org/10.1021/ja108912x` (cit. on pp. 18, 23, 94).

[158] J. Walter, H. Wang, B. Luo, C. D. Frisbie, and C. Leighton, *ACS Nano* **10**, 7799 (2016) `10.1021/acsnano.6b03403` (cit. on pp. 18, 23, 26).

[159] L. Hu and K. Xu, *Proceedings of the National Academy of Sciences* **111**, 3205 (2014) `10.1073/pnas.1401033111` (cit. on p. 18).

[160] A. Hammami, N. Raymond, and M. Armand, *Nature* **424**, 635 (2003) `10.1038/424635b` (cit. on p. 18).

[161] M. Armand, F. Endres, D. R. MacFarlane, H. Ohno, and B. Scrosati, *Nature Materials* **8**, 621 (2009) `10.1038/nmat2448` (cit. on p. 18).

[162] M. J. Panzer and C. D. Frisbie, *Advanced Functional Materials* **16**, 1051 (2006) `10.1002/adfm.200600111` (cit. on p. 19).

[163] M. Toupin, T. Brousse, and D. Bélanger, *Chemistry of Materials* **16**, 3184 (2004) `10.1021/cm049649j` (cit. on pp. 19, 22, 50, 69, 70).

[164] H. Du, X. Lin, Z. Xu, and D. Chu, *Journal of Materials Science* **50**, 5641 (2015) `10.1007/s10853-015-9121-y` (cit. on pp. 20, 21, 124).

[165] Panasonic, *Technical Data of Conductive Polymer Hybrid Aluminum Electrolytic Capacitors* (2016), `https://industrial.panasonic.com/.../AL%7B%5C_%7Dtechnical%7B%5C_%7Dguide%7B%5C_%7DE.pdf` (cit. on p. 21).

[166] H. L. T. Zednicek, J. Sikula, *AVX, a Kyocera Group Company* (2006), `https://escies.org/download/webDocumentFile?id=62194` (cit. on p. 21).

[167] A. Albertsen, *Jianghai Europe Electronic Components GmbH*, 1 (2012), `http://jianghai-europe.com/wp-content/uploads/JIANGHAI-Spannungsfestigkeit-AAL.pdf` (cit. on p. 21).

[168] J. H. Cho, J. Lee, Y. Xia, B. Kim, Y. He, M. J. Renn, T. P. Lodge, and C. Daniel Frisbie, *Nature Materials* **7**, 900 (2008) `10.1038/nmat2291` (cit. on pp. 21, 96).

[169] J. H. Cho, J. Lee, Y. He, B. Kim, T. P. Lodge, and C. D. Frisbie, *Advanced Materials* **20**, 686 (2008) `10.1002/adma.200701069` (cit. on pp. 21, 96).

[170] C. Reitz, P. M. Leufke, R. Schneider, H. Hahn, and T. Brezesinski, *Chemistry of Materials* **26**, 5745 (2014) `10.1021/cm5028282` (cit. on pp. 21, 26, 69).

[171] A. K. Mishra, C. Bansal, M. Ghafari, R. Kruk, and H. Hahn, *Physical Review B - Condensed Matter and Materials Physics* **81**, 1 (2010) `10.1103/PhysRevB.81.155452` (cit. on p. 21).

[172] K. Shimamura, D. Chiba, S. Ono, S. Fukami, N. Ishiwata, M. Kawaguchi, K. Kobayashi, and T. Ono, *Applied Physics Letters* **100** (2012) `10.1063/1.3695160` (cit. on pp. 21, 25).

[173] A. K. Mishra, A. J. Darbandi, P. M. Leufke, R. Kruk, and H. Hahn, *Journal of Applied Physics* **113**, 033913 (2013) `10.1063/1.4778918` (cit. on pp. 21, 26, 69, 76).

[174] J. Weissmüller, R. N. Viswanath, D. Kramer, P. Zimmer, R. Würschum, and H. Gleiter, *Science* **300**, 312 (2003) `10.1126/science.1081024` (cit. on pp. 21, 24).

[175] D. Kramer, R. N. Viswanath, and J. Weissmüller, *Nano Letters* **4**, 793 (2004) `10.1021/nl049927d` (cit. on p. 21).

[176] P. Simon and Y. Gogotsi, *Nature Materials* **7**, 845 (2008) `10.1038/nmat2297` (cit. on p. 21).

[177] V. Augustyn, P. Simon, and B. Dunn, *Energy & Environmental Science* **7**, 1597 (2014) `10.1039/c3ee44164d` (cit. on pp. 21, 22, 50, 69, 73, 74).

[178] M. R. Lukatskaya, B. Dunn, and Y. Gogotsi, *Nature Communications* **7**, 1 (2016) `10.1038/ncomms12647` (cit. on pp. 21, 23, 49, 90, 94).

[179] B. E. Conway, *Journal of the Electrochemical Society* **138**, 1539 (1991) `10.1149/1.2085829` (cit. on pp. 21, 22, 24, 50, 69, 72, 73, 90).

[180] B. Conway, V. Birss, and J. Wojtowicz, *Journal of Power Sources* **66**, 1 (1997) `10.1016/S0378-7753(96)02474-3` (cit. on pp. 21, 22, 50, 69, 72, 73).

[181] B. D. Choi, G. E. Blomgren, and P. N. Kumta, *Advanced Materials*, 1178 (2006) `10.1002/adma.200502471` (cit. on p. 22).

[182] T. Brezesinski, J. Wang, S. H. Tolbert, and B. Dunn, *Nature Materials* **9**, 146 (2010) `10.1038/nmat2612` (cit. on pp. 22, 74).

[183] T.-C. Liu, *Journal of The Electrochemical Society* **145**, 1882 (1998) `10.1149/1.1838571` (cit. on p. 22).

[184] S. C. Pang, M. A. Anderson, and T. W. Chapman, *Journal of The Electrochemical Society* **147**, 444 (2000) `10.1149/1.1393216` (cit. on pp. 22, 70).

[185] M. Toupin, T. Brousse, and D. Belanger, *Chemistry of Materials* **14**, 3946 (2002) `10.1021/cm020408q` (cit. on p. 22).

[186] V. Subramanian, H. Zhu, R. Vajtai, P. M. Ajayan, and B. Wei, *Journal of Physical Chemistry B* **109**, 20207 (2005) `10.1021/jp0543330` (cit. on p. 22).

[187] O. Ghodbane, J. L. Pascal, and F. Favier, *ACS Applied Materials and Interfaces* **1**, 1130 (2009) `10.1021/am900094e` (cit. on pp. 22, 70).

[188] P. Ragupathy, H. N. Vasan, and N. Munichandraiah, *Journal of The Electrochemical Society* **155**, A34 (2008) `10.1149/1.2800163` (cit. on p. 22).

[189] P. Ragupathy, D. H. Park, G. Campet, H. N. Vasan, S. J. Hwang, J. H. Choy, and N. Munichandraiah, *Journal of Physical Chemistry C* **113**, 6303 (2009) `10.1021/jp811407q` (cit. on p. 22).

[190] J.-K. Chang, M.-T. Lee, W.-T. Tsai, M.-J. Deng, H.-F. Cheng, and I.-W. Sun, *Langmuir* **25**, 11955 (2009) `10.1021/la9012119` (cit. on pp. 22, 50, 72).

[191] C. Guan, J. Liu, Y. Wang, L. Mao, Z. Fan, Z. Shen, H. Zhang, and J. Wang, *ACS nano*, 5198 (2015) `10.1021/acsnano.5b00582` (cit. on p. 22).

[192] Z. Ren, J. Li, Y. Ren, S. Wang, Y. Qiu, and J. Yu, *Scientific Reports* **6**, 20021 (2016) `10.1038/srep20021` (cit. on p. 22).

[193] C. Lin, J. A. Ritter, and B. N. Popov, *Journal of The Electrochemical Society* **145**, 4097 (1998) `10.1149/1.1838920` (cit. on pp. 22, 100).

[194] K.-C. Liu, *Journal of The Electrochemical Society* **143**, 124 (1996) `10.1149/1.1836396` (cit. on pp. 22, 100).

[195] V. Augustyn, J. Come, M. A. Lowe, J. W. Kim, P.-L. Taberna, S. H. Tolbert, H. D. Abruña, P. Simon, and B. Dunn, *Nature Materials* **12**, 518 (2013) `10.1038/nmat3601` (cit. on p. 22).

[196] J. T. Mefford, W. G. Hardin, S. Dai, K. P. Johnston, and K. J. Stevenson, *Nature Materials* **13**, 726 (2014) `10.1038/nmat4000` (cit. on pp. 22, 39, 70, 73, 98).

[197] M. Winter, M. Winter, J. O. Besenhard, J. O. Besenhard, M. E. Spahr, M. E. Spahr, P. Novák, and P. Novák, *Advanced Materials* **10**, 725 (1998) `10.1002/(SICI)1521-4095(199807)10:10<725::AID-ADMA725>3.0.CO;2-Z` (cit. on p. 23).

[198] J. M. Tarascon and M. Armand, *Nature* **414**, 359 (2001) `10.1038/35104644` (cit. on p. 23).

[199] A. S. Aricò, P. G. Bruce, B. Scrosati, J.-M. Tarascon, and W. van Schalkwijk, *Nature Materials* **4**, 366 (2005) `10.1038/nmat1368` (cit. on p. 23).

[200] J. B. Goodenough and Y. Kim, *Chemistry of Materials* **22**, 587 (2010) `10.1021/cm901452z` (cit. on p. 23).

[201] P. G. Bruce, S. A. Freunberger, L. J. Hardwick, and J.-M. Tarascon, *Nature Materials* **11**, 19 (2012) `10.1038/NMAT3191` (cit. on p. 23).

[202] A. G. Pandolfo and A. F. Hollenkamp, *Journal of Power Sources* **157**, 11 (2006) `10.1016/j.jpowsour.2006.02.065` (cit. on pp. 24, 69).

[203] H. Drings, R. N. Viswanath, D. Kramer, C. Lemier, J. Weissmüller, and R. Würschum, *Applied Physics Letters* **88** (2006) `10.1063/1.2216897` (cit. on p. 24).

[204] C. Lemier, S. Ghosh, R. N. Viswanath, G.-T. Fei, and J. Weissmüller, *MRS Proceedings* **876**, R2.6 (2011) `10.1557/PROC-876-R2.6` (cit. on p. 24).

[205] S. Ghosh, C. Lemier, and J. Weissmueller, *INTERMAG 2006 - IEEE International Magnetics Conference* **42**, 835 (2006) `10.1109/INTMAG.2006.374866` (cit. on p. 24).

[206] A. K. Mishra, C. Bansal, M. Ghafari, R. Kruk, and H. Hahn, *Physical Review B* **81**, 1 (2010) `10.1103/PhysRevB.81.155452` (cit. on p. 24).

[207] M. Endo, D. Chiba, H. Shimotani, F. Matsukura, Y. Iwasa, and H. Ohno, *Applied Physics Letters* **96**, 91 (2010) `10.1063/1.3277146` (cit. on p. 25).

[208] S. Zhao, Z. Zhou, B. Peng, M. Zhu, M. Feng, Q. Yang, Y. Yan, W. Ren, Z. G. Ye, Y. Liu, and M. Liu, *Advanced Materials* **29** (2017) `10.1002/adma.201606478` (cit. on pp. 25, 92, 93, 125).

[209] C. Reitz, D. Wang, D. Stoeckel, A. Beck, T. Leichtweiss, H. Hahn, and T. Brezesinski, *ACS Applied Materials & Interfaces*, acsami.7b01978 (2017) `10.1021/acsami.7b01978` (cit. on p. 26).

[210] H. Kuang, J. Wang, F. X. Hu, Y. Y. Zhao, Y. Liu, R. R. Wu, J. R. Sun, and B. G. Shen, *Applied Physics Letters* **108**, 0 (2016) `10.1063/1.4942803` (cit. on p. 26).

[211] J. Lourembam, J. Wu, J. Ding, W. Lin, and T. Wu, *Physical Review B* **89**, 1 (2014) `10.1103/PhysRevB.89.014425` (cit. on pp. 26, 36, 81).

[212] T. Traussnig, S. Topolovec, K. Nadeem, D. V. Szabó, H. Krenn, and R. Würschum, *Physica Status Solidi - Rapid Research Letters* **5**, 150 (2011) `10.1002/pssr.201004483` (cit. on p. 26).

[213] S. Topolovec, P. Jerabek, D. V. Szabó, H. Krenn, and R. Würschum, *Journal of Magnetism and Magnetic Materials* **329**, 43 (2013) `10.1016/j.jmmm.2012.09.071` (cit. on p. 26).

[214] E. M. Steyskal, S. Topolovec, S. Landgraf, H. Krenn, and R. Würschum, *Beilstein Journal of Nanotechnology* **4**, 394 (2013) `10.3762/bjnano.4.46` (cit. on p. 26).

[215] K. Duschek, D. Pohl, S. Fähler, K. Nielsch, and K. Leistner, *Applied Physics Letters Materials* **032301** (2016) `10.1063/1.4942636` (cit. on p. 26).

[216] K. Duschek, M. Uhlemann, H. Schlörb, K. Nielsch, and K. Leistner, *Electrochemistry Communications* **72**, 153 (2016) `10.1016/j.elecom.2016.09.018` (cit. on p. 26).

[217] K. Leistner, N. Lange, J. Hänisch, S. Oswald, F. Scheiba, S. Fähler, H. Schlörb, and L. Schultz, *Electrochimica Acta* **81**, 330 (2012) `10.1016/j.electacta.2012.07.055` (cit. on p. 26).

[218] K. Leistner, J. Wunderwald, N. Lange, S. Oswald, M. Richter, H. Zhang, L. Schultz, and S. Fähler, *Physical Review B* **87**, 224411 (2013) `10.1103/PhysRevB.87.224411` (cit. on p. 26).

[219] K. Leistner, N. Lange, S. Oswald, and L. Schultz, *ECS Transactions* **50**, 49 (2013) `10.1149/05010.0049ecst` (cit. on p. 26).

[220] L. Reichel, S. Oswald, S. Fähler, L. Schultz, and K. Leistner, *Journal of Applied Physics* **113**, 0 (2013) `10.1063/1.4799413` (cit. on p. 26).

[221] S. Dasgupta, B. Das, M. Knapp, R. A. Brand, H. Ehrenberg, R. Kruk, and H. Hahn, *Advanced Materials* **26**, 4639 (2014) `10.1002/adma.201305932` (cit. on pp. 27, 69).

[222] T. Yamada, K. Morita, K. Kume, H. Yoshikawa, and K. Awaga, *Journal of Materials Chemistry C* **2**, 5183 (2014) `10.1039/c4tc00299g` (cit. on p. 27).

[223] Q. Zhang, X. Luo, L. Wang, L. Zhang, B. Khalid, J. Gong, and H. Wu, *Nano Letters* **16**, 583 (2016) `10.1021/acs.nanolett.5b04276` (cit. on pp. 27, 69, 87, 93).

[224] S. Dasgupta, B. Das, Q. Li, D. Wang, T. T. Baby, S. Indris, M. Knapp, H. Ehrenberg, K. Fink, R. Kruk, and H. Hahn, *Advanced Functional Materials* **26**, 7507 (2016) `10.1002/adfm.201603411` (cit. on pp. 27, 87).

[225] C. Reitz, C. Suchomski, D. Wang, H. Hahn, and T. Brezesinski, *J. Mater. Chem. C* **4**, 8889 (2016) `10.1039/C6TC02731H` (cit. on p. 27).

[226] G. Wei, L. Wei, D. Wang, Y. Chen, Y. Tian, S. Yan, L. Mei, and J. Jiao, *Applied Physics Letters* **110**, 062404 (2017) `10.1063/1.4975773` (cit. on p. 27).

[227] G. Wei, L. Wei, D. Wang, Y. Tian, Y. Chen, S. Yan, L. Mei, and J. Jiao, *RSC Advances* **7**, 2644 (2017) `10.1039/C6RA26422K` (cit. on p. 27).

[228] B. Cui, C. Song, G. Wang, Y. Yan, J. Peng, J. Miao, H. Mao, F. Li, C. Chen, F. Zeng, and F. Pan, *Advanced Functional Materials* **24**, 7233 (2014) `10.1002/adfm.201402007` (cit. on p. 27).

[229] C. Ge, K. J. Jin, L. Gu, L. C. Peng, Y. S. Hu, H. Z. Guo, H. F. Shi, J. K. Li, J. O. Wang, X. X. Guo, C. Wang, M. He, H. B. Lu, and G. Z. Yang, *Advanced Materials Interfaces* **2**, 1 (2015) `10.1002/admi.201500407` (cit. on pp. 28, 74).

[230] N. Lu, P. Zhang, Q. Zhang, R. Qiao, Q. He, H.-B. Li, Y. Wang, J. Guo, D. Zhang, Z. Duan, Z. Li, M. Wang, S. Yang, M. Yan, E. Arenholz, S. Zhou, W. Yang, L. Gu, C.-W. Nan, J. Wu, Y. Tokura, and P. Yu, *Nature* **546**, 124 (2017) `10.1038/nature22389` (cit. on p. 28).

[231] V. E. Wood and A. E. Austin, *International Journal of Magnetism* **5.4**, 303 (1974) (cit. on p. 28).

[232] J. Zhai, Z. Xing, S. Dong, J. Li, and D. Viehland, *Applied Physics Letters* **88**, 1 (2006) `10.1063/1.2172706` (cit. on p. 28).

[233] C. Israel, S. Kar-Narayan, and N. D. Mathur, *IEEE Sensors Journal* **10**, 914 (2010) `10.1109/JSEN.2009.2037728` (cit. on p. 28).

[234] M. Vopsaroiu, J. Blackburn, and M. G. Cain, *Journal of Physics D: Applied Physics* **40**, 5027 (2007) `10.1088/0022-3727/40/17/003` (cit. on p. 28).

[235] Y. Zhang, Z. Li, C. Deng, J. Ma, Y. Lin, and C. W. Nan, *Applied Physics Letters* **92**, 90 (2008) `10.1063/1.2912032` (cit. on p. 28).

[236] H. Greve, E. Woltermann, H.-J. Quenzer, B. Wagner, and E. Quandt, *Applied Physics Letters* **96**, 182501 (2010) `10.1063/1.3377908` (cit. on p. 28).

[237] J. L. Hockel, T. Wu, and G. P. Carman, *Journal of Applied Physics* **109** (2011) `10.1063/1.3553885` (cit. on p. 28).

[238] R. C. O'Handley, J. K. Huang, D. C. Bono, and J. Simon, *IEEE Sensors Journal* **8**, 57 (2008) `10.1109/JSEN.2007.912899` (cit. on p. 28).

[239] S. Dong, J. Zhai, J. F. Li, D. Viehland, and S. Priya, *Applied Physics Letters* **93** (2008) `10.1063/1.2982099` (cit. on p. 28).

[240] Y. K. Fetisov and G. Srinivasan, *Applied Physics Letters* **88** (2006) `10.1063/1.2191950` (cit. on p. 29).

[241] J. Lou, M. Liu, D. Reed, Y. Ren, and N. X. Sun, *Advanced Materials* **21**, 4711 (2009) `10.1002/adma.200901131` (cit. on pp. 29, 123).

[242] C. Pettiford, S. Dasgupta, J. Lou, S. D. Yoon, and N. X. Sun, *IEEE Transactions on Magnetics* **43**, 3343 (2007) `10.1109/TMAG.2007.893790` (cit. on p. 29).

[243] A. B. Ustinov and G. Srinivasan, *Applied Physics Letters* **93** (2008) `10.1063/1.2996585` (cit. on p. 29).

[244] C. Binek and B. Doudin, *Journal of Physics: Condensed Matter* **17**, L39 (2005) `10.1088/0953-8984/17/2/L06` (cit. on p. 29).

[245] M. Bibes and A. Barthélémy, *Nature Materials* **7**, 425 (2008) `10.1038/nmat2189` (cit. on p. 29).

[246] J. M. Rondinelli, M. Stengel, and N. A. Spaldin, *Nature Nanotechnology* **3**, 46 (2008) `10.1038/nnano.2007.412` (cit. on pp. 29, 100).

[247] J. Schwarzkopf and R. Fornari, *Progress in Crystal Growth and Characterization of Materials* **52**, 159 (2006) `10.1016/j.pcrysgrow.2006.06.001` (cit. on p. 31).

[248] A. Chanthbouala, A. Crassous, V. Garcia, K. Bouzehouane, S. Fusil, X. Moya, J. Allibe, B. Dlubak, J. Grollier, S. Xavier, C. Deranlot, A. Moshar, R. Proksch, N. D. Mathur, M. Bibes, and A. Barthélémy, *Nature Nanotechnology* **7**, 101 (2011) `10.1038/nnano.2011.213` (cit. on p. 31).

[249] M. Wissinger, D. Fuchs, L. Dieterle, H. Leiste, R. Schneider, D. Gerthsen, and H. V. Löhneysen, *Physical Review B* **83**, 144430 (2011) `10.1103/PhysRevB.83.144430` (cit. on p. 31).

[250] S. Jin, T. H. Tiefel, M. McCormack, R. A. Fastnacht, R. Ramesh, and L. H. Chen, *Science* **264**, 413 (1994) `10.1126/science.264.5157.413` (cit. on pp. 31, 36).

[251] E. Fabbri, D. Pergolesi, and E. Traversa, *Science and Technology of Advanced Materials* **11**, 044301 (2010) `10.1088/1468-6996/11/4/044301` (cit. on p. 31).

[252] B. Madhavan and A. Ashok, *Ionics* **21**, 601 (2015) `10.1007/s11581-014-1340-8` (cit. on p. 31).

[253] P. A. Sukkurji, A. Molinari, A. Benes, C. Loho, V. S. K. Chakravadhanula, S. K. Garlapati, R. Kruk, and O. Clemens, *Journal of Physics D: Applied Physics* **50**, 115302 (2017) `10.1088/1361-6463/aa5718` (cit. on pp. 31, 127).

[254] M. M. Lee, J. Teuscher, T. Miyasaka, T. N. Murakami, and H. J. Snaith, *Science* **338**, 643 (2012) `10.1126/science.1228604` (cit. on p. 31).

[255] A. Mei, X. Li, L. Liu, Z. Ku, T. Liu, Y. Rong, M. Xu, M. Hu, J. Chen, Y. Yang, M. Gratzel, and H. Han, *Science* **345**, 295 (2014) `10.1126/science.1254763` (cit. on p. 31).

[256] H. Zhou, Q. Chen, G. Li, S. Luo, T.-B. Song, H.-S. Duan, Z. Hong, J. You, Y. Liu, and Y. Yang, *Science* **345**, 542 (2014) `10.1126/science.1254050` (cit. on p. 31).

[257] Y. Tokura and Y. Tomioka, *Journal of Magnetism and Magnetic Materials* **200**, 1 (1999) `10.1016/S0304-8853(99)00352-2` (cit. on pp. 32–34).

[258] B. Dabrowski, X. Xiong, Z. Bukowski, R. Dybzinski, P. W. Klamut, J. E. Siewenie, O. Chmaissem, J. Shaffer, C. W. Kimball, J. D. Jorgensen, and S. Short, *Physical Review B* **60**, 7006 (1999) `10.1103/PhysRevB.60.7006` (cit. on pp. 32, 70, 74, 80).

[259] O. Chmaissem, B. Dabrowski, S. Kolesnik, J. Mais, J. Jorgensen, and S. Short, *Physical Review B* **67**, 1 (2003) `10.1103/PhysRevB.67.094431` (cit. on pp. 32, 35, 70, 74, 80).

[260] E. Dagotto, T. Hotta, and A. Moreo, **344**, 76 (2000) `10.1016/S0370-1573(00)00121-6` (cit. on pp. 33, 36, 37).

[261] Y. Tokura and N. Nagaosa, *Science* **288**, 462 (2000) `10.1126/science.288.5465.462` (cit. on p. 33).

[262] B. N. Figgis and M. A. Hitchman, *Ligand Field Theory and Its Applications* (2000), ISBN: 978-0-471-31776-0 (cit. on p. 33).

[263] P. W. Anderson, *Physical Review* **79**, 350 (1950) `10.1103/PhysRev.79.350` (cit. on p. 34).

[264] C. Zener, *Physical Review* **82**, 403 (1951) `10.1103/PhysRev.82.403` (cit. on pp. 34, 35).

[265] J. B. Goodenough, *Physical Review* **100**, 564 (1955) `10.1103/PhysRev.100.564` (cit. on p. 35).

[266] H. Boschker, M. Huijben, A. Vailionis, J. Verbeeck, S. van Aert, M. Luysberg, S. Bals, G. van Tendeloo, E. P. Houwman, G. Koster, D. H. a. Blank, and G. Rijnders, *Journal of Physics D: Applied Physics* **44**, 205001 (2011) `10.1088/0022-3727/44/20/205001` (cit. on pp. 35, 36, 38, 53, 54, 59).

[267] X. Xiong, B. Dabrowski, O. Chmaissem, Z. Bukowski, S. Kolesnik, R. Dybzinski, C. Kimball, and J. Jorgensen, *Physical Review B* **60**, 10186 (1999) `10.1103/PhysRevB.60.10186` (cit. on p. 35).

[268] H. Hwang, S. Cheong, N. Ong, and B. Batlogg, *Physical Review Letters* **77**, 2041 (1996) `10.1103/PhysRevLett.77.2041` (cit. on p. 36).

[269] J.-H. Park, E. Vescovo, H. Kim, and C. Kwon, *Nature* **392**, 794 (1998) `10.1038/33883` (cit. on p. 36).

[270] P. G. De Gennes, *Physical Review* **118**, 141 (1960) `10.1103/PhysRev.118.141` (cit. on p. 36).

[271] A. J. Millis, B. I. Shraiman, and R. Mueller, *Physical Review Letters*, 175 (1996) (cit. on p. 36).

[272] A. Moreo, M. Mayr, A. Feiguin, S. Yunoki, and E. Dagotto, *Physical Review Letters* **84**, 5568 (2000) `10.1103/PhysRevLett.84.5568` (cit. on pp. 36, 37, 65).

[273] T. Becker, C. Streng, Y. Luo, V. Moshnyaga, B. Damaschke, N. Shannon, and K. Samwer, *Physical Review Letters* **89**, 237203 (2002) `10.1103/PhysRevLett.89.237203` (cit. on pp. 36, 37, 65, 81).

[274] A. Moreo, S. Yunoki, and E. Dagotto, *Science* **283**, 2034 (1999) (cit. on pp. 36, 81, 125).

[275] L. Brey, *Physical Review B* **75**, 8 (2007) `10.1103/PhysRevB.75.104423` (cit. on pp. 36, 38, 59, 65).

[276] M. Fäth, S. Freisem, A. Menovsky, Y. Tomioka, J. Aarts, and J. Mydosh, *Science* **285**, 1540 (1999) `10.1126/science.285.5433.1540` (cit. on pp. 36, 37).

[277] M. Uehara, S. Mori, C. H. Chen, and S. W. Cheong, *Nature* **399**, 560 (1999) `10.1038/21142` (cit. on pp. 36, 37).

[278] L. Zhang, C. Israel, A. Biswas, R. L. Greene, and A. de Lozanne, *Science* **298**, 805 (2002) `10.1126/science.1077346` (cit. on pp. 36, 37).

[279] G. R. Blake, L. Chapon, P. G. Radaelli, D. N. Argyriou, M. J. Gutmann, and J. F. Mitchell, *Physical Review B* **66**, 144412 (2002) `10.1103/PhysRevB.66.144412` (cit. on p. 37).

[280] M. Tokunaga, Y. Tokunaga, and T. Tamegai, *Physical Review Letters* **93**, 037203 (2004) `10.1103/PhysRevLett.93.037203` (cit. on p. 37).

[281] P. M. Leufke, A. K. Mishra, A. Beck, D. Wang, C. Kübel, R. Kruk, and H. Hahn, *Thin Solid Films* **520**, 5521 (2012) `10.1016/j.tsf.2012.04.064` (cit. on pp. 38, 41, 53–56, 58, 59, 61, 64).

[282] M. Angeloni, G. Balestrino, N. G. Boggio, P. G. Medaglia, P. Orgiani, and A. Tebano, *Journal of Applied Physics* **96**, 6387 (2004) `10.1063/1.1812599` (cit. on pp. 38, 53–55, 59, 65, 66).

[283] C. Aruta, G. Balestrino, A. Tebano, G. Ghiringhelli, and N. B. Brookes, *Europhys. Lett.* **80**, 37003 (2007) `10.1209/0295-5075/80/37003` (cit. on pp. 38, 53–55, 60).

[284] J. M. De Teresa, *Science* **286**, 507 (1999) `10.1126/science.286.5439.507` (cit. on pp. 38, 53, 54).

[285] J. Dho, N. H. Hur, I. S. Kim, and Y. K. Park, *Journal of Applied Physics* **94**, 7670 (2003) `10.1063/1.1628831` (cit. on pp. 38, 53, 54).

[286] D. Esteve, K. Postava, P. Gogol, G. Niu, B. Vilquin, and P. Lecoeur, *Physica Status Solidi (B)* **247**, 1956 (2010) `10.1002/pssb.200983960` (cit. on pp. 38, 53, 54).

[287] U. Gebhardt, N. Kasper, A. Vigliante, P. Wochner, H. Dosch, F. Razavi, and H.-U. Habermeier, *Physical Review Letters* **98**, 096101 (2007) `10.1103/PhysRevLett.98.096101` (cit. on pp. 38, 53, 54).

[288] M. Huijben, L. W. Martin, Y.-H. Chu, M. B. Holcomb, P. Yu, G. Rijnders, D. H. A. Blank, and R. Ramesh, *Physical Review B* **78**, 22 (2008) `10.1103/PhysRevB.78.094413` (cit. on pp. 38, 53–55, 64–66).

[289] A. M. Haghiri-Gosnet, J. Wolfman, B. Mercey, C. Simon, P. Lecoeur, M. Korzenski, M. Hervieu, R. Desfeux, and G. Baldinozzi, *Journal of Applied Physics* **88**, 4257 (2000) `10.1063/1.1309040` (cit. on pp. 38, 53, 54, 61, 64).

[290] T. Petrisor, M. S. Gabor, A. Boulle, C. Bellouard, C. Tiusan, O. Pana, and T. Petrisor, *Journal of Applied Physics* **109**, 1 (2011) `10.1063/1.3596807` (cit. on pp. 38, 41, 53–55, 58).

[291] J. H. Haeni, P. Irvin, W. Chang, R. Uecker, P. Reiche, Y. L. Li, S. Choudhury, W. Tian, M. E. Hawley, B. Craigo, A. K. Tagantsev, X. Q. Pan, S. K. Streiffer, L. Q. Chen, S. W. Kirchoefer, J. Levy, and D. G. Schlom, *Nature* **430**, 758 (2004) `10.1038/nature02773` (cit. on p. 38).

[292] M. Kawasaki, T. Maeda, R. Tsuchiya, and H. Koinuma, *Science* **266**, 1540 (1994) `10.1126/science.266.5190.1540` (cit. on pp. 38, 54, 55, 129).

[293] G. Koster, B. L. Kropman, G. J. H. M. Rijnders, D. H. A. Blank, and H. Rogalla, *Applied Physics Letters* **73**, 2920 (1998) `10.1063/1.122630` (cit. on pp. 38, 54, 55, 129).

[294] M. Kareev, S. Prosandeev, J. Liu, C. Gan, A. Kareev, J. W. Freeland, M. Xiao, and J. Chakhalian, *Applied Physics Letters* **93**, 061909 (2008) `10.1063/1.2971035` (cit. on pp. 38, 54, 55, 129).

[295] R. Peng, H. C. Xu, M. Xia, J. F. Zhao, X. Xie, D. F. Xu, B. P. Xie, and D. L. Feng, *Applied Physics Letters* **104**, 0 (2014) `10.1063/1.4866461` (cit. on pp. 38, 59).

[296] J. Simon, T. Walther, W. Mader, J. Klein, D. Reisinger, L. Alff, and R. Gross, *Applied Physics Letters* **84**, 3882 (2004) `10.1063/1.1738930` (cit. on pp. 38, 59, 62, 65, 91).

[297] A. Tebano, A. Orsini, P. G. Medaglia, D. Di Castro, G. Balestrino, B. Freelon, A. Bostwick, Y. J. Chang, G. Gaines, E. Rotenberg, and N. L. Saini, *Physical Review B* **82**, 214407 (2010) `10.1103/PhysRevB.82.214407` (cit. on pp. 38, 59, 65).

[298] H. Boschker, J. Kautz, E. P. Houwman, W. Siemons, D. H. A. Blank, M. Huijben, G. Koster, A. Vailionis, and G. Rijnders, *Physical Review Letters* **109**, 157207 (2012) `10.1103/PhysRevLett.109.157207` (cit. on pp. 38, 64).

[299] K. M. Abraham and M. Alamgir, *Journal of The Electrochemical Society* **137**, 1657 (1990) `10.1149/1.2086749` (cit. on p. 39).

[300] K. Murata, S. Izuchi, and Y. Yoshihisa, *Electrochimica Acta* **45**, 1501 (2000) `10.1016/S0013-4686(99)00365-5` (cit. on p. 39).

[301] B. Smitha, S. Sridhar, and A. A. Khan, *Journal of Membrane Science* **259**, 10 (2005) `10.1016/j.memsci.2005.01.035` (cit. on p. 39).

[302] X. Chen, K. Khor, S. Chan, and L. Yu, *Materials Science and Engineering: A* **335**, 246 (2002) `10.1016/S0921-5093(01)01935-9` (cit. on p. 39).

[303] R. Pornprasertsuk, O. Kosasang, K. Somroop, M. Horprathum, P. Limnonthakul, P. Chindaudom, and S. Jinawath, *Solid State Sciences* **13**, 1429 (2011) `10.1016/j.solidstatesciences.2011.04.015` (cit. on p. 39).

[304] S. P. Tung and B. J. Hwang, *Journal of Membrane Science* **241**, 315 (2004) `10.1016/j.memsci.2004.06.003` (cit. on p. 39).

[305] T. Sato, G. Masuda, and K. Takagi, *Electrochimica Acta* **49**, 3603 (2004) `10.1016/j.electacta.2004.03.030` (cit. on pp. 39, 72, 96).

[306] S. Zhang, N. Sun, X. He, X. Lu, and X. Zhang, *Journal of Physical and Chemical Reference Data* **35**, 1475 (2006) `10.1063/1.2204959` (cit. on p. 39).

[307] H. Abe and Y. Yoshimur, in *Ionic liquids: theory, properties, new approaches* (InTech, Feb. 2011), pp. 271–301, `10.5772/14335` (cit. on p. 39).

[308] C. Nanjundiah, S. McDevitt, and V. Koch, *Journal of the Electrochemical Society* **144**, 3392 (1997) `10.1149/1.1838024` (cit. on p. 39).

[309] T. Takekiyo, Y. Imai, H. Abe, and Y. Yoshimura, *Advances in Physical Chemistry* **2012**, 13 (2012) `10.1155/2012/829523` (cit. on p. 40).

[310] C. Largeot, C. Portet, J. Chmiola, P. L. Taberna, Y. Gogotsi, and P. Simon, *Journal of the American Chemical Society* **130**, 2730 (2008) `10.1021/ja7106178` (cit. on pp. 40, 72, 73).

[311] M. Ohring, *The Materials Science of Thin Films* (Elsevier, 1992), pp. 1–704, `10.1016/C2009-0-22199-4` (cit. on pp. 40, 55, 56).

[312] D. Bowen, *High resolution X-ray diffractometry and topography* (Taylor & Francis, 1998), ISBN: 0850667585 (cit. on p. 43).

[313] C. Hammond, *Measurement Science and Technology* **13**, 232 (2002) `10.1088/0957-0233/13/2/708` (cit. on p. 43).

[314] J. Clarke and A. I. Braginski, eds., *The SQUID Handbook. Vol. I Fundamentals and Technology of SQUIDs and SQUID Systems*, Vol. 21, 5 (Wiley-VCH, 2004), ISBN: 3-527-40229-2 (cit. on p. 45).

[315] J. Clarke and A. I. Braginski, eds., *The SQUID Handbook. Vol. II, Applications of SQUIDs and SQUID Systems* (Wiley-VCH, 2006), ISBN: 978-3-527-40408-7 (cit. on pp. 45, 46).

[316] B. D. Cullity and C. D. Graham, *Introduction to Magnetic Materials*, Vol. 53, 9 (John Wiley & Sons, Inc., 2008), pp. 1–30, `10.1002/9780470386323` (cit. on pp. 45, 46, 52).

[317] A. J. Bard and L. R. Faulkner, in *Electrochemical Methods: Fundamentals and Applications* (John Wiley & Sons, Inc., 2001), ISBN: 0471043729 (cit. on p. 48).

[318] M. Z. Bazant, B. D. Storey, and A. A. Kornyshev, *Physical Review Letters* **106**, 4 (2011) `10.1103/PhysRevLett.106.046102` (cit. on pp. 50, 72, 73, 94).

[319] M. F. El-Kady, M. Ihns, M. Li, J. Y. Hwang, M. F. Mousavi, L. Chaney, A. T. Lech, and R. B. Kaner, *Proceedings of the National Academy of Sciences* **112**, 4233 (2015) `10.1073/pnas.1420398112` (cit. on p. 50).

[320] S. Topolovec, H. Krenn, and R. Würschum, *Review of Scientific Instruments* **86**, 063903 (2015) `10.1063/1.4922462` (cit. on pp. 51, 52).

[321] A. Vailionis, H. Boschker, W. Siemons, E. P. Houwman, D. H. A. Blank, G. Rijnders, and G. Koster, *Physical Review B* **83**, 064101 (2011) `10.1103/PhysRevB.83.064101` (cit. on p. 54).

[322] T. Ohnishi, K. Shibuya, M. Lippmaa, D. Kobayashi, H. Kumigashira, M. Oshima, and H. Koinuma, *Applied Physics Letters* **85**, 272 (2004) `10.1063/1.1771461` (cit. on pp. 54, 55, 129).

[323] Y. Liang and D. A. Bonnell, *Surface Science* **310**, 128 (1994) `10.1016/0039-6028(94)91378-1` (cit. on pp. 55, 62, 91).

[324] R. Witte, R. Kruk, A. Molinari, D. Wang, S. Schlabach, R. A. Brand, V. Provenzano, and H. Hahn, *Journal of Physics D: Applied Physics* **50**, 025007 (2017) `10.1088/1361-6463/50/2/025007` (cit. on p. 56).

[325] L. Tauxe, *Paleomagnetic principles and practice*, 17 (Kluwer Academic Publishers, 1998), ISBN: 0792352580 (cit. on p. 58).

[326] M. Birkholz, *Thin Film Analysis by X-ray Scattering* (Wiley, Oct. 2006), pp. 1–11, `10.1002/3527607595` (cit. on p. 60).

[327] T. Santos, S. May, J. Robertson, and A. Bhattacharya, *Physical Review B* **80**, 155114 (2009) `10.1103/PhysRevB.80.155114` (cit. on p. 60).

[328] M. Sirena, L. Steren, and J. Guimpel, *Thin Solid Films* **373**, 102 (2000) `10.1016/S0040-6090(00)01113-5` (cit. on p. 60).

[329] R. Herger, P. R. Willmott, C. M. Schlepütz, M. Björck, S. A. Pauli, D. Martoccia, B. D. Patterson, D. Kumah, R. Clarke, Y. Yacoby, and M. Döbeli, *Physical Review B* **77**, 1 (2008) `10.1103/PhysRevB.77.085401` (cit. on pp. 62, 65, 91).

[330] T. T. Fister, D. D. Fong, J. A. Eastman, P. M. Baldo, M. J. Highland, P. H. Fuoss, K. R. Balasubramaniam, J. C. Meador, and P. A. Salvador, *Applied Physics Letters* **93**, 151904 (2008) `10.1063/1.2987731` (cit. on pp. 62, 91).

[331] D. Pesquera, G. Herranz, A. Barla, E. Pellegrin, F. Bondino, E. Magnano, F. Sánchez, and J. Fontcuberta, *Nature Communications* **3**, 1189 (2012) `10.1038/ncomms2189` (cit. on p. 64).

[332] L. Li, Z. Liao, Z. Diao, R. Jin, E. W. Plummer, J. Guo, and J. Zhang, *Physical Review Materials* **1**, 034405 (2017) `10.1103/PhysRevMaterials.1.034405` (cit. on p. 65).

[333] J. Z. Sun, D. W. Abraham, R. A. Rao, and C. B. Eom, *Applied Physics Letters* **74**, 3017 (1999) `10.1063/1.124050` (cit. on p. 65).

[334] A. Tebano, C. Aruta, S. Sanna, P. G. Medaglia, G. Balestrino, A. A. Sidorenko, R. De Renzi, G. Ghiringhelli, L. Braicovich, V. Bisogni, and N. B. Brookes, *Physical Review Letters* **100**, 2 (2008) `10.1103/PhysRevLett.100.137401` (cit. on p. 65).

[335] M. Bibes, L. Balcells, S. Valencia, J. Fontcuberta, M. Wojcik, E. Jedryka, and S. Nadolski, *Physical Review Letters* **87**, 067210 (2001) `10.1103/PhysRevLett.87.067210` (cit. on p. 65).

[336] J.-H. Liao, T.-B. Wu, S.-T. Ho, Y.-T. Chen, S.-U. Jen, and Y.-D. Yao, *Journal of Physics D: Applied Physics* **40**, 4586 (2007) `10.1088/0022-3727/40/15/033` (cit. on p. 65).

[337] A. Molinari, P. M. Leufke, C. Reitz, S. Dasgupta, R. Witte, R. Kruk, and H. Hahn, *Nature Communications* **8**, 15339 (2017) `10.1038/ncomms15339` (cit. on pp. 69, 71–79, 82, 83, 93, 94).

[338] Y. Zhu, S. Murali, M. D. Stoller, K. J. Ganesh, W. Cai, P. J. Ferreira, A. Pirkle, R. M. Wallace, K. A. Cychosz, M. Thommes, D. Su, E. A. Stach, and R. S. Ruoff, *Science* **332**, 1537 (2011) `10.1126./science.1200770` (cit. on p. 69).

[339] J. Liu, J. Essner, and J. Li, *Chemistry of Materials* **22**, 5022 (2010) `10.1021/cm101591p` (cit. on p. 69).

[340] M. S. Halper and J. C. Ellenbogen, in *Supercapacitors: a brief overview* (The MITRE Corporation, 2006) (cit. on p. 69).

[341] A. Lewandowski and M. Galiński, *Journal of Physics and Chemistry of Solids* **65**, 281 (2004) `10.1016/j.jpcs.2003.09.009` (cit. on p. 72).

[342] Y. Yoshida and G. Saito, *Physical Chemistry Chemical Physics* **13**, 20302 (2011) `10.1039/c1cp21783f` (cit. on p. 73).

[343] A. Molinari, H. Hahn, and R. Kruk, *Advanced Materials* **1703908**, 1703908 (2017) `10.1002/adma.201703908` (cit. on pp. 87–90, 92–95).

[344] H. Yuan, H. Shimotani, A. Tsukazaki, A. Ohtomo, M. Kawasaki, and Y. Iwasa, *Advanced Functional Materials* **19**, 1046 (2009) `10.1002/adfm.200801633` (cit. on p. 96).

[345] S. Dasgupta, G. Stoesser, N. Schweikert, R. Hahn, S. Dehm, R. Kruk, and H. Hahn, *Advanced Functional Materials* **22**, 4909 (2012) `10.1002/adfm.201200951` (cit. on pp. 96, 100).

[346] M. Favaro, B. Jeong, P. N. Ross, J. Yano, Z. Hussain, Z. Liu, and E. J. Crumlin, *Nature Communications* **7**, 12695 (2016) `10.1038/ncomms12695` (cit. on p. 97).

[347] M. A. Brown, Z. Abbas, A. Kleibert, R. G. Green, A. Goel, S. May, and T. M. Squires, *Physical Review X* **6**, 1 (2016) `10.1103/PhysRevX.6.011007` (cit. on p. 97).

[348] T. Iwasita and F. C. Nart, *Progress in Surface Science* **55**, 271 (1997) `10.1016/S0079-6816(97)00032-4` (cit. on p. 97).

[349] K.-I. Ataka, T. Yotsuyanagi, and M. Osawa, *The Journal of Physical Chemistry* **100**, 10664 (1996) `10.1021/jp953636z` (cit. on p. 97).

[350] Y. R. Shen and V. Ostroverkhov, *Chemical Reviews* **106**, 1140 (2006) `10.1021/cr040377d` (cit. on p. 97).

[351] D. M. Kolb, *Angewandte Chemie International Edition* **40**, 1162 (2001) `10.1002/1521-3773(20010401)40:7<1162::AID-ANIE1162>3.0.CO;2-F` (cit. on p. 97).

[352] I. Siretanu, D. Ebeling, M. P. Andersson, S. L. S. Stipp, A. Philipse, M. C. Stuart, D. van den Ende, and F. Mugele, *Scientific Reports* **4**, 4956 (2015) `10.1038/srep04956` (cit. on p. 97).

[353] J.-J. Velasco-Velez, C. H. Wu, T. a. Pascal, L. F. Wan, J. Guo, D. Prendergast, and M. Salmeron, *Science* **346**, 831 (2014) `10.1126/science.1259437` (cit. on p. 97).

[354] J. Hoffman, X. Hong, and C. H. Ahn, *Nanotechnology* **22**, 254014 (2011) `10.1088/0957-4484/22/25/254014` (cit. on pp. 98, 99).

[355] K.-I. Kobayashi, T. Kimura, H. Sawada, K. Terakura, and Y. Tokura, *Nature* **395**, 677 (1998) `10.1038/27167` (cit. on p. 98).

[356] M. B. Okatan, M. W. Cole, and S. P. Alpay, *Journal of Applied Physics* **104**, 104107 (2008) `10.1063/1.3026719` (cit. on p. 126).

[357] J. C. Jiang, Y. Lin, C. L. Chen, C. W. Chu, and E. I. Meletis, *Journal of Applied Physics* **91**, 3188 (2002) `10.1063/1.1446221` (cit. on p. 126).

[358] S. Bauer, S. Lazarev, A. Molinari, A. Breitenstein, P. Leufke, R. Kruk, H. Hahn, and T. Baumbach, *Journal of Synchrotron Radiation* **21**, 1 (2014) `10.1107/S1600577513034358` (cit. on p. 126).

Appendices

A Supplementary material

A.1 Introduction

A.1.1 About the definition(s) of ME coupling coefficient

The magnetoelectric (ME) coupling coefficients $\alpha_D = \Delta P/\Delta H$ (see Eq. 1.1) and $\alpha_C = \Delta M/\Delta E$ (see Eq. 1.2) are commonly used as benchmarks to describe the strength of the mutual coupling between electric and magnetic order parameters. Typically, α_D is expressed in units of [m s^{-1}] or [V cm^{-1} Oe^{-1}] (with inverse units for α_C). As pointed out by Eerenstein *et al.* [9], direct and converse ME coefficients are equal in strength only in the highly-restrictive scenario of (i) stress-free (ii) non-ferroic materials with linear coupling. On the one hand, (i) is given by the fact that when strain is used as mediator of the ME coupling, piezoelectricity provide a linear electromechanical response, whereas magnetostriction is a nonlinear magnetomechanical effect [2]. On the other hand, (ii) is directly related to the hysteretic (i.e. non linear[1]) behavior of magnetization and polarization of ferromagnets and ferroelectrics to an applied magnetic and electric field, respectively. As a workaround to obviate the inconvenience of non linearity, in presence of ferroelectricity/ferromagnetism α is conventionally calculated considering the values of electric/magnetic switching fields.

Although Eq. 1.1 and 1.2 convey the most general definitions of ME coupling, variant formulations of α can be found in the literature. Lou *et al.* [241] examined the ME coupling in FeGaB/PZN-PT heterostructures under conditions of resonance frequency. The ME coupling coefficient was calculated by $\alpha_C = \Delta H/\Delta E$, which links the electric field with the magnetic field instead of the magnetization M present in Eq. 1.2. From the same perspective, it was observed that as a substitute of Eq. 1.1, the direct ME effect can be described as $\alpha_D = \varepsilon_0 \chi \Delta E/\Delta H$, which considers the electric field (and not the electric polarization) induced by a magnetic field (with ε_0 the permittivity of vacuum and χ the electric susceptibility). The latter relation is also referred as ME *voltage* coefficient [31]. Heron *et al.* [13] investigated the behavior of the resistance versus magnetic and electric fields in $Co_{0.9}Fe_{0.1}/Cu/Co_{0.9}Fe_{0.1}/BiFeO_3$ spin valve heterostructures. An unconventional definition of $\alpha_C = \frac{2\mu_0 M_S t}{R_{AP} - R_P} \frac{dR(V)}{dV}$, which included the resistance as a parameter, was used to evaluate the ME effect (more details in [13]). Henrichs *et al.* [83] analyzed the ME effect on the microscale in multiferroic clusters of $(BiFe_{0.9}Co_{0.1}O_3)_{0.4}$–$(Bi_{1/2}K_{1/2}TiO_3)_{0.6}$ via piezoresponse and magnetic force microscopies. To estimate the change of polarization over a range of magnetic fields, a calibration factor K_{BFC} served to correlate the locally-measured piezoreponse force microscopy signal and the macroscopically-measured polarization of the bulk crystals. The ME coupling coefficient was estimated as $\alpha_D = \frac{2P_S m}{K_{BFC}}$ (more details in [83]). Leufke *et al.* [109] studied the electric field control of magnetism in $La_{1-x}Sr_xMnO_3/Pb_{1-y}Zr_yTiO_3$ (LSMO/PZT) composite heterostructures. Since the authors were able to quantitatively determine the values

---

[1] On the contrary linearity occurs for paramagnets and paraelectrics.

of magnetization M in LSMO and of electric-field-induced charge Q at the LSMO/PZT interface, the magnitude of ME coupling was computed considering $\alpha_C = \Delta M/\Delta Q$.

Possibly, the reason of using different definitions of α instead of the basic relations in Eq. 1.1 and 1.2 is due to the constraints given by experimental conditions and involved parameters. Nonetheless, since the variants of α are based on different physical quantities, caution should be taken before making a straight comparison of the values reported in the literature. As an example, it is interesting to critically compare the values of α_C calculated by Cherifi *et al.* [14] and Molegraff *et al.* [11] for state-of-the-art strain-mediated MEs and electrostatically-charged MEs, respectively.

Cherifi *et al.* [14] reported on a variation of magnetization in FeRh films of up to $\approx 550\,\mathrm{emu\,cm^{-3}}$ (with $\approx 70\,\mathrm{emu\,cm^{-3}}$ of reversible contribution) by exploiting strain coupling with an underlying BTO single crystal substrate poled by $E = \pm 0.4\,\mathrm{kV\,cm^{-1}}$ (with an applied voltage of ± 21 V). The corresponding shift in ferromagnetic ordering temperature was about 25 K, while the calculated giant ME coupling cofficient was $\alpha_C = \mu_0 \Delta M/\Delta E = 1.65 \cdot 10^{-5}\,\mathrm{s\,m^{-1}} = 8.2\,\mathrm{Oe\,cm\,V^{-1}}$ (i.e. $\alpha_C = 1\,\mathrm{Oe\,cm\,V^{-1}}$ considering $\approx 70\,\mathrm{emu\,cm^{-3}}$ of reversible contribution).

Molegraff *et al.* [11] attained via interfacial charge carrier doping in LSMO/PZT heterostructures $\alpha_C = 0.8 \cdot 10^{-3}\,\mathrm{Oe\,cm\,V^{-1}}$ by poling PZT with about ± 10 V (which considering a PZT thickness of 250 nm gives an electric field of $\pm 400\,\mathrm{kV\,cm^{-1}}$) at 100 K. The respective change in magnetization was $\approx 0.14\,\mu_B\,\mathrm{u.c.}^{-1} \approx 22\,\mathrm{emu\,cm^{-3}}$ (estimated by considering an LSMO unit cell volume of $0.0589 \cdot 10^{-21}\,\mathrm{cm^3}$). The overall shift of T_C was about 20 K. As stated by the authors, a direct comparison to bulk materials was difficult because of the interfacial nature of the ME effect.

From the values of $\alpha_C = \Delta M/\Delta E$ it is evident that the ME effect is much stronger in strain-mediated than electrostatically-doped solid-state systems. Apparently, this may be simply ascribed to the long-range nature of strain effects which affect larger portions of the magnetic active volume comparing to interfacial electrostatic charge doping. Indeed, the variation in magnetization ΔM is more than one order of magnitude larger with the strain-mediated approach (although the reversible contribution is almost comparable to electrostatic charging). Nonetheless, it is worth noticing that in the calculations of α_C the main parameter "killing" the size of ME effect in the work of Molegraaf *et al.* is the huge value of electric field E (three orders of magnitude larger than in Cherifi *et al.*). The reason is related to the prominent difference in thicknesses d of the respectively-used BTO substrate and PZT film, although in both cases the applied voltage V is commensurate (with the electric field given by $E = V/d$). Analogously, it can be easily shown that the "blind" usage of Eq. 1.2 is even more detrimental in case electrolyte-gating is exploited to control magnetism of a metallic electrode. Indeed, although only a few volts are applied, the formation of a sub-nanometer gap capacitor at the solid/liquid interface implies the presence of ultra-high electric fields of up to tens of $\mathrm{MV\,cm^{-1}}$ [20], as far as the effective thickness d of the gate-dielectric is only of a few nm [164]. Paradoxically, one could successfully manage to switch on/off magnetization by applying ultra-low voltages, but α_C would result to be several orders of magnitude lower than in the examples shown above. Thus, it becomes rather natural to question whether the current widely-used definition of α_C, which includes the electric field, is an appropriate choice to define the strength of ME coupling when comparing systems so different in their nature.

As an additional remark, it is worth commenting on some of the difficulties arising for the determination of an apparently-standard physical quantity such as the electric field.

It is well known that the response to an external electric field varies substantially from material to material. In general, owing to the screening produced by free charge carriers, E can penetrate only a fraction of unit cell in metals, while it goes several nanometers deep in semiconductors and even more in insulators. A precise quantification of the E-field screening length λ is by far a non-trivial task [137] and often (rough) approximations have to be made. In presence of inhomogeneous materials or phenomena such as phase separation [274], λ can remarkably change in different regions of the same specimen. Further, the value of λ may vary with temperature in case of materials undergoing a phase transition. Another important factor is the quality of surfaces and interfaces: making an analogy with dielectric capacitors, usually the electric field is calculated considering a parallel plate configuration with sharp interfaces (with $E = V/d$, as shown above). Although this assumption is widely accepted in macroscopic devices - in particular if the surface area is much larger than the dielectric thickness - the same criterion applied to nanoscale devices calls for atomically flat surfaces over large areas, which is often challenging to obtain. In addition, the parallel plate approximation is not valid anymore when E-fields are applied via local probe techniques such as scanning tunnelling miscroscopy or piezoresponse force microscopy due to the non-uniform field underneath the tip. This obstacle was also underlined by Henrichs *et al.* [83] for the calculation of α_C.

Considering the aforementioned problems related to the usage and determination of E, the question rises whether an alternative physical quantity may be appropriate for the evaluation of α. From a practical perspective, it is true that since the initial studies on ME coupling the *voltage* is the measured or applied control parameter in direct or converse ME effect [43, 51], respectively.

We now propose to consider $\alpha_C = \Delta M/\Delta V$ as a variant of Eq. 1.2. This definition was for example recently used by Zhao *et al.* [208], who reported on a ferromagnetic resonance frequency shift of 219 Oe under an E-bias of 1.5 V, which translates in $\alpha_C = 146$ Oe V^{-1}, in ultrathin films ($\approx$ 2.5 nm) of Co charged via IL. By applying the new definition of ME coupling coefficient to the experimental parameters of Cherifi and Molegraaf (considering the conversion factor $1\,\mathrm{emu\,cm^{-3}} = 4\pi\,\mathrm{Oe}$), it is obtained $\alpha_C = 164\,\mathrm{Oe\,V^{-1}}$ (and $21\,\mathrm{Oe\,V^{-1}}$ of reversible contribution) and $14\,\mathrm{Oe\,V^{-1}}$, respectively.

It is not our purpose here to further comment on the validity or non-validity of the proposed definition comparing to the more-established Eq. 1.2. We limit to underline that $\alpha_C = \Delta M/\Delta V$ may be more representative for better comparing the strength of ME coupling realized via different ME approaches. Furthermore, it may provide a valuable workaround to the often non-trivial determination of the electric field. Nonetheless, before validation of the presented considerations, a deeper analysis, in particular from theory, will be required.

Given the uncertainty in the utilization of an adequate standardized definition of α, in the Introduction of the current dissertation no values of ME coupling coefficient were provided, but rather the values of variation in magnetic response (such as saturation magnetization, Curie temperature or magnetic coercivity) on application of an external electric stimuli. In Chapters 4 and 5, data analysis and interpretation were presented on the basis of the definitions of α considered most meaningful and therein formulated.

A.2 Materials & Methods

A.2.1 Growth studies of $Ba_{1-x}Sr_xTiO_3$ perovskite films

$Ba_{1-x}Sr_xTiO_3$ (BST) is a dielectric material that may be utilized for realizing microwave tunable devices [356] and dynamic random access memories [357]. Its dielectric properties strongly depend on the structural quality. We investigated [358] the growth process of BST films onto MgO substrates by combining *in situ* pulsed laser deposition (PLD) and synchrotron diffraction techniques. The acquisition of time-resolved diffraction profiles during PLD growth allowed to perform a thickness dependence study. It was found that in the initial growth process, BST was epitaxially deposited onto MgO, but beyond a critical thickness of about 140 nm a new crystalline phase was formed. The onset of the second phase was attributed to strain relaxation mechanisms in the BST film, primarily due to the lattice mismatch with the underlying MgO substrate.

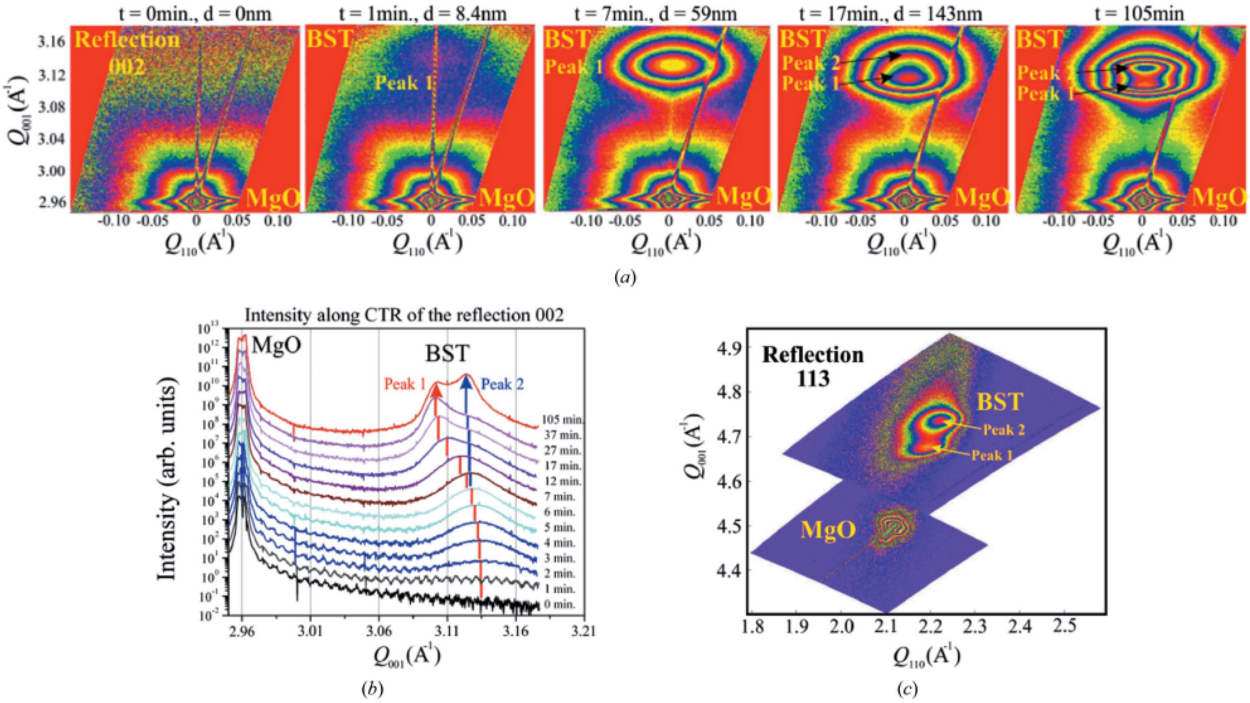

Figure A.1.: In situ XRD analysis of BST films grown on MgO substrate via PLD. (a) 2D reciprocal space maps (RSMs) recorded after 0, 1, 7, 17 and 105 min PLD deposition times. (b) Intensity profiles derived from the 2D-RSMs along the crystal truncation rod (CTR) of the 002 MgO reflection. The BST peak 1 shifts continuously and splits into peak 2 on increasing the film thickness. (c) 2D-RSM of the asymmetric 113 reflection after growth completion. (Reprinted with permission of the INTERNATIONAL UNION OF CRYSTALLOGRAPHY, Ref. [358], http://journals.iucr.org/)

A.2.2 Growth studies of $BaFeO_3$ perovskite films

$BaFeO_3$ may be implemented as a cathode material to realize protonic ceramic fuel cells, due to its potential ability to conduct both protons and electrons. $BaFeO_3$ films [253] with a thickness of about 25 nm were epitaxially grown on (001)-oriented STO:Nb substrates by PLD method using a fluence of 1.9 J cm^{-2}, a temperature of 700 °C and a pure oxygen pressure of 0.018 mbar (see Fig. A.2). The growth process was monitored via Reflection High Energy Electron Diffraction (RHEED). Afterwards microstructure, chemical composition and conducting properties were studied for $BaFeO_3$ films and their hydrated forms. It was found that water incorporation enhances the electronic and protonic conductivity as compared to argon-annealed films. Nonetheless, proton conduction in the films is lower than in $BaFeO_3$ bulk powders, possibly caused by strain effects induced by the substrate.

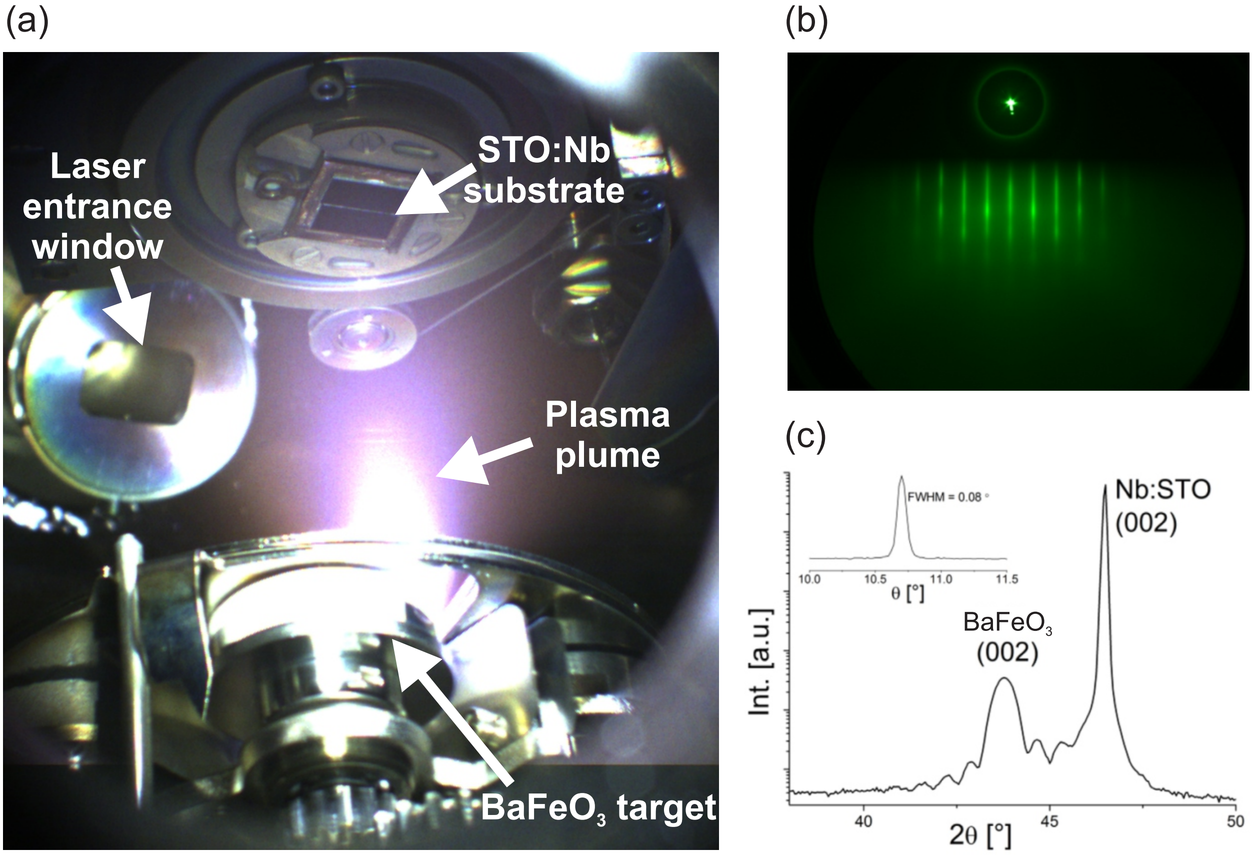

Figure A.2.: (a) Optical photograph taken during PLD deposition of $BaFeO_3$ films onto STO:Nb substrates. (b) RHEED pattern of an as-grown $BaFeO_3$ film. The streaky lines indicate the presence of a smooth film surface. (c) XRD pattern of an as-deposited $BaFeO_3$ thin film on STO:Nb with the presence of Laue fringes; the inset shows the rocking curve of the (001) film reflection. (Figures (b,c) reprinted by permission from IOP PUBLISHING: *Journal of Physics D: Applied Physics* [253], copyright 2017)

A.2.3 Temperature calibration of the LDMS system

As mentioned in Section 2.3.1, a temperature calibration (see Fig. A.3) was performed in order to precisely monitor the actual substrate temperature during Large-Distance Magnetron Sputtering (LDMS) deposition. The substrate is mounted on a stainless-steel sample holder whose backside is irradiated by four heating lamps. A type-K thermocouple located close to the lamps give constant reading of the temperature. Despite the short distance between lamps and sample holder, the substrate (that is placed on the front side of the holder) may have a significantly lower temperature due to faster heat dissipation (e.g. faster heat transfer with argon and oxygen gas inside the chamber). For this reason, a temperature calibration was carried out by mounting another type-K thermocouple tightly clamped between two metal sheets on the front side of the sample holder. The values of the two thermocouples were compared in a wide range of temperatures, thus leading to a relation for estimating more precisely the substrate temperature. Each temperature value was measured after waiting about 10-15 min in order to reach thermal equilibrium. Such temperature calibration method was found to be more reliable than monitoring the current flowing through the lamps, since its value may change after prolonged chamber usage due to increase in contact resistance after oxidation of lamp sockets and clamping screws.

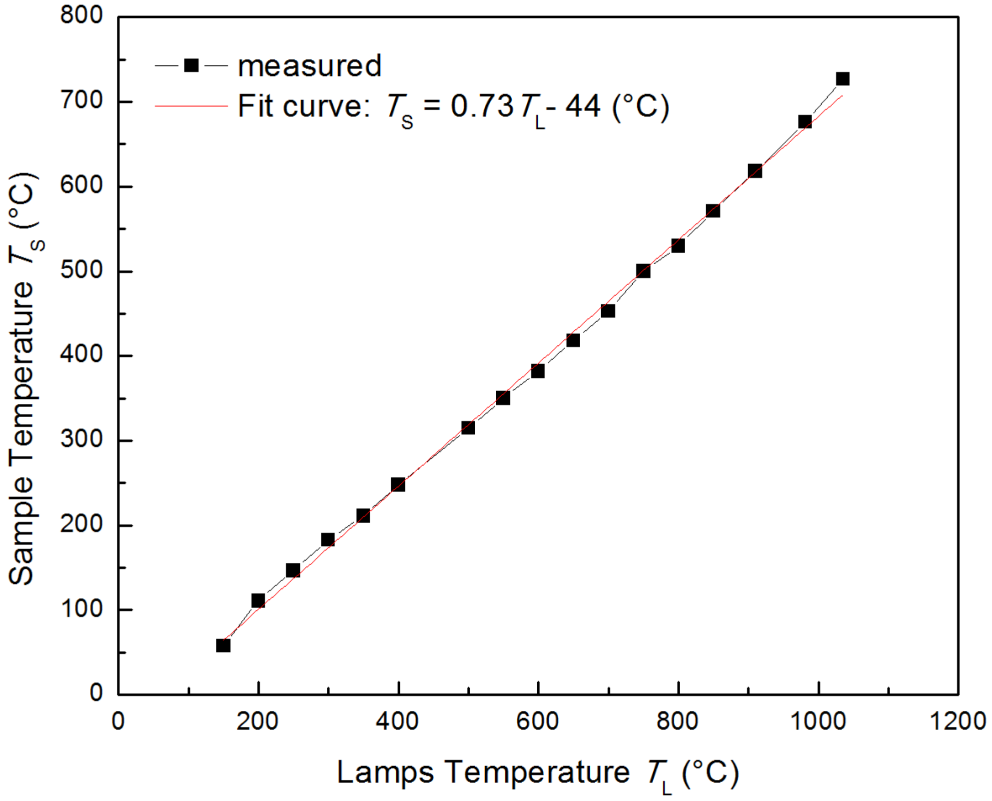

Figure A.3.: Temperature calibration of heated LDMS manipulator. Dependence of substrate temperature (front side of sample holder) on the temperature measured in proximity of the heating lamps (back side of sample holder). The equation represents the linear fit for extrapolation of the actual substrate temperature.

A.3 Growth and characterization of epitaxial thin films of LSMO

A.3.1 Surface treatment procedure of STO substrates

The atomic control of the STO crystal surface was realized for the first time by Kawasaki et al. [292] in 1994. Considering that $SrTiO_3$ is a cubic perovskite composed of TiO_2 (an acidic oxide) and SrO (a basic oxide) stacking layers, it was demonstrated that by controlling the pH of a wet etch solution it is possible to selectively dissolve one of the two components and attain an atomically smooth surface terminated with the non-etched layer. A TiO_2 coverage of about 100% was attained by etching SrO atomic planes using a NH_4F-HF solution. Subsequently, it was found that also alternative (and less dangerous) solutions such as HCl-HNO_3 can be used for the treatment of STO substrates and that high-temperature annealing in air enhances surface reconstruction [293, 294, 322].

The following points list the steps carried out for improving the STO surface quality in case that too many particles and impurities were present on the as-received epi-polished substrates:

- Ultrasonic cleaning in deionized water at 70 °C with for 25 min. The purpose is the formation of SrOH complexes from SrO.
- Ultrasonic cleaning in HCl:HNO3 (3:1) at room temperature for 12 min. The acid selectively etches and removes the SrOH present at the surface, leaving a TiO2 terminated surface.
- Rinsing of the substrates in DI water, followed by ultrasonic cleaning for 5 min acetone and then 5 min in methanol at room temperature. These steps are necessary for removing any residual of eventual acidic contamination.
- Annealing for 30 min at 1000 °C in air. This is fundamental in order to achieve atomically flat terraces with 1 u.c. steps (chemical etching alone is generally not enough).

The same procedure was also performed on STO:Nb substrates, which displayed final characteristics similar to undoped STO.

A.4 Magnetoelectric coupling in LSMO thin films gated with DEME-TFSI ionic liquid

Table A.1.: Summary of the ME results of the temperature-dependence study for $\Delta Q \approx 4\,\mu\mathrm{C\,cm^{-2}}$.

T (K)	ΔV (mV)	ΔQ (μC cm^{-2})	C (μF cm^{-2})	α (μ_B/h^+)
326	350	3.4	10.4	+0.5
325	380	3.9	10.8	+1.4
324	380	3.6	10.1	+2.7
323	400	3.8	10.1	+4.3
322	420	3.9	9.9	+5.2
321	420	3.7	9.6	+5.5
320	420	3.7	9.4	+5.7
315	440	3.7	8.8	+6.2
300	500	3.9	8.2	+5.9
290	530	3.9	7.8	+4.7
280	560	4.1	7.8	+3.2
270	560	3.9	7.6	+1.8
260	580	3.9	7.4	+0.2
258	580	4.0	7.0	+0.02
255	580	3.7	7.0	-0.5
250	600	3.9	7.0	-1.3
245	600	3.9	6.8	-1.9
240	600	4.1	7.2	-2.6
235	600	4.5	8.0	-2.9
230	550	4.5	8.5	-3.2
225	400	3.3	8.8	-2.9
220	420	3.8	9.7	-3.0

Table A.2.: Summary of the ME results of the isothermal charge-dependence study at 220 K. The lettering corresponds to the plots in Fig. 4.7. The data of plot **f** refer to an experiment performed with a starting bias voltage $V_b \approx -1.3\,\mathrm{V}$. Unless specified, the errors on the reported data are within a 5% accuracy.

Plot	ΔV (mV)	$\Delta Q\,(\mu\mathrm{C\,cm^{-2}})$	$C\,(\mu\mathrm{F\,cm^{-2}})$	$\alpha\,(\mu_B/h^+)$
	200	1.5	8.1	-2.9
	300	2.5	9.0	-3.1
a	400	3.7	9.8	-3.1
	500	5.0	10.6	-2.9
	600	6.5	11.3	-3.0
	700	8.0	12.0	-2.9
	800	9.7	12.6	-2.8
	1000	13.1	13.7	-2.7
	1500	23.3	16.3	-2.6
b	2000	38.0	20.0	-2.5
	2500	57.2	24.3	-2.1
c	2900	87.1	32.1	-1.8(2), +1.3
d	3300	163.4	53.8	-1.7(2), +1.8(2)
e	3700	266.5	85.6	-1.4(6), +2.0(5)
f	300	6.7	27.6	+2.2

Table A.3.: Summary of the ME results of the isothermal charge-dependence study at 270 K. The lettering corresponds to the plots in Fig. 4.8. The data of plot **e** refer to an experiment performed with a starting bias voltage $V_b \approx +0.8\,\mathrm{V}$. Unless specified, the errors on the reported data are within a 5% accuracy.

Plot	ΔV (mV)	$\Delta Q\,(\mu\mathrm{C\,cm^{-2}})$	$C\,(\mu\mathrm{F\,cm^{-2}})$	$\alpha\,(\mu_B/h^+)$
a	800	19	30	+1.6
b	1200	47	48	+1.8, –0.7
c	1600	72	54	+2.4, –0.6
d	2500	169	83	+2.5, –1.1(3)
e	400	4	18	–2.0

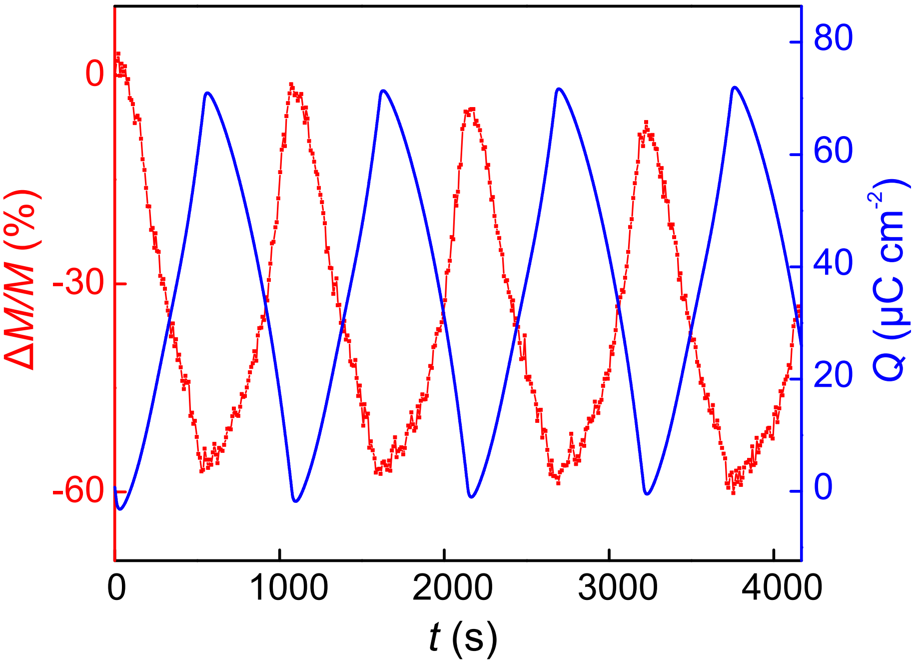

Figure A.4.: ME effect in an ultrathin LSMO film (≈ 4 nm). A maximum magnetic modulation $|\Delta M/M| \approx 60\%$ was attained at 232 K using a potential window of 1.6 V. Application of a larger ΔV resulted in a loss of reversibility.

List of Figures

List of Tables

List of acronyms and symbols

Acronyms

AC	Alternating Current
AFM	Atomic Force Microscopy
AF	Antiferromagnetic
BF_4	tetrafluoroborate
BFO	$BiFeO_3$
BTO	$BaTiO_3$
CMR	Colossal Magnetoresistance
CE	Counter Electrode
CV	Cyclic Voltammogram
DC	Direct Current
DE	Double-Exchange
DEME	Diethylmethyl(2-methoxyethyl)ammonium
DTFO	$Dy_{0.70}Tb_{0.30}FeO_3$
EB	Exchange Bias
EDL	Electric Double Layer
EDX	Energy-Dispersive X-ray Spectroscopy
EMI	1-Ethyl-3-methylimidazolium
FC	Field Cooling
FET	Field-Effect Transistor
FE	Ferroelectric
FIB	Focused Ion Beam
FM	Ferromagnetic
FWHM	Full Width at Half Maximum
GMR	Giant Magnetoresistance

HRXRD	High-Resolution X-ray Diffraction
IL	Ionic Liquid
LBMO	$La_{1-x}Ba_xMnO_3$
LCMO	$La_{1-x}Ca_xMnO_3$
LDMS	Large-Distance Magnetron Sputtering
LSAT	$(La_{0.3}Sr_{0.7})(Al_{0.65}Ta_{0.35})O_3$
LSCO	$La_{1-x}Sr_xCoO_3$
LSMO	$La_{1-x}Sr_xMnO_3$
MBE	Molecular Beam Epitaxy
MDL	Magnetic Dead Layer
ME	Magnetoelectric
MF	Multiferroic
MOKE	Magneto-Optical Kerr Effect
MPMS	Magnetic Properties Measurement System
MR	Magnetoresistance
OCP	Open Circuit Potential
PEEK	Polyether Ether Ketone
PLD	Pulsed Laser Deposition
PM	Paramagnetic
PMMA	Poly(Methyl MethAcrylate)
PPMS	Physical Properties Measurement System
PS	Pseudocapacitance
PVD	Physical Vapor Deposition
PZT	$PbZrTiO_3$
QCM	Quartz Crystal Microbalance
RBS	Rutherford Backscattering Spectroscopy
RC	Rocking Curve
RE	Reference Electrode
RF	Radio Frequency

RMS	Root Mean Squared
RSM	Reciprocal Space Map
RSO	Reciprocating Sample Option
r.s.u.	reciprocal space units
RT	Room Remperature
SC	Supercapacitor
SE	Superexchange
SEM	Scanning Electron Microscopy
SQUID	Superconductive Quantum Interference Device
STEM	Scanning Transmission Electron Microscopy
STM	Scanning Tunneling Microscopy
STO:Nb	$SrTiO_3$:Nb
STO	$SrTiO_3$
TEM	Transmission Electron Microscopy
TFSI	Bis(trifluoromethylsulfonyl)imid
TMP	Turbo Molecular Pump
TMR	Tunnel Magnetoresistance
u.c.^{2}	unit cell area
u.c.	unit cell
UHV	Ultra-High Vacuum
VSM	Vibrating Sample Magnetometer
WE	Working Electrode
XAS	X-ray Absorption Spectroscopy
XPS	X-ray Photoelectron Spectroscopy
XRD	X-ray Diffraction
XRR	X-ray Reflectometry
ZFC	Zero-Field Cooling

Symbols

A	area
a	in-plane lattice parameter
a_{pc}	pseudocubic lattice constant
α	ME coupling coefficient
α_{D}	direct ME coupling coefficient
α_{C}	converse ME coupling coefficient
c	out-of-plane lattice parameter
C	capacitance
d	film thickness
ΔV	potential window
$d_{h,\,k,\,l}$	lattice plane spacing
d_{sep}	target-substrate separation
e	electron
E	electric field
ε_0	vacuum permittivity
ε	strain
Γ	tolerance factor
$h,\ k,\ l$	Miller indices
h^+	electron hole
H	magnetic field
H_{c}	coercive magnetic field
J	current density
κ	relative permittivity
M	magnetization
M_{sat}	saturation magnetization
M_{σ}	magnetization per u.c.^{2}
M	magnetization
M_{r}	remanent magnetization

μ_0	vacuum permeability
μ_B	Bohr magneton
n_0	charge carrier density
p_{O2}	O_2 partial pressure
p_{work}	working pressure
P	polarization
φ	azimuth angle
Q	surface charge
R	resistance
ρ	resistivity
σ	stress
t	time
T	temperature
T_C	Curie temperature
T_{cross}	crossover temperature of ME modulation
T_{MI}	metal-insulator transition temperature
θ	Bragg angle
τ	time constant
V	voltage
V_{bias}	bias voltage
ω	angle of incidence
x	doping level
χ	eucentric angle of tilting

Personal data

Curriculum vitae

Personal Data

Name:	Alan Molinari
Date of birth:	09.07.1986
Place of birth:	Bologna
Citizenship:	italian/british

Scientific Education

September 2000 – July 2005	Scientific high school *Leonardo da Vinci*, Casalecchio di Reno (BO), Italy
October 2005 – December 2010	Bachelor of Science (B. Sc.) in Physics at University of Bologna (UNIBO), Italy
December 2010 – December 2012	Master of Science (M. Sc.) in Physics of Matter at UNIBO, Italy. Master thesis "Synthesis of ordered nanodots for hydrogen storage by molecular beam epitaxy using ultra-thin alumina masks" in joint project with the Institute of Nanotechnology (INT) - Karlsruhe Institute of Technology (KIT), Germany
March 2013 – present	Doctoral studies in Material Science at INT - KIT

Scientific Career

January 2011 – July 2011	Research collaborator at the Institute of Physics (UNIBO) for measurements of mechanical properties via instrumented nanoindentation
February 2012 – October 2012	Erasmus placement internship and guest student at INT - KIT. Practical experience with a molecular beam epitaxy apparatus (MBE)
March 2013 – present	Research associate at INT - KIT. Scientist in charge of sputtering and pulsed laser deposition (PLD) units of the Tunable group. Training of new operators in sputtering, MBE and PLD growth techniques

Publications

Journal articles

Proton Conduction in Grain-Boundary-Free Oxygen-Deficient $BaFeO_{2.5+\delta}$ Thin Films
A. Benes, A. Molinari, R. Witte, R. Kruk, J. Brötz, R. Chellali, H. Hahn, and O. Clemens, **Materials** 11, 52 (2017), 10.3390/ma11010052.

Voltage-Controlled On/Off Switching of Ferromagnetism in Manganite Supercapacitors
A. Molinari, H. Hahn, and R. Kruk, **Advanced Materials** 1703908 (2017), 10.1002/adma.201703908.

Hybrid supercapacitors for reversible control of magnetism
A. Molinari, P. M. Leufke, C. Reitz, S. Dasgupta, R. Witte, R. Kruk, and H. Hahn, **Nature Communications** 8, 15339 (2017), 10.1038/ncomms15339.

Structure and conductivity of epitaxial thin films of barium ferrite and its hydrated form $BaFeO_{2.5-x+\delta}(OH)_{2x}$
P. A. Sukkurji, A. Molinari, A. Benes, C. Loho, V. S. K. Chakravadhanula, S. K. Garlapati, and O. Clemens, **Journal of Physics D: Applied Physics** 50, 115302 (2017), 10.1088/1361-6463/aa5718.

Epitaxial strain-engineered self-assembly of magnetic nanostructures in FeRh thin films
R. Witte, R. Kruk, A. Molinari, D. Wang, S. Schlabach, R. A. Brand, V. Provenzano, and H. Hahn, **Journal of Physics D: Applied Physics** 50, 025007 (2017), 10.1088/1361-6463/50/2/025007.

Interface and strain effects on the H-sorption thermodynamics of size-selected Mg nanodots
A. Molinari, F. D'Amico, M. Calizzi, Y. Zheng, C. Boelsma, L. Mooij, Y. Lei, H. Hahn, B. Dam, and L. Pasquini, **International Journal of Hydrogen Energy** 41, 9841 (2016), 10.1016/j.ijhydene.2016.02.003.

Isotropic microscale mechanical properties of coral skeletons
L. Pasquini, A. Molinari, P. Fantazzini, Y. Dauphen, J-P. Cuif, O. Levy, Z. Dubinsky, E. Caroselli, F. Prada, S. Goffredo, M. Di Giosia, M. Reggi, and G. Falini, **Journal of the Royal Society Interface** 12 (2015), 10.1098/rsif.2015.0168.

The power of *in situ* pulsed laser deposition synchrotron characterization for the detection of domain formation during growth of $Ba_{0.5}Sr_{0.5}TiO_3$ on MgO
S. Bauer, S. Lazarev, A. Molinari, A. Breitenstein, P. Leufke, R. Kruk, H. Hahn, and T. Baumbach, **Journal of Synchrotron Radiation** 21, 386 (2014), 10.1107/S1600577513034358.

Conference contributions

Magnetoelectric effect in $La_{(1-x)}Sr_xMnO_3$ thin films gated via an ionic liquid
A. Molinari, R. Kruk, S. Dasgupta, and H. Hahn,
International Conference on Magnetic Materials and Applications (ICMAGMA), 1–3 February 2017, *Hyderabad* (India).

Voltage-induced tuning of magnetism in $La_{1-x}Sr_xMnO_3$ thin films by means of an ionic liquid

A. Molinari, P. M. Leufke, C. Reitz, S. Dasgupta, R. Kruk and H. Hahn,
61st Annual Conference on Magnetism and Magnetic Materials (MMM), 31 October - 4 November 2016, *New Orleans* (USA).

Reversible control of magnetism in $La_{1-x}Sr_xMnO_3$/ionic liquid systems

A. Molinari, P. M. Leufke, C. Reitz, S. Dasgupta, R. Kruk and H. Hahn,
Frühjahrstagung der Deutsche Physikalische Gesellschaft (DPG), 9–11 March 2016, *Regensburg* (Germany).

Magnetoelectric coupling at the $La_{1-x}Sr_xMnO_3$/ionic liquid interface

A. Molinari, P. M. Leufke, C. Reitz, R. Kruk and H. Hahn,
Frühjahrstagung der Deutsche Physikalische Gesellschaft (DPG), 15–20 March 2015, *Berlin* (Germany).

In situ PLD synchrotron characterization for the detection of domain formation during $Ba_{0.5}Sr_{0.5}TiO_3$ growth on MgO

S. Bauer, A. Molinari, S. Lazarev, A. Breitenstein, P. Leufke, R. Kruk, H. Hahn, and T. Baumbach,
Frühjahrstagung der Deutsche Physikalische Gesellschaft (DPG), 30 March - 4 April 2014, *Dresden* (Germany).

Kinetics and thermodynamics of hydrogen sorption in Mg-Ti nanostructures

L. Pasquini, M. Calizzi, A. Molinari, H. Hahn, Y. Zheng, Y. Lei, C. Boelsma, and B. Dam,
International Symposium on Materials for Energy Storage and Conversion (^{m}ESC-IS), 7—9 September 2015, *Ankara* (Turkey).

Acknowledgments

I would like to express my sincere gratitude to my supervisor, Prof. Horst Hahn. He gave me the opportunity to grow as a young scientist in a very stimulating working environment and to make practical experience with extraordinary experimental facilities. I am deeply grateful for his constant support and professional guidance during my PhD project.

I wish to thank my Co-referee, Prof. Ralph Krupke, and the other members of the PhD examination committee, Prof. Wolfgang Ensinger and Prof. Heiko Wende, for the time devoted to evaluating my work.

Then I would like to thank my group leader, Dr. Robert Kruk. The door of his office was always open whenever I had a doubt about a scientific topic. His in-depth knowledge of many physical concepts and his ability to explain them in a clear and easy manner rendered our discussions as enjoyable as formative.

I owe a lot to several members of the Hahn group that shared their experience and knowledge with me. Philipp Leufke, who I consider as a second mentor, introduced me to the fundamentals of electric field control of magnetism in LSMO. Furthermore, he trained me in the fabrication of LSMO films via Large-Distance Magnetron Sputtering. Christian Reitz initiated me to the gating experiments on LSMO/IL devices. He also did a great job in keeping the SQUID lab in optimum working conditions. Ralf Witte is an invaluable fellow that instructed me in the usage of the X-ray diffractometer and supported me in many other circumstances when I needed help. The critical eye of Subho Dasgupta allowed me to look at my results from a different perspective, which eventually led to a deeper analysis and so a better understanding of the charging phenomena at the LSMO/IL interface. I had the luck to benefit of the useful suggestions offered by an expert scientist as Richard Brand. The highly-skilled hands of our technician, Martin Limbach, greatly facilitated the maintenance and customization of the lab equipment.

I acknowledge the TEM group at the Institute of Nanotechnology (INT), in particular Christian Kübel and Amari Houari, and André Beck from the Institut für Festkörperphysik, that performed structural-TEM and chemical-RBS characterization of some LSMO samples, respectively.

I wish to thank Birgit Limmer, Patricia Jäger, Christine Fischer, Hase Antje, Susanne Speck and Renate Hernichel, for their availability and assistance in administrative matters.

The financial support by Deutsche Forschungsgemeinschaft (DFG) under Grant No. HA1344/34-1 is gratefully acknowledged.

I would like to thank current and previous members of the Tunable, Printable and Nanoglass groups. There is always a nice atmosphere at work and amusing moments during lunch, coffee breaks and group outings never miss.

Friends have been a precious source of moral support during the last years. Thanks to Nico, Thomas, Hannah, Caro, Santi, Ralf, Mohsen, Elena, Francesco, Alessia, Cristina and Ivan for the good time spent together in Karlsruhe. I cannot forget to mention the relaxing and delightful weekends together with Davide and Melanie in Tübingen. A special thank also to my friends in Bologna, who make me feel as if I never left Italy every time I have the chance to visit them.

My deepest appreciation goes to my family, in particular my parents and brothers, and Alice for their love and for being ever present in good and hard times.